National Library of Canada
Acquisitions and Bibliographic Services Branch
395 Wellington Street
Ottawa, Ontario
K1A 0N4

Bibliothèque nationale du Canada
Direction des acquisitions et des services bibliographiques
395, rue Wellington
Ottawa (Ontario)
K1A 0N4

Your file Votre référence

Our file Notre référence

NOTICE

The quality of this microform is heavily dependent upon the quality of the original thesis submitted for microfilming. Every effort has been made to ensure the highest quality of reproduction possible.

If pages are missing, contact the university which granted the degree.

Some pages may have indistinct print especially if the original pages were typed with a poor typewriter ribbon or if the university sent us an inferior photocopy.

Reproduction in full or in part of this microform is governed by the Canadian Copyright Act, R.S.C. 1970, c. C-30, and subsequent amendments.

AVIS

La qualité de cette microforme dépend grandement de la qualité de la thèse soumise au microfilmage. Nous avons tout fait pour assurer une qualité supérieure de reproduction.

S'il manque des pages, veuillez communiquer avec l'université qui a conféré le grade.

La qualité d'impression de certaines pages peut laisser à désirer, surtout si les pages originales ont été dactylographiées à l'aide d'un ruban usé ou si l'université nous a fait parvenir une photocopie de qualité inférieure.

La reproduction, même partielle, de cette microforme est soumise à la Loi canadienne sur le droit d'auteur, SRC 1970, c. C-30, et ses amendements subséquents.

Canada

AUTOMATED MANUFACTURING OF COMPOSITE COMPONENTS BY THERMOPLASTIC TAPE WINDING AND FILAMENT WINDING

Sanjay Kumar Mazumdar

A Thesis
in The Department
of
Mechanical Engineering

Presented in Partial Fulfilment of the Requirements
for the Degree of Doctor of Philosophy at
Concordia University
Montreal, Quebec, Canada

October 1994

National Library
of Canada

Acquisitions and
Bibliographic Services Branch

395 Wellington Street
Ottawa, Ontario
K1A 0N4

Bibliothèque nationale
du Canada

Direction des acquisitions et
des services bibliographiques

395, rue Wellington
Ottawa (Ontario)
K1A 0N4

Your file Votre référence

Our file Notre référence

ISBN 0-612-01285-9

Canada

ABSTRACT

Automated Manufacturing of Composite Components by Thermoplastic Tape Winding and Filament Winding

Sanjay Kumar Mazumdar, Ph D
Concordia University, 1994

Advanced composites are capable of meeting many demanding requirements for automobile and aircraft structures However lack of efficient manufacturing techniques and higher fabrication cost prohibit their widespread use This study deals with two manufacturing processes thermoplastic tape winding and filament winding on a two-axis machine These techniques have potential for automation and low fabrication cost.

For the thermoplastic tape winding process, laser and hot nitrogen gas are used as heat sources for on-line consolidation of incoming APC-2 thermoplastic tape with preconsolidated laminate Since consolidation is a common step in many of the forming processes, the knowledge gained by this study can be beneficial for various processing methods including repair and joining of thermoplastic composites. In the thermoplastic tape winding process several processing parameters influence the quality of a part. The dominant parameters are heat intensity, tape feed rate and consolidation pressure Effect of these three process parameters on temperature history, crystallinity, process induced deformations and quality of bond are examined Process models which relate the heat intensity, tape speed and consolidation pressure to the temperature history and degree of intimate contact are presented for an on-line tape consolidation process. Suitable manufacturing conditions for well consolidated part are determined. Because of lack of a standard technique for the characterization of quality of bond for ring specimens, short beam shear tests, double cantilever curved beam tests, and scanning electron microscopic tests were performed. The effectiveness of each method in evaluating the bond quality was determined. The Taguchi method was implemented for estimating the contribution of individual process parameters on the development of bond strength In addition, a kinematic model for the manufacture of non-axisymmetric cylindrical components using laser as a heat source was developed. Based on this model, an experimental set-up was designed and built Elliptical rings were fabricated using laser as a heat source

For filament winding using two axis machines, a new method, the Geometric Approach, is presented. This method allows one to determine the winding motion for various kinds of mandrel shapes such as axisymmetric, non-axisymmetric, cylindrical and non-cylindrical The method is found to be faster and more cost-effective as compared to teach-in-programming, simulation and CAD/CAM techniques. For certain shapes, such as mandrels with polygonal cross-sections, the Geometric Approach gives exact solution for determining the winding motion Techniques for the prediction of fiber angle distribution for known machine motion are not available Closed form and numerical solutions are presented for computing the fiber angle distribution for known equations of machine motions. This is important during start-up and reversal period of the filament winding operation.

ACKNOWLEDGMENTS

Since I have undertaken the difficult task of acknowledging the contributions of others in my thesis work, I should admit in the beginning that I can not do full justice to every individual who contributed directly or indirectly in my thesis

First of all, with great devotion I acknowledge the grace of God for successful completion of my thesis.

The amount of work, which I completed during my Ph.D. work could not be done without the help of my supervisor, friends and colleagues. My sincere gratitude to all of those with whom I discussed several topics of my thesis.

The role of a supervisor during the Ph.D work of a student is very important in making the student's life comfortable I am very grateful to Professor S.V. Hoa for his supervision, help, pleasant attitude and support throughout my thesis. Because of his co-operation I spent a comfortable life in Montreal. Professor Hoa provided excellent experimental facilities for my research. He also provided financial support for attending international conferences to improve the quality of my research and to broaden my knowledge about the subject. The financial support for this thesis work came from Natural Science and Engineering Research Council (NSERC), Canada.

I am thankful to Professor Xinran Xiao for fruitful discussions, encouragement and help during my research work. I express my thanks to my thesis committee members: Professors Latinovic, Mcqueen, Feldmen and Gillespie for their time and effort in evaluating my thesis. I highly appreciate the co-operation and discussion of my colleagues and friends during my research work. Special thanks to Paul Ouellette, Mustaq Ahmed, G.K. Adil, Bharat Bhushan, Greg Rohrauer, Tarique, John Klironomous, Larry Craig, Han, Kim, Danielle, and Li Lan.

I am grateful to the Concordia University community and staff for providing me pleasant atmosphere, good working conditions and service during my Ph D. work My special thanks to machine shop staff Paul, Hans, Brian and Ernst for building expermental set-ups for my research work Thanks to John Elliot and Joe for their assistance in my experimental work. I also wish to express thanks to Janete for helping me in preparing the samples for microstructure study and to Donna for performing DSC tests. My sincere thanks to International Student Advisors Claudette and Pat for improving international students' life in Montreal.

I wish to express my sincere thanks to the scientific community of the world for building the scientific structures I needed to carry out my Ph.D work. Their discoveries were the stepping stones for this thesis work.

In addition to academic life, I had very good social life in Montreal. My special thanks to Sanjay Patel, Maya Patel, Mahesh, Rajan, Jayant, Ramalingom, Rabindran, Balchander, Sanju, Kanan, Dinakar, Narayan Swamy, Valluru, Subbu, Sumana, Kshitija, Anindita, Meenakshi, Sutanuka, Somitro, Sakuntala, Arun, Meenakshi and many others. Because of them, I had smooth, peaceful and happy life during my stay at Concordia University.

My heartfelt regards to my parents. Because of their support, love, sacrifice and blessings I could pursue my Ph.D. program. Thanks to my brothers, sisters, and relatives for their encouragement and best wishes towards my goal. Finally I wish to express my deep appreciation to my wife Gargi whom I married on May 2, 1993. Because of her patience, understanding, charming, warm and caring nature, I had a marvellous life during last phase of my thesis.

Surrendered to the
Lord of Universe

TABLE OF CONTENTS

PART I THERMOPLASTIC TAPE WINDING

PART II FILAMENT WINDING

Chapter 9 DIRECT KINEMATICS OF FILAMENT WINDING 236

LIST OF TABLES

LIST OF FIGURES

CHAPTER 1

INTRODUCTION

Composite materials have fully established themselves as important engineering materials and are now quite common place around the world Early military applications during World War II led to large-scale commercial applications, particularly in the marine industry during the late 1940s and early 1950s. Today, industries such as aircraft, automobiles, sporting goods, electronics, and appliances are using many components made of fiber-reinforced plastics, and these composites are routinely designed, manufactured, and used The advantages of designing with polymer composites over metals include weight savings of 20 to 50 % when compared to aluminum as well as excellent long-term properties such as creep, fatigue and corrosion resistance.

A composite material is a combination of several materials, two in most cases, namely the matrix resin and the reinforcing fiber. Fibers are made of carbon, glass, kevlar, aramid, metal or ceramic. The matrix may be polymeric, metallic or ceramic. An overview of composite materials, their mechanical properties compared to other materials and the different manufacturing techniques used to process them can be found in references [1,2]. A composite material offers the advantage of exhibiting higher performance than any of its components In addition, selective mechanical properties can be obtained in composites. The isotropic structure of alloys and metals does not allow such selective properties. Polymer composites offer a unique combination of light weight, high stiffness and strength, corrosion and solvent resistance, and good electrical properties not available with other materials. In polymer composites, thermosets and thermoplastics are two of the main matrix materials of interest.

Early in the 1980s, the composites industry began evaluating a new generation of composites utilizing thermoplastic matrix polymers. These products like APC-2 (PEEK matrix composites) - have generated tremendous interest due to several advantages that thermoplastic composites offer over thermosetting composites Interesting work has been done on these materials. Recently two books were written on various aspects of PEEK/Carbon thermoplastic composites [3,4] In general thermoplastic composites have better solvent resistance, greater damage tolerance, longer shelf life and most importantly, they have potential for lower manufacturing costs than thermosetting composites Epoxy (thermoset) based composites have lengthy cure cycles ranging from 2 to 10 hrs due to the slow reaction kinetics of the resin Repair of thermoset composites is a complicated process, requiring adhesives and careful surface preparation Thermoplastic resins can be welded together, making repair and joining of parts more simple than for thermosets. However, the higher viscosity of thermoplastic resins makes some manufacturing processes more difficult such as a prepregging operation Thermoplastic composites typically require higher forming temperatures and pressures than comparable thermoset systems. Therefore, thermoplastic composites do not enjoy as high a level of integration as is currently obtained with thermosetting systems As a consequence of this, the fabrication of thermoplastic composite parts has drawn a lot of attention from researchers to overcome the problems.

In an effort to reduce the cost of composite components, fabrication by automation is necessary. Automation can be applied to both thermoplastic and thermoset composites. This thesis develops techniques for the automation of two processes: the tape winding for thermoplastic composites and filament winding using two axis machine for thermoset composites. The thesis is divided into two parts, the first part of the thesis focuses on the automated processing of APC-2 composites using laser and hot gas as heat sources and the second part deals with the filament winding of complex shapes on a simple machine with two degrees of freedom.

Recently several researchers have addressed various aspects of the thermoplastic tape laying and tape winding process Beyeler and Guceri [5], Grove [6], Nejhad et al [7] and Anderson and Colton [8] developed models for the prediction of a temperature history for known amount of heat supply and known tape speed for tape laying operation. None of these researchers determined the temperature profile experimentally Anderson and Colton [8] reported the difficulties in measuring the temperature during a thermoplastic tape laying operation Mantell and Springer [9] developed a model for thermoplastic tape laying and tape winding operations They included the problem of consolidation, crystallinity and residual stress in their model Nejhad et al. [10] included the crystallinity and process induced stresses in their model. Experimental investigation on the crystallinity and process induced deformations are not reported by above authors Mantell and Springer [11] performed some experiments for thermoplastic tape laying operation and experimentally determined the degree of intimate contact and the extent of bonding Their intimate contact model predicted the degree of intimate contact with good accuracy whereas for the case of bonding, they found 50% difference in test results and predicted results Experimental determination of degree of intimate contact was done by conducting C-scan tests whereas extent of bonding was determined by performing short beam shear (SBS) tests and lap shear tests. The above difference in bonding results is unclear [11]. However, they suggested that, although the overall degree of intimate contact was high, there were small areas at various interfaces which had poor intimate contact and poor bonding. These small areas serve as damage initiation sites which grow rapidly when load is applied [11].

A few other researchers [12,13,14,15,16] studied the experimental aspects of thermoplastic tape winding. Beyeler, Phillips and Guceri [12] discussed the feasibility of laser processing by producing several rings using Ryton AC 40-60 prepreg tapes. Hauber and his coworkers [13,14] used robots and hot nitrogen gas for the manufacture of circular cylinders. Werdermann et al. [15] designed and fabricated an on-line consolidation facility for the manufacture of circular rings and short tubes for thermoplastic composites. They used infrared and hot nitrogen gas for heating the preimpregnated tow. Carpenter and Colton [16] used hot air as a heat source for the fabrication of circular rings. The major emphasis in these works [12-16] was on the design and development of experimental set-up and in the determination of quality of consolidation by optical microscopic study.

None of the above researchers [12-16] experimentally determined the temperature history, process induced deformations, crystalinity and quality of bond

In all the above works in terms of model development [5-10] and in terms of experimental work [11], processing of APC-2 composites is performed in the range of 350°C to 390°C similarly to compression molding and autoclave processing Effects of higher heating rate and shorter melt time on processing temperature were not investigated Agarwal [17] studied the effect of laser power on crystallinity, void content, temperature distribution, and interlaminar bond quality for a constant tape speed of 15 4 mm/sec In an on-line consolidation process, there is a strong coupling between laser power and tape speed, therefore tape speed needs to be varied to obtain optimum bond quality

In general, automated processing of thermoplastic composites can be performed using several types of heat source The following heating techniques were considered for melting and consolidation of the thermoplastic tape;

High frequency waves can heat the material by causing the molecules in the thermoplastic to oscillate. However, this method only works with thermoplastics containing polar molecules. In addition, these waves are difficult to generate and to concentrate, and can be hazardous to electronic equipment and to human beings [15]

Hot rollers could be induction or resistance heated. This heating needs to be provided from the top of incoming tape and can not be applied between incoming tape and preconsolidated laminate. The problem with this kind of heating is that the thermoplastic sticks to the surface of the roller and causes problem during winding

Resistance heating requires an electric current to be sent through the carbon fibers. This is theoretically possible, but it is very complicated for simultaneous continuous winding. Moreover, it does not work for glass and aramid fibers.

Open flame and acetylene gas torch provide a high density of energy, but they are usually so hot that they may degrade the polymer Moreover, chances of spontaneous combustion is high

Hot air or hot gas has poor efficiency, since not only the tape but also the gas has to be heated However, the efficiency of heating system does not have to be a major concern, since the amount of energy that has to be applied at the consolidation point is much smaller for localized heating. Moreover, these systems are economical to use for processing Hot air causes degradation of thermoplastics because of presence of oxidative atmosphere, therefore hot air was not selected for localized heating In the present case, hot nitrogen gas was selected for determining the feasibility of processing

Laser has already been used for processing of thermoplastics during tape winding operation [12] Laser assisted processing provides a clean atmosphere without any need of ventilation In hot nitrogen gas aided processing, the gas at high temperature comes out at high velocity and requires a ventilating system. Laser has additional advantage of real time control during processing The major concern with laser heating is that the equipment is expensive However, the cost of equipment may decrease in the future with rapid improvement in laser technology. A survey made by Belforte [18] reported an increase in the use of multi-axis laser processing systems by a factor of 20 from 1985 to 1990. By 1990, there were 18,000 industrial laser systems installed in the world's manufacturing industries [18]. For space applications, laser is very suitable for performing various operations such as drilling, welding, trimming, joining, etc which are not possible by other heat sources Cost of equipment can be sacrificed for such applications References [18-25] can be consulted for a detailed study on the CO_2 laser and its applications.

For reasons stated above, the laser and hot nitrogen gas were selected for automated processing of APC-2 thermoplastic composites for the present study. At the beginning of this work, information on influence of amount of heat supply, tape speed and consolidation pressure on heating rate, cooling rate, process-induced deformation, crystallinity and the quality of bond was not available Because of lack of numerical and experimental results and insufficient understanding about the effects of process parameters on the quality of a part, the first part of the thesis (chapters 2, 3, 4, 5 and 6) concentrates on the automated processing of APC-2 composites using laser and hot gas as heat sources

Process models which relate the amount of heat supply, tape speed and consolidation pressure to the temperature distribution, heating rate, cooling rate, melt time, and degree of intimate contact are presented in chapter 2 Based on these models, a computer code was developed for generating results for any specific combinations of process parameters

Experimental investigation on the laser-assisted processing of APC-2 composites is presented in chapter 3. An experimental set-up was designed and developed for determining the feasibility of the laser-assisted processing of APC-2 thermoplastic composites Temperature history for laser processing was determined for different process conditions Accuracy of numerical results on the temperature profile and degree of intimate contact were assessed by experimental test results Effects of the laser power, tape speed, and consolidation pressure on the crystallinity, process-induced deformations, and quality of consolidation are discussed Influences of the heating rate, melt time duration, and cooling rate on the quality of consolidation are investigated Mechanical testing and analysis of interply bonding was performed. Short beam shear test, double cantilever beam test and fracture surface study using scanning electron microscope were performed to investigate which method most easily detect the differences in interply bond quality.

In a manufacturing process where several factors influence the performance of a part, the Taguchi method can be used as a powerful tool for selecting the optimum process parameters. Implementation of the Taguchi method for an on-line consolidation process using the laser as a heat source is presented in chapter 4 The percentage contribution of individual parameters on the quality of the bond is estimated by ANOVA technique

Chapter 5 discusses the hot-gas-assisted processing of APC-2 composites Influences of the dominant process parameters such as amount of heat supplied, tape feed rate, and consolidation pressure on the temperature history, process-induced deformation, crystallinity, and quality of consolidation are investigated. Manufacturing condition for hot-gas-aided processing is estimated for better interply bond quality.

At the beginning of this work, use of the thermoplastic tape winding was limited to the manufacture of circular cylinder shapes. This thesis work extends the technology to the fabrication of non-axisymmetric cylindrical components by tape winding technique. For this, a kinematic model for the manufacture of non-axisymmetric cylindrical structures was developed and is explained in chapter 6. Based on the model, an experimental set-up was designed and built for the production of non-axisymmetric components. Verification of the model was performed by fabricating elliptical rings using the laser as a heat source. Several problems during the manufacture of non-axisymmetric shapes are discussed and solutions to these problems are presented. A kinematic model for the manufacture of open structures by the tape laying operation is also presented.

The second part of the thesis discusses the use of filament winding technique for the manufacture of complex composite shapes. Fabrication of composite part by filament winding technique is completed in four major steps In the first step, material and part geometry are selected depending on the requirement of a product. In the second step fiber winding angle distribution, fiber volume fraction and thickness of the part are calculated by performing stress analysis. In the third step, machine motions are determined to get the desired fiber angle distribution on the surface of the mandrel. Finally, the filament winding process is modeled to determine the optimum process parameters for desired quality of the part. The present work focuses on the third step which deals with the kinematics of filament winding.

In the literature very little has been found on the kinematics of non-axisymmetric shapes. Until today, most of research activities deal with the manufacture of rocket motor cases, pressure vessels, tanks and piping systems [1,26-29] These structures are all axisymmetric Recently, several process models which relate the processing variables to the chemical and mechanical behaviour of the composite component are developed by Calius [30], Lee and Springer [31], and Cai, Gutowski and Allen [32]. All these models deal with the manufacture of a circular cylinder by a filament winding technique. Use of filament winding is limited to the manufacture of simple structures such as pipes, tanks and pressure vessels because of insufficient understanding about the kinematics of filament winding and higher cost involved in manufacturing complicated shapes. Focus of the present investigation is to develop models for the determination of winding motion to obtain desired fiber-winding angle on axisymmetric, non-axisymmetric, cylindrical, and non-cylindrical mandrel shapes.

In the filament winding, the determination of the motion of delivery point can be obtained from a variety of sources. The suppliers of the filament winding machine sometimes provide application programs for the winding of standard shapes such as rings, cylinders, pipes, and pressure vessels. In another approach, winding motions are determined by teach-in-programming technique, in which fiber trajectory is first marked on the mandrel surface and then delivery point is positioned incrementally by trial and error method in such a way that the fiber band lies along the marked line [29] Various co-ordinate points of the delivery point are stored to get the desired fiber trajectory. The teach-in-programming technique is still largely used in many industries. Sometimes sophisticated and highly interactive graphics packages are used for smoothing and editing the stored data [33,34] Once the required data for one complete stroke is calculated then these data are generally repeated after indexing the mandrel. Delivery point motion can also be determined by simulation of the filament winding process [33]

Latest development in technology offered new generation computer controlled filament winding machine with floppy disk and hard disk drives and RS 232 input ports

[35,36,37] The equipment is configured such that it relies on real time control of several servo axes, analog outputs, digital outputs and tension controllers Winding motion is generated from data transferred from other sources using floppy disk. Manufacturing engineers use computer graphics to simulate the winding pattern, record the data and then feed the resulting data to the computer through a line or floppy disk.

CAD/CAM systems have also been developed for the filament winding [38,39] which integrate a 3-D surface modeller, specific filament winding software and design software. A three dimensional surface modeller is used to model the component geometries, lay the fiber on geodesic or non-geodesic path, and to determine the fiber orientation by performing stress analysis and using failure criteria. Once winding path is known, the filament winding software simulates the winding process by defining successive straight lines tangential to the winding path at each point. The ends of these straight lines define the path of delivery point in the mandrel frame of reference At this stage intersection calculation is applied to check for possible regions of collision. Once an acceptable winding circuit is generated, delivery point locations are converted from the mandrel frame of reference to a co-ordinate system which corresponds to the kinematics of filament winding machine. Most difficult part here is to convert these data into the five or six simultaneous axes of the filament winding machine Machine motion for each degree of freedom is then determined in such a way that the net effect of motion of each degree of freedom should match with the desired movement of the delivery point location. Sometimes machine motion by this technique is quite complex and requires sophisticated filament winding machine with a large number of degrees of freedom.

Robots have also been introduced in the filament winding of small complex shape structures [40,41]. In many cases of robotic filament winding and CNC (Computer Numerical Controlled) filament winding, motion of the delivery point is obtained directly from the stable fibre path predictions on the mandrel surface [41,42] In this case it is assumed that the distance between the delivery point and mandrel surface is zero and delivery point moves on the mandrel surface along desired fiber trajectory. In actual case, since the distance between delivery point and mandrel surface is not zero, the accuracy of fiber placement is less than that offered by regular filament winding machine [41] Other possible restrictions which may prevent the robot from performing its prescribed task are collisions with the mandrel or other objects, singularity positions or joint angle limitations of the robot arm, machine dynamics [40,41]

In above techniques, winding motions for the delivery point are determined either by trial and error method or by using sophisticated equipment The emphasis on low cost manufacturing indicates that super sophistication in equipment is not always necessary in the production process. A survey made by Wilson [37] shows that extremely sophisticated winders will have limited market in future for the production of composite components. The majority of the market place will emphasize low cost and specific capabilities of equipment to manufacture a distinct product [37].

With above discussion in mind, development of analytical formulas to determine the winding motion can be helpful to lower the cost of a filament wound composite component. Allard et al. [43] reported that the kinematics on elliptical cross-section is very complex. Hamouda et al. [44] developed an analytical model which provides the laws of motion of the traverse stroke relative to the mandrel to ensure that the filament lay down is along the predetermined path. They developed differential equation of winding to predict layer by layer geometry using the mandrel shape as the initial boundary condition. Their model is similar to the model developed by Emerov [45,46] for the textile industry and is for circular cylinder and axisymmetric mandrel shapes

None of the above work on filament winding explains the effects of delivery point distance, fiber winding angle distribution, mandrel shape geometry on the winding motion of filament winding machine. This is very important in reducing the experimental set-up time. For instance it takes around 40 hrs. to change the experimental set - up for a mechanical filament winder with two degrees of freedom if size of the component changes. This increases the cost of manufacturing a component.

In this thesis a new technique, Geometric Approach, is presented for the manufacture of a wide variety of composite components such as axisymmetric, non-axisymmetric, cylindrical and non-cylindrical mandrel shapes The best part of this approach is that it is applied for the simplest form of filament winding machine which has two degrees of freedom The approach is simple and uses geometrical and trigonometrical relations to determine the winding motion. For some shapes such as cylindrical mandrels with polygonal cross-sections or non-cylindrical mandrels with polygonal cross-sections, the method requires some simple hand calculations without the use of computer to determine the winding motion It reduces the experimental set-up time and is very helpful in low cost manufacturing of composite components The approach is not only useful in filament winding operations but the concept can be applied to other fields such as thermoplastic tape winding and laser cutting operations.

Based on the Geometric Approach, various kinematic models are presented in chapters 7-10 for the manufacture of axisymmetric, non-axisymmetric, cylindrical, and non-cylindrical mandrels These models are suitable for thermoset filament winding. These models together with the model developed in chapter 6 can be applied for thermoplastic tape winding and thermoplastic filament winding Chapter 7 presents a generalized model for achieving desired fiber angle distribution on non-axisymmetric cylindrical mandrels with smooth convex curved cross-section. The experimental verification of the model is done on a cylindrical mandrel with elliptical cross-section. The method presented in chapter 7 can not be used for getting desired fiber winding angle on mandrels with rectangular, hexagonal or any other polygonal cross-sections, where first derivative of the surface is not continuous To solve this problem, a method is presented in chapter 8 for filament winding of cylindrical mandrels with polygonal cross-section The method was verified by performing experiments on cylindrical mandrels with rectangular and hexagonal cross-sections. Effects of location of delivery point, mandrel geometry, and fiber winding angle on machine motions are discussed for the above cases. The methods presented in chapters 7 and 8 are used for the filament winding of only cylindrical parts. A generalized analytical model is presented in chapter 9 for determining machine motions for laying down the fiber on a predetermined path of the axisymmetric, non-axisymmetric, cylindrical, and non-cylindrical mandrels. The method described in chapter 9 can be used for the kinematic analysis of cylindrical mandrels but the algorithms presented in chapters 7 and 8 are simple because of mandrel's cylindrical nature.

Techniques for the prediction of fiber angle distribution on a variety of mandrel shapes for known machine motions are not available in the literature. In chapter 10, a novel approach was developed for determining the fiber lay-down path for known equation of motion of the delivery point. This is important during start-up and reversal period of the filament winding operation.

Finally conclusions and contributions of present thesis are described in chapter 11. Suggestions for future work in the area of the thermoplastic tape winding and filament winding process are also presented

PART I THERMOPLASTIC TAPE WINDING

CHAPTER 2

LASER-ASSISTED PROCESSING - PROCESS MODELS

2.1 Summary

A heat transfer model and a intimate contact model are presented for on-line consolidation of thermoplastic composites. The heat transfer model is based on the governing equation for anisotropic heat conduction whereas the intimate contact model is based on the Mantell and Springer model. Based on the models, a computer code is developed to determine the effect of laser power, tape speed, and consolidation force on the temperature history, heating rate, cooling rate, melt time, and degree of intimate contact.

2.2 Introduction

The selection of process parameters during the manufacture of composite components has a significant effect on the quality and cost of the finished product. In the thermoplastic tape winding process, the dominant processing variables are heat intensity, tape speed, and consolidation force. These variables should be carefully chosen to improve the quality at reduced cost and reduced experimental time. This can be achieved by the development of process models. In recent years several models are developed to simulate the thermoplastic tape laying and tape winding process [5,6,7,9]. Beyeler and Guceri [5], Grove [6], and Nejhad et al. [7] presented numerical solutions for the prediction of temperature distribution for laser-assisted processing. All of them presented numerical results for different sets of processing variables without performing any experimental verification. The results predicted by above researchers can not be used for the verification of the model with the experimental results obtained during this thesis because of lack of suitable selection of process parameters. Beyeler and Guceri [5] determined the temperature distribution for 15.4 W laser power at 10 mm/sec tape speed, 38.1 W at 50 mm/sec tape speed, and 45.7 W at 80 mm/sec tape speed. Their selection of process parameters was made such that the maximum temperature reached during processing was in the range of 360°C to 400°C. Grove [6] predicted the temperature profile for laser powers of 1,500 W to 2,500W whereas in the present study laser power in the range of 30W to 60W is selected for processing APC-2 thermoplastic composites. Nejhad et al. [7] determined the temperature distribution for laser powers in the range of 146.4W to 366.0W such that the maximum temperature reached during laser processing is 400°C whereas according to the present finding, maximum temperature reached during laser processing need to be more than 500°C for better bonding of the plies. Cirino [47] examined the problem of the thermoplastic tape winding where the entire surface of the cylinder was at uniform heat flux. The major emphasis in above models was on the heat transfer process during tape laying/winding operation. Mantell and Springer [9] incorporated crystallinity and consolidation with their heat transfer model. They also determined the processing conditions for maximum temperature of 360°C to 400°C during thermoplastic tape laying operation. Loos and his co-workers [48,49] developed a model for the degree of intimate contact between ply interfaces during consolidation of thermoplastic composites. The model was developed using prepreg surface topology characterization with a resin flow analysis. Validation of their model was performed by comparing the results of the model with the data obtained by compression moulded samples for graphite-polysulfone and graphite-PEEK prepregs [49]. None of the above researchers validated their model for a thermoplastic tape winding operation.

The objective of this investigation is to determine the temperature, heating rate, cooling rate, melt time, and consolidation as a function of time and position for a given heat intensity, tape speed, and consolidation force. The study on the laser-assisted processing is separated into 3 chapters. This chapter describes the process models, namely the heat transfer model and intimate contact model. The heat transfer model is developed using governing equation for anisotropic heat conduction. The intimate contact model is based on the concepts proposed by Loos and his co-workers [48,49] and by Lee and

Springer [50]. Based on these models, a computer code designated by TAPEW is developed to generate numerical results and to select appropriate processing conditions for a thermoplastic tape winding process. The accuracy of the models is assessed by comparing the numerical results with the experimental results and is discussed in detail in the next chapter. Chapter 3 describes the development of an experimental set-up, the thermal characterization, and the influence of dominant process parameters on process-induced deformations, crystallinity, and consolidation quality. Chapter 4 describes the use of Taguchi method for process and property enhancement of laser-assisted fabrication method.

2.3 Heat Transfer Model

During the processing of thermoplastic composites, information about the temperature history is very important to predict the heating rate, cooling rate, melt time, and degree of intimate contact. In order to predict the temperature distribution during processing of thermoplastic composites, a suitable heat transfer model is needed. Prediction of temperature profile is also important in order to control the process for tape winding and tape laying operation since direct sensing of temperature is not currently feasible.

The thermal analysis of the laser-assisted processing during the thermoplastic tape winding process is based on an anisotropic heat conduction model. The working material is considered to be an anisotropic, two dimensional medium. If the heat source is uniformly distributed over the width of the laminate, then the present problem can be considered as a two dimensional problem. For the development of the model, mandrel diameter is considered to be very large. Therefore, the consolidated laminate near the consolidation zone is considered to be flat as shown in Fig. 2.1.

Governing differential equation for unsteady state heat conduction is:

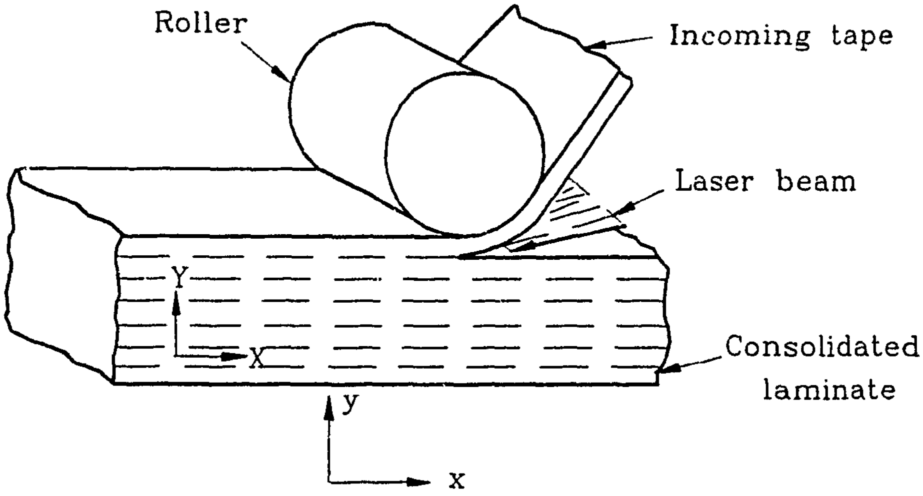

Fig. 2.1 Local application of heat and pressure during tape consolidation process.

$$\frac{\delta}{\delta X}(k_{1}\cdot\frac{\delta T}{\delta X}+k_{12}\frac{\delta T}{\delta Y})+\frac{\delta}{\delta Y}(k_{21}\frac{\delta T}{\delta X}+k_{22}\frac{\delta T}{\delta Y})+U=\rho c\frac{\delta T}{\delta t} \tag{2.1}$$

where X and Y are co-ordinates in the moving domain as shown in Fig. 2.1 and k, U, p, c, T, t are thermal conductivity, heat generation, density, heat capacity, temperature, and time respectively. The above unsteady state problem can be converted to a steady state problem by assuming a co-ordinate system (x, y) outside of the moving domain as shown in Fig. 2.1. With respect to (x,y) co-ordinate system, temperature distribution does not change except during the beginning and end of the process. For a continuous process, above Eq. 2.1 is converted to a steady state problem as follows using a local co-ordinate system (x,y).

$$x=x_o+X+v_xt \tag{2.2}$$

$$y=y_o+Y+v_yt \tag{2.3}$$

where (x_0, y_0) is the origin of (X,Y) co-ordinate system in the beginning, and v_x and v_y are velocity of moving domain with respect to (x,y) co-ordinate system. Converting the various differential terms of Eq. 2.1 to the local co-ordinate system,

$$\frac{\delta T}{\delta X}=\frac{\delta T}{\delta x}\cdot\frac{\delta x}{\delta X}=\frac{\delta T}{\delta x} \tag{2.4}$$

$$\frac{\delta^2 T}{\delta X^2}=\frac{\delta^2 T}{\delta x^2} \tag{2.5}$$

$$\frac{\delta T}{\delta Y} = \frac{\delta T}{\delta y}.\frac{\delta y}{\delta Y} = \frac{\delta T}{\delta y} \tag{2.6}$$

$$\frac{\delta^2 T}{\delta Y^2} = \frac{\delta^2 T}{\delta y^2} \tag{2.7}$$

$$\frac{\delta T}{\delta t} = \frac{\delta T}{\delta x}.\frac{\delta x}{\delta t} + \frac{\delta T}{\delta y}.\frac{\delta y}{\delta t} = \frac{\delta T}{\delta x}v_x + \frac{\delta T}{\delta y}v_y \tag{2.8}$$

Substituting differential form of temperature from equations 2.4 to 2.8 in equation 2.1 gives,

$$\frac{\delta}{\delta x}(k_{11}\frac{\delta T}{\delta x} + k_{12}\frac{\delta T}{\delta y}) + \frac{\delta}{\delta y}(k_{21}\frac{\delta T}{\delta x} + k_{22}\frac{\delta T}{\delta y}) + U = \rho c(\frac{\delta T}{\delta x}v_x + \frac{\delta T}{\delta y}v_y) \tag{2.9}$$

The above steady state equation 2.9 can also be obtained by an Eulerian approach for a continuous process [5]. This is possible since at every instant, the temperature distribution would remain unchanged with respect to a fixed co-ordinate system (x,y). In this formulation, the velocity terms v_x and v_y on right hand side represent the local material velocities with respect to the (x, y) co-ordinate system. Beyeler and Guceri [5] solved the above equation 2.9 using numerical grid generation method with body-fitted co-ordinate system. This technique combines the geometric flexibility of finite element methods with the simplicity of the finite-difference approaches [5]. Grove [6] used finite element method to solve the problem of laser-assisted processing for tape laying operation. Nejhad et al. [7] performed three-dimensional thermal analysis for the case of localized heating during the tape winding operation. Don, Pitchumani and Gillespie [51] used one dimensional transient heat conduction equation to predict the temperature profile during the tape laying operation They predicted the temperature profile across the thickness of the tows (y direction) It was assumed that the temperature gradients in the x and width directions are negligible [51] In order to predict the temperature distribution at desired combinations of process parameters and to validate the model with the experimental results, it was decided to develop a computer code based on the finite element method. For finite element method, variational formulation of equation 2.9 is performed by multiplying it by a test function v as follows.

$$-\int v.[\frac{\delta}{\delta x}(k_{11}\frac{\delta T}{\delta x}+k_{12}\frac{\delta T}{\delta y})+\frac{\delta}{\delta y}(k_{21}\frac{\delta T}{\delta x}+k_{22}\frac{\delta T}{\delta y})+U]dxdy$$

$$+\int v.\rho c(\frac{\delta T}{\delta x}v_x+\frac{\delta T}{\delta y}v_y)dxdy = 0 \qquad (2.10)$$

where v is a test function or interpolation function. Upon performing the integration,

$$\int[\frac{\delta v}{\delta x}(k_{11}\frac{\delta T}{\delta x}+k_{12}\frac{\delta T}{\delta y})+\frac{\delta v}{\delta y}(k_{21}\frac{\delta T}{\delta x}+k_{22}\frac{\delta T}{\delta y})-v.U$$

$$+v.\rho c(\frac{\delta T}{\delta x}v_x+\frac{\delta T}{\delta y}v_y)]dxdy - \oint_S v[n_x(k_{11}\frac{\delta T}{\delta x}+k_{12}\frac{\delta T}{\delta y})$$

$$+n_y(k_{21}\frac{\delta T}{\delta x}+k_{22}\frac{\delta T}{\delta y})]ds = 0 \qquad (2.11)$$

Three types of boundary conditions as shown in Fig. 2.2 are used in the present case. In the first boundary, the temperature of incoming tape T_{tape} is specified. In the

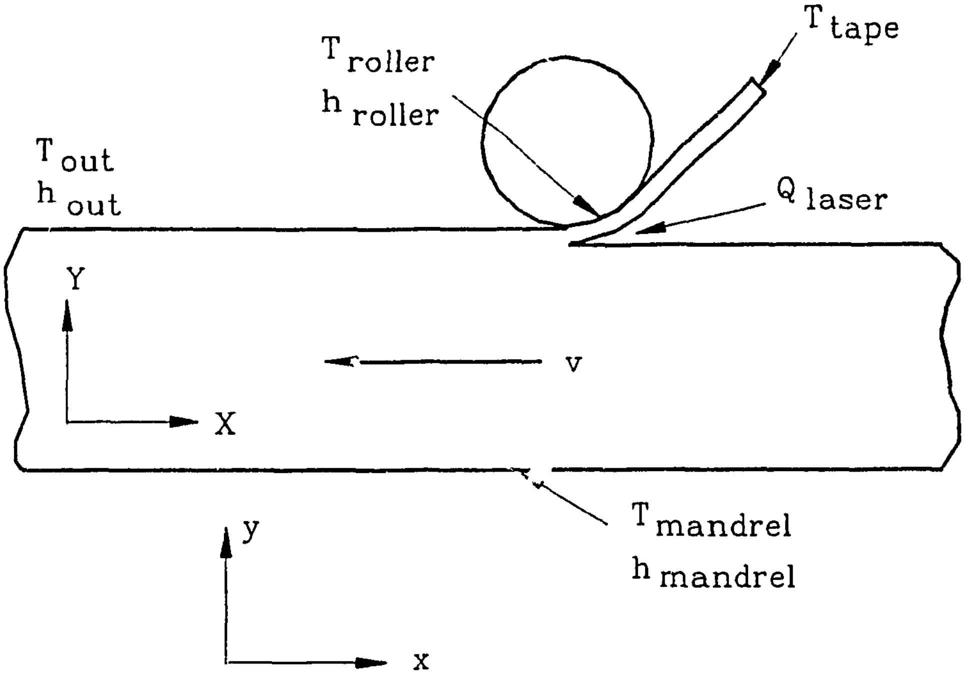

Fig. 2.2 Boundary conditions for heat transfer model.

second boundary, the heat flux, Q_{laser}, at the consolidation point is specified. In the third boundary i.e. at the interface of the mandrel and laminate, or the roller and laminate, convection coefficient and temperature is specified The boundary condition for the present problem can be written as follows;

$$(k_{11}\frac{\delta T}{\delta x}+k_{12}\frac{\delta T}{\delta y})\,n_x+(k_{21}\frac{\delta T}{\delta x}+k_{22}\frac{\delta T}{\delta y})\,n_y+h(T-T_o)+q\ =\ 0 \qquad (2.12)$$

where q is the heat flux and h is the convection coefficient.

Upon substituting the above boundary condition into Eq. 2.11, it yields,

$$\int[\frac{\delta v}{\delta x}(k_{11}\frac{\delta T}{\delta x}\ +k_{12}\frac{\delta T}{\delta y})+\frac{\delta v}{\delta y}(k_{21}\frac{\delta T}{\delta x}\ +k_{22}\frac{\delta T}{\delta y})-v.U$$

$$+\ v.\rho c(\frac{\delta T}{\delta x}v_x+\frac{\delta T}{\delta y}v_y)]\,dxdy\ -\ \oint_{S_2}v.qds+\ \oint_{S_3}v.h(T-T_o)ds\ =\ 0 \qquad (2.13)$$

Here S_2 is the boundary surface where heat flux q is specified and S_3 is the boundary, where the convection coefficient is specified.

Let,

$$T\ =\ \sum_{j=1}^{n}T_j\phi_j\ ,\qquad v\ =\ \phi_i \qquad (2.14)$$

Upon substituting the value of T and v in Eq. 2.13, we obtain,

$$\sum_{j=1}^{n} [K_{ij}^{e}+H_{ij}^{e}].T_j^e = F_i^e+P_i^e \tag{2.15}$$

where, for an element ,e,

$$K_{ij}^{e} = \int[\frac{\delta\phi_i}{\delta x}(k_{11}\frac{\delta\phi_j}{\delta x}+k_{12}\frac{\delta\phi_j}{\delta y})+\frac{\delta\phi_i}{\delta y}(k_{21}\frac{\delta\phi_j}{\delta x}+k_{22}\frac{\delta\phi_j}{\delta y})$$

$$+\ \phi_i.\rho\, c(\frac{\delta\phi_j}{\delta x}v_x+\frac{\delta\phi_j}{\delta y}v_y)]\,dxdy \tag{2.16}$$

$$H_{ij}^{e} = h\oint_{S_3}\phi_i.\phi_i ds \tag{2.17}$$

$$F_i^e = \int U\phi_i dxdy \tag{2.18}$$

$$P_i^e = -\oint_{S_2}\phi_i.q\,ds+\oint_{S_3}\phi_i.hT_o ds \tag{2.19}$$

The above integral can be solved by selecting a suitable element, e.g. triangular element, rectangular element, etc. [52]. For the present case, a triangular element is selected, for which the shape function is defined by [52],

$$\phi_i = \frac{1}{2A_e}.(\alpha_i+\beta_i x+\gamma_i y) \tag{2.20}$$

where, α, β and γ are constants used for defining the shape function ϕ. A_e is the area of the element e.

For a triangular element, a mesh is generated as shown in Fig. 2.3. The exact solution for various integral term for above shape function is given by,

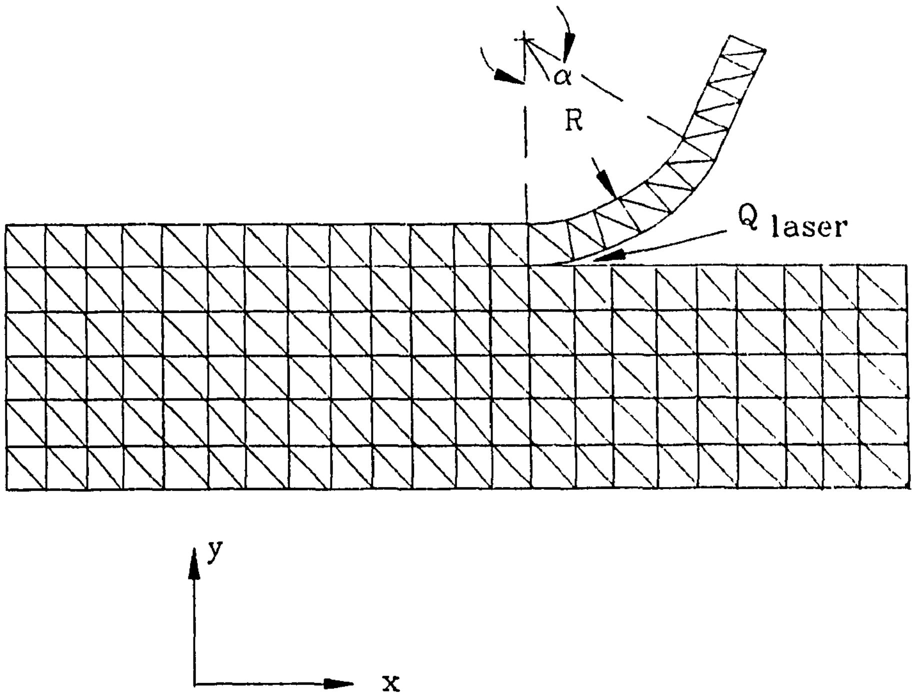

Fig. 2.3 Mesh generation during tape consolidation process.

$$\int \frac{\delta\phi_i}{\delta x}.\frac{\delta\phi_j}{\delta x}dx.dy = \frac{1}{4A_e}\beta_i.\beta_j \tag{2.21}$$

$$\int \frac{\delta\phi_i}{\delta x}.\frac{\delta\phi_j}{\delta y}dx.dy = \frac{1}{4A_e}\beta_i.\gamma_j \tag{2.22}$$

$$\int \frac{\delta\phi_i}{\delta y}.\frac{\delta\phi_j}{\delta x}dx.dy = \frac{1}{4A_e}\gamma_i.\beta_j \tag{2.23}$$

$$\int \frac{\delta\phi_i}{\delta y}.\frac{\delta\phi_j}{\delta y}dx.dy = \frac{1}{4A_e}\gamma_i.\gamma_j \tag{2.24}$$

$$\int \phi_i.\frac{\delta\phi_j}{\delta x}dx.dy = \frac{1}{6}\beta_j \tag{2.25}$$

$$\int \phi_i.\frac{\delta\phi_j}{\delta y}dx.dy = \frac{1}{6}\gamma_j \tag{2.26}$$

For a triangular element, the coefficient matrices H_{ij}^e, P_i^e, and F_i^e are given by,

$$H_{ij}^{e} = \frac{h_{12}^{e} l_{12}^{e}}{6}\begin{vmatrix} 2 & 1 & 0 \\ 1 & 2 & 0 \\ 0 & 0 & 0 \end{vmatrix} + \frac{h_{23}^{e} l_{23}^{e}}{6}\begin{vmatrix} 0 & 0 & 0 \\ 0 & 2 & 1 \\ 0 & 1 & 2 \end{vmatrix} + \frac{h_{31}^{e} l_{31}^{e}}{6}\begin{vmatrix} 2 & 0 & 1 \\ 0 & 0 & 0 \\ 1 & 0 & 2 \end{vmatrix} \tag{2.27}$$

$$F_{i}^{e} = \frac{UA}{3}\begin{vmatrix} 1 \\ 1 \\ 1 \end{vmatrix} \tag{2.28}$$

$$P_{i}^{e} = \frac{h_{12}^{e} T_{o} l_{12}^{e}}{2}\begin{vmatrix} 1 \\ 1 \\ 0 \end{vmatrix} + \frac{h_{23}^{e} T_{o} l_{23}^{e}}{2}\begin{vmatrix} 0 \\ 1 \\ 1 \end{vmatrix} + \frac{h_{31}^{e} T_{o} l_{31}^{e}}{2}\begin{vmatrix} 1 \\ 0 \\ 1 \end{vmatrix} \tag{2.29}$$

Where, h_{ij} are the convective coefficients for side i-j of an element e, and l_{ij} is the length of the side i-j. The results on the prediction of temperature distributions by the present model are described in chapter 3 for any specified process conditions.

2.4 Intimate Contact Model

Intimate contact refers to the removal of surface irregularities of the tows in contact so as to achieve a good interfacial contact between adjacent tows. As intimate contact progresses, the interfacial voids between the surfaces in contact are expelled. For a thermoplastic tape winding process, the mechanism of interfacial void removal is dependent upon the relative surface roughness, and the applied pressure, temperature, and time at the interfaces of the newly laid tow and the substrate.

A degree of intimate contact, D_{ic}, is defined such that it takes a value of unity in the case of complete interfacial contact. Lee and Springer [50] modeled the surface roughness of a prepreg tape as a series of rectangles as shown in Fig. 2.4 This concept was originally used by Dara and Loos [48] to describe the surface of a composite part. Lee and Springer [50] however used the viscosity of APC-2 in their modeling, which includes the effect of fibers on the resin viscosity.

According to the Springer and Lee model [50], D_{ic} is defined by

$$D_{ic} = \frac{b}{w_0 + b_0} \tag{2.30}$$

where b_0 and b are the initial ($t \leq 0$) and instantaneous (at time t) widths of each rectangular element, respectively, and w_0 is the initial distance between two adjacent elements. Physically it denotes the ratio of the base width of an asperity to the wave length of an idealized periodic arrangement of asperities. During processing the volume of each element remains constant, therefore,

$$V_0 = a_0 b_0 = ab \tag{2.31}$$

where a_0 and a are the initial and instantaneous heights of each rectangular element. Equations 2.30 and 2.31 yield following expression for degree of intimate contact.

$$D_{ic} = \frac{a_0/a}{1 + w_0/b_0} \tag{2.32}$$

Mantell and Springer [9] derived an expression as follows for the calculation of intimate contact for thermoplastic tape winding operation using the law of conservation of mass to a control volume.

$$D_{ic} = \frac{1}{w^*}[1 + a^* \frac{f}{\mu_{mf} \omega r_c H_r}]^{1/5} \tag{2.33}$$

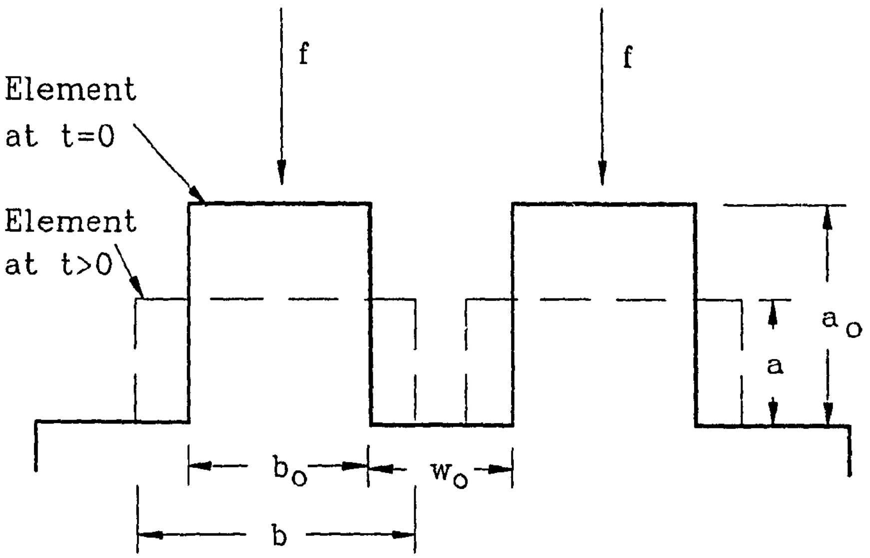

Fig. 2.4 Rectangular elements representing the uneven surface of a thermoplastic tape.

where ω is the speed at which the mandrel rotates, f is the consolidation force, H_r is the width of the roller and r_c is the radius of the cylinder at the interface at which the degree of intimate contact is being evaluated. w* and a* are defined as;

$$w^* = 1 + \frac{w_0}{b_0} \quad , \qquad a^* = 5w^*(\frac{a_0}{b_0})^2 \tag{2.34}$$

Equation 2.33 can be further simplified in the following form for thermoplastic tape laying/winding operations with APC-2 thermoplastic tape [9,51].

$$D_{ic} = 0.29[\frac{f}{\mu_{mf}\omega r_c H_r}]^{1/5} \tag{2.35}$$

The viscosity μ_{mf} for PEEK/Carbon (APC-2) composites is defined by [9],

$$\mu_{mf} = 132.95\exp(\frac{2969}{T(K)}) \ \frac{N.s}{m^2} \tag{2.36}$$

Above Eq. 2.36 is provided by manufacturer [9] and shows that μ_{mf} is directly a function of temperature. At this point it is not sure how accurate the above equation is for laser-assisted processing where the heating rate is higher than 20,000°C/min and melt time is less than 2 sec.

2.5 Method of Solution

The models described in previous sections 2.3 and 2.4 were used to calculate the temperature distribution and degrees of intimate contact for specific combinations of process parameters. The procedure consisted of first determining the temperature profile for different sets of laser power and tape speed, and subsequently using the result of temperature distribution, the degrees of intimate contact were predicted.

Based on above formulation, a computer code TAPEW was developed to predict the temperature distribution, heating rate, cooling rate, melt time, and degree of intimate contact. The code is written using FORTRAN language and all the computations were performed on a VAX/VMS system The beam interaction area was taken to be 2 X 6.35 mm^2, therefore P watt laser power would result 0.787 P MW/m^2 heat flux. The material properties used are those reported by Grove and Short [53], Cattanagh and Cogswell [54], and Blundell and Willmouth [55] for APC-2, with 60 % fiber volume fraction, i e. k_L = 6.0 W/m.°C, k_T = 0.72 W/m.°C, density = 1562 kg/m^3, melting point 343°C, and glass transition temperature 143°C. The boundary conditions as shown in Fig 2.2 are selected as h_{base}= 500 W/m^2, h_{roller} = 500 W/m^2, h_{out} = 5 W/m2, T_{base} = 130°C, T_{roller} = 20°C and T_{tape} = 20°C. For the intimate contact model, the values of consolidation force, tape speed, and roller width are fed into equation 2.35. The viscosity term (Eq. 2.36) was calculated for the maximum temperature obtained by thermal analysis. The numerical results for temperature profile and degree of intimate contact are presented in chapter 3 for specific combinations of process conditions.

2.6 Conclusions

Models for calculating temperature profile, heating rate, cooling rate, melt time and degrees of intimate contact for laser-assisted tape winding process are presented. Based on these models, a computer code designated as TAPEW was developed for generating numerical results for any combinations of laser power, tape speed, and consolidation force. The models and computer code can be used in studying the tape consolidation process and in establishing the process parameters most suitable for a given material and application.

CHAPTER 3

LASER-ASSISTED PROCESSING - EXPERIMENTAL RESULTS

3.1 Summary

Experimental investigation on the processing of Carbon/PEEK (APC-2) thermoplastic composites using laser as a heat source was performed for the thermoplastic tape winding process. An experimental set-up was developed to produce multi-ply thermoplastic composite rings.

During the thermoplastic tape winding process, localized melting causes a high rate of heating and cooling, which requires different processing conditions from compression molding and autoclave processing. APC-2 composites is processed in the range of 380°C to 400°C for autoclave, hot press and diaphragm molding processes. It was found that a temperature greater than 500°C gave better interply consolidation during laser-assisted on-line consolidation process. The temperature history during the process is recorded using a thermocouple.

Three important parameters for thermoplastic tape winding process are heat intensity, tape speed, and consolidation force. A proper understanding of the effects of above parameters on the properties of the end product can help in controlling the quality of a part. Influence of these parameters on process-induced deformations, crystallinity, and quality of consolidation are examined.

There is no standard technique available to determine the extent of interply bond strength of ring specimens fabricated by thermoplastic tape winding technique. Short beam shear tests, double cantilever curved beam tests, and fracture surface study using scanning electron microscope are performed to investigate which method most easily detect the differences in the quality of interply bond

It is found that for a particular heat source, there are optimum values of tape speed and consolidation force at which the quality of the bond is superior The short beam shear test gives the best measure of interply bonding and it can be used for quality control purposes.

3.2 Introduction

Two types of processes have generally been used to produce thermoplastic composite structures These processes are known as discontinuous process and continuous process. In the discontinuous process such as hot press, autoclave, and diaphragn molding, plies are arranged into a predetermined form and then suitable temperature and pressure are applied to the work piece [3,4]. In the continuous process such as in a thermoplastic tape laying and tape winding operation, the tape is melted using laser, infrared, or hot gas and is consolidated while the tape is being laid down. Methods for arranging the material into a desired form and applying heat and pressure depend upon the selection of the process. In this chapter automated processing of advanced APC-2 thermoplastic composites using laser as a heat source is described for tape winding operation.

The objective of this study is to determine the effect of laser power, tape speed, and consolidation force on temperature distribution, crystallinity, void content, process-induced deformation, and bond strength. An experimental set-up is designed and built for the fabrication of thermoplastic composite rings by laser-assisted processing. The models developed in chapter 2 are verified by experimental results for temperature distribution and degrees of intimate contact Manufacturing conditions for laser-aided processing are determined. Effects of heating rate and melt time on manufacturing condition during laser-aided processing are explained in this chapter.

3.3 Development of Thermoplastic Tape Winding Machine

3.3.1 Requirements of the machine

The four major requirements for designing an experimental set-up for fabricating rings are as follows

1. The mandrel dimensions should comply with the requirements of ASTM test method [56]. This test method recommends the ring diameter to be 146.05 mm (5.75") and width to be 6.35 mm (0.25"). A mandrel was constructed to meet this requirement.

2. In the processing of thermoplastic composites using a tape winding technique, three dominant process parameters are the heat intensity, consolidation force and tape speed. All parameters must be a variable since the purpose of this study is to determine the optimum combination of these parameters.

3. The set-up should provide easy access to the mandrel for on-line measurement and control of the process parameters. For example, measurement of the temperature history during processing requires one side of the mandrel to be free from end support to avoid interference of thermocouple wire with the end support and shaft during winding.

4. The set-up should present an easy assembly and dissembly of the mandrel for the removal of the rings after it is manufactured.

3.3.2 Design of the machine

The basic concept on which the machine was built up can be seen in Fig. 3.1. The photograph of the set-up is shown in Fig.3.2. The thermoplastic tape which is held in a spool with the help of a tensioner is delivered to the mandrel for winding. Heat is supplied at the contact point of the mandrel and roller to consolidate the incoming tape

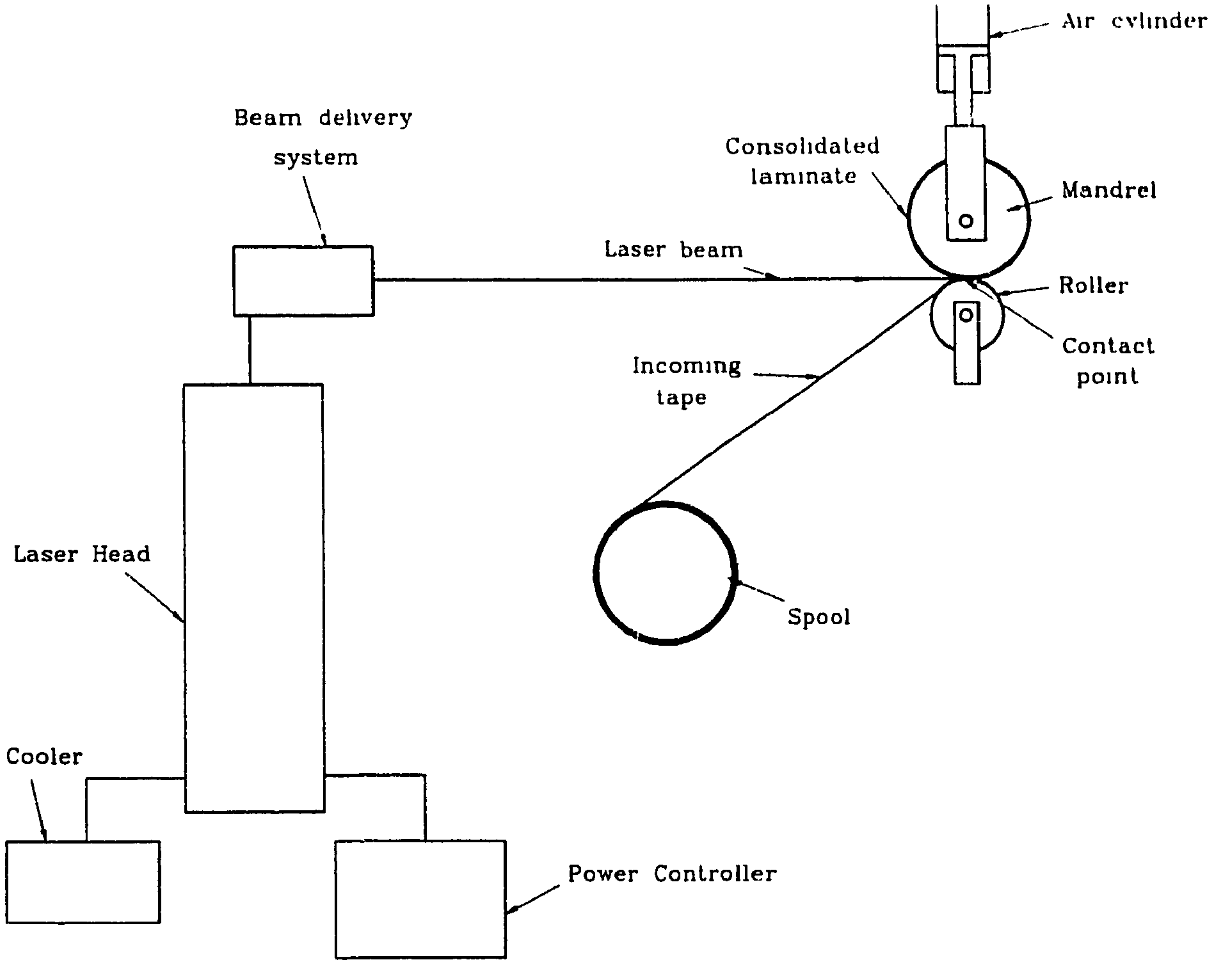

Fig. 3.1 Schematic diagram of the thermoplastic tape winding process.

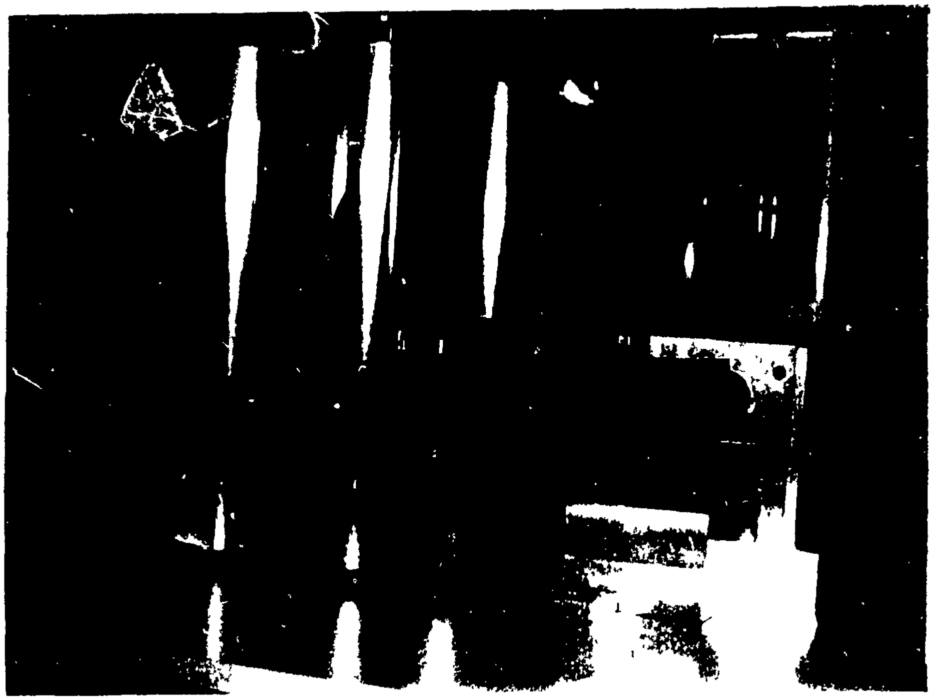

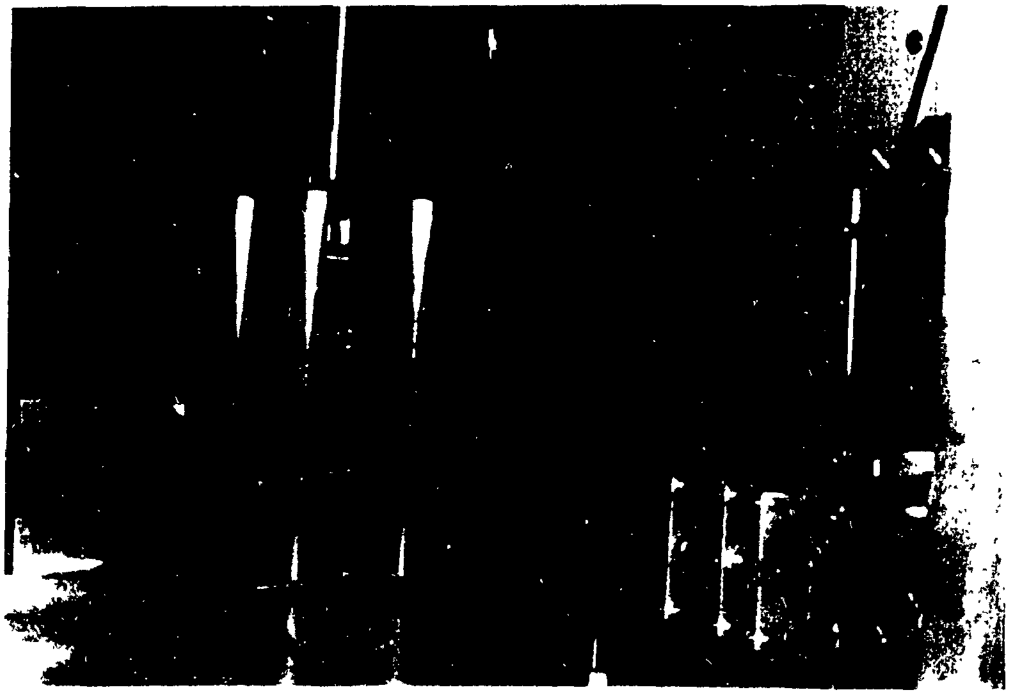

Fig. 3.2 Photographs from back and front side of the thermoplastic tape winding machine

with the preconsolidated laminate. The amount of heating should be sufficient to create good bonding between the plies The tape speed is controlled by a computer controlled motor. The consolidation roller applies pressure at the contact point to improve the intimate contact. The pressure is applied with the help of an air cylinder. During the development of the set-up, following design aspects were considered.

3.3.2.1 Fixed heat source or fixed mandrel

During the thermoplastic tape winding process, either the heat source needs to move with the increase in thickness of the ring or the mandrel must move in order to have the same heating point. For the movement of heat source, an additional controller is required to direct the laser beam at the contact point with the increase in thickness of the ring. Moreover, it was found that the little misalignment in the direction of the laser beam caused component quality to suffer drastically [12]. On the other hand, movement of the mandrel is achieved easily with the help of an air cylinder and found to be economical. Therefore in the present case, it was decided to have the fixed heat source.

3.3.2.2 Selection of the mandrel axis of rotation

The mandrel can be rotated either around a horizontal axis or around a vertical axis. Since the heat source is kept stationary, it is critical to design the work table to minimize the positioning error. It was found that the horizontal axis of rotation gives a simple design of the set-up and also provides easy assembly and dissembly. Moreover, it avoids axial force in the mandrel drive shaft. Therefore in this case, a horizontal axis of rotation was selected.

3.3.2.3 The mandrel and roller

The size and shape of the mandrel determines the inside contour of the end product. In the present case outside diameter of the mandrel is fixed at 146.05 mm as required by ASTM D2344 [56] standard. The roller has a diameter of 60 mm.

In the beginning aluminum was used as a roller and mandrel material but it was found to be ineffective in getting desired bonding between layers. Consolidation was found to be improper in first few layers because of the high heat dissipation in the mandrel and roller. Later steel was used as a tool material. It was found to be effective because thermal conductivity of steel is 6 times lower than the aluminum. The speed of the mandrel and roller was controlled by a computer controlled motor. The position of the roller was fixed in order to ensure that the laser beam would constantly hit the contact point. The mandrel presses against the roller with the help of an air cylinder and moves upwards as the thickness builds up. Other than rotational axis of the mandrel, the mandrel could move around another horizontal axis parallel to the direction of the incoming tape in order to get uniform distribution of the force along the width of the tape. In the begining without this additional freedom of the movement of mandrel there used to be point contact instead of line contact between the roller and mandrel. This is due to irregularity of tape surface or misalignment of different parts of the set-up. An additional degree of freedom ensures better distribution of pressure at the consolidation point even with rough surfaces of the tape.

3.3.2.4 Tape guiding system

Design of guiding system is very important in laying up the tape at desired orientation. In the case of manufacture of multi-ply hoop rings, design of guiding system is simple as compared to the manufacture of angle ply cylinders. In the present case, two circular plates were attached on two sides of the roller for guiding the incoming tape on top of substrate (Fig. 3.2).

3.3.2.5 The tensioner

The task of tensioner is to maintain constant tension while the tape is unwound from the spool All tensioner systems have a shaft to hold the spool, a locking system to hold the spool on the shaft, and a brake to create a torque in the shaft. Depending on the torque controls, various kinds of tensioning devices are available in the market [15]. In the present case, a simple tensioning system as shown in Fig 3.3 was built where torque is controlled by using compression springs.

3.3.2.6 The heat source

There are several techniques available for heating the thermoplastic at the consolidation point. Pros and cons of these heating techniques are discussed in chapter 1. For the present work, two heat sources were selected. These were CO_2 laser and hot nitrogen gas. The 65 Watt CO_2 laser with a wavelength of 10.6 μm (MPB Technologies Inc.) was used. A six millimeter dia. laser beam was directed to the contact point using two mirrors. Circular laser beam size was converted to an elliptical beam with semi-major axis of 3.6 mm and semi-minor axis of 1 mm by two coplanar lens to obtain more concentrated heat source at the contact point.

3.4 Preliminary Experiments

To have a fast and rough estimate of the processing window, two-ply flat laminates were first fabricated using the same experimental set up as shown in Fig.3.2. These two tapes, one in contact with the roller and another in contact with the mandrel, were pressed together at the contact point. Laser heat was supplied at the contact point to consolidate the laminate. At first, the laser heat intensity of 60 Watt and a consolidation force per unit width of 100.8 kN/m was selected. Then two ply laminates at various speeds starting from 5 mm/sec to 30 mm/sec were manufactured. From the preliminary experiments it was found that the two layers did not join at a speed in the range from 5 mm/sec to 10 mm/sec because of degradation of the thermoplastics. As the speed increased, peeling of the layers became difficult. From the experiments, best consolidations were achieved in the range of 20 mm/sec to 30 mm/sec for the

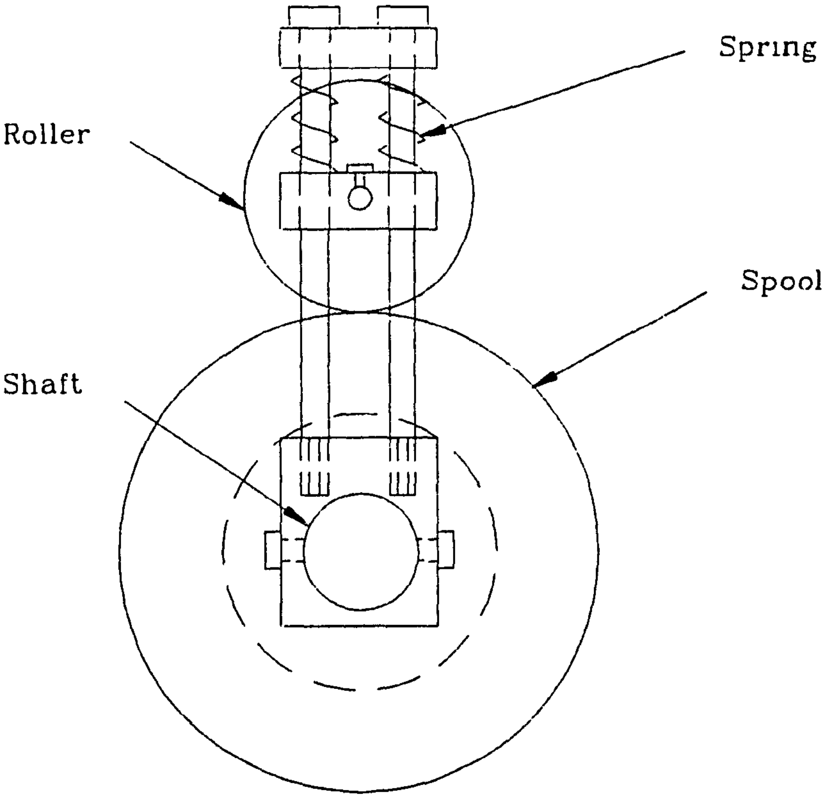

Fig. 3.3 Schematic diagram of a tensioning device for thermoplastic tape winding machine.

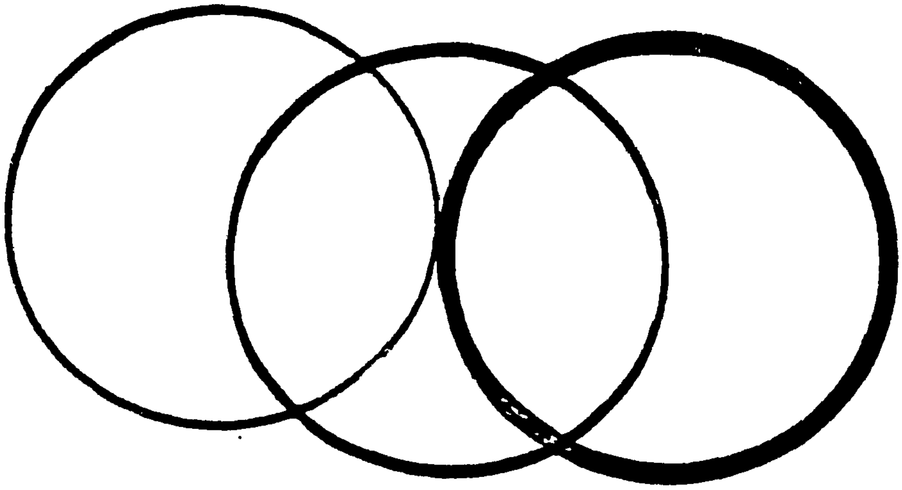

Fig. 3.4 Sample rings having 10, 15 and 45 plies produced by laser assisted processing.

60 W laser power. Increasing the speed further resulted in poor consolidation due to the insufficient melting of the thermoplastic tape Similarly the tape speed for various laser powers and consolidation pressures were determined It was found that for every laser power the speed range can be divided into three categories; low speed range (thermoplastic degrades), medium speed range (good consolidation), and high speed range (insufficient melting). It became obvious that the preliminary experiments help in giving rough estimate of the processing window and saves a lot of time and material.

Based on the results of the preliminary experiments, suitable values of the laser power, tape speed, and consolidation force were selected for the present experiments. For perfoming various studies ten-ply rings were selected This number of plies was found to be suitable while limiting the material use to a reasonable amount. Sample rings having 10, 15 and 45 plies are shown in Fig. 3 4. All the rings were fabricated in the set-up shown in Fig 3 2 using the laser as a heat source

3.5 Effect of Beam Incident Angle

The laser beam is a highly concentrated heat source, thus it can be used to produce a good quality part. During laser heating of the tape, some of the laser energy is reflected from the surface instead of being fully absorbed [6]. Grove [6] reported that the amount of reflected energy varies from 19% to 45% at high incident angles. Reflection of the laser energy depends on the polarization of the laser radiation, optical properties of the material, and the angle of incidence, i.e. the angle between the laser beam and the feed tape or the substrate. The angle of incidence in the laser process is dependent on the local curvature of the feed tape and the mandrel. Agarwal [17] carried out a detailed study on the effect of beam incident angle on reflectivity using Maxwell's equations. He then calculated the maximum consolidation temperature as a function of the laser energy for a known laser power. The analysis does not take into account the possibility of multiple reflections and the absorption of the beam energy by the opposite side. Grove [6] studied the effect of multiple reflections and reported that as more reflection takes place, the intensity of the heat flux at any point decreases, and the maximum temperature attained by the material falls Mean value of the surface reflectance for APC-2 has been reported as 0.28 along longitudinal direction (along the tape length) [6]. Tung et al. [57] found different results and reported that the surface of APC-2 absorbs the energy of a 10.6 μm laser wavelength beam in its entirety.

From the preliminary experiments it was found that the small change in location of the beam near the contact point can affect the bond strength drastically because of the change in beam reflection pattern as shown in Fig.3.5 Therefore accurate positioning of the laser beam during processing is required for attaining a desired temperature distribution. Beyeler et al. [12] reported that any misalignment of the laser beam produces unpredictable melting and results in improper consolidation The invisible nature of the CO_2 laser beam, due to its long wave length, makes it difficult to precisely position and align the beam. In the present case, a Helium - Neon laser was used to locate the direction of the beam. Size and shape of the roller and mandrel influences the reflection pattern and thus can affect the quality of a part.

3.6 Numerical and Experimental Reults for Temperature History:

Numerical and experimental results on the interface temperature profile during laser-assisted tape consolidation were obtained for various combinations of process parameters. Numerical results were obtained based on a model developed in chapter 2. Accuracy of numerical results was assessed by comparing the results with experimental results.

3.6.1 Numerical Results:

Figures 3.6 to 3.12 show the predicted interface temperature profile through computer simulation. Temperature profiles along the length of a 0.625 mm thick laminate, which corresponds to 5 plies for a ply thickness of 0.125 mm, are presented in Fig. 3 6

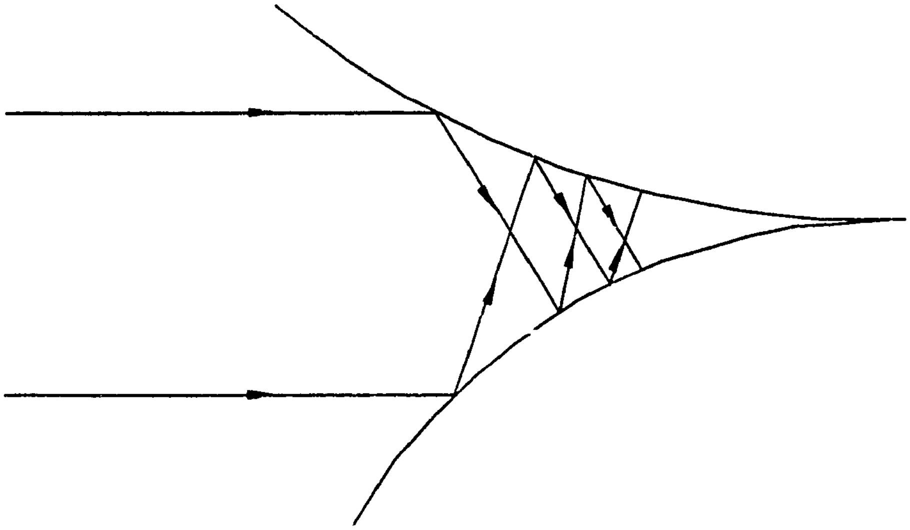

Fig. 3.5 Schematic reflection of incident laser beam during tape winding process.

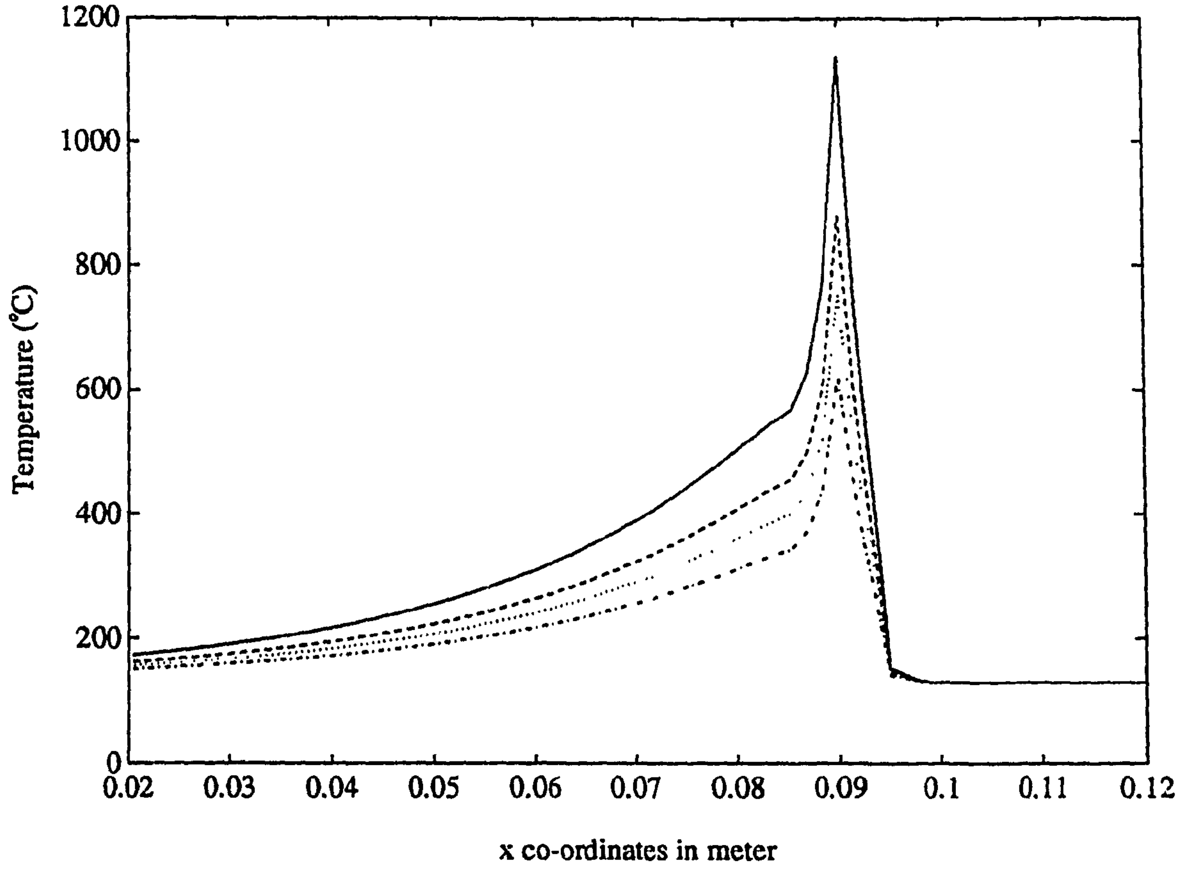

Fig. 3.6 Numerical prediction of temperature profile for 80W (—), 60W (--), 50W (...) and 40W (-.) laser powers at 10 mm/sec tape speed.

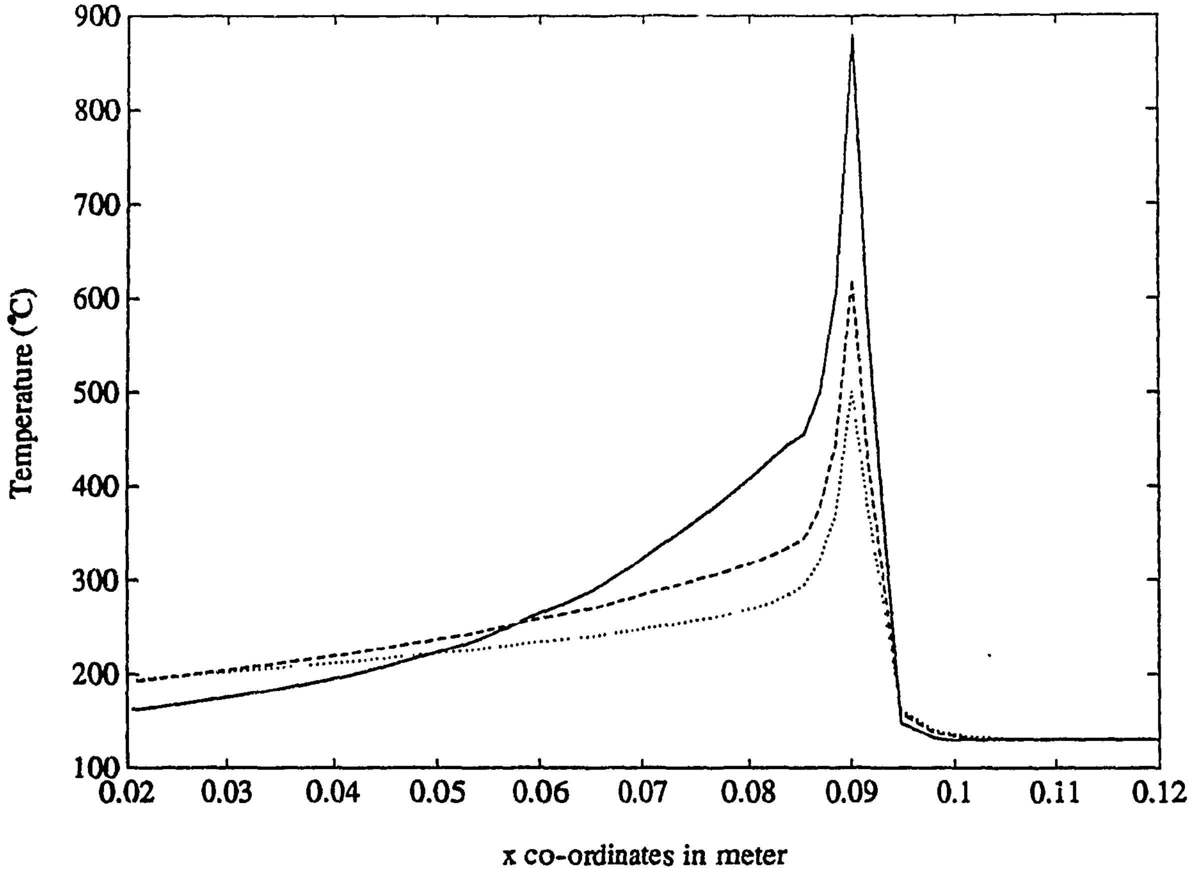

Fig. 3.7 Temperature profile obtained by computer simulation for 60W laser power and at 10mm/sec (—), 20 mm/sec (--) and 30 mm/sec (...) tape speeds.

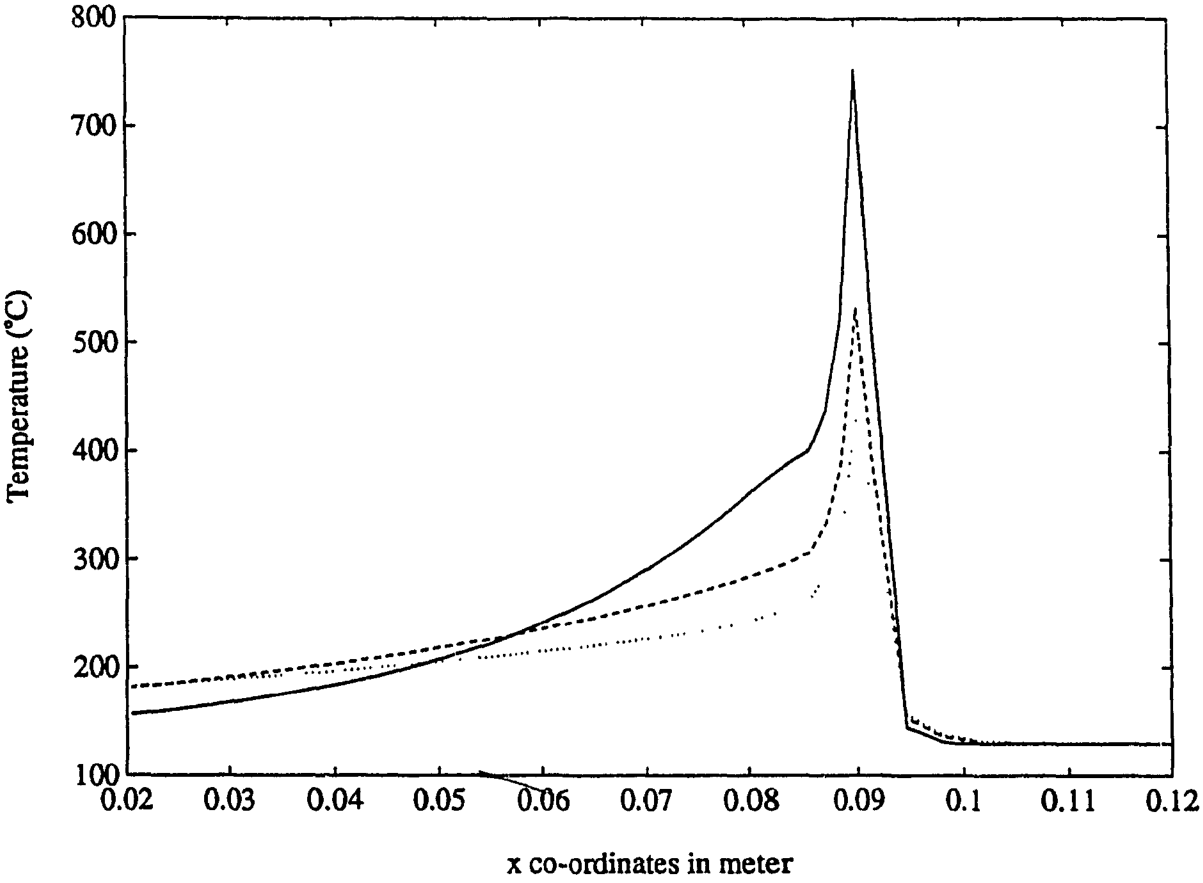

Fig. 3.8 Effect of tape speed on temperature distribution for a 5 ply thick laminate with 50W laser power and 10 mm/sec (—), 20 mm/sec (--), and 30 mm/sec (...) tape speeds.

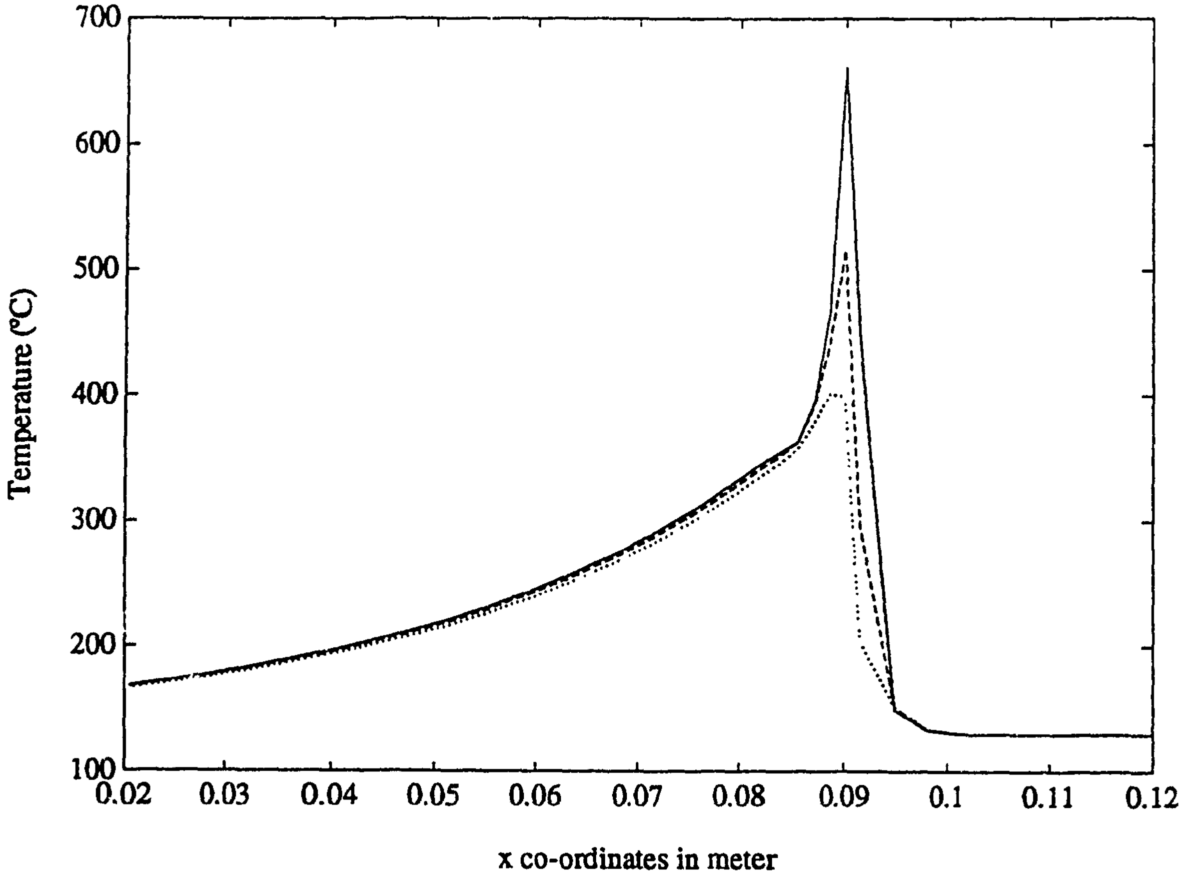

Fig. 3.9 Temperature distribution at different ply interfaces for a 5 ply thick laminate at 50 W laser power and 13 mm/sec tape speed. (—), (--), and (...) represents 5th, 4th and 3rd ply.

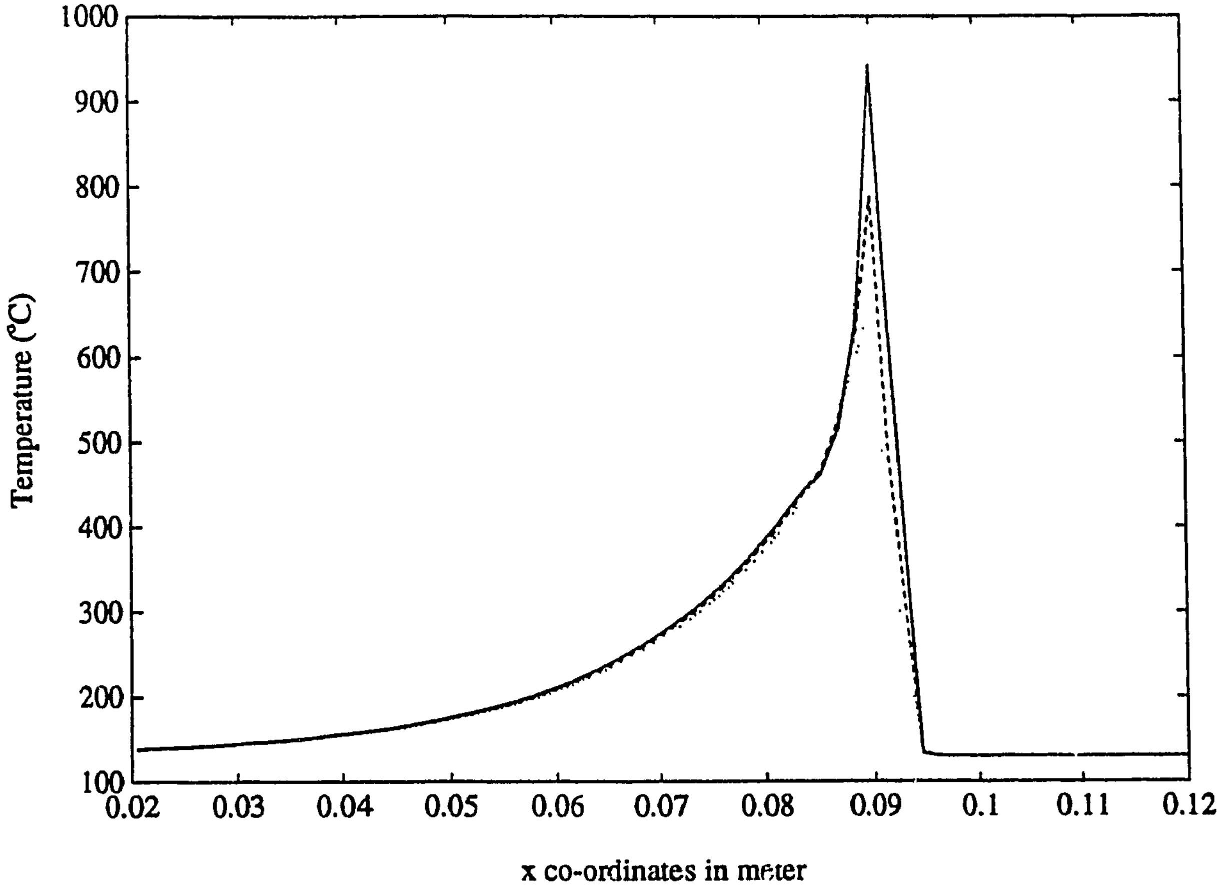

Fig. 3.10 Temperature distribution at different ply interfaces for a 5 ply thick laminate at 50 W laser power and 6.28 mm/sec tape speed. (—), (--), and (...) represents 5th, 4th and 3rd ply.

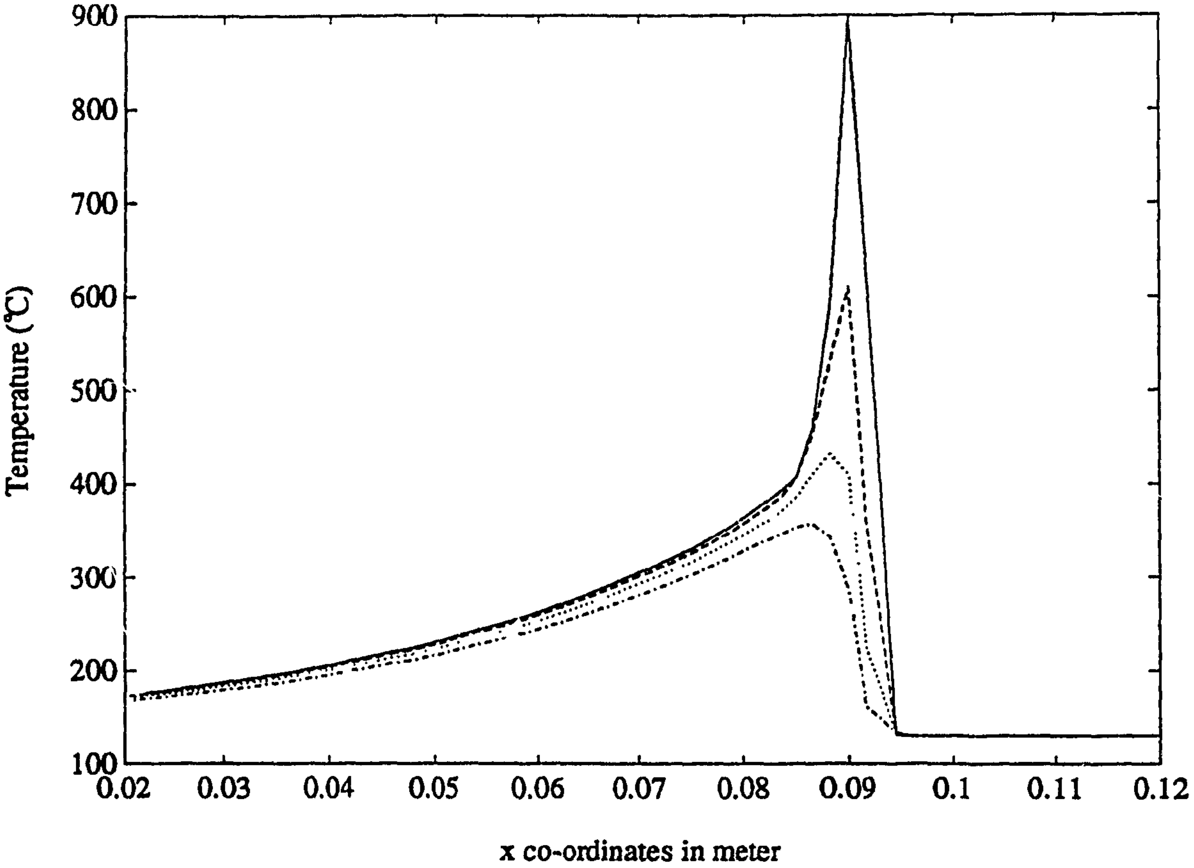

Fig. 3.11 Predicted temperature profile at different ply interfaces for a 10 ply thick laminate at 50 W laser power and 6.28 mm/sec tape speed. (—), (--), (...), and (.-) represents 10th, 8th, 6th and 4th ply.

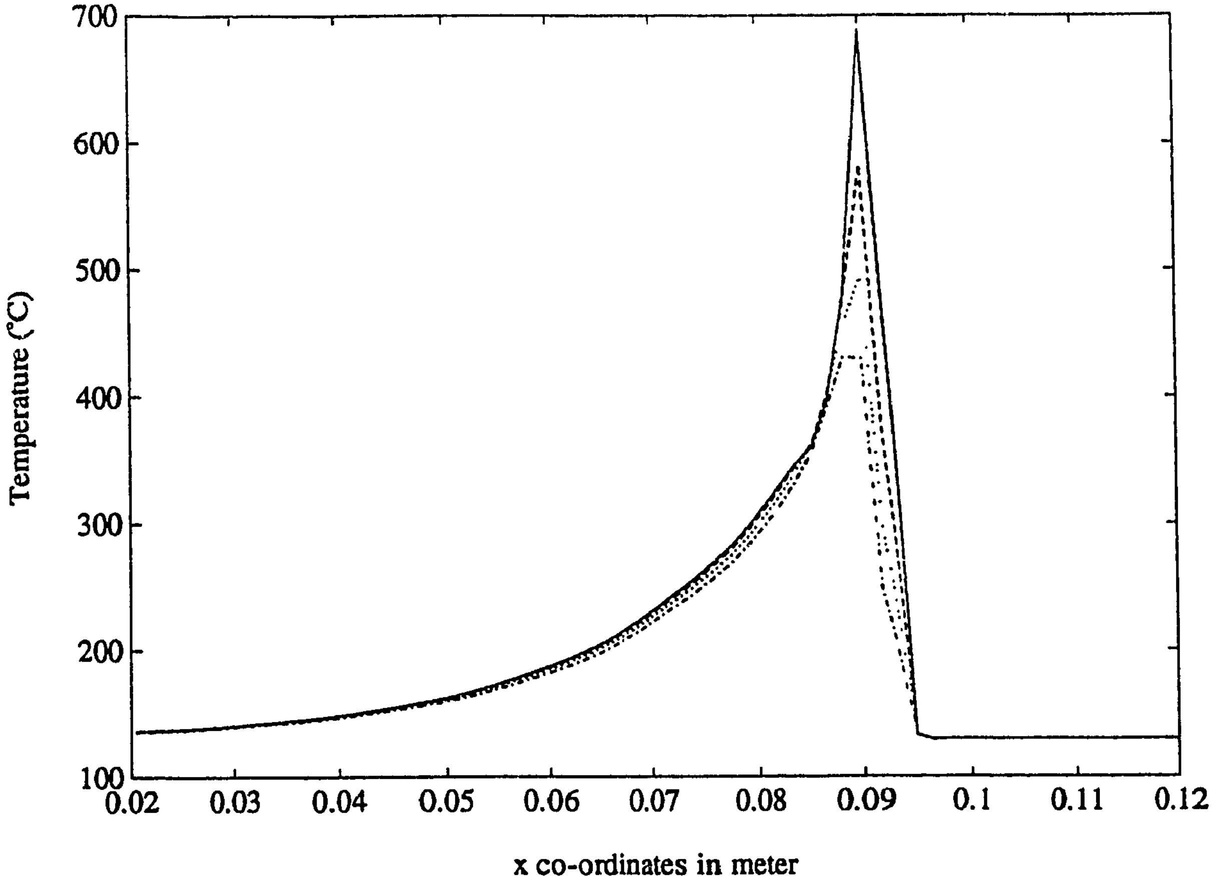

Fig. 3.12 Predicted temperature profile at different ply interfaces for a 5 ply thick laminate at 35 W laser power and 6.28 mm/sec tape speed. (—), (--), (...), and (.-) represents 5th, 4th, 3rd, and 2nd ply.

for 80W, 60W, 50W, and 40W laser powers at a tape speed of 10 mm/sec At this consolidation speed, the temperature in the laminate becomes significantly higher than the melting temperature (343°C) of PEEK thermoplastics. Maximum temperature reached for a 40W laser power was found to be 621°C, whereas for a 80W laser power, it was 1138°C. Because of the localized heating, the temperature rises very sharply and cools down at a faster rate in the beginning The heating rate for a 80W laser power was found to be 63,896°C/min and for a 40W laser power was found to be 31,108°C/min. The cooling rates for the first 2 seconds from the maximum temperature reached during processing were 22,455°C/min and 10,890°C/min for 80W and 40W laser powers respectively In all the cases, it was assumed that the laser power was uniformly distributed over a rectangular area of 6.35 X 2 mm^2, which simulates the elliptical beam of present system.

Effect of variation in tape speed for a laser power of 60W is shown in Fig. 3.7, for a 0.625 mm thick laminate. It is obvious from the figure that the maximum temperature reached in the laminate decreases with the increase in tape speed. The heating rate was found to be higher at a higher tape speed. The heating rates for 10 mm/sec, 20 mm/sec and 30 mm/sec tape speeds are calculated to be 47,518°C/min, 61,998°C/min, and 70,549°C/min respectively. The cooling rates for the first 2 seconds are found to be 16,671°C/min, 11,430°C/min, and 8,930°C/min for 10, 20 and 30 mm/sec respectively. With the decrease in laser power from 60W to 50W for same tape speeds of 10-30mm/sec, the maximum temperature reached in the laminate decreases as shown in Fig. 3.8.

To investigate the extent of melting in the laminate, temperature profiles at different ply interfaces were calculated. Figure 3.9 shows the temperature profile at the top of 5th ply, 4th ply, and 3rd ply for a laser power of 50W and a tape speed of 13 mm/sec. In this case, laser heating was performed between 5th and 6th ply. It is clear from the figure that the temperature in successive ply decreases with the increase in distance from the consolidation point. The maximum temperatures were calculated to be

661°C, 515°C and 401°C for 5th ply, 4th ply and 3rd ply. In this processing condition, top 3 plies were found to be above melting temperature (343°C) of APC-2 composites With the decrease in tape speed from 13 mm/sec to 6 28 mm/sec for the same laser power of 50W, top 7 plies were found to go above melting temperature for 10 ply laminates as shown in Figs.3.10 and 3.11. This is because that at lower tape speed, the material is exposed to laser heating for longer duration of time. Figure 3 10 shows the temperature profile for a 5 ply thick laminate whereas Fig. 3.11 shows the temperature profile for a 10 ply thick laminate. With the decrease in laser power from 50W to 35 W for the same tape speed of 6 28 mm/sec, maximum temperature in each ply decreases as shown in Fig. 3.12.

3.6.2 Experimental Results:

Experimental determination of the temperature profile for the verification of heat transfer model was performed using a thermocouple. At the beginning dual wave length pyrometer was used to monitor the temperature but it was found to be ineffective.

For the measurement of the temperature history, a thin (0.125 mm dia) K type thermocouple was inserted between the 5th and 6th ply without interrupting the process. Because of the high rate of change of the temperature near the consolidation point, a thermocouple with a small response time was selected for greater accuracy in measuring the temperature history. The thermocouple was connected to a digital process indicator (DP-86, Omega Eng. , Inc.) . The reading rate of the indicator was 0.5 sec. DP-86 has analog converter to convert the temperature range to a suitable voltage range. The output voltage from the indicator was fed into a LeCroy 9400, dual 125 MHz digital oscilloscope to store the data. The temperature histories obtained by oscilloscope are shown in Figs. 3.13, 3.14 and 3.15 for various processing conditions. In all the cases the mandrel and roller were preheated to 130°C by an air heater.

Figures 3.13, 3.14, and 3.15 show the temperature profiles recorded by the

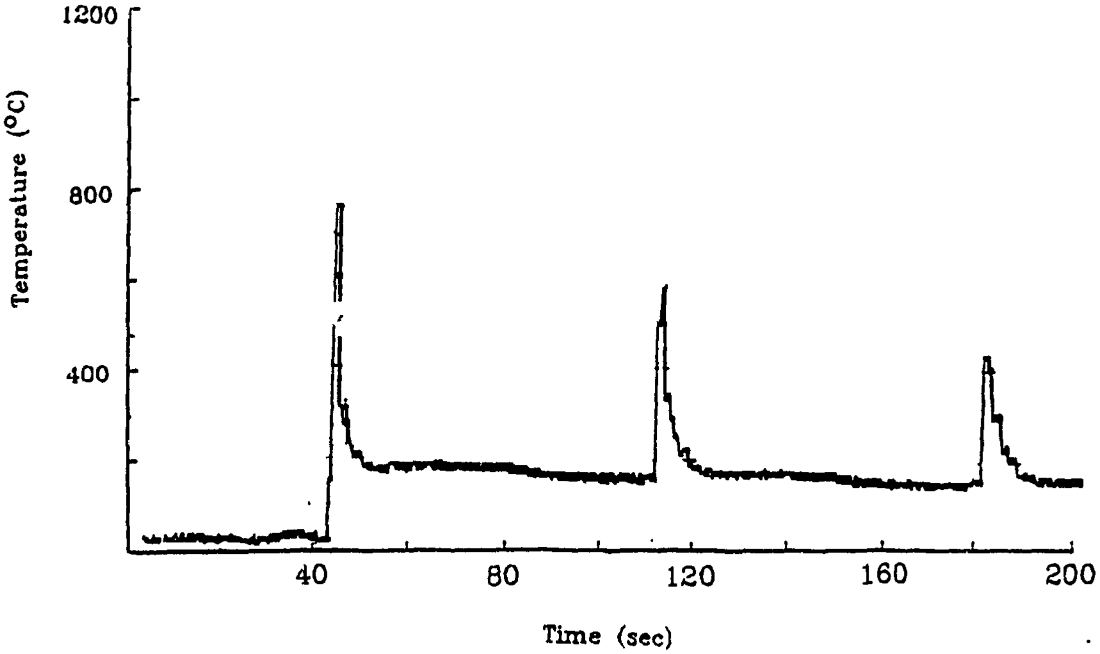

Fig. 3.13 Experimental temperature history during laser processing for 35 W laser power, 6.28 mm/sec tape speed and 67.2 kN/m consolidation pressure.

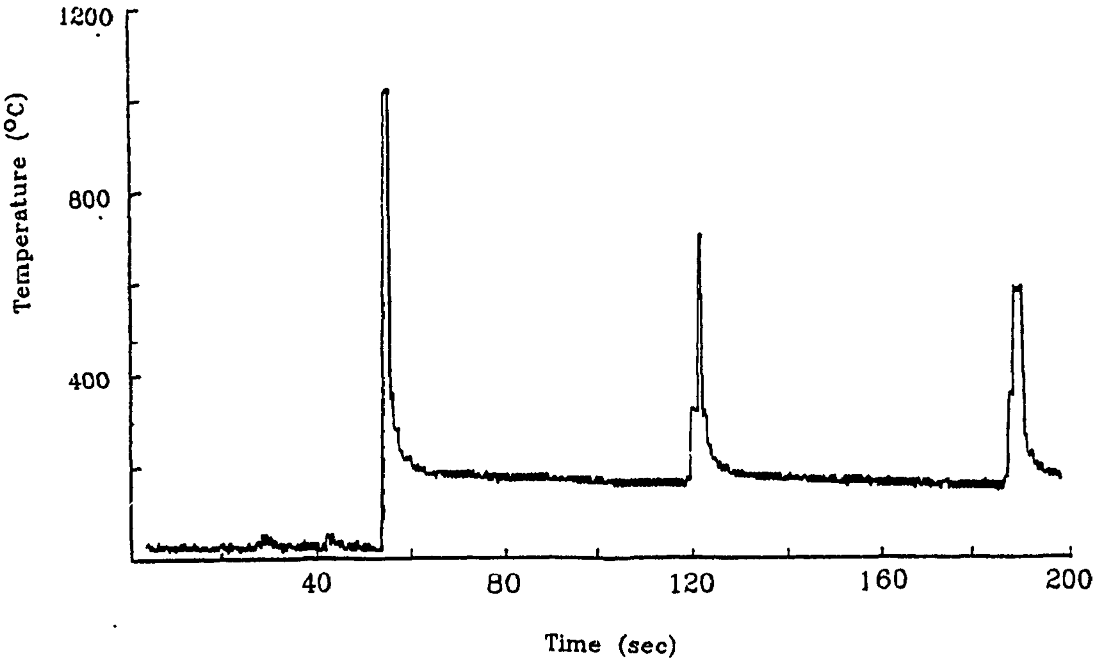

Fig. 3.14 Experimental temperature profile for 50 W laser power, 6.28 mm/sec tape speed and 67.2 kN/m consolidation pressure.

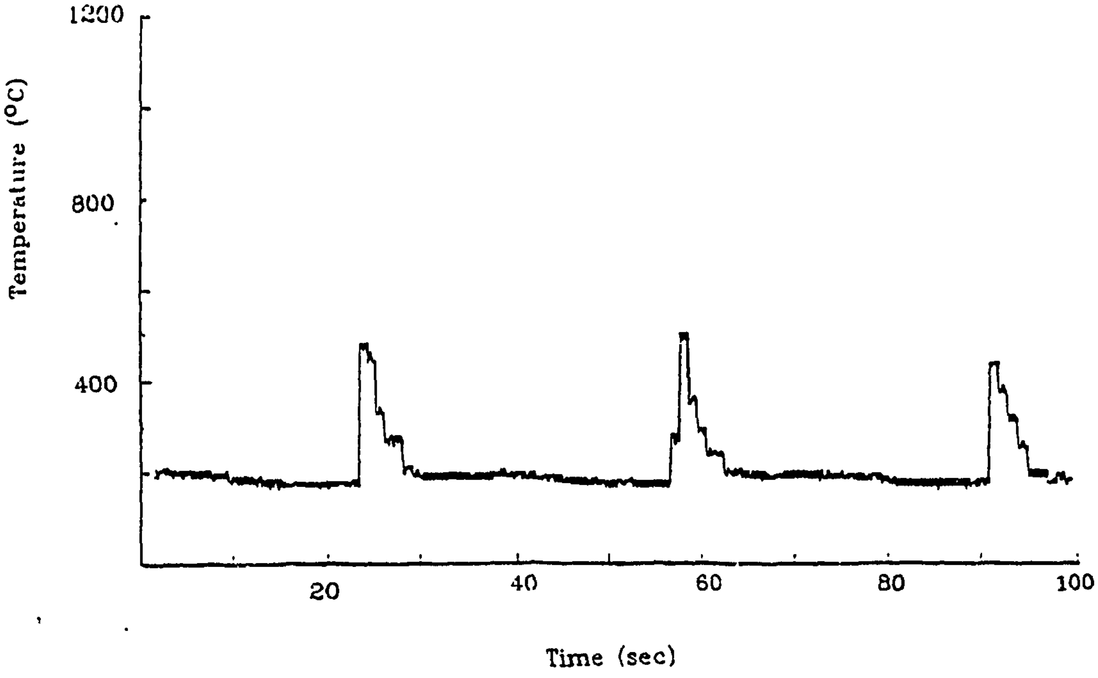

Fig. 3.15 Experimental temperature history during laser processing for 50 W laser power, 13.3 mm/sec tape speed and 67.2 kN/m consolidation pressure.

oscilloscope during 3 consecutive heating cycles. In Figs. 3 13 and 3 14, temperature profiles are shown just after putting the thermocouple near the contact point whereas Figure 3.15 represents the temperature profile after nearly one heating cycle The temperature recorded by the oscilloscope is not smooth because of the lower sampling rate of the instruments General trend in the temperature history during a tape winding process is that the maximum temperature decreases as the thermocouple goes away from the consolidation point.

It is evident from Figs. 3.13, 3.14 and 3.15 that only in a small region near the consolidation point, matrix material was heated above its melting temperature. It is noted that the several layers beneath the consolidation point were heated above melting temperature. Also maximum temperature reached in a ply decreases with the increase in distance from the consolidation point. The initial temperature during the first rotation was due to direct heating of the thermocouple by the laser beam At this instance the thermocouple was not sufficiently in contact with the tape consequently, the temperature obtained from the thermocouple does not represent the true maximum temperature of the composite surface during insertion of the thermocouple As the thermocouple reached the consolidation point, it came into contact with the prepreg tape and substrate, and became imbedded into the materials. After this point, the temperature measured by the thermocouple represents the true temperature of the surface

Figure 3.13 shows the temperature distribution for 35 W laser power, 6 28 mm/sec tape speed, and 67.2 kN/m consolidation force per unit width of the tape The maximum temperature during first spike reached above 740°C, during second spike it was above 570°C and during third spike it was above 420°C This test result was compared with the numerical results for 35W laser power and 6.28 mm/sec tape speed shown in Fig 3 12 Good agreement in the test results and predicted results were found The maximum temperature predicted by the computer simulation was calculated to be 689°C for 5th ply, 582°C for 4th ply and 495°C for 3rd ply. The maximum temperature during first spike as measured by thermocouple was found to be higher than the predicted results by 7.2%

probably because of direct heating of thermocouple with the laser beam Maximum temperatures recorded during second spike and 3rd spike were found to be less than the predicted results because of the fact that the peak temperature can not be measured accurately due to lower sampling rate of the set-up The heating rate for the top laminate predicted by the computer simulation was 45,038°C/min and experimentally it was calculated to be more than 43,500°C/min The experimental cooling rate was estimated to be more than 8,550°C/min during first spike. The cooling rate for this case is measured for the material to cool down from maximum temperature to around 180°C (Fig. 3.13) The experimental melt time was measured from the experimental temperature history and was found to be in the range of 0 5 sec to 1.5 sec. The predicted results on heating rates, cooling rate and melt time are discussed in detail in next section 3.7.

The temperature profile for a 50 W laser power, 6 28 mm/sec tape speed, and 67.2 kN/m consolidation force per unit width is shown in Fig. 3.14. With the increase in laser power from 35 W to 50 W, the maximum temperature reached in a spike also increases. For this case maximum temperatures were above 1,000°C, 700°C and 590°C during first, second and third spikes respectively. On comparing the experimental result with the predicted result for 50W laser power and 6.28 mm/sec tape speed (Fig. 3.10) good agreement in the test results and numerical results were observed. Maximum temperatures predicted by computer simulation were 943°C, 787°C and 662°C for 5th ply, 4th ply and 3rd ply respectively.

Figure 3.15 shows the temperature history during the thermoplastic tape winding for a 50 W laser power, 13.3 mm/sec tape speed, and 67.2 kN/m consolidation force. It is obvious from Figs. 3 14 and 3.15 that the maximum temperature in respective spike went down with the increase in tape speed. It is to be noted here that the Fig.3.15 represents the temperature profile after first cycle Maximum temperatures during second and third rotations were found to be more than 500°C. Maximum temperature during second rotation was found to be a little less than the third rotation because of insufficient sampling rate of the instrument. The result from the computer simulation for 50W and 13 mm/sec tape speed (Fig 3.9) shows that the maximum temperatures in this case are 661°C, 515°C and 401°C in 5th ply, 4th ply and 3rd ply respectively

The temperature history during the tape winding process was found to be complex It is clear from the figures that for different combinations of laser power and tape speed, temperature profiles are different. At lower speeds, the temperature at the consolidation point was higher compared to the temperature at higher speed for the same heat intensity. This is because the material at the consolidation point is heated for a longer time at a lower speed compared to at a higher speed. In most cases, to obtain a good interply bond strength, the temperature at consolidation point reached above manufacture recommended processing temperature of APC-2 composites. From the microstructure study, no visible degradation of the matrix material was observed even when the temperature at the consolidation point reaches above 650°C for the laser processing. The reason for no visible degradation above manufacturer recommended processing temperature could be possibly due to higher heating rate and shorter melt time during processing Day and coworker [58] studied the effect of heating rate on the degradation of PEEK thermoplastics. They performed experiments in nitrogen and air atmosphere at nine heating rates in the range of 0.01°C/min to 10°C/min using thermogravimetric analysis (TGA). Degradation in terms of weight loss was measured and it was found that in air the weight loss process is more complex, involving several reaction mechanisms They observed that an increase in heating rate from 0.01°C/min to 10°C/min, caused the degradation temperature to shift from 420°C to 550°C in nitrogen atmosphere and from 330°C to 550°C in air. Below the degradation temperature PEEK was found to be almost stable. It is expected during the laser processing, where the heating rate is higher than 20,000°C/min., degradation temperature would be higher than 700°C.

3.7 Effect of heating rate on the manufacturing condition

The bonding between plies results mainly from wetting and interdiffusion of molecular chains. Wetting predominates at low welding temperatures close to the polymer melting point and involves the surface tension and viscosity of the two surfaces in contact Interdiffusion of macromolecular chains of the two surfaces in contact predominates at fairly high temperature and welding time [59] During hot gas processing of APC-2 thermoplastic composites [60], it was found that for a good interply bonding, the processing temperature goes above 600°C whereas for the hot pressing and autoclave processing, manufacturer recommended processing temperature is 380°C to 400°C.

Models developed in previous chapter 2 were also used for the prediction of heating rate, cooling rate, and melt time for a specific combinations of process parameters. Effect of laser power on heating rate as found by model prediction is shown in Fig. 3.16 for a tape speed of 10 mm/sec With the increase in laser power, the heating rate is found to be increasing. The heating rate for 40W laser power was calculated to be 31,108°C/min whereas for 80W laser power, it was 63,896°C/min. With the increase in tape speed, the heating rate is found to be increasing as shown in Fig 3.17. In all the cases heating rate was more than 31,108°C/min. The melt time, i.e the duration for which, temperature during processing remains more than the melt temperature (343°C) of PEEK thermoplastics, was calculated to be in the range of 0 04 sec to 1.75 sec for 50W and 60W laser powers and for 10 mm/sec to 30 mm/sec tape speeds. Effects of laser power and tape speed on the melt time as predicted by model are shown in Fig 3 18 The cooling during the laser processing was found to be non-linear as shown in Figs. 3.6 to 3 12 Because of this reason, average cooling rates were measured for two intervals such as first 2 seconds from the maximum temperature reached during consolidation and next 2 to 4 seconds. The cooling rates for the first 2 seconds were found to be quite high as compared to the next 2 seconds as shown in Figs 3.19 and 3 20. Shorter melt times (0.04 sec to 1.75 sec) and higher heating rates (more than 30,000°C/min) during the tape winding process limit the amount of diffusion therefore higher processing temperature is needed for sufficient molecular interdiffusion. Higher processing temperatures would result in lower viscosity and higher diffusivity which will cause greater degree of resin flow and interdiffusion. Higher degree of resin flow and interdiffusion would result in the better interply bond properties. Saint-Royre and his co-workers [59] found that the

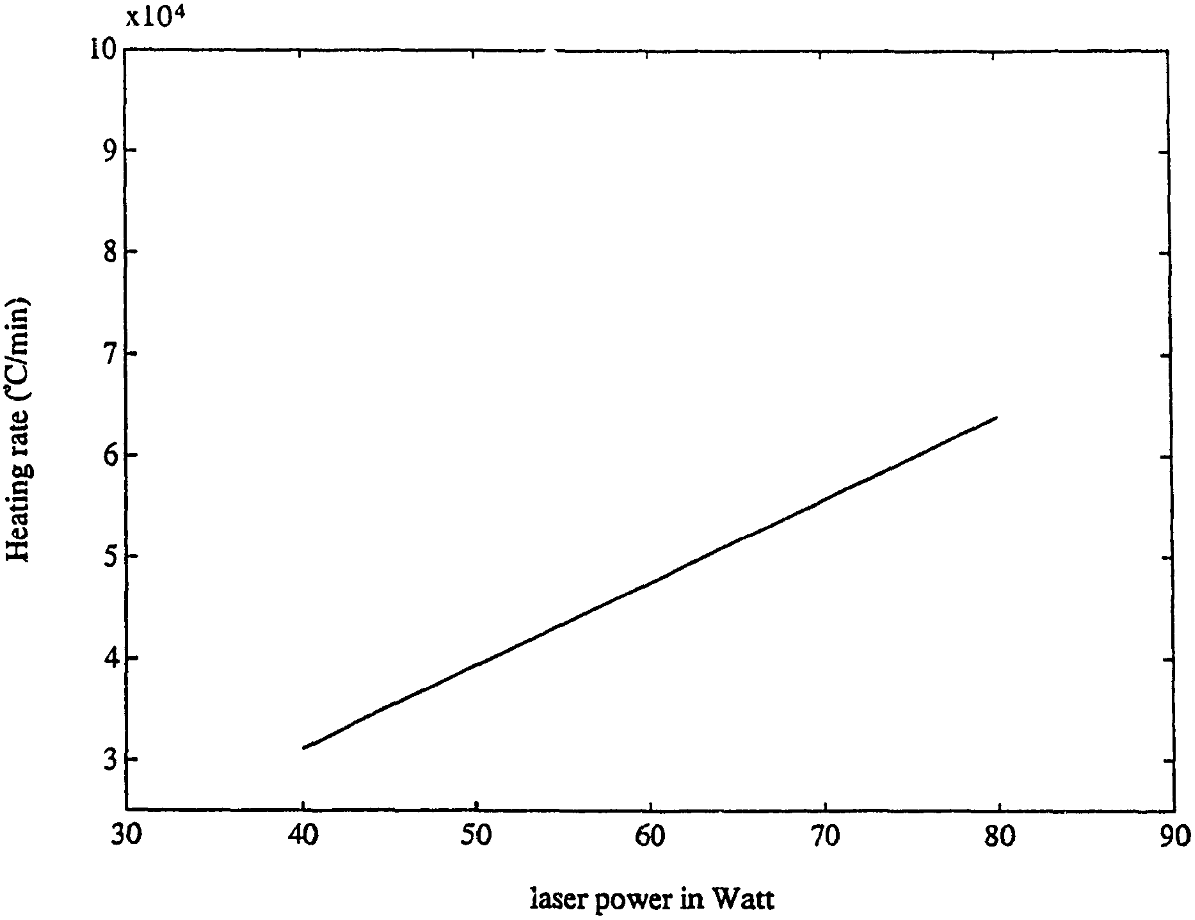

Fig. 3.16 Effect of laser power on heating rate during tape consolidation process.

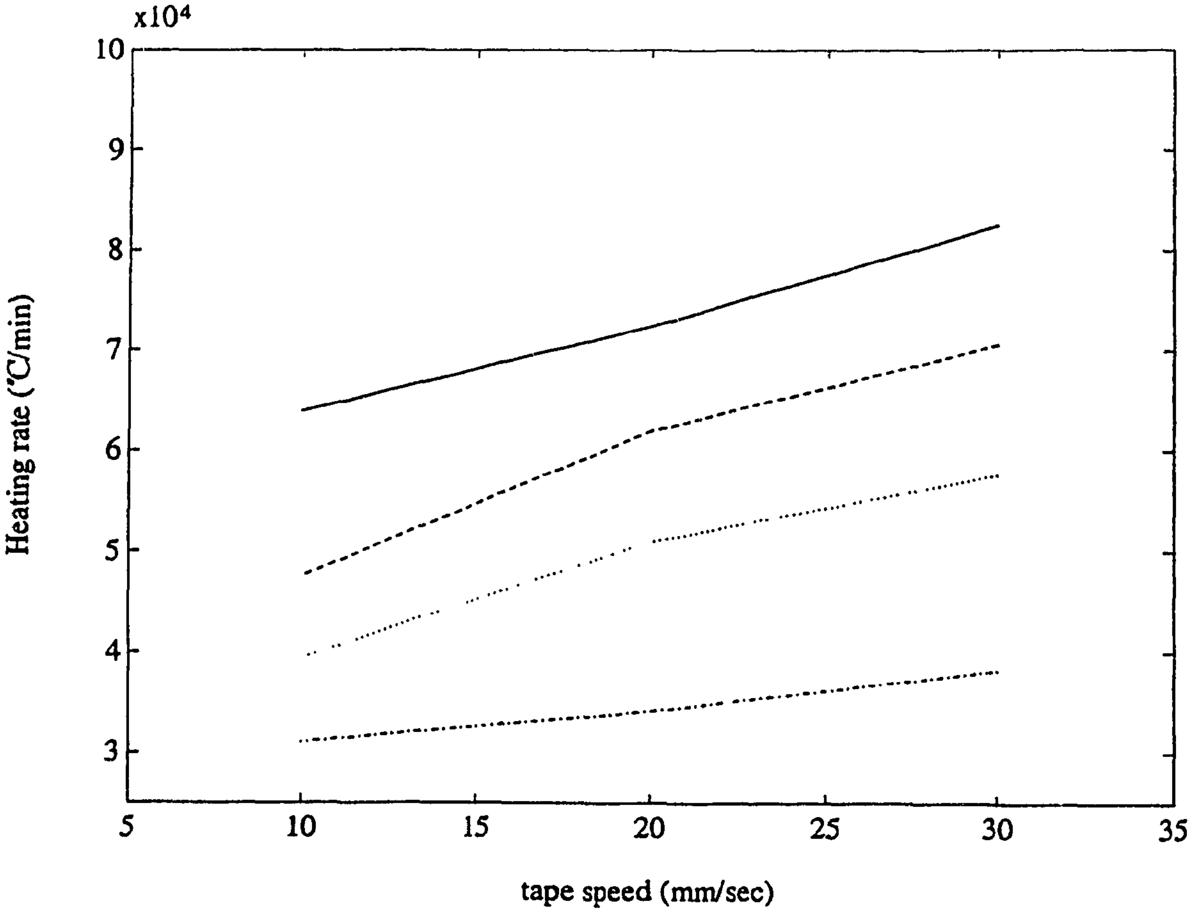

Fig. 3.17 Effect of tape speed on heating rate. (—), (--), (...), and (.-) represents 80W, 60W, 50W and 40W laser powers.

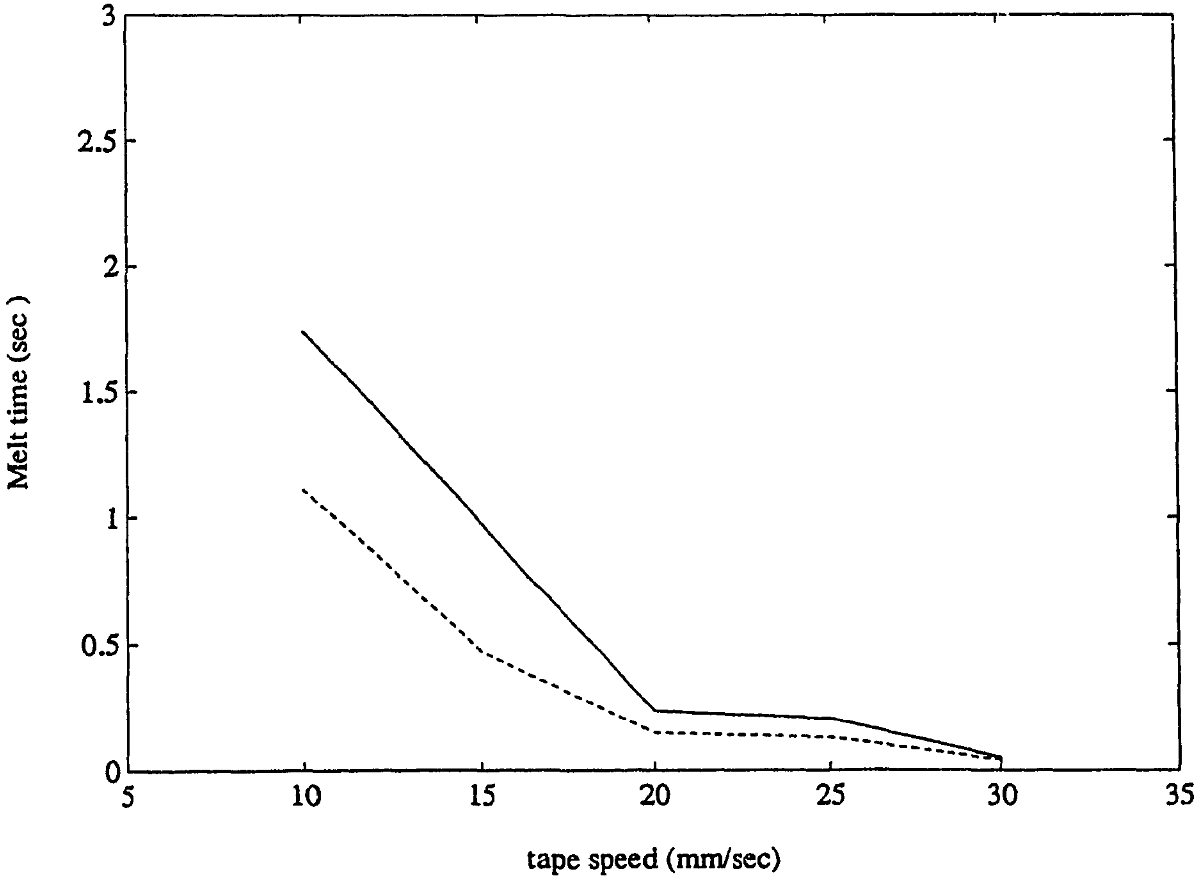

Fig. 3.18 Effect of laser power and tape speed on melt time. (—) and (--) represents 60W and 50 W laser powers.

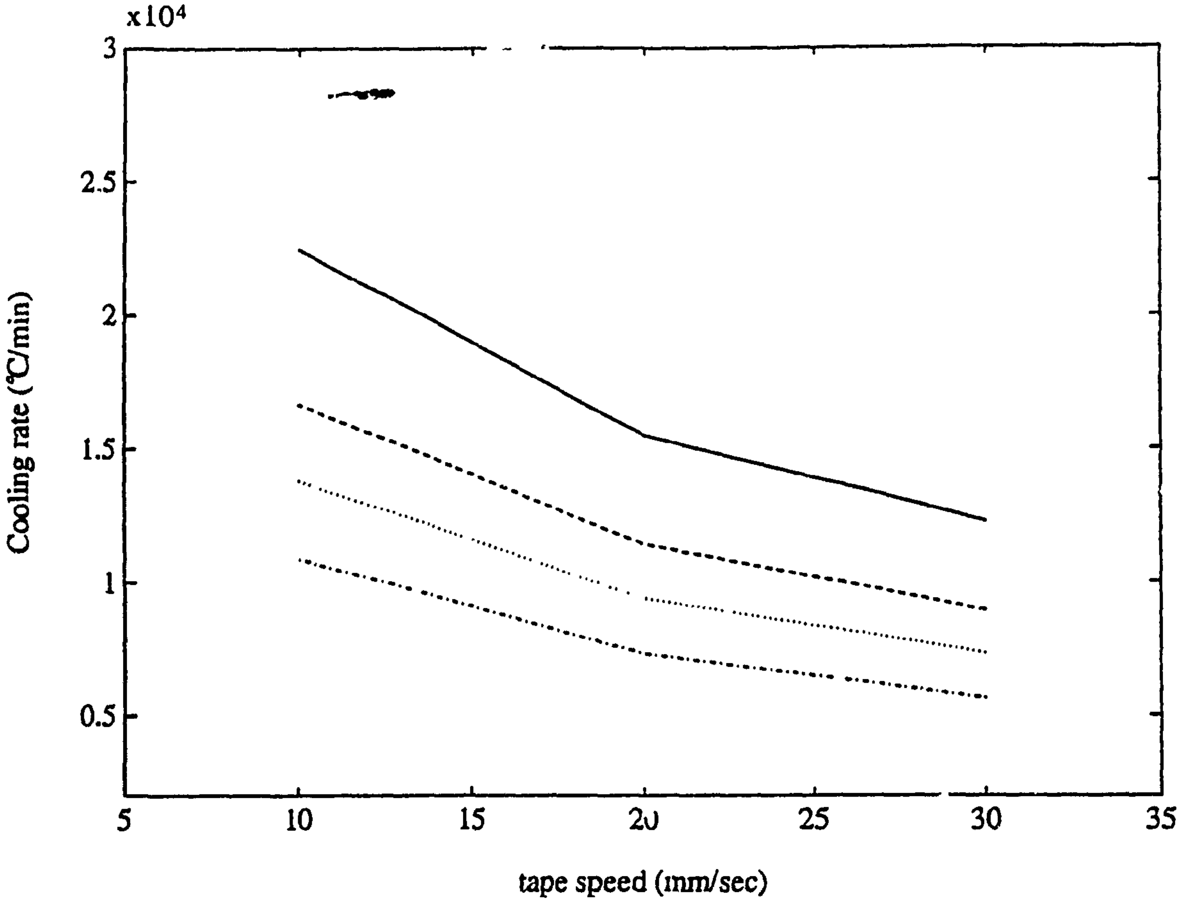

Fig. 3.19 Effect of tape speed on cooling rate for the first 2 seconds after the maximum temperature. (—), (--), (...), and (.-) represents 80W, 60W, 50W and 40W laser powers.

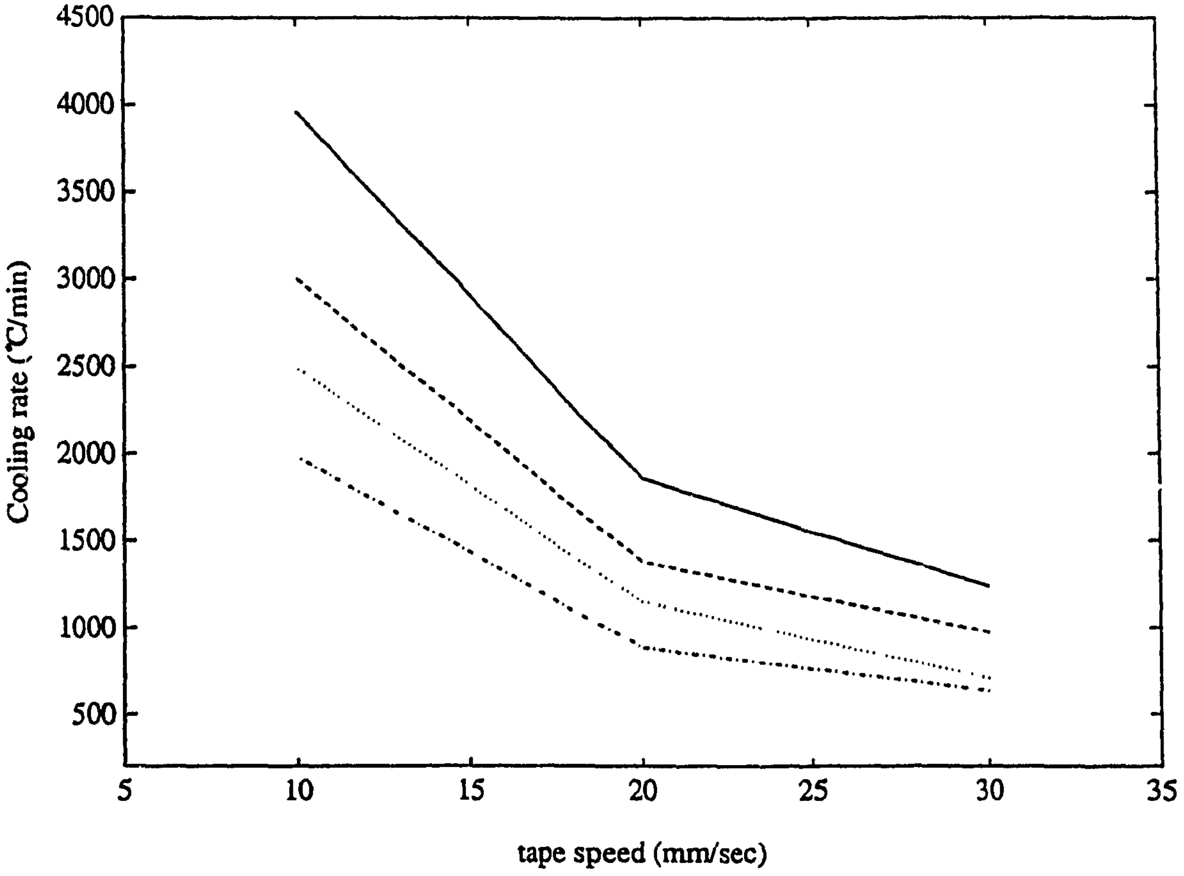

Fig. 3.20 Effect of tape speed on cooling rate for the next 2 to 4 seconds after the maximum temperature. (—), (--), (...), and (.-) represents 80W, 60W, 50W and 40W laser powers.

minimum temperature required for good weld conditions for polyethylene layers increases from 145°C to 214°C with the increase in heating rate from 20°C/min to 400°C/min.

For laser processing, immediate bonding was achieved above 400°C but for better bond strength, temperature required is above 500°C. For investigating the bond quality, SBS tests were conducted for various processing conditions and it was found that for 50 W laser power, better bond strength was achieved at around 13 mm/sec tape speed. The maximum temperature in this case is more than 500°C during second spike and around 500°C during third spike (Fig. 3 15).

3.8 Numerical and Experimental Results on Degree of Intimate Contact

The temperature history generated from the heat transfer model was used to study the intimate contact phenomenon. It is clear from the previous discussion that the intimate contact is a function of tape speed, consolidation force and composites viscosity which in turn is influenced by temperature history. Effect of consolidation force on degree of intimate contact (D_{ic}) for a 60W laser power at 28 mm/sec tape speed is shown in Fig. 3.21. Consolidation force per unit width of the tape was calculated based on the assumption that there is a line contact between roller and ply surface. The average width of the tape was 6.35 mm (0.25"). It is clear from the figure that a force more than 50 kN/m was needed to have complete intimate contact A consolidation force of 25.2 kN/m resulted in poor intimate contact and was verified through the experiments.

Effect of variation in tape speed on intimate contact for 50W and 60W laser powers are shown in Fig. 3.22. The results show that for 50W and 60W laser powers, complete intimate contact was achieved for tape speeds below 30 mm/sec. An increase in tape speed above 30 mm/sec caused a decrease in intimate contact value as shown in Fig. 3.22.

Experimental measurements of the degree of intimate contact (D_{ic}) can be

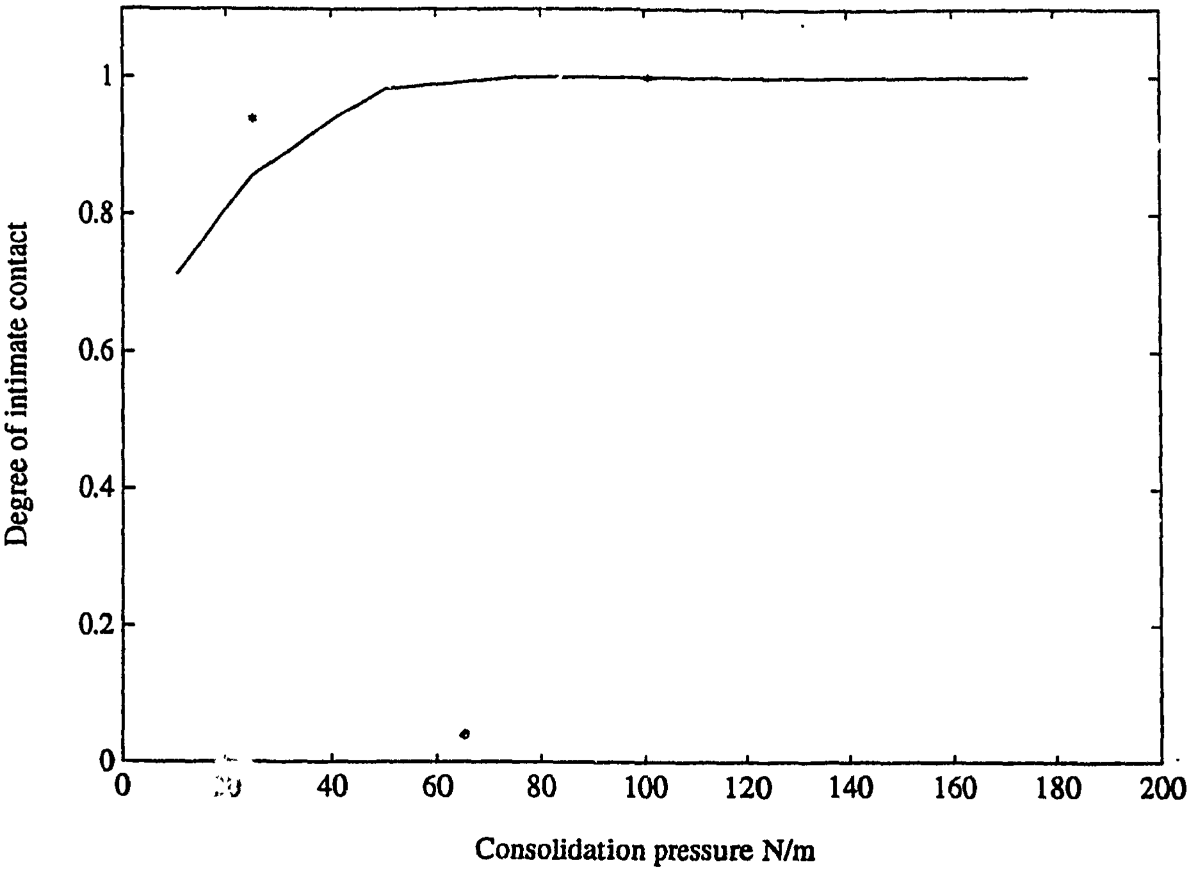

Fig. 3.21 Effect of consolidation pressure on degree of intimate contact for 60W laser power and 28.0 mm/sec tape speed. (—) represents model prediction and (*) represents experimental value.

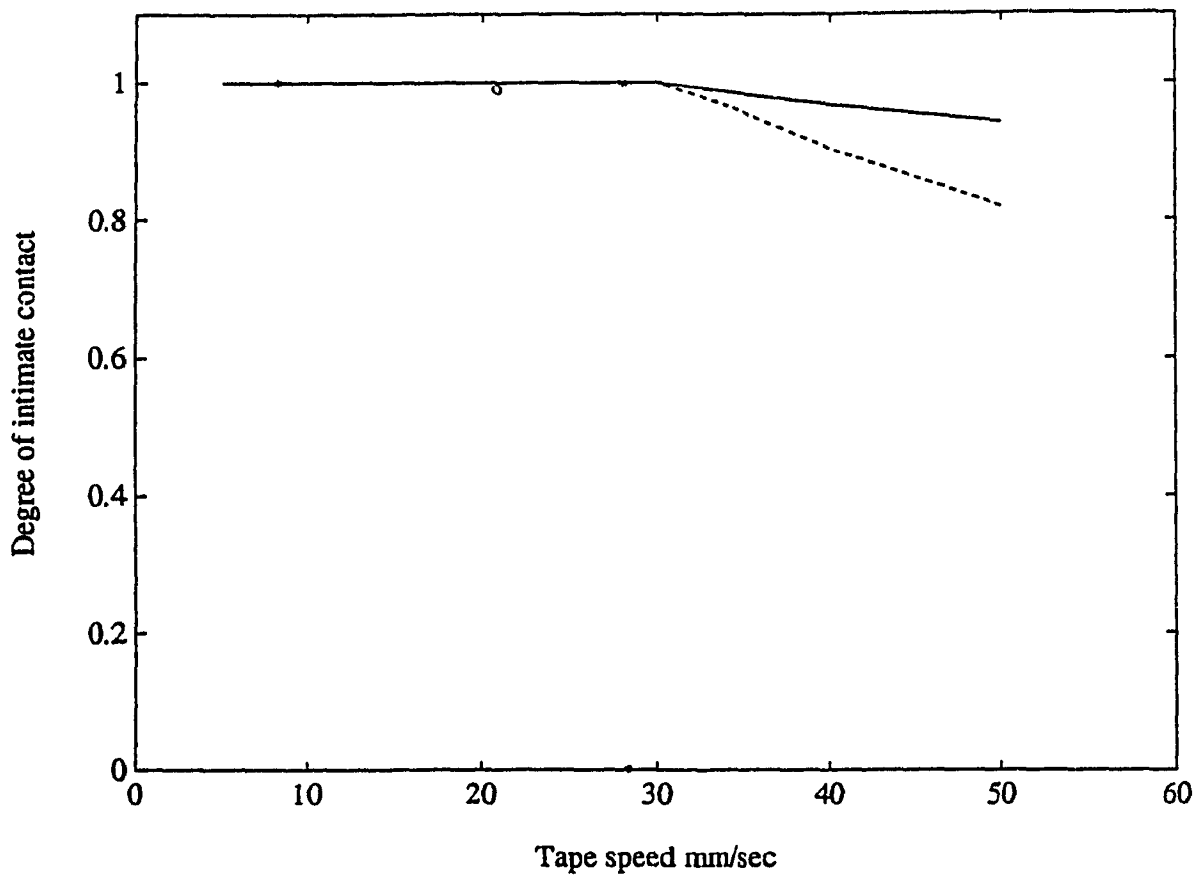

Fig. 3.22 Degree of intimate contact for various tape speeds and at 100.8 kN/m consolidation pressure. (—) and (--) represents predicted value for 60 W and 50W laser powers. (*) and (o) are experimental values for 60W and 50W laser powers.

Fig. 3.23 Micrograph of a cross-section for a ring processed at 60 W laser power, 27.6 mm/sec tape speed, and 25.2 kN/m consolidation pressure (100X).

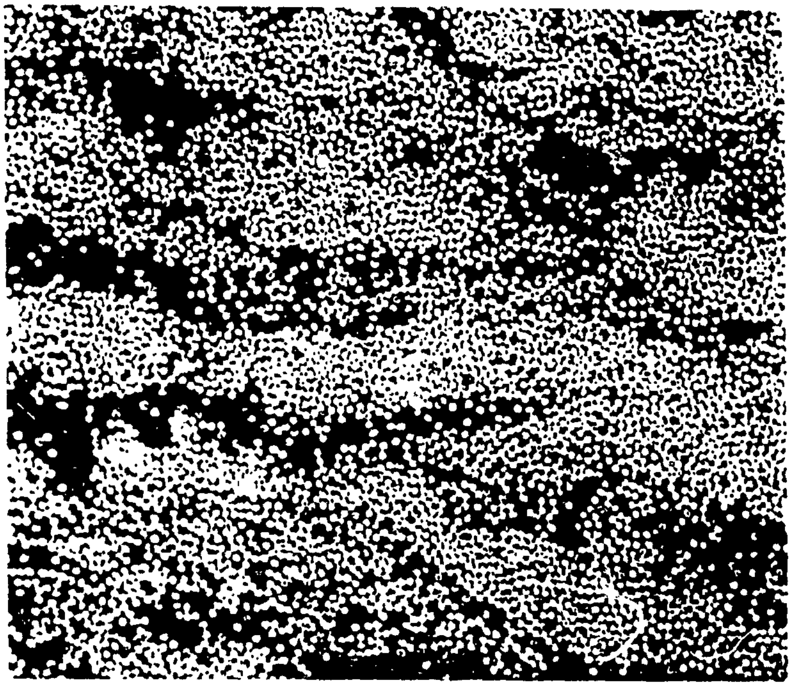

Fig. 3.24 Cross-sectional view of the consolidation for a ring processed at 60 W laser power, 27.0 mm/sec tape speed, and 100.8 kN/m consolidation pressure (200X).

performed by C-scan [11] or by optical microscopic study [49] In the C-scan method, degree of intimate contact is determined from the C-scan pictures by comparing the area in good contact to the total area [11] In the present case, the degree of intimate contact was measured by microscopic examination of the sample Since intimate contact refers to the removal of surface irregularities at the interply interfaces coming into contact, microscopic method is suitable to determine the spatial gap and incomplete contact at the interface level. In the present study following formula is defined for the experimental measurements of the degree of intimate contact by an optical microscopic method.

$$(D_{ic})_{exp} = 1 - \frac{\textit{Non-contact interface length}}{\textit{Total interface length}} \qquad (3.1)$$

Photomicrographs of samples at various combinations of processing variables were taken as shown in Figs 3 23 and 3.24. From the photograph, total interface length and length of interface where intimate contact was not achieved were measured. Then using equation 3.1, value of degree of intimate contact was measured. Experimental results on the degree of intimate contact are included in Figs. 3.21 and 3.22 for various process conditions. There is a good agreement between the results of the model and the data over the range of process parameters used in the test

3.9 Crystallinity Study

The thermal processing history of semicrystalline thermoplastic polymers establishes its degree of crystallinity, which affects the physical and mechanical properties of the finished composite part. For example, with the increase in crystallinity, the modulus increases but the toughness decreases. Also a certain level of crystallinity is needed for solvent resistance.

Effects of thermal histories on the crystallization of neat PEEK resin and its composites with continuous carbon fibre (APC-2) had been investigated by reserachers

[61-64]. Blundell et al [61] determined crystallinity for a wide range of cooling rates for APC-2 composites For cooling rates from about 10°C/min up to about 600°C/min, the percent crystallinity appears to be from 25 to 30 %, and increases relatively slowly with decreasing cooling rate. For very slow cooling rates of the order of 0 5°C/min, higher crystallinity in excess of 35% can be achieved For a cooling rate of the order of 2,500°C/min, the material is found to be amorphous In second set of experiments, Blundell et al [61] investigated the effect of annealing on the crystallinity of APC-2 samples. APC-2 plaques were prepared in amorphous state by rapid cooling and then crystallized by post annealing for 30 minutes. The results show that over a wide range of annealing temperatures from about 200 to 300°C the crystallinity attains a fairly steady value with only a gradual increase with temperature. Annealing at 200°C for 30 minutes gave crystallinty around 20% Only at the highest annealing temperature (320°C) does the crystallinity achieve a value in excess of 35%.

Numerical and experimental results on temperature histories during the tape winding process are shown in Figs. 3.6 - 3.15. It is clear that the regions close to the consolidation point are remelted and some or all of the initial crystallinity must have been destroyed. The material undergoes complex temperature history such as higher heating rate (more than 30,000°C/min.), shorter dwell time (0.04 sec to 1.75 sec) and higher cooling rate (more than 4,000°C/min near consolidation point) Inside layers undergo several such heating and cooling cycles compared to the outer layers Because of these variations in heating and cooling cycles for different plies, crystallinity at different plies may vary. From experimental results (Figs 3.13-3 15), it was found that the material was cooled in the range of 170°C to 200°C at a rate higher than 4,000°C The material undergoes annealing process at 170°C to 200°C temperature range, which affects the crystallinity of the sample. As shown in figures 3 13-3.15, regions away from the contact point are subjected to annealing which can increase the degree of crystallinity

For the measurement of crystallinity, approximately 5 mg samples were taken from different layers. It is to be noted here that the ply thickness is 0.125 mm therefore it may be possible to have sampling errors for each layers To get more accuracy in taking out the sample from different layers, rings were manufactured by putting aluminum foil between the 5th and 6th layers Rings were cut and separated between 5th and 6th ply. Samples were taken from inside layers as well as from top layers for various process parameters Measurement of crystallinity was done by using a differential scanning calorimeter (DSC) The DSC scans were done from 100°C to 400°C with the scanning rates of 20°C/min. as shown in Figs. 3.25-3 28 In all the cases of laser processed samples for laser powers more than 50 W, cold crystallization exotherm peak similar to the unprocessed APC-2 tape were observed around 175°C Figure 3 25 shows the DSC thermogram of an as received APC-2 tape and Figs. 3 26-3 28 show the DSC thermogram of laser processed samples. For the case of laser processed samples at 30 W and 40 W laser power, and tape speeds below 6 4 mm/sec, cold crystalliztion peak is not observed (Fig.3 26) Cold crystallization for 50 W and 60 W laser powers are shown in Figs 3.27 and 3.28. The percentage crystallinity of the polymer present before glass transition temperature is determined from following expression [63],

$$c = \frac{H_T}{H_{ULT}} . \frac{100}{W_m} \tag{3.2}$$

where H_T is the net amount of heat absorbed on heating from the glass transition temperature (143°C) to 380°C as measured by the DSC. H_{ULT} is the ultimate heat of crystallization of 100% crystalline polymer and is taken to be 130 J/g [63]. W_m is the weight fraction of polymer in the composite and is considered to be 35% in this case. The results of the crystallinity for various combination of process parameters are tabulated in Table 3.1 The crystallinity of the as received APC-2 composite is found to be 29 40%. In this study, crystallinity above 25 % are obtained in most cases. It is to be noted here that in the present case the material cooled down to around 180°C at a rate higher than 4,000°C/min (Figs. 3 13-3.15). The material remained at 180°C for a long time and goes through annealing process which might have increased the amount of crystallinity. The increased amount of crystallinity may be also due to the presence of residual crystallinity.

Table 3 1 Effect of processed parameters on the crystallinity of laser processed samples

Number	Processing parameters				DSC results		
	Laser power (Watt)	Tape speed (mm/sec)	Consolidation pressure (load/unit width) lb/in	Consolidation pressure (load/unit width) kN/m	Layer Number	Crystallinity	Melting Temperature
1	60	8 33	576	100 8	5	matrix loss	-
2	60	20 8	576	100 8	4	37 89 %	338 45°C
3	60	27 0	902.4	158 0	5	35 09 %	339 06°C
4	60	27 0	576	100 8	5 Top layer	36 17 % 29 78 %	339 72°C 339 45°C
5	63	32 72	576	100 8	3	35 49 %	339 56°C
6	50	6.28	576	100 8	5	matrix loss	-
7	50	12.7	576	100 8	5	30.95 %	339 44°C
8	50	27 76	576	100 8	4	34 52 %	339 92°C
9	40	6 42	576	100 8	5	32 52 %	338 49°C
10	40	13 3	576	100 8	4	32 48 %	339 43°C
11	30	4.49	576	100.8	6	24 37 %	337 80°C

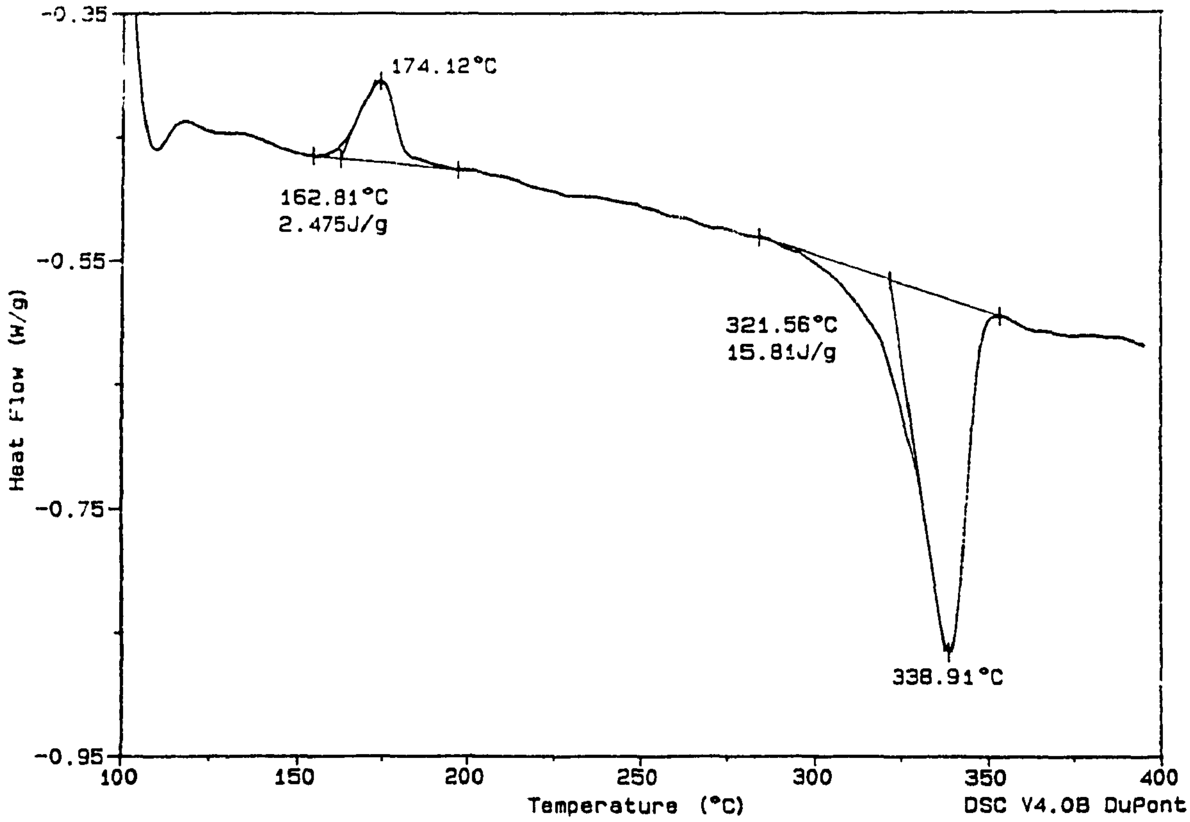

Fig. 3.25 DSC thermogram for unprocessed APC-2 tape sample at 20°C/min. heating rate.

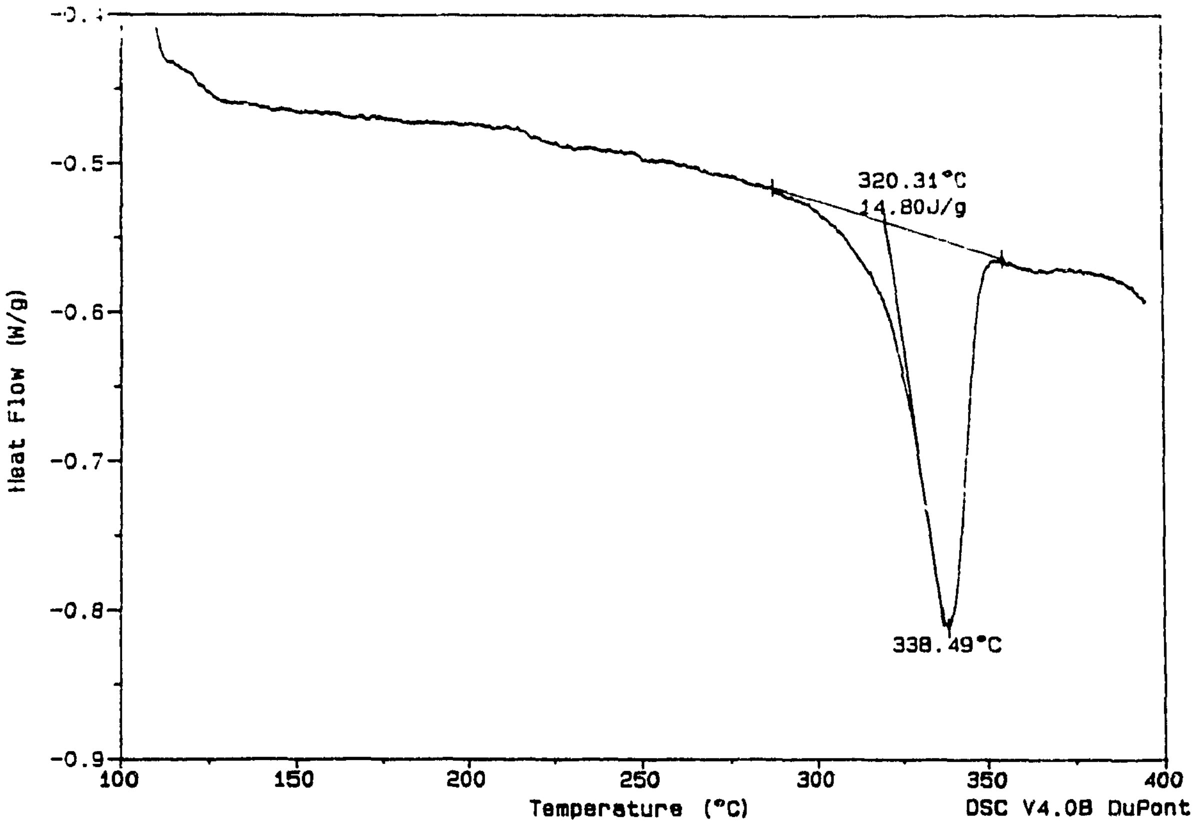

Fig. 3.26 DSC thermogram of a laser processed sample at 40 W laser power, 6.42 mm/sec tape speed and 100.8 kN/m consolidation pressure. The sample was obtained from 4th layer.

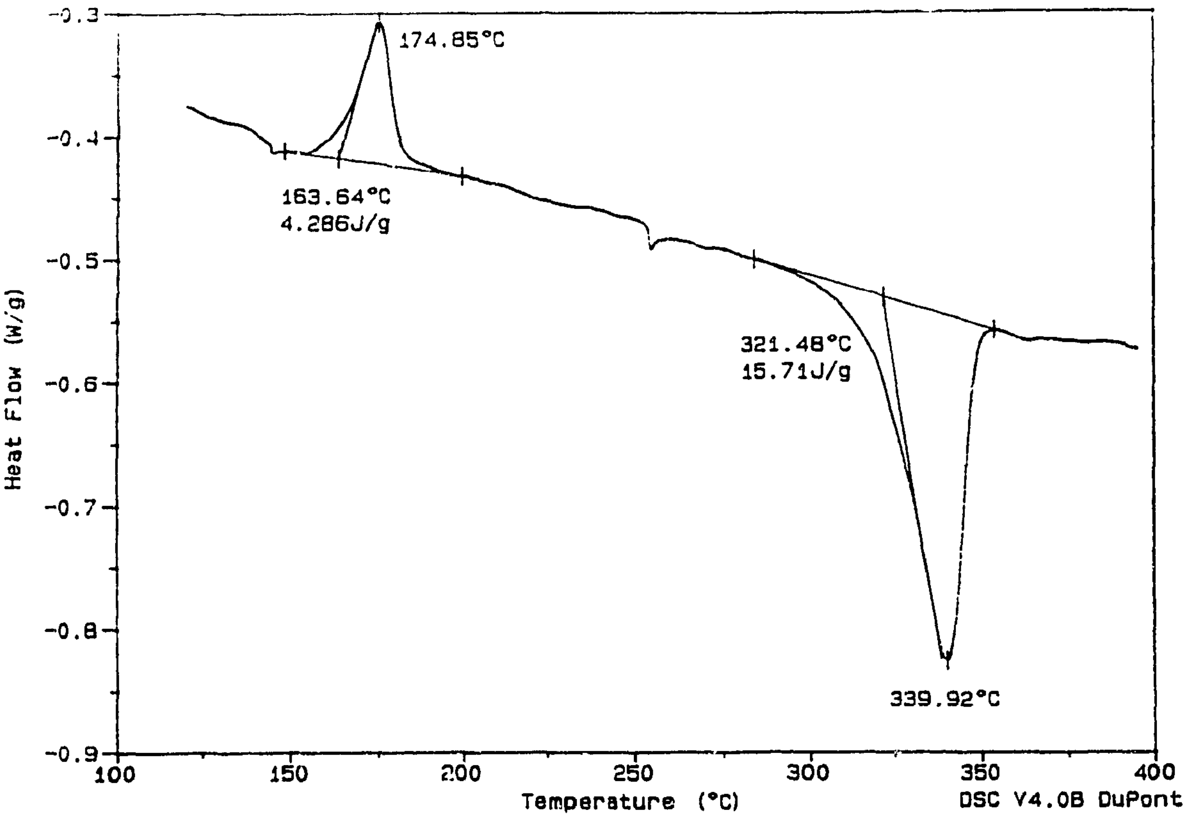

Fig. 3.27 DSC thermogram of a laser processed sample at 50 W laser power, 27 mm/sec tape speed and 100.8 kN/m consolidation pressure. The sample was obtained from 5th layer.

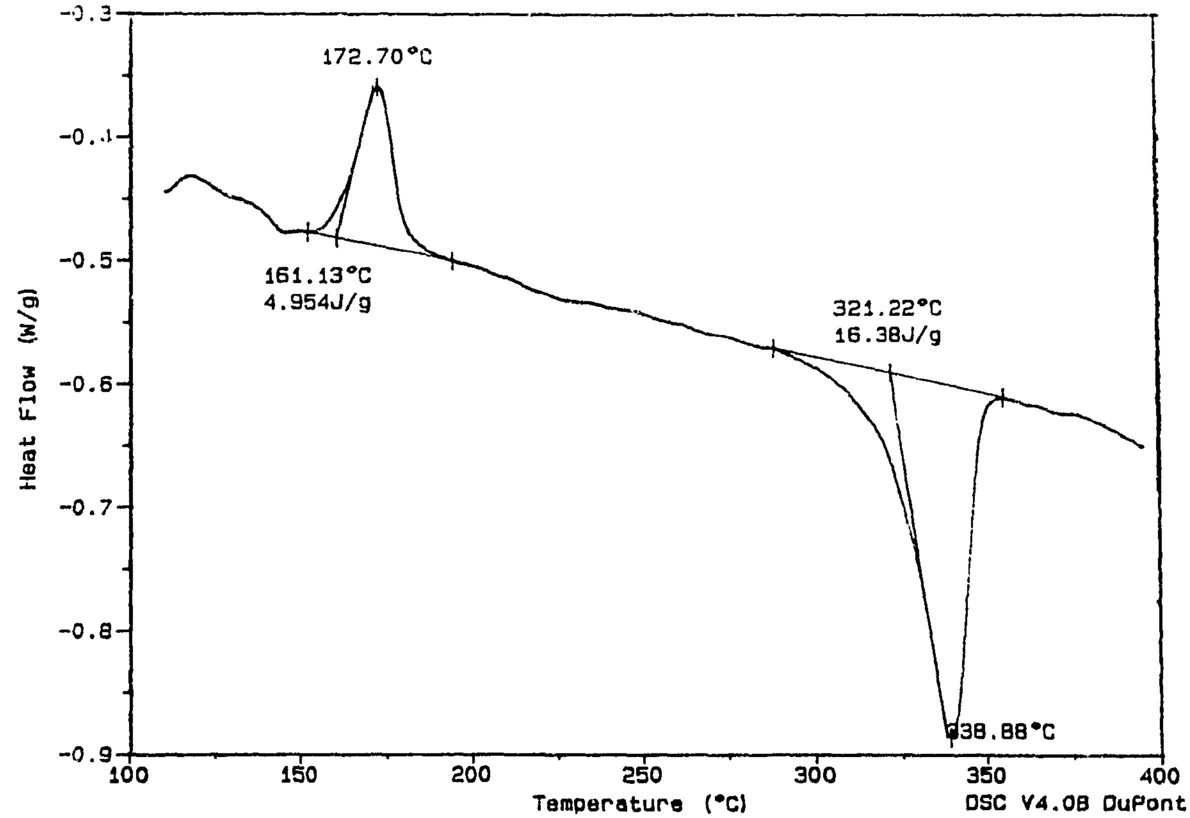

Fig. 3.28 DSC thermogram of a laser processed sample at 60 W laser power, 27 mm/sec tape speed and 100.8 kN/m consolidation pressure. The sample was obtained from 5th layer.

Lee [64] observed that the crystal structure requires considerable time to be completely destroyed

3.10 Optical Microscopic Study

An optical microscopic study was performed along the cross-section and longitudinal direction of the sample for investigating the quality of consolidation. For better understanding, the microstructure study was first performed on unprocessed single APC-2 tape Poor fiber distribution and extreme tow height non-uniformity was observed as shown in Fig.3.29, where two single tapes are shown at a magnification of 200 Agarwal [17] measured the distribution of void content in the unprocessed APC-2 sample using optical micrograph of cross-sections and found that the tape contained regions of high voids (greater than 6%) and regions of very low void conent (less than 0 5%). Black spots in Fig 3.24 show the presence of voids Studies on laser processed samples do not show the presence of interlaminar voids [17,65] Figures 3 23, 3 24, 3.30 and 3.31 show the micrographs of rings processed at various combinations of process parameters.

From the study it was found that at lower consolidation force (around 25.2 kN/m) bonding between plies was not proper because of the voids and resin rich area as shown in Fig 3.23. It is reported that volatile materials generally generate voids during processing when the partial pressure of the volatile exceeds the fluid (resin) restraining pressure [1]. During thermoplastic tape winding process, a pressure below 25.2 kN/m may not be sufficient to create good intimate contact between layers. At low consolidation force, void content is mainly a function of original roughness of the prepreg tape and extent of resin flow during consolidation. Micrograph shown in Fig. 3.23 is taken at a magnification of 100X for a ring processed at 60 W laser power, 27.6 mm/sec. tape speed, and 25 2 kN/m consolidation force. From the microstructure study, absence of interply voids were observed for consolidation forces of 50.4 kN/m, 100.8 kN/m and 151 2 kN/m There were not significant difference in the quality of the inter ply bond in these force ranges. Figure 3.24 shows a micrograph at a magnification of 200X for

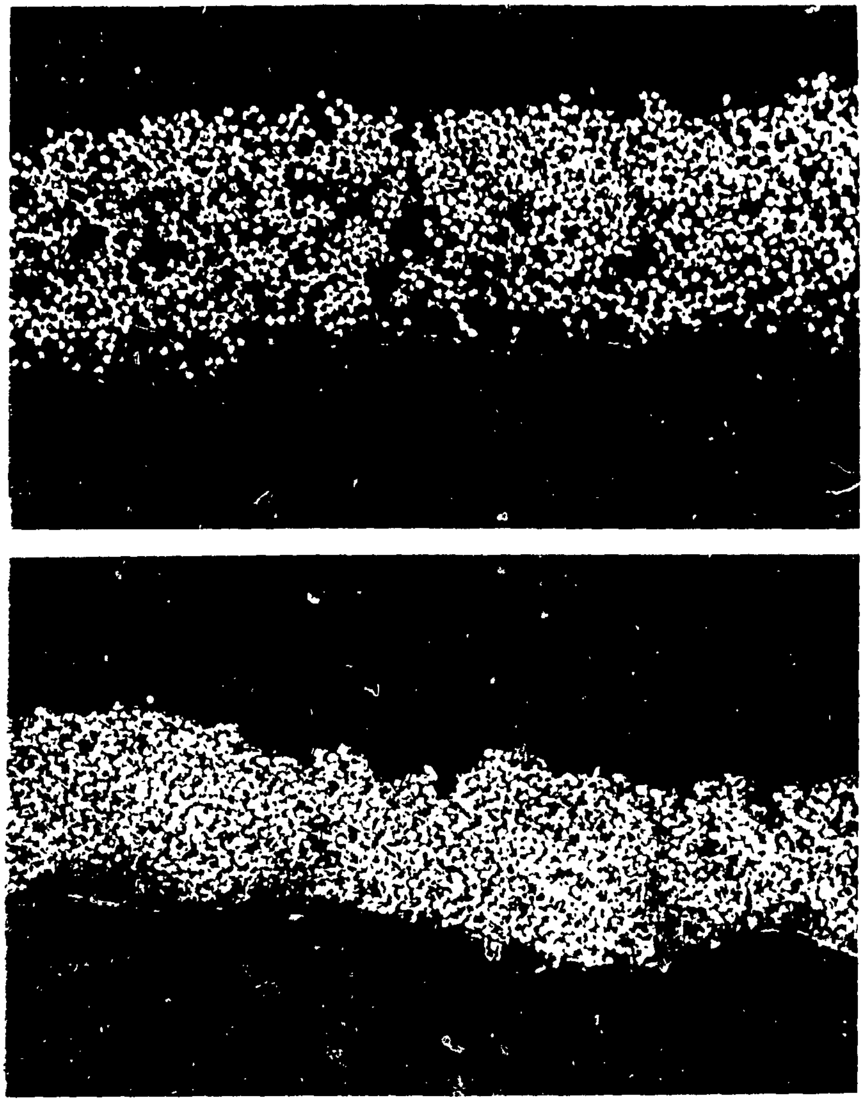

Fig. 3.29 Cross-sectional micrograph of unprocessed APC-2 tape (200X).

Fig. 3.30 Matrix degradation during processing at low speed (100X).

Fig. 3.31 Edge effect during laser processing (100X).

60 W laser power, 100 8 kN/m consolidation force, and at a tape speed of 27 0 mm/sec. It is clear from the Fig 3 24 that the bond quality is good without any visible voids Figure 3 30 shows matrix degradation for a ring at a magnification of 200X and at a tape speed of 8 33 mm/sec for a 60 W laser power and 100 8 kN/m consolidation force From the study it was observed that the matrix degradation is more near the center of the width because of higher temperature at the center of the width compared to the edges for an elliptical beam spot Edge effect for a ring at 50 W laser power, 100 8 kN/m consolidation force and at a tape speed of 20.8 mm/sec is shown in Fig 3 31. For 6.35 mm wide thermoplastic tape, consolidation was improper at edges of the ring at an average of 6.7% of the total width

3.11 Process-Induced Deformation

One of the most significant problems in the processing of thermoplastic composites is the generation of residual stresses due to processing at high temperatures. The formation of large residual stresses and deformations during the manufacture of thermoplastic composites is due to high processing temperature (which may lead to high temperature gradients) as well as large volumetric shrinkage of these polymers Residual stresses can be identified either at micro level or at macro level. Residual stress at micro-level results from difference in the thermal expansion of constituent material. Residual stress at macro-level is associated with fiber orientation at different plies and processing histories such as cooling rate. Process-induced residual stress can be high enough to cause matrix cracking, debonding, delamination, warpage and voids at the interface. Cracking in the matrix can expose the fibers to degradation by chemical attack Mechanical strength of the composite parts is affected by the residual stresses. An on-line consolidation process decreases the level of these stresses and deformations (compared with hot pressing and autoclave processing) because of localized heating

There is no direct method for the measurement of residual stress. Process-induced stress is calculated by measuring the strain or deformation caused by the stress. To measure the process-induced deformations, rings were cut using a very fine (0 3mm thick) diamond cutter at a low speed. After cutting it was found that the rings deformed as shown in Fig 3 32 Amount of opening for different sets of process conditions are shown in Figs. 3.33 and 3 34 for 10 ply rings

Process-induced deformations were determined by measuring the distance between two ends of the ring. Ring deformation took place in the same plane (r-θ plane of the ring) without twisting in the z direction It was found that after deformation the rings did not remain circular and the curvature at different points on the ring were found to be different For one set of experiments, when the laser beam was not focused exactly at the center of the tape, twisting of the ring along z direction was observed In this case ring became like a helix. Therefore positioning of the laser beam at the contact point must be accurately controlled to avoid undesirable deformations

Process-induced deformations for different combinations of laser power, tape speed and consolidation force are shown in Figs. 3.33 and 3 34 Figure 3.33 shows process-induced deformations for a constant consolidation force per unit width of 100.8 kN/m with different sets of laser power and tape speeds It is found that the increase in laser power decreases the process-induced deformations. Effect of consolidation pressure on the process-induced deformations is shown in Fig 3.34. For 60 W laser power and at 27mm/sec tape speed, consolidation force per unit width in the range of 25.2 kN/m to 158 kN/m does not affect the process-induced deformations.

3.12 Characterization of interply bonding

In the fabrication of a composite component from fiber reinforced thermoplastic prepreg, interfacial bonding between plies influences mechanical properties of the component because interfacial bond transfer stress from one ply to the other. Thus, fracture behaviour of the interfacial ply bond influences the fracture strength and toughness of the composite component.

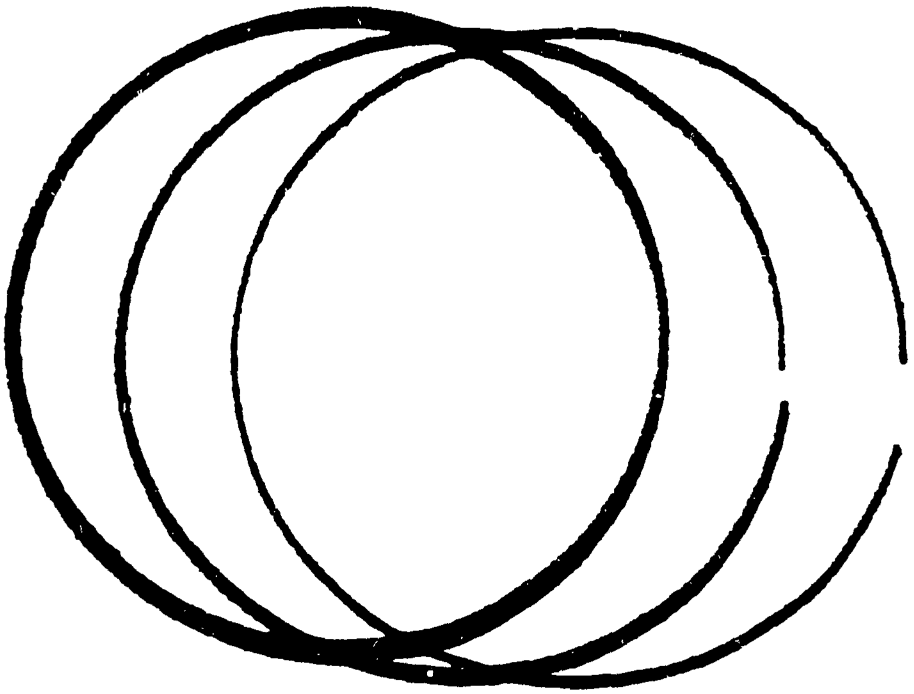

Fig. 3.32 Process induced deformations due to internal stresses for 10 ply rings.

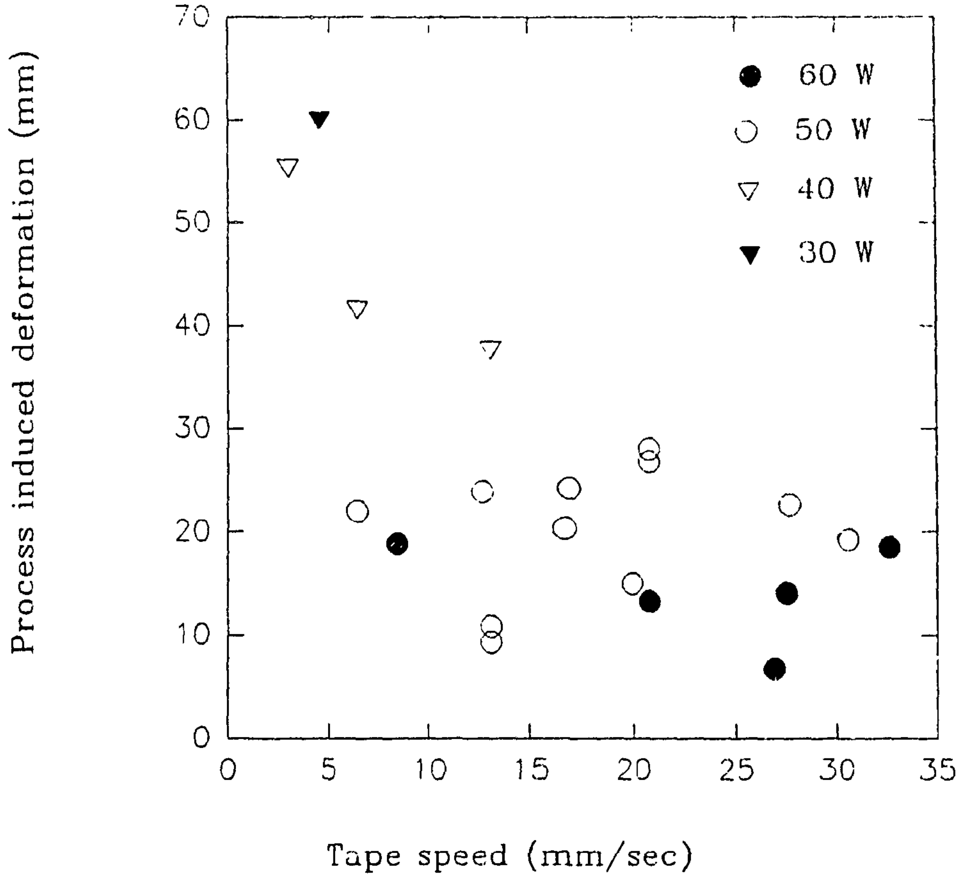

Fig. 3.33 Effect of laser power and tape speed on process induced deformations for consolidation pressure of 100.8 kN/m.

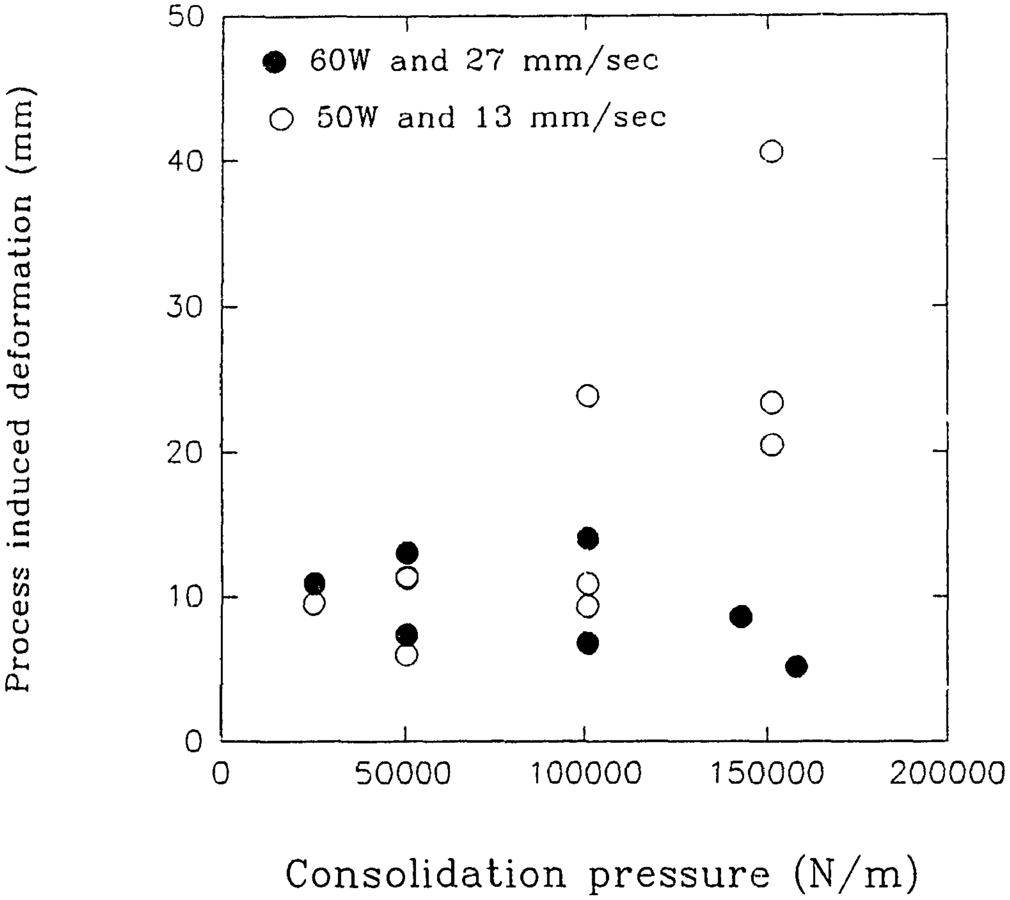

Fig. 3.34 Effect of consolidation pressure on the process induced deformation.

Much effort was made to characterize the interfacial fiber/matrix bond [66,67,68] This was determined by the extent of physical and chemical bonding between the fiber and matrix. Interfacial ply bonding in thermoplastic composites is generally decided by the molecular interdiffusion, adhesion between rough surfaces and joining by flow of molten material [69] In the literature, charaterization of interply bonding for rings manufactured by an on-line consolidation method can not be found There is no technique available to determine the extent of bond strength between two plies for a ring specimen. Aim of the work in this thesis is to investigate a testing method which is more sensitive to the interfacial ply bond. Short beam shear tests, double cantilever curved beam tests and fracture surface study using scanning electron microscope were performed on carbon/PEEK (APC-2) thermoplastic composites to characterize the interfacial ply bonding of ring specimens Based on the characterization of interply bonding, optimum process parameters for laser-assisted processing of APC-2 composites were determined A flow chart showing different stages in the development of a composite ring by a thermoplastic tape winding technique is shown in Fig. 3 35.

3.12.1 Experimental Procedure

For the present investigation, ten-ply rings were manufactured at various processing conditions. Short beam shear (SBS) tests, double cantilever curved beam (DCCB) test, fracture surface study by scanning electron microscope (SEM) were performed to determine which method most easily detects differences in the interply bond Specimens were prepared by cutting the ring into required dimension using a very fine (0.3mm thick) diamond cutter at a slow speed For DCCB test, initial crack length of 38.1 mm was introduced by putting aluminum foil between the 5th and 6th plies Aluminum foil was introduced without interrupting the process

Short beam shear strength is measured as described in ASTM D2344 [56]. This test method recognizes that the measured strength is not the true strength. Short beam

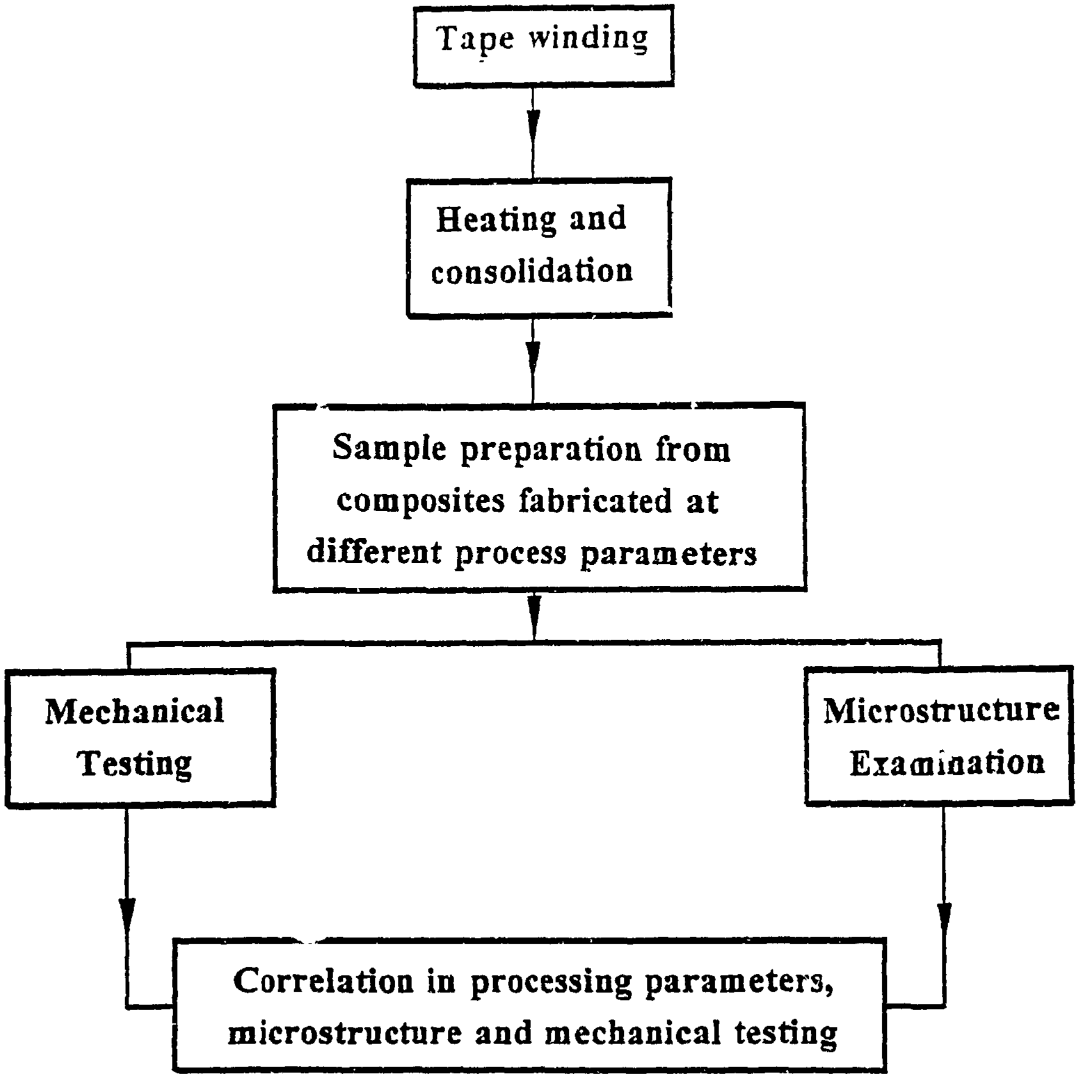

Fig. 3.35 Flow chart showing various stages involved during the development of composite components by thermoplastic tape winding process.

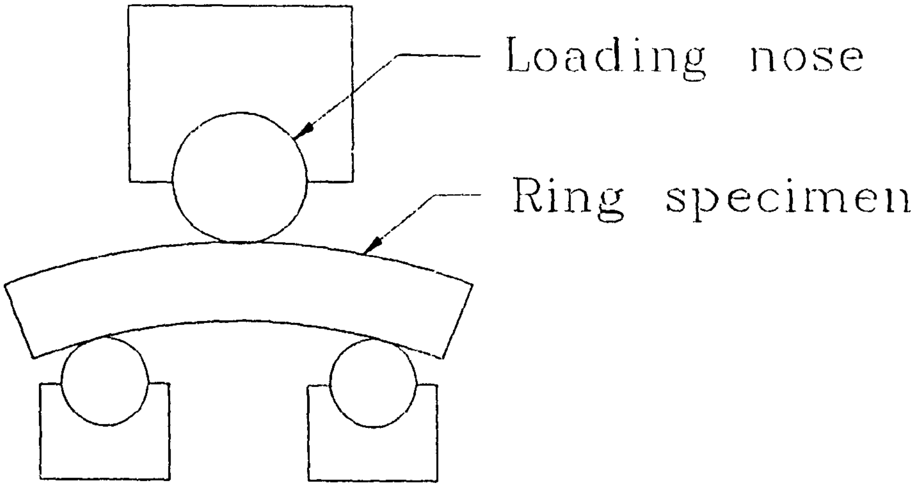

Fig. 3.36 Loading diagram for short beam shear test.

shear tests are mainly used for estimating the quality of interply/interfacial bonding and not for design purposes The apparent shear strength obtained in this test can not be used as a design criteria, but can be utilized for comparative testing of composite materials, if all failures are in horizontal shear [56]

For the short beam shear test , specimen having approximately 1 5 mm thickness, 16 mm length, 6 3 mm width and 10.5 mm span were loaded in 3 point bend mode at a cross head speed of 2 mm/min. The loading diagram for SBS test is shown in Fig. 3 36. For all the cases of SBS tests, the failure mode is found to be dominant by horizontal shear and thus can be used for comparative study of interply bond quality. Shear strength, S, was calculated using following equation (ASTM D2344)

$$S = \frac{3P}{4wt} \tag{3.3}$$

where P is the load at failure, W is the specimen width and t is the specimen thickness.

3.12.2 Results

3.12.2.1 Short Beam Shear Tests

In a short beam shear test, failure may occur at the ply interface or at the fiber/matrix interface. Values of apparent interlaminar shear strength yielded by short beam shear tests are shown in table 3.2 for laser processed APC-2 rings. It is clear that a too low or too high a speed for a particular heat intensity results in poor interply bonding. Based on this fact the tape speed is divided into three categories: lower speed range, medium speed range, and higher speed range Lower speed would result in polymer degradation, medium speed would result in good consolidation and higher speed would result insufficient bonding between plies because of insufficient melting and diffusion. Thus for a particular material there are optimum processing parameters for which mechanical properties of the component is superior

During the SBS test shallow depression at the center of the specimen was observed for samples where matrix material remains ductile after processing To study various failure mechanisms during SBS tests and to examine the damage on the specimen caused by the center point loading, microscopic examinations of the samples were performed For this, specimens were examined under the microscope after the SBS test and photographs were taken at a magnification of 50 as shown in Figs 3 37 - 3 45 The objective of performing the microscopic study of SBS test coupon is twofold to investigate the failure mode such as shear, tensile, compressive, etc during the SBS test, and to determine the effect of contact stress on damage mechanism at the center point loading.

Figure 3 37 shows a shallow depression and interply failure caused during a SBS test on center portion of a sample. The sample was processed at 50W laser power, 12 69 mm/sec tape speed and at 100 8 kN/m consolidation force per unit width and had apparent ILSS of 35.09 MPa. Because of the contact stress and maximum load at the center point, matrix at the center region deforms plastically. Squeezing of the matrix material below the loading point stops the propagation of delaminations near the center region (Fig 3.37). Matrix crushing and fiber breakage were not observed near the loading point. Multiple interlaminar failures were noticed Load - displacement curve for the sample is shown in Fig 3.38. For another sample for similar processing parameters at 50W laser power, interply failure is found to be propagating towards the end of the sample along neutral axis (Fig.3.39).

For all the samples, no interlaminar failure was found to be propagating from the cut edge of the sample. Cutting of the sample with thin diamond cutter gave no visible delamination at the cut edge (Fig.3 39). Agarwal [17] performed SBS test on laser processed samples and found that cutting of the sample with a band saw caused delamination at the cut edge.

Table 3 2 Effect of processing parameters on the quality of the interply bond for laser processed APC-2 samples.

Number	Processing parameters				Quality of the bond		
	Laser power (Watt)	Tape speed (mm/sec)	Consolidation pressure (load/unit width)		Interlaminar shear strength (MPa)	DCCB test	
			lb/in.	kN/m		Crack length (mm)	Crack propagation load/unit width (N/mm)
1	60	8.33	576	100.8	37.06	26 46	2.2
2	60	20.8	576	100.8	47.53	29.85	0.89
3	60	26.99	902.4	158 0	34.50	28.53	0.88
4	63	32.72	576	100 8	23.41	30.87	0.75
5	50	6.28	576	100.8	29.05	28.49	1.72
6	50	12.69	576	100 8	35.09	28.50	0.69
7	50	27 76	576	100.8	29.79	29.20	0.57
8	40	6 42	576	100.8	26.66	30.77	1.24
9	30	4.49	576	100 8	20.89	28 93	0 49

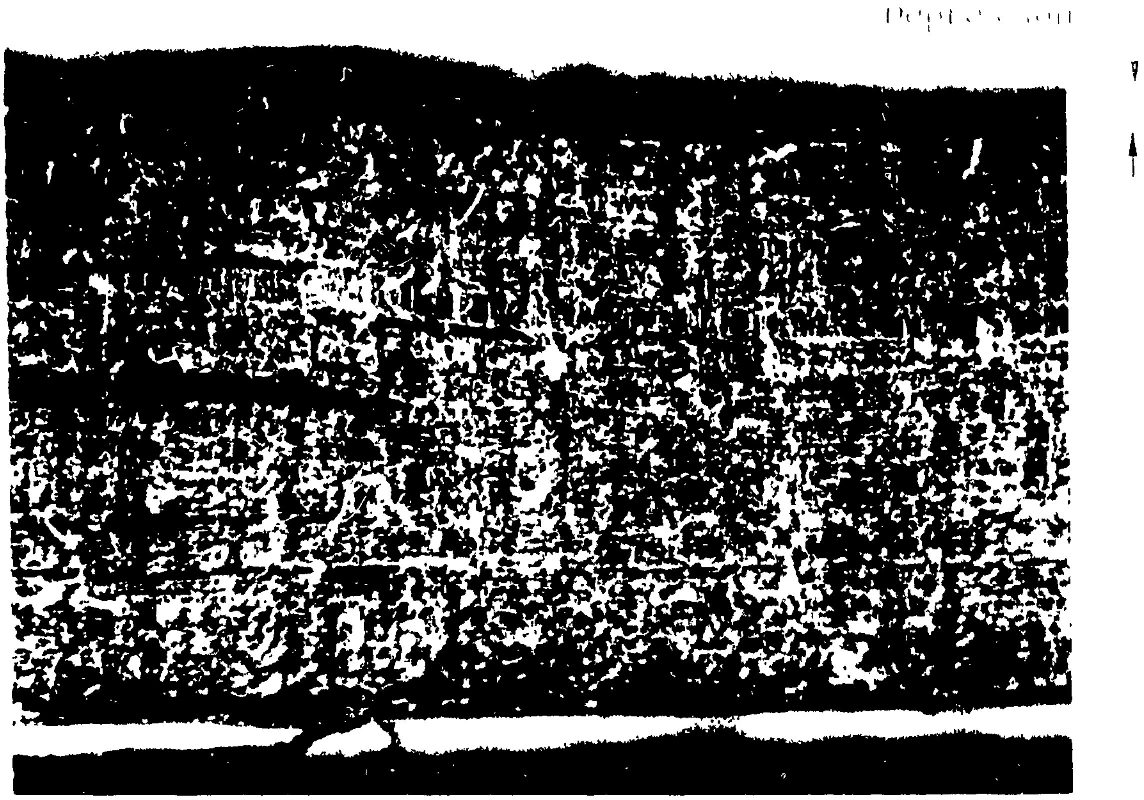

Fig. 3.37 Micrograph of a sample processed at 50W laser power, 12.69 mm/sec tape speed, and 100.8kN/m consolidation pressure. Sample was failed during SBS test.

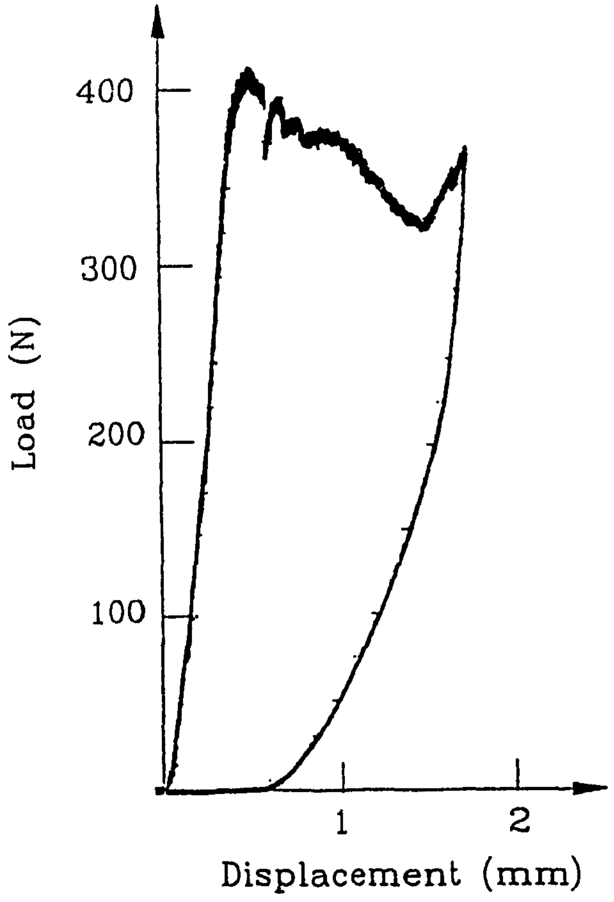

Fig. 3.38 Load displacement curve during SBS test for a sample processed at 50W laser power, 12.69mm/sec tape speed, and 100.8kN/m consolidation pressure.

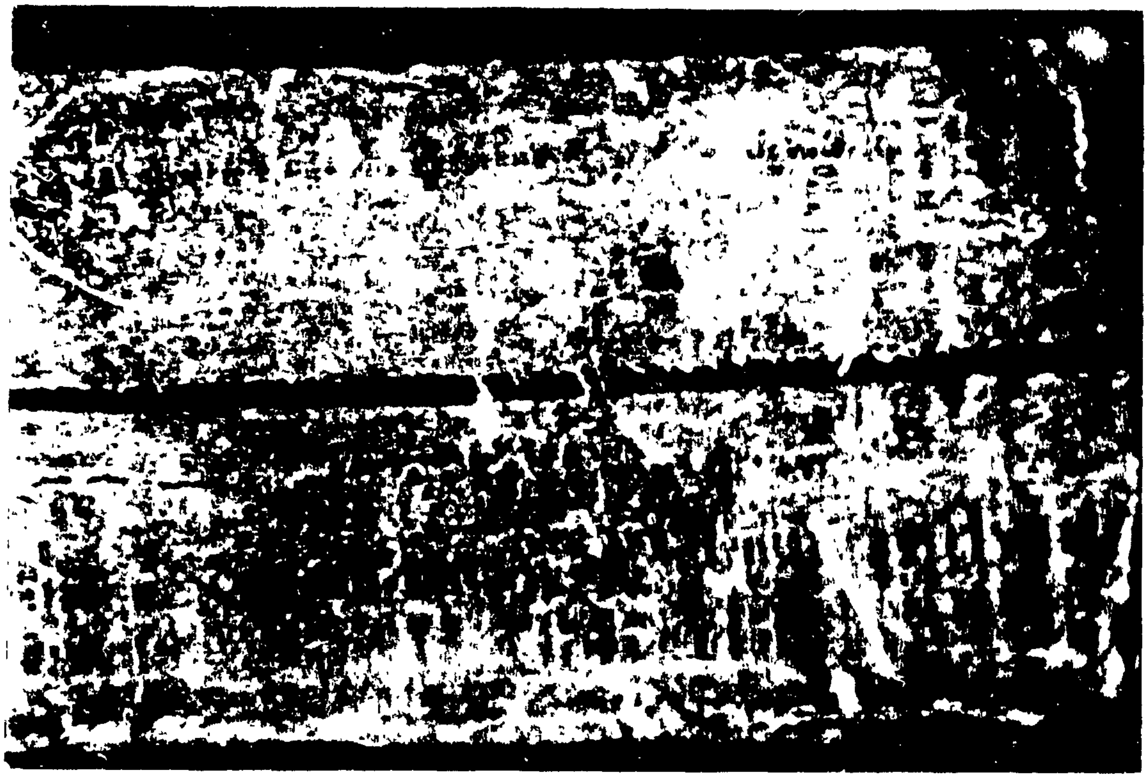

Fig. 3.39 Failure caused during SBS test for a sample processed at 50W laser power, 12.69mm/sec tape speed, and 100.8kN/m consolidation pressure.

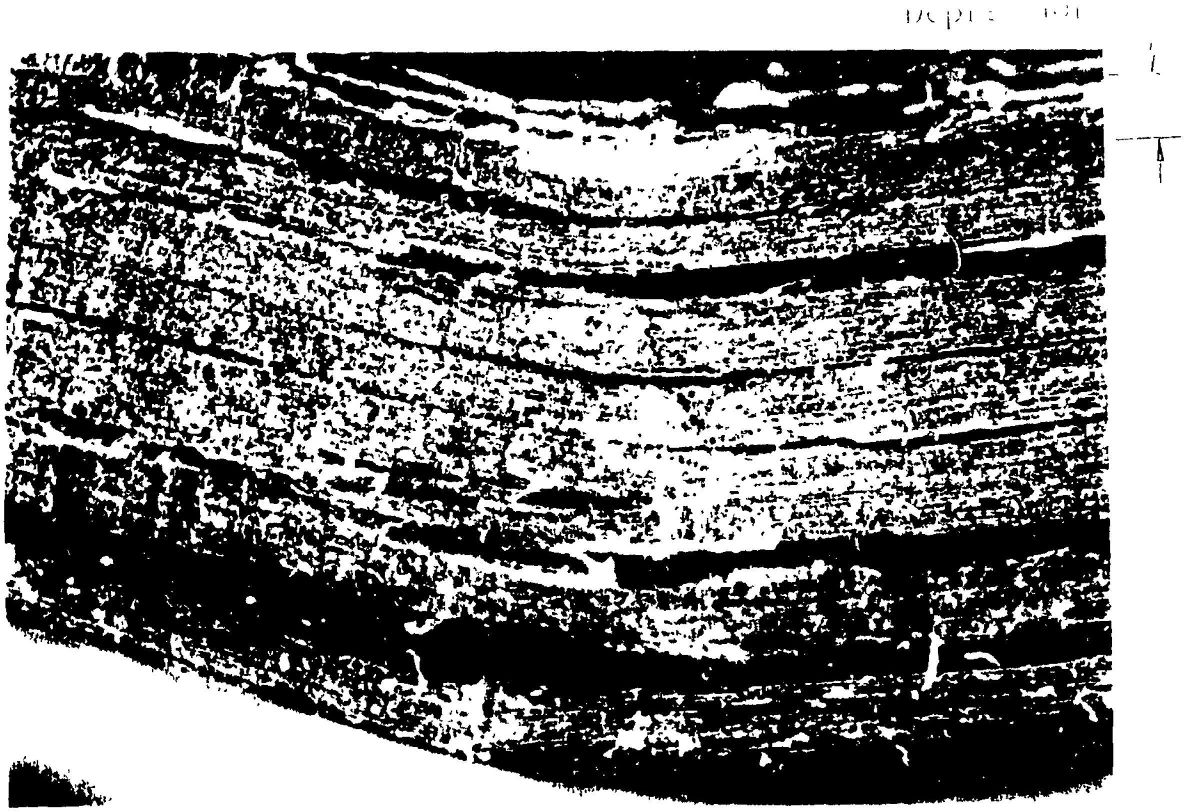

Fig. 3.40 Damage caused by SBS test for a sample processed at 60W laser power, 32.72mm/sec tape speed, and 100.8kN/m consolidation pressure.

Fig. 3.41 Micrograph showing the failure mode during SBS test. The sample was processed at 60W laser power, 26.99mm/sec tape speed, and 100.8kN/m consolidation pressure.

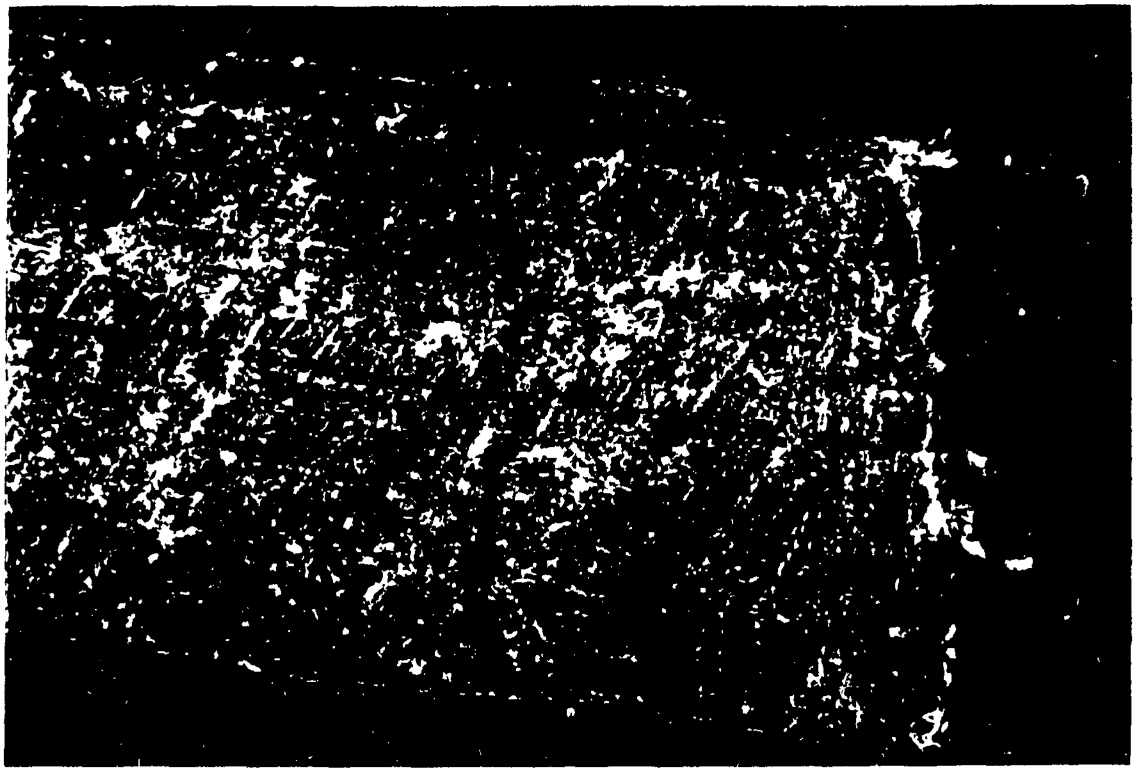

Fig. 3.42 Failure near the end of the specimen. The sample was processed at 60W laser power, 26.99mm/sec tape speed, and 100.8kN/m consolidation pressure.

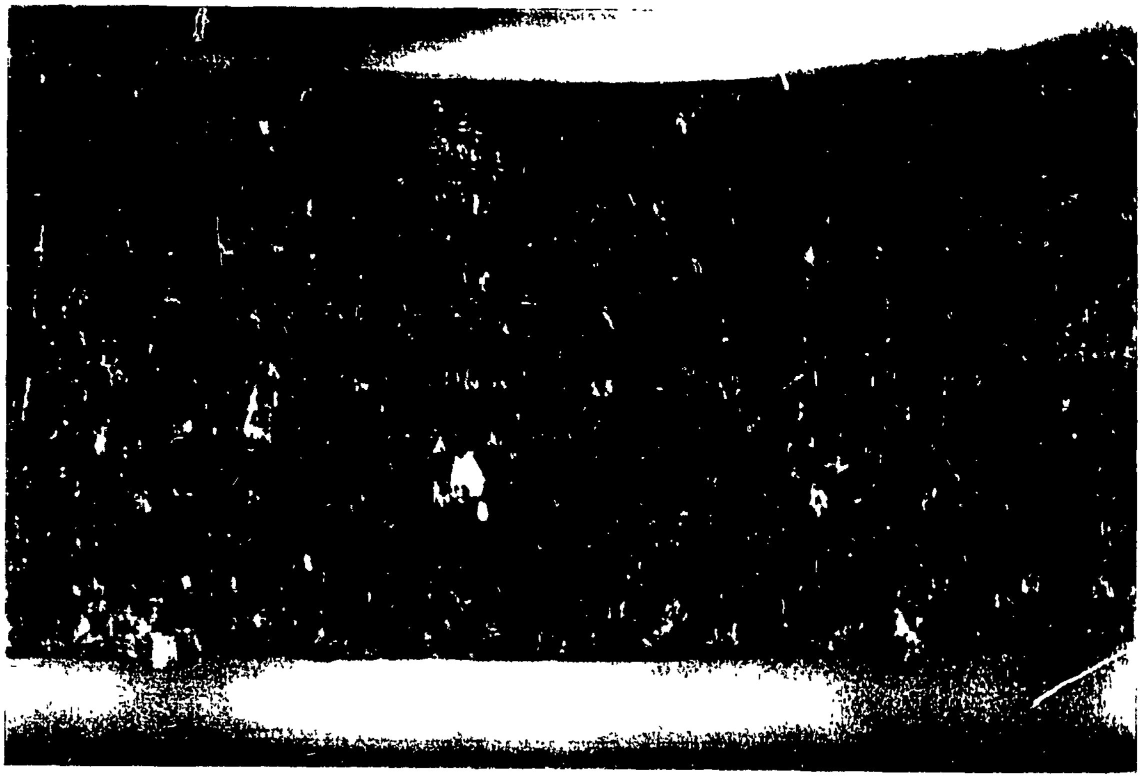

Fig. 3.43 Damage near the center point loading of a sample processed at 60W laser power, 20.72mm/sec tape speed, and 100.8kN/m consolidation pressure.

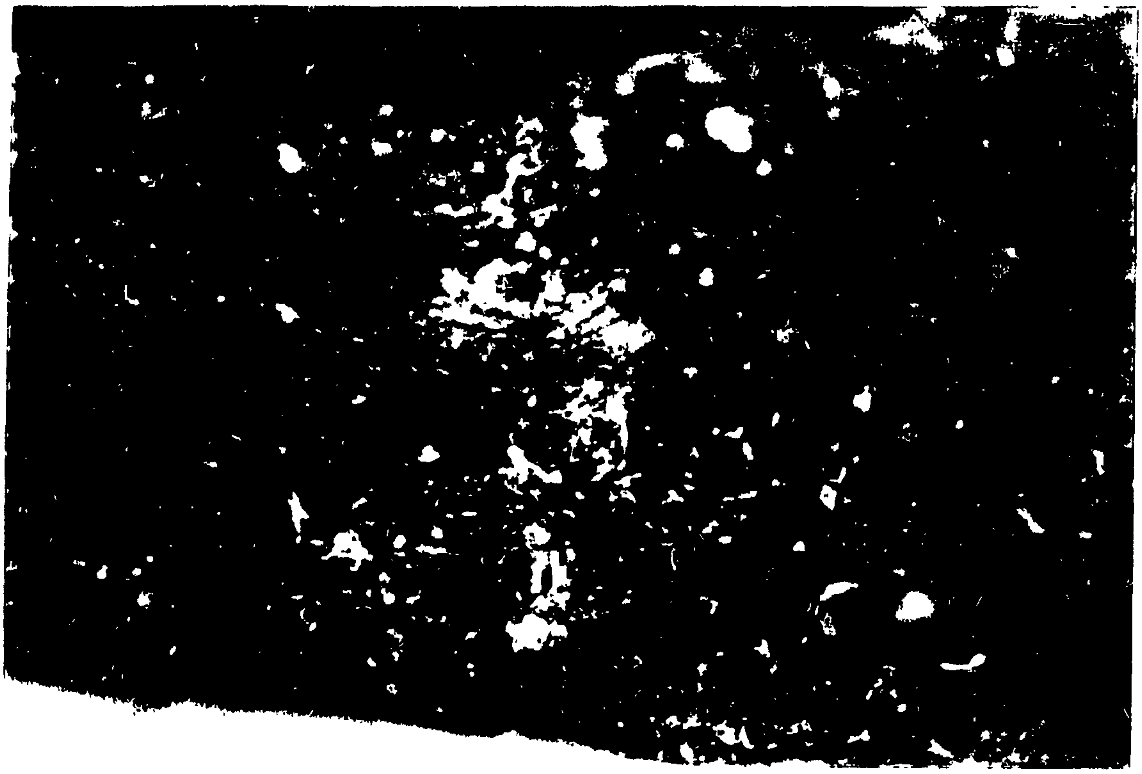

Fig. 3.44 Photograph of a damaged specimen. The specimen was processed at 60W laser power, 8.33mm/sec tape speed, and 100.8kN/m consolidation pressure.

Fig. 3.45 A failed specimen, which was processed at 40W laser power, 6.42 mm/sec tape speed, and 100.8kN/m consolidation pressure.

For most of the samples processed at 60 W laser power, plastic deformation at center point loading was not observed Failed test specimens frequently exhibited compressive damage on the top surface Interply failures at the center region of a sample processed at 63 W laser power and at 32 72 mm/sec tape speed are shown in Fig 3 40 Because of the poor bond quality, several interply failures are noticed The apparent ILSS for this case is found to be 23 41 MPa With the reduction in tape speed to 26 99 mm/sec for 60 W laser power, apparent ILSS increases to 34 5 MPa A micrograph showing the damage in this sample (26 99 mm/sec tape speed and 60W laser power) is given in Fig 3 41. Shallow depression for this case was not observed. Instead matrix crushing below the center point loading was observed Propagation of delamination below the center point loading can be noticed Photograph of the end of the same sample is shown in Fig. 3 42. Interply failure along neutral axis and below the neutral axis can be observed Out of five samples processed at 60W and 26 99 mm/sec tape speed, two exhibited shallow depression on the surface of the sample

For a sample processed at 60 W laser power and 20 8 mm/sec tape speed, shallow depression below the center point loading was observed (Fig 3.43). Apparent interlaminar shear strength was found to be maximum (47 5 MPa) for this case as compared to other cases of laser processed samples As shown in the figure, interply failure below the center point loading is not visible A few interlaminar and intralaminar delaminations were observed between the end and center of the specimen Figure 3 44 shows a micrograph of a damaged sample processed at 60W laser power, and 8.33 mm/sec tape speed. Several interply failures on right hand side of the sample are noticed The apparent ILSS is 37 06 MPa for this case Because of the degradation of the thermoplastics, ILSS value deteriorated for lower speed.

Figure 3.45 shows a center portion of a specimen failed by SBS test. The specimen was processed at 40 W laser power and at 6 42 mm/sec tape speed Apparent interlaminar shear strength of this sample was found to be 26.66 MPa. Interlaminar failures were observed on both sides (right hand and left hand) of the sample Delaminations below the center point loading are observed

3.12.2.2 Double Cantilever Curved Beam (DCCB) Tests

A double cantilever beam (DCB) test is popular for determining mode I fracture toughness of a flat composite sample Similar to the DCB test, one quarter length (114 mm arc length) of the sample as shown in Fig 3 46 was loaded on a MTS machine at a cross head speed of 1 mm/min The samples were ground on both edges and liquid paper (white correction fluid) was applied to the edges to aid in seeing the crack growth, which was monitored using a telescope connected to a video camera The DCCB test of a curved specimen creates a complex state of stress at the crack tip The crack initially propagates in mode I, since the propagation direction is perpendicular to the applied force The mode II component increases as the crack propagates around the curved specimen and changes the angle of propagation relative to the applied force For curved beam sample, delaminations above the line of desired crack propagation was observed for the cases where interply bond is weak Because of the initiation of multiple cracks during a DCCB test, fracture toughness of the sample was not measured Interlaminar stresses through the thickness is the cause of delamination for curved samples Therefore for the present study, maximum load required for the crack propagation is considered as a parameter for qualitative analysis of the interply bond. It is noted here that the fracture toughness is proportional to the crack propagation load in the absence of any additional crack or delamination A typical load-displacement curve during the test is shown in Fig 3 47 Stable and unstable crack propagation regions were observed.

Results on the DCCB tests are shown in Figs 3 48, 3 49 and 3 50 for laser-assisted processing of APC-2 composites and micrographs of the samples are shown in Figs. 3 51 - 3.53 Figure 3.48 shows the effect of laser power on the crack propagation load for 100.8 kN/m consolidation force. It is obvious from the figure that the quality of the bond enhances with the increase in laser power For a fixed laser power and

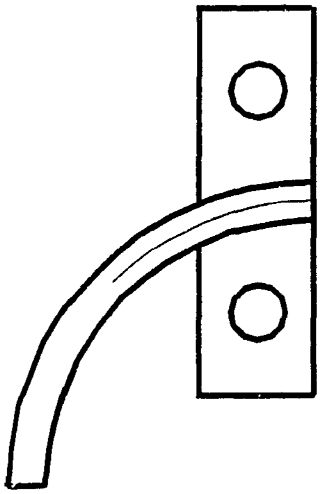

Fig. 3.46 Schematic diagram of a DCCB sample.

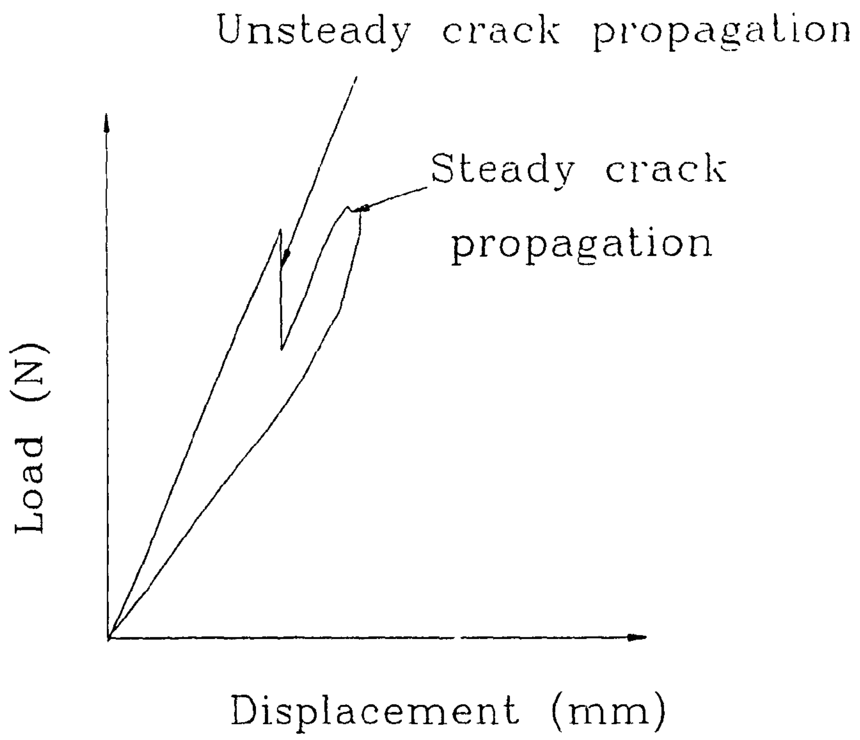

Fig. 3.47 A typical load - displacement curve during DCCB test.

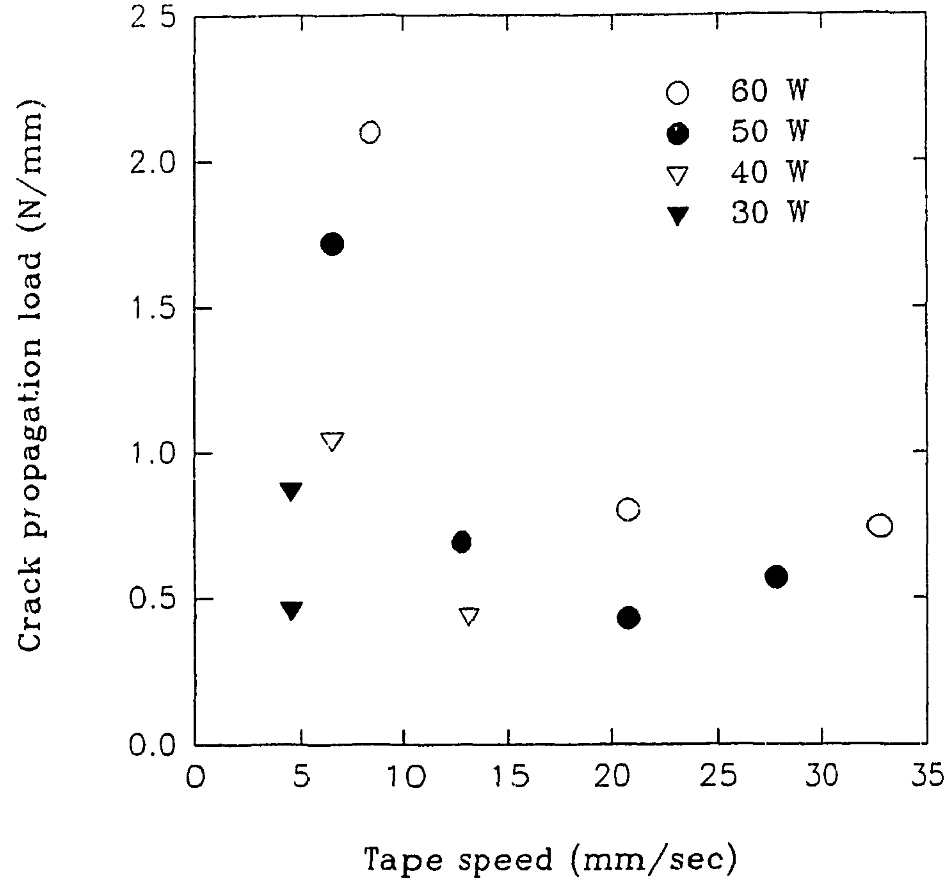

Fig. 3.48 Effect of laser power on crack propagation load for 100.8 kN/m consolidation pressure.

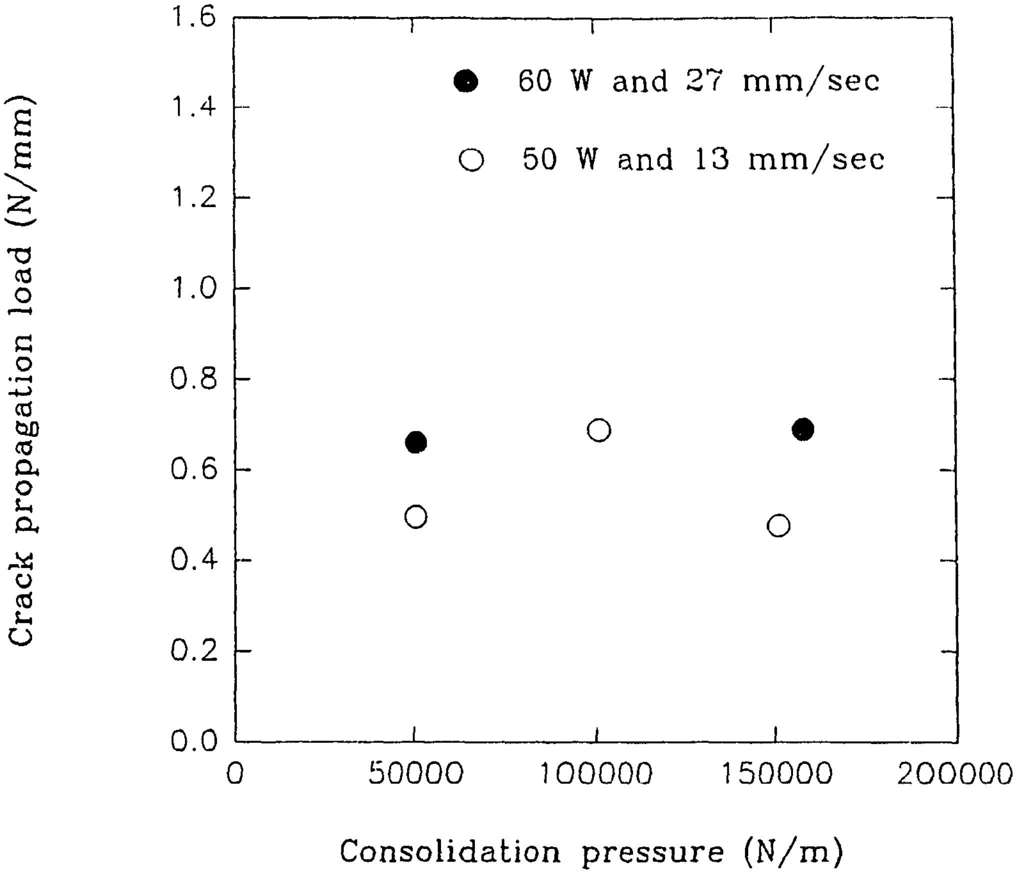

Fig. 3.49 Effect of consolidation pressure on crack propagation load.

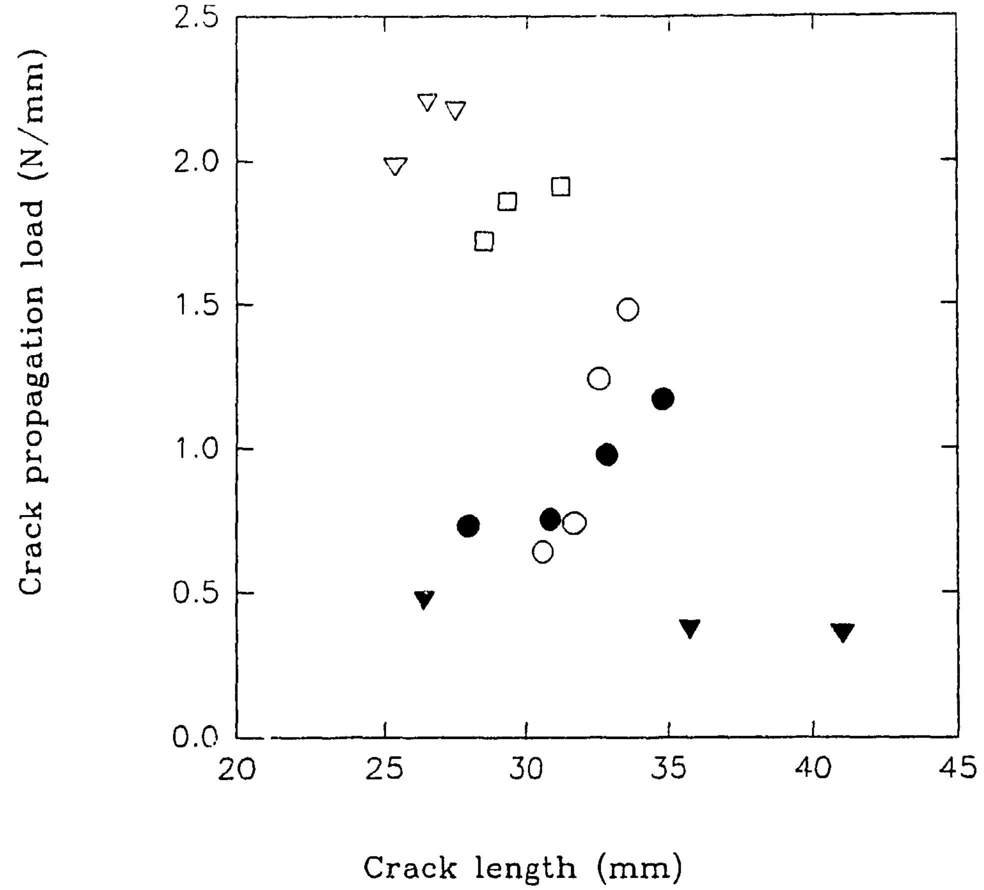

Fig. 3.50 Crack propagation load at different crack length and processing conditions. O (60W, 27 mm/sec, 158 kN/m), ● (60W, 32.7 mm/sec, 100.8kN/m), ▽ (60W, 8.3 mm/sec, 100.8kN/m), ▼ (50W, 20.8 mm/sec, 100.8kN/m) and □ (50W, 6.46 mm/sec, 50.4kN/m) represents samples at different processing conditions.

Fig. 3.51 Delamination growth during DCCB test for a sample processed at 40W laser power, 6.42mm/sec tape speed, and 100.8kN/m consolidation pressure.

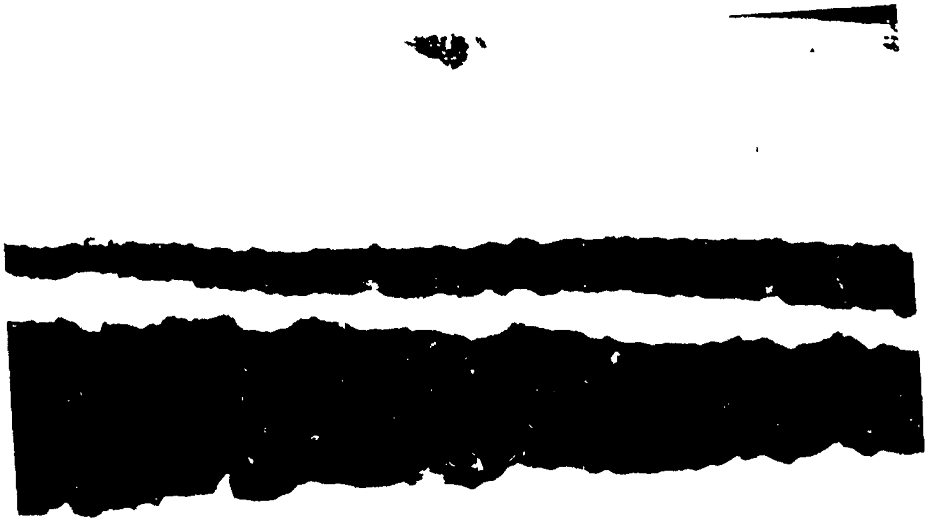

Fig. 3.52 Development of a delamination above initial crack. The sample was processed at 50W laser power, 12.69mm/sec tape speed, and 100.8kN/m consolidation pressure.

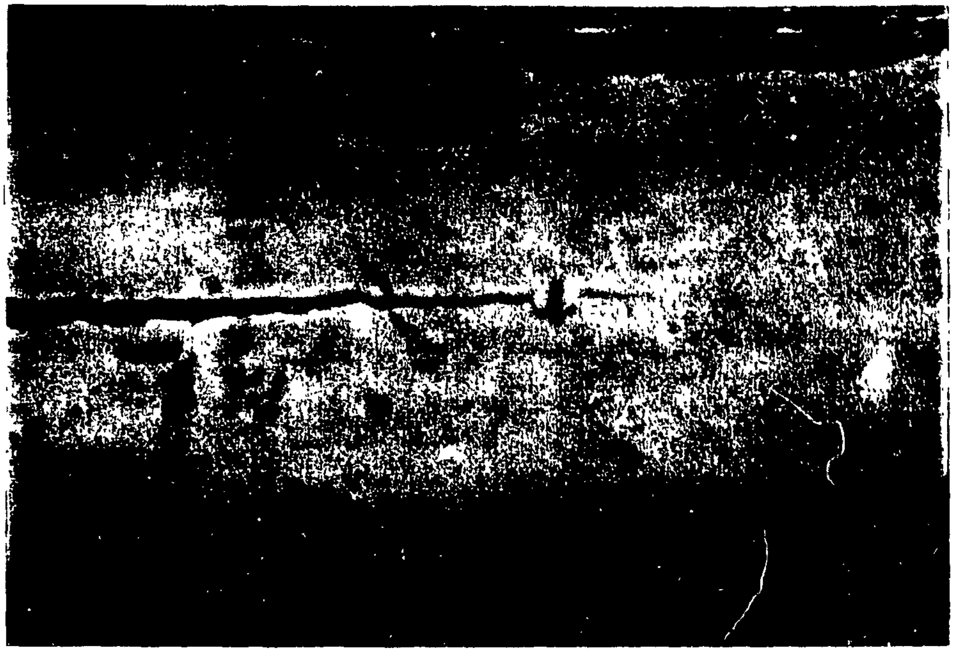

Fig. 3.53 Crack growth during DCCB test for a specimen processed at 60W laser power, 27.0 mm/sec tape speed, and 100.8kN/m consolidation pressure.

consolidation force, it is found that the crack propagation load is high at lower tape speeds. The increased fiber bridging contribution during low tape speed is believed to be the cause of the rise in crack propagation load. Presence of fiber bridging for samples processed at lower speed range is found by SEM study and is discussed in next section.

Effect of consolidation force on the crack propagation load is shown in Fig.3.49. From the figure it can be observed that the bond strength is independent of consolidation force in the range of 50.4 kN/m to 158 kN/m. The reason can be that the resin rich area between the plies does not get affected in above pressure range as found by the microscopic study. From the DCCB test it was found that the crack propagation load increases in most cases with the increase in crack length for 60 W laser power as shown in Fig.3.50. For most of the cases for 50 W laser power, crack propagation load decreases with the increase in crack length.

After the test, samples were examined using optical microscope and photographs were taken at a magnification of 50. Figure 3.51 shows delaminations above the initial crack for 40 W laser power, 100.8 kN/m consolidation force per unit width, and 6.42 mm/sec tape speed. Delamination growth for a sample processed at 50 W laser power with 12.69 mm/sec tape speed and 100.8 kN/m consolidation force per unit width is shown in Fig. 3.52. These cracks above the initial crack were observed because of complex state of stress during the test. Because of presence of these multiple cracks for curved samples, fracture toughness of the specimen was not measured. For some cases where interply bond is stronger, delamination above the initial crack was not observed. A photograph demonstrating the crack growth during DCCB test for a 60 W laser power, 26.99 mm/sec tape speed is shown in Fig.3.53. No delamination above the initial crack was noticed.

3.12.2.3 Fractography

The type of fracture surface is a good indicator of the type of bond at the interface A strong, an intermediate and a weak bond each results in a distinctly different fracture surface From the appearance of interlaminar fracture surface, it is possible to gain a qualitative indication of the degree of bonding between ply interface and fiber/matrix interface To study the fracture surface details, smaller specimens were cut from the crack propagation zone of DCCB samples processed at different processing conditions and were viewed in the SEM as shown in Figs 3 54 - 3.57 Prior to this operation, specimen was coated with a thin [10 nm] gold layer

The major contribution to energy absorption during interlaminar fracture can be attributed to the deformation and fracture of the polymer matrix, whereas minor effect can be due to fiber fracture events For studying the fiber fracture events, photographs were taken at a magnification of 70 and for the purpose of studying matrix failure between plies and fiber/matrix interface, photographs were taken at a magnification of 500 In a sample processed by the laser, it was found that the fracture surface was different across the width of the sample due to non-uniformity in the laser power distribution as well as due to the heat transfer limitations At a 60W laser power and at a lower speed range (sample 1 of Table 3.2), bare fibers and matrix ribbons were observed in the central region of the fracture surface as shown in Fig 3 54 It is because that at lower speed range, matrix vaporization takes place [65]. From the fracture surface, fiber bundles can be easily separated from middle region which shows lack of matrix material Crack propagation load is found to be maximum for this case because of fiber bridging phenomena. Fiber bridging causes the toughness measurements to be higher than the actual toughness of the resin Fiber fracture events caused by fiber bridging can be observed in Fig.3.55 for same sample at a magnification of 70 Fiber fractures are more towards the central region. As the speed increases to the medium speed range, number of fiber fracture events decreases At 60W and 26 99mm/sec tape speed, resin fracture was observed as shown in Figs 3 56 and 3 57 Small resin blocks are left on fibre surfaces without evidence of large deformations, revealing a relatively brittle fracture mode Absence of bare fibers shows good interface bonding between the fiber and matrix. Fiber fractures are not visible. Fracture surface observed at this combination of processing

Fig. 3.54 SEM micrograph of a fracture surface of a sample processed at 60W laser power, 8.33mm/sec tape speed, and 100.8kN/m consolidation pressure (500X).

Fig. 3.55 Fracture surface of a sample processed at 60W laser power, 8.33 mm/sec tape speed, and 100.8kN/m consolidation pressure (70X).

Fig. 3.56 Micrograph of a fracture surface for a sample processed at 60W laser power, 27.0 mm/sec tape speed, and 100.8kN/m consolidation pressure (500X).

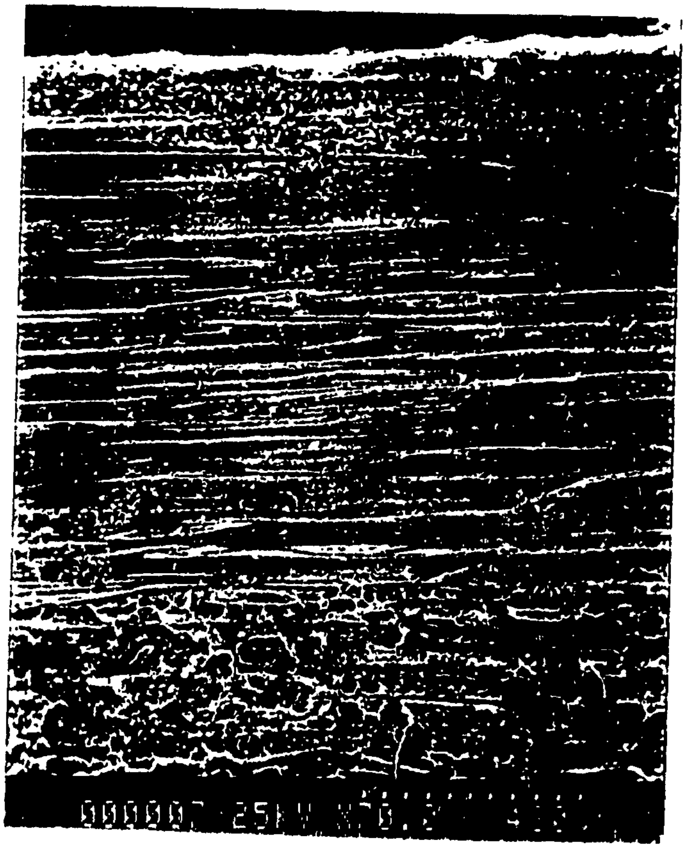

Fig. 3.57 SEM image of a sample processed at 60W laser power, 27.0 mm/sec tape speed, and 100.8kN/m consolidation pressure (70X).

I and II fracture surface of APC-2 samples processed in an autoclave or hot press as reported in the literature [1,70,71] In general, mode I test of GR/PEEK specimens results formation of hackles and river patterns [1] The fracture surface of a mode II shear specimen is a much more ductile delamination with its ductile hackles than that of a mode I tension specimen [1] It can be noted here that the temperature history during tape winding process is more complex as compared to the hot press or autoclave operation [72,73] As shown in Fig. 3 56 small matrix fractures are found to be spreaded at the interface. The reason of this kind of fracture surface is still unknown but probably change in the size of spherulite during processing could be the possible cause.

3.12.2.4 Discussion

It is evident from the test results that with the increase in laser power from 30 W to 60 W, apparent interlaminar shear strength and crack propagation load increase. Agarwal [17] also reported similar trend in improvement of ILSS with the increase in laser power from 20W to 60W. Agarwal determined the ILSS of samples processed at laser powers from 20W to 75W and at a constant tape speed of 15.4 mm/sec. He observed that with the increase in laser power from 20W to 60W, ILSS increases. With further increase in the laser power to 75W for the same 15.4 mm/sec tape speed, ILSS decreases because of polymer degradation [17]. Because of the selection of constant tape speed for all the laser powers, effect of increasing the laser power on the mechanical properties of the component can not be properly understood. Probably for 75W laser power, speed higher than 15 4 mm/sec is required to get higher ILSS Mazumdar and Hoa [65,72] found that for every heat intensity, there is an optimum tape speed for which mechanical properties of the composite is maximized. From the present study, 20.8 mm/sec tape speed at 60 W laser power gives higher ILSS compared to other processing conditions studied for laser power. It is observed that with the increase in laser power, optimum tape speed for better consolidation also increases For example better consolidation at 50 W laser power is achieved at around 12.69 mm/sec tape speed and for 60 W laser power it is near 20 8 mm/sec tape speed. Therefore higher laser power reduces the processing time and gives better consolidation With the increase in heat intensity, temperature at the consolidation point increases Higher temperature would result in higher amount of molecular interdiffusion and resin flow. With the increase in diffusion of polymer chains across the interface, improved interlaminar properties can be achieved At this point it is not sure what is the maximum laser power for which highest interply bonding could be achieved. It is suspected that there must be a limit on maximum heat intensity beyond which the quality of consolidation will start deteriorating. Because of the limitation of current laser unit, processing of APC-2 composites was not performed for laser powers higher than 65 W.

3.12.2.5 Comparative study of SBS, DCCB, and fractography tests

It is clear that the DCCB test measures the quality of the interply bond between two specific layers because of the presence of a crack initiator, whereas SBS test determines the quality of bond for a wider test zone Table 3.2 shows that as tape speed decreases to lower speed range (sample 1 at 60W and 8.33 mm/sec, table 3 2), crack propagation load increases whereas ILSS decreases Increase in the crack propagation load can be attributed to increase in fiber fracture events caused by fiber bridging, whereas decrease in ILSS can be attributed to polymer degradation. Therefore, it can be said that the SBS test measures the effect of degradation whereas the DCCB test can not identify the matrix degradation phenomena because of fiber bridging. Matrix vaporization at lower tape speed range was verified during experiments and from SEM study Fractography can show the excessive matrix degradation in terms of fiber fracture events and bare fibers but can not measure the extent of degradation quantitatively. Moreover, DCCB test results and fractography measure the bond quality between two specific plies and do not measure the overall bond quality It is noted here that the bond quality during tape winding process is not uniform through out the thickness, therefore a testing method which can measure the interlaminar properties for a wider test zone is more suitable. SBS test to some extent determines the bond quality for a wider testing region.

From the test results it can be observed that the SBS test in most cases gives better percentage difference in results for two process parameters This shows that the SBS test provides higher sensitivity to characterize the interply bonding For example, a comparison in test results for samples numbered 2, 3, and 4 (table 3 2), show that a reduction in tape speed from 32.72 mm/sec to 26 99mm/sec increases the ILSS by 47.4 % whereas crack propagation load increases by 17.3% Further decrease in tape speed from 26 99 mm/sec to 20.8 mm/sec, increases the ILSS by 37.8 % and crack propagation load by 1%. A comparison in test results with samples produced at lower speed range is not made here because of the increase in fiber fracture events during a DCCB test. It is clear from the previous study that at low speed range matrix degradation in terms of matrix loss takes place. The matrix vaporization was observed during the experiment and loss of matrix material was found from SEM study for low speed range. The SBS test results show that there is a loss of bond strength for low speed range. Therefore the SBS test can identify the matrix degradation For a DCCB test, crack propagation load increases for samples processed at low speed range because of fiber fracture events. An increase in laser power from 30W to 60W (sample numbered 9 and 2) increases the ILSS by 127.5% and crack propagation load by 81 5%. Thus the SBS test can measure the differences in bond quality more easily.

Above discussions show that the SBS test provides better comparison in interply bond quality as compared to the DCCB test and fractography.

3.13 Conclusions

Results of experiments on laser-assisted tape winding of APC-2 thermoplastic composite are presented. Use of the laser during a tape winding process is found to be a clean operation.

During the tape winding process, the temperature history is found to be complex. In the tape winding process, localized heating causes a high rate of heating (more than

20,000°C/min.) and cooling (more than 4,000°C/min.) near the consolidation point. For the laser-assisted processing, it was found that for good interply bonding, required processing temperature goes above 500°C as compared to 380°C to 400°C for hot pressing, autoclave processing, and diaphragm molding. It is because that the shorter melt times and higher heating rates achieved during laser-aided processing require a higher processing temperature for sufficient molecular interdiffusion.

In the thermoplastic tape winding process, several parameters influence the properties of the end product. Effect of dominant processing parameters on crystallinity, process-induced deformation, and consolidation quality are examined. Crystallinity higher than 25% are observed even for complex temperature histories for laser processed samples. With the increase in laser power, process-induced deformation is found to be decreasing.

Test results show that the quality of the interply bond is strongly influenced by the selection of processing conditions. Improvement in interlaminar properties are found with the increase in the heat intensity for the process conditions studied in this chapter. It was found that the short beam shear test provides higher sensitivity to characterize the interply bond quality.

Based on SBS test results, best process parameters for enhanced quality of interply bonding are found to be 60W laser power, 20.8mm/sec tape speed and 100.8 kN/m consolidation force per unit width of the tape for laser processed ten-ply rings. Above values are obtained for processing conditions studied in this chapter. Further improvement in the quality is possible for higher laser powers.

CHAPTER 4

IMPLEMENTATION OF TAGUCHI METHOD

4.1 Summary

During laser-assisted processing of thermoplastic composites, the individual effect of the heat intensity, tape speed, and consolidation force on the interply bond strength is not easily separated unless a large number of experiments is carried out Because the properties of a end product depend upon the selection of processing conditions, it is essential that the conditions under which a well consolidated part is obtained should be defined. The previous chapter deals with the qualitative analysis of the influence of process parameters on the bond quality, whereas this chapter performs studies on the quantitative analysis of the effect of process parameters on the bond quality For this, Carbon/PEEK (APC-2) thermoplastic composite rings were manufactured by a thermoplastic tape winding process at selected conditions and influence of dominant process parameters on the interply bond strengths were evaluated.

Optimum processing conditions for higher quality products are determined by the Taguchi method. The Taguchi method is a powerful tool to bring quality into the product through design and not by inspection or trial and error method. The influence of three dominant factors such as laser power, consolidation force and tape speed on the bond strength are investigated. Experimental design was performed using L_9 orthogonal arrays. Percentage contribution of each factor on the quality of bond are estimated by ANOVA technique

4.2 Introduction

In the manufacture of a composite component, several processing variables influence the performance of the product. The technique of defining and investigating all possible conditions in an experiment involving multiple factors is known as the design of experiments. In the old days it was believed that the scientifically correct way to conduct an experiment was to vary just one factor at a time, holding everything else fixed Thus for a full factorial design the number of possible designs N is

$$N = L^m \tag{4.1}$$

where L = Number of levels for each factor

and m = Number of factors

Thus, if the quality of a given product depends on three factors A, B, and C and each factor is to be tested at three levels then Eq. 1 indicates 3^3 (27) possible design configurations. It means the experimenter has to conduct 27 tests to understand the process. As the number of factors or number of levels increases, the total number of tests also increases. For example if an engineer wants to determine the effect of seven factors at two levels then the total number of experiments becomes 2^7 (128), which will increase the cost of experiments.

Techniques such as fractional factorial design are used to simplify the design of experiments. Fractional factorial design investigates only a fraction of all the possible combinations. This approach saves considerable time and money but requires rigorous mathematical treatment, both in the design of the experiment and in the analysis of the results to correctly understand about the process Each experimenter may design a different set of fractional factorial experiments. Therefore, there is a need for developing a systematic approach to determine the effect of process parameters on the quality of an end product and also to investigate which process parameters are required to be controlled to get a minimum variation in the results. Herein lies Taguchi's contribution to the science of the design of experiments. He simplified and standardized the fractional factorial designs using a special set of orthogonal arrays. According to Taguchi's experimental design, only a minimum of 8 experiments instead of 128 experiments for seven factors at two levels are required to get enough information about the process. Detail explaination of Taguchi Methodology can be find in [74,75,76]

For manufacturing processes where large numbers of factors influence the final outcome, Taguchi approach can be utilized to arrive at the best parameters for the optimum design configuration with the least number of analytical investigations. Therefore Taguchi method has great potential in the area of low cost composites manufacturing and materials processing. Still the use of statistical techniques in the area of composites manufacturing is lacking. Recently, Wilkins et al [77] have used Taguchi method for property and process enhancement in the Resin Transfer Molding (RTM) process.

In chapter 3, qualitative analysis of influence of process parameters on physical and mechanical behaviours of an end product is performed, whereas this chapter provides quantitative effect of individual parameters on the bond quality. Taguchi method is implemented for the experimental design of a thermoplastic tape winding process. Percentage contribution of individual parameters on the bond quality are estimated by ANOVA technique.

4.3 Objectives

The present study is performed to fulfil the following two objectives.

1. To use statistical method for analyzing the results of experiments
2. To estimate the contribution of individual process parameters such as laser power, consolidation force, and tape speed on the quality of bond.

4.4 Experimental Procedure

For the present investigation, ten-ply rings were manufactured at selected processing parameters using laser as a heat source. Same experimental set-up as described in chapter 3 is used for the fabrication of rings. In the previous chapter, interfacial ply bonding of ring specimens are characterized using short beam shear (SBS) tests, double cantilever curved beam (DCCB) tests, and fracture surface study by scanning electron microscope (SEM). It was found that the SBS test is sensitive to the interply bonding and can easily detect differences in the interply bond Therefore, for the present case SBS tests were conducted for quality control purposes. The SBS test was measured according to the method described in ASTM D2344 [56].

4.5 Implementation of Taguchi Method

4.5.1 Designing the experiment :

Experimental design involves defining all the possible conditions in an experiment involving multiple factors. An experimental design must satisfy two objectives. In the first, the number of trials is calculated and in the second, conditions for each trial are specified Taguchi developed several sets of orthogonal arrays (OAs) for designing experiments with various factors and levels. In the present case three factors at three levels are studied as listed in Table 4.1. Three levels are selected when it is suspected that the influence of a factor on the result can be non-linear For the present case, an L_9 OA as shown in Fig.4.1 is suitable for the experimental design. There are nine independent conditions in an L_9. These conditions are described by the numbers in the rows. Experiments were performed at laser powers of 40W, 50W, 60W, consolidation force of 50.4 kN/m, 100.8kN/m, 151.3 kN/m, tape speeds of 6.42 mm/sec, 13.00mm/sec and 27.00mm/sec. Here consolidation force is measured in terms of load per unit width of the laminate with the assumption that there is a linear contact between the consolidation roller and laminate For clarity, the experimental conditions of Fig. 4.1 can be explained as follows.

Experiment No. 1: 40W (A_1), 50.4 kN/m (B_1), 6.42 mm/sec (C_1)
Experiment No. 2: 40W (A_1), 100.8 kN/m (B_2), 13.0 mm/sec (C_2)

Table 4.1 Control factors and their levels.

Factor	Level 1	Level 2	Level 3
Laser Power (W)	40	50	60
Consolidation Pressure (kN/m)	50.4	100.8	151.3
Tape Speed (mm/sec)	6.42	13.0	27.0

Factors Trials	A Laser Power	B Pressure	C Tape Speed	Y SBS test results (MPa)
1	1	1	1	25.66
2	1	2	2	28.00
3	1	3	3	20.65
4	2	1	2	35.09
5	2	2	3	29.79
6	2	3	1	29.15
7	3	1	3	35.66
8	3	2	1	35.73
9	3	3	2	39.57

Fig. 4.1 An experimental layout using L_9 array.

Experiment No 3: 40W (A_1), 151.3 kN/m (B_3), 27 0 mm/sec (C_3)
Experiment No. 4: 50W (A_2), 50 4 kN/m (B_1), 13 0 mm/sec (C_2)
Experiment No. 5. 50W (A_2), 100.8 kN/m (B_2), 27.0 mm/sec (C_3)
Experiment No. 6 50W (A_2), 151.4 kN/m (B_3), 6.42 mm/sec (C_1)
Experiment No. 7: 60W (A_3), 50.4 kN/m (B_1), 27 0 mm/sec (C_3)
Experiment No. 8: 60W (A_3), 100.8 kN/m (B_2), 6.42 mm/sec (C_1)
Experiment No. 9: 60W (A_3), 151.4 kN/m (B_3), 13.0 mm/sec (C_2)

For the present case only one experiment at each of the above conditions was performed to see the main effects of individual processing parameters. The optimum condition is identified by studying the main effects of each of the factors.

4.5.2 Analysis of the results:

As described above, rings at specified conditions were manufactured and the results of the SBS test, in terms of a quality characteristic, Y, were measured as shown below:

Y_1 = 25.66 MPa, Y_2 = 28.00 MPa, Y_3 = 20.65 MPa
Y_4 = 35.09 MPa, Y_5 = 29.79 MPa, Y_6 = 29.15 MPa
Y_7 = 35.66 MPa, Y_8 = 35.73 MPa, Y_9 = 39.57 MPa

These results are recorded in the right most column of the OA (Fig.4.1). Since, there was only one test for each condition, the results are recorded in one column. For some trial conditions such as experiment numbers 4 and 7, multiple tests were performed. The standard deviation for experiment number 4 with two test runs was found to be 0.564 and standard deviation for experiment number 7 with three test runs was found to be 1.773. Once the main effects are known then new levels for control factors are selected to locate the best condition for higher performance.

To speed up the analysis, Taguchi has provided some key procedures which are used here. When these steps are strictly followed by different individuals performing the analysis, they are likely to arrive at the same conclusions.

4.5.3 Computation of Average Performance:

To compute the average performance of the factor A at level 1 i e. A_1 at 40 W laser power, add results for trials including factor A_1 , and then divide by the number of such trials. For A_1, look in the column for A and find that level 1 occurs in experiment numbers 1, 2 and 3. The average effect of A_1 , is therefore calculated by adding the results, Y of these three trials as follows:

$$A_{1av} = (Y_1 + Y_2 + Y_3) / 3 = (25.66 + 28.00 + 20.65) / 3 = 24.77$$

The average effects of other factors are computed in a similar manner.

$$A_{2av} = (Y_4 + Y_5 + Y_6) / 3 = 31.34$$
$$A_{3av} = (Y_7 + Y_8 + Y_9) / 3 = 36.99$$
$$B_{1av} = (Y_1 + Y_4 + Y_7) / 3 = 32.14$$
$$B_{2av} = (Y_2 + Y_5 + Y_8) / 3 = 31.17$$
$$B_{3av} = (Y_3 + Y_6 + Y_9) / 3 = 29.79$$
$$C_{1av} = (Y_1 + Y_6 + Y_8) / 3 = 30.18$$
$$C_{2av} = (Y_2 + Y_4 + Y_9) / 3 = 34.22$$
$$C_{3av} = (Y_3 + Y_5 + Y_7) / 3 = 28.70$$

Above values are plotted in Fig. 4.2 to see the main effects of the each factor on the bond quality. It is clear from the figure that the increase in laser power increases the bond strength whereas effect of consolidation force in the range of 50.4 kN/m to 151.3 kN/m is negligible. Influence of tape speed on the bond strength is found to be nonlinear.

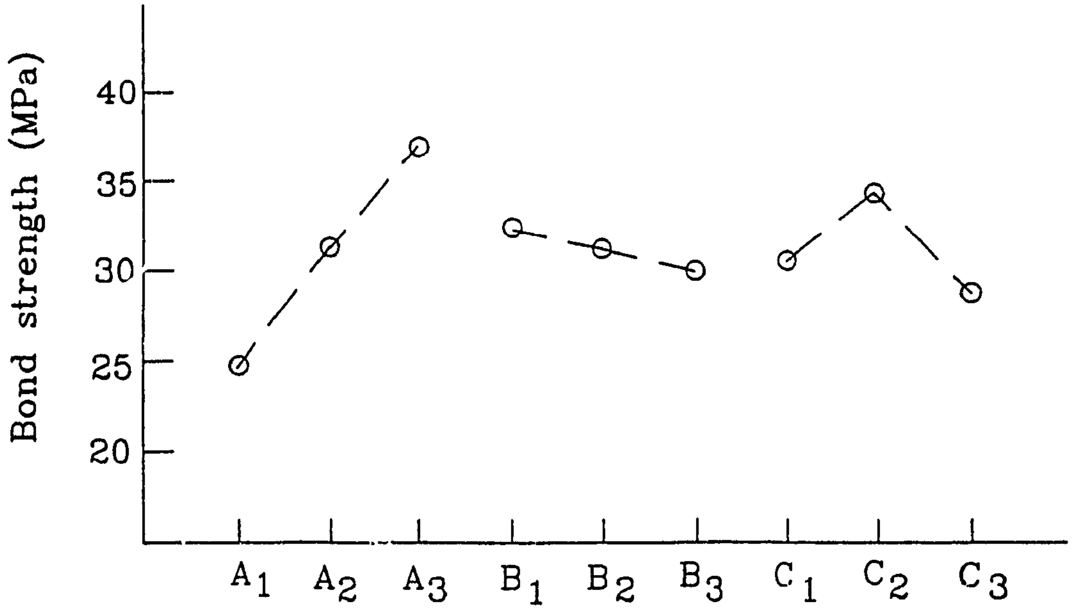

Fig. 4.2 Main effects of the factors on SBS test results.

Quality of interlaminar properties is found to be poor at lower and higher tape speeds

The reason for increase in interply bond strength with the increase in laser power is that the higher laser power causes a higher temperature at the consolidation point Higher processing temperatures would result in lower viscosity and higher intermolecular diffusion which will cause greater degree of resin flow and molecular interdiffusion and results in better interply bond properties [60] Variation in the consolidation force in the range of 50 4 kN/m to 151 3 kN/m on the wetting and intimate contact at the ply interfaces is found to be negligible [65] Decreasing the consolidation force to 25 kN/m causes poor wetting and improper bonding between plies. Because of the sufficient wetting between plies in the range of 50 4 kN/m to 151 3 kN/m consolidation forces, variation in the interply bond strength is found to be a minimal The effect of the tape speed on the SBS test result is found to be non-linear. Because of the polymer degradation at lower speeds and insufficient wetting at higher speeds, the interply bond strength is reduced.

4.5.4 Quality Characteristics

For a product obtained by the tape winding, the bigger the value of the bond strength, the better the quality of a product. Thus from Fig 4.2 the A_3 (60 W) , B_1 (50 4 kN/m) and C_2 (13.0 mm/sec) combination will likely produce the best result. From Fig 4 2 it can be observed that the influence of the tape speed on the bond strength is non-linear. The exact trend of the curve is not known. More tests at 60 W laser power and at tape speeds in the range of 13 0 mm/sec to 27 0 mm/sec are needed to locate the optimum conditions. It is obvious from the result of Fig 4 2 that to further improve the quality of the laser processed parts, one should study the effect of laser powers above 60W and tape speeds higher than 13 3 mm/sec. In the present case, tests higher than the 60W laser power is not conducted because of limitation of the equipment

4.5.5 Relative Contributions of Variables

The relative tribution of processing parameters are established by comparing their variances The technique, analysis of variance (ANOVA) is used for this purpose. Results of ANOVA in terms of percent contribution of each process parameters are found as mentioned below

$P_A = 79.08$ %, $P_B = 2.72$% , $P_C = 17.05$ %

The results show that the laser power contributes around 79.08% in the development of the bond strength, therefore the laser power should be controlled properly. Contribution of consolidation force in the development of bond strength is only 2.72%, therefore variation in the consolidation force during processing would not significantly affect the quality of the bond. Influence of the tape speed during an on-line consolidation is found to be 17.05% Calculations of different terms of ANOVA are omitted here. For detailed study on ANOVA refer to [74].

In most cases variation in the quality of a product is unavoidable. This variation can be brought to a minimum by understanding about the effects of process parameters. In the present case, the laser power has the highest influence on the variation in the properties of a tape wound product. Therefore during the tape winding, variation in the heat intensity should be minimized in order to get a consistent quality of the end product.

The present results can be very helpful in designing new processing equipment for manufacturing complex composite components. In the fabrication of non-axisymmetric shapes, the tape speed varies for a constant mandrel speed [78,79,80]. For example, during manufacturing of rings of elliptical cross-sections with semi-major axis of 7.8 cm and semi-minor axis of 3.9 cm, it is found that the tape speed varies from 2 cm/sec to 16.2 cm/sec during one revolution at a constant mandrel rotation of 10 rpm [78]. With the change in tape speed, laser power can not be kept constant for uniform bonding between the layers. To solve this problem, either the laser power should be varied to compensate for changes in the tape speed or tape speed should be maintained constant in order to prevent the variation in the laser power. Results obtained in this thesis work show that the laser power should be kept at a maximum level (60W in this case) for higher bond quality. Reduction in the laser power will decrease the bond strength. Therefore in the production of complex shapes by a tape winding technique, variation in the laser power should be prevented and the tape speed should remain constant in order to keep the laser power at a maximum level.

4.5.6 Projection of the Optimum Performance:

From the above analysis A_3 B_1 C_2 is found to be the optimum condition for the interply bond strength. The actual result for the above condition is not known because it is not among the trial runs performed for the present case. Prediction of the result at the optimum condition is determined by the following relation [74].

$$Y_{opt} = T/N + (A_{3av} - T/N) + (B_{1av} - T/N) + (C_{2av} - T/N) \tag{4.2}$$

= average performance + contribution of A_3, B_1, and C_2 above average performance

where,

T = Grand total of all results

N = Total number of results

Y_{opt} = Performance at optimum condition

In this case:

T = 279.3, N = 9, A_{3av} = 36.99, B_{1av} = 32.14, C_{2av} = 34.22

therefore,

$$Y_{opt} = 31.03 + (36.99-31.03) + (32.14 - 31.03) + (34.22 - 31.03)$$

$$Y_{opt} = 41.28$$

which is slightly above the 39.57 MPa value obtained during trial run 9.

4.6 Conclusions

Taguchi method was applied for the experimental design of a thermoplastic tape winding process. Using Taguchi method, only nine experiments were sufficient to determine the percent contribution of each process parameter on the quality of bond. The optimum condition for the tape winding process is estimated.

It was found that the bond strength increases with an increase in laser power within a range of 30W to 60W. The effect of consolidation force on bond strength was found to be negligible. The influence of tape speed on the quality of bond is found to be non-linear with the highest strength at a medium tape speed. It is estimated that the laser power has a major contribution on the improvement of bond quality. Percent contributions to the enhancement of bond quality by laser power, consolidation force, and tape speed are found to be 79.08 %, 2.72% and 17.05 % respectively.

CHAPTER 5

HOT-NITROGEN-GAS-AIDED PROCESSING

5.1 Summary

Manufacturing of Carbon/PEEK (APC-2) thermoplastic composite rings by thermoplastic tape winding using hot-nitrogen-gas as a heat source was studied. During the fabrication of thermoplastic composite parts using the thermoplastic tape winding process, several parameters such as heat intensity, tape speed, consolidation force, preheating temperature of tape and tool material, and cooling rate can affect the property of the end product Effects of dominant processing parameters on temperature distribution, process-induced deformation, quality of consolidation, and crystallinity are examined

5.2 Introduction

Chapter 3 described the processing of APC-2 composites using laser as a heat source. Because of higher equipment cost involved with the laser, the hot-nitrogen-gas is used for processing APC-2 composites. This chapter describes the feasibility of hot-nitrogen-gas aided processing of Carbon/PEEK thermoplastic composites. To the author knowledge, no experimental results are available on the effect of processing parameters on the temperature history, crystallinity and process-induced deformation during the tape winding process using the hot-nitrogen-gas as a heat source. In this chapter, temperature histories for various processing parameters are determined. Effects of dominant process parameters such as heat intensity, tape speed, and consolidation force on crystallinity, process-induced deformation, and interply bond quality are examined. Effect of heating rate on the minimum temperature required for a well consolidated part is discussed. Characterization of the interply bonding for hot-gas processed samples by short beam shear tests, double cantilever curved beam tests and scanning electron microscopic tests is performed.

5 .3 Experimental

Same experimental set-up as described in chapter 3 for laser-assisted processing is used for the manufacture of circular rings using hot-nitrogen-gas as a heat source. Schematic diagram of the set-up with a heat source is shown in Fig. 5.1. Hot-nitrogen-gas was supplied to the contact point of the mandrel and roller at various flow rates. The temperature of nitrogen gas just before leaving the nozzle was measured by a thermocouple and was controlled at a temperature of 905°C. Outlet of the nozzle tip had elliptical cross-section with a semi-major axis of 4.7 mm and semi-minor axis of 3.05 mm. The nozzle tip was kept 25.4 mm away from the contact point during the processing. The unit for supplying hot-nitrogen-gas was obtained from Automated Dynamics Corporation. Ten-ply rings were manufactured under various processing parameters and found to be suitable for various studies while limiting material use to a reasonable amount.

From the initial experiments, with 146 SCFH (Specific Cubic Feet per Hour) nitrogen flow rate at 905°C, and at tape speeds of 6.28 mm/sec to 13.3 mm/sec, immediate bonding between plies was not achieved though the tape temperature recorded was higher than 650°C. In that speed range, the outer ply, i.e., one circumferential length of the ring could be easily peeled off. The layers beneath the outer layer had good bonding. It is to be noted here that in contrast to the outer layer, the inner layers undergo more than one heating and cooling cycle. For a similar temperature history during laser processing, immediate bond formation was achieved. In laser processing, heat is supplied by radiation, whereas in hot-gas processing, heat is supplied at the contact point by forced flow convection. Probably high nitrogen velocity may be affecting the immediate bond formation. Using a lower tape speed of 3.58 mm/sec during hot-gas processing, immediate bonding was achieved. By increasing the nitrogen gas flow rate to 264 SCFH, immediate bond formation was achieved for 13.3 mm/sec and 28.0 mm/sec tape speeds.

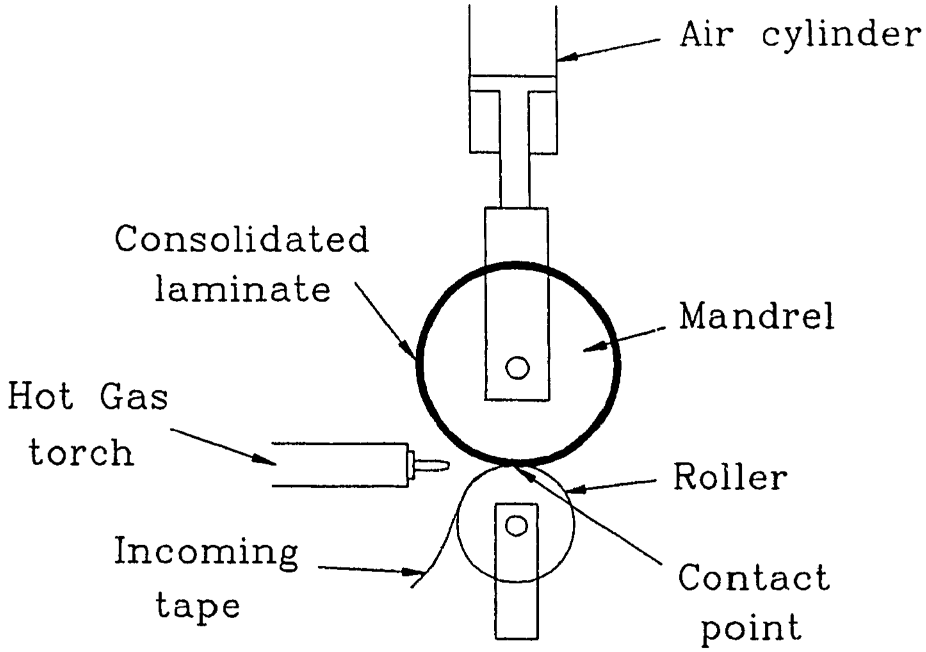

Fig. 5.1 Schematic diagram of thermoplastic tape consolidation using hot gas as a heat source.

5.4 Temperature History During Hot-gas Aided Processing

Experimental measurement of temperature during hot-gas assisted processing was done similar to that described in chapter 3 for laser processing A digital process indicator (DP 86, Omega Eng Inc), LeCroy 9400, dual 125 MHz digital oscilloscope, and 0.125 mm diameter K type thermocouple were used to record the temperature profile during processing. For the measurement of the temperature history, a thermocouple was inserted between the fifth and sixth plies without interrupting the process. In all the cases, the mandrel and roller were preheated to 130°C by an air heater (heat gun) just before winding, and then the heat gun was switched off

Figures 5 2, 5.3 and 5.4 represent the temperature profiles recorded by the oscilloscope during three consecutive heating cycles. In Fig. 5.2, the temperature profile is shown just after placing the thermocouple near the contact point whereas figures 5.3 and 5.4 represent the temperature profile nearly after one heating cycle. The temperature recorded by the oscilloscope is not smooth because of the low sampling rate of the instruments. The general trend in temperature history during the thermoplastic tape winding process is that the maximum temperature decreases as the thermocouple goes away from the contact point. In figure 5.4 the maximum temperature recorded by the oscilloscope atter first heating cycle is found to be slightly lower than the temperature measured after the second heating cycle. This can be attributed to the insufficient sampling rate of the instrument.

It is evident from Figs 5.2-5.4 that temperature profile depends upon the selection of process parameters. It is noted that the several layers beneath the consolidation point go above melting temperature (343°C) of PEEK thermoplastics. The general trend is that the temperature reached in a ply decreases as the ply goes away from the consolidation point. It is found for all the speed ranges that the maximum temperature recorded by the instrument during insertion of the thermocouple (first spike) is around 1,000°C (Fig.5.2). Maximum temperature recorded during second spike onwards differed with the change

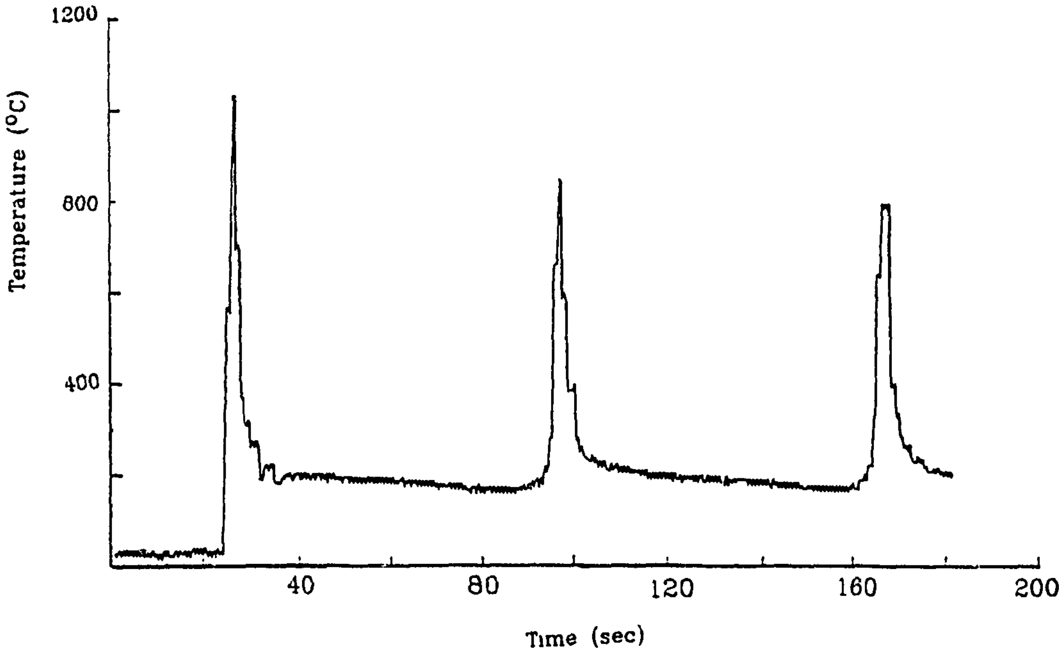

Fig. 5.2 Temperature history during hot gas processing for nitrogen flow rate of 146 SCFH, 6.28 mm/sec tape speed, and 67.2 kN/m consolidation pressure.

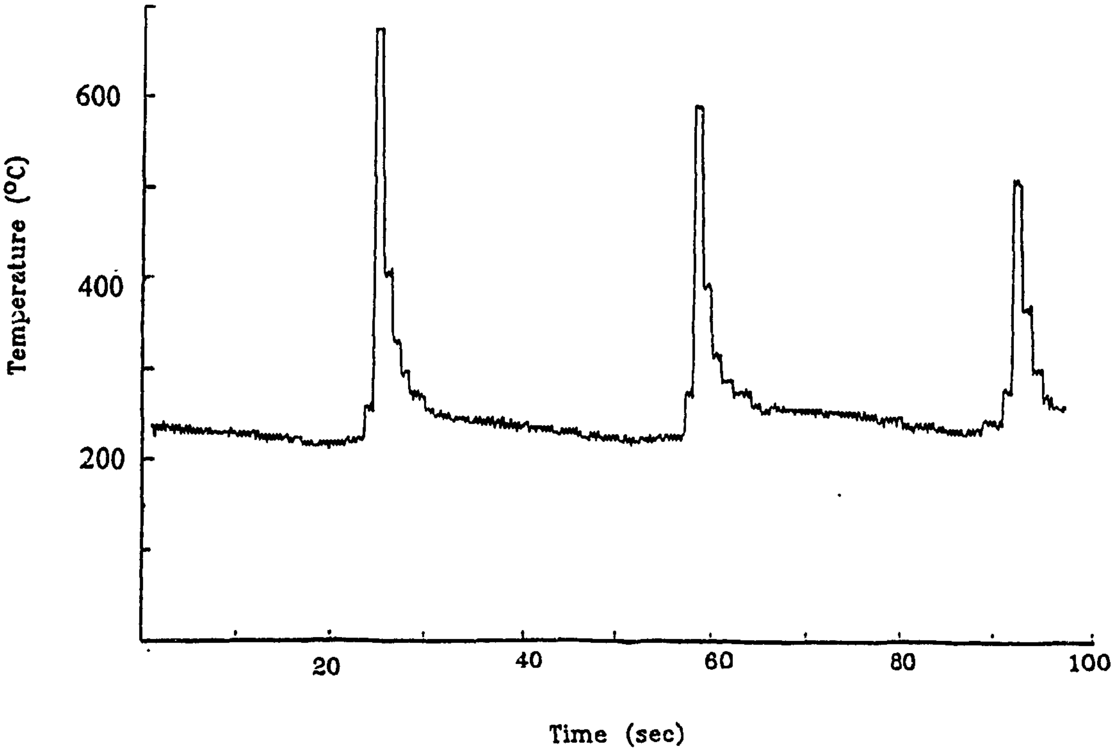

Fig. 5.3 Temperature profile during hot gas processing for nitrogen flow rate of 146 SCFH, 13.3 mm/sec tape speed, and 67.2 kN/m consolidation pressure.

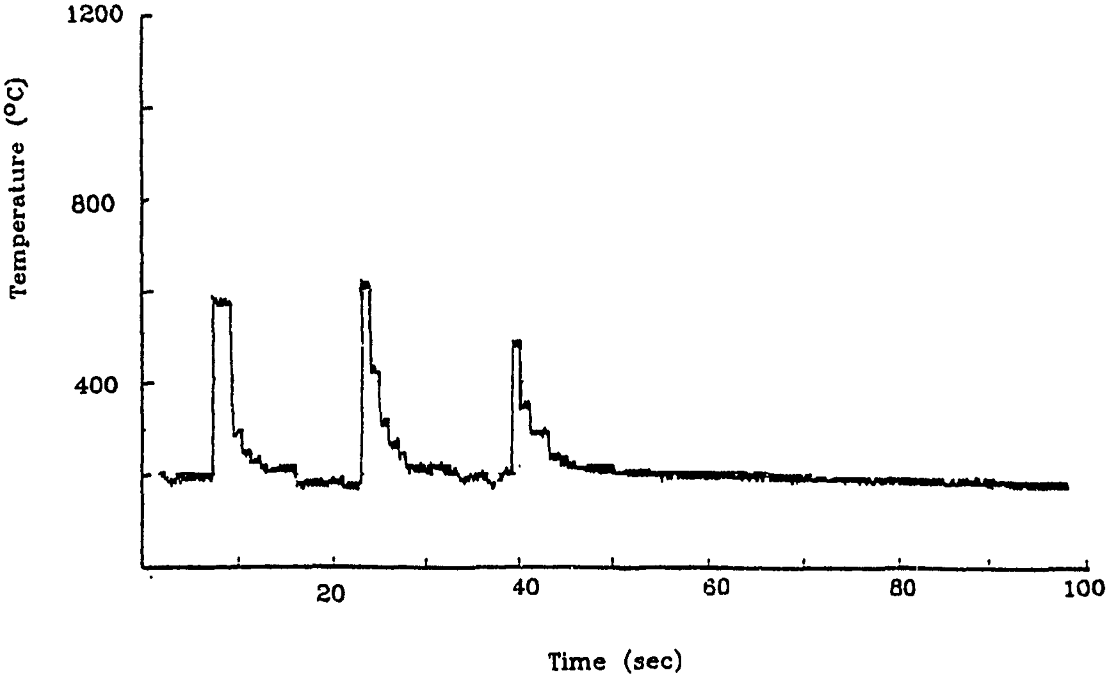

Fig. 5.4 Temperature history during hot gas processing for nitrogen flow rate of 264 SCFH, 28.0 mm/sec tape speed, and 67.2 kN/m consolidation pressure.

in tape speed and heat intensity The initial increase in the temperature during first spike is due to the direct heating of the thermocouple by hot-nitrogen-gas As the thermocouple reaches the consolidation point, it comes into contact with the prepreg tape and substrate and becomes embedded in the material The material begins to cool immediately as it moves away from the heat source The heating rates and cooling rates are calculated to be more than 20,000°C/min and 5,000°C/min, respectively, for Figs 5 2 and 5 3. For 264 SCFH flow rate and at a tape speed of 28 0 mm/sec (Fig 5.4), the heating rate is found to be more than 45,000°C/min, and the cooling rate is measured to be more than 5,800°C/min The melt time during hot-gas processing is found to be in the range of 1 sec to 4 sec, which is slightly higher than that during laser processing.

5.5 Effect of Heating Rate on Minimum Temperature Required for Good Consolidation

A majority of the work in polymer bonding is focused on amorphous polymers. In amorphous polymers, interdiffusion occurs above the glass transition temperature. In semicrystalline polymers, the interdiffusion would not occur below the melting or crystallization temperature because the crystal structure effectively locks the movement of molecules. Wetting predominates at low welding temperatures close to the polymer melting point and involves the surface tension and viscosity of the two surfaces in contact. Interdiffusion of macromolecular chains of the two surfaces in contact predominates at fairly high temperature and welding times [59] During hot-gas processing of APC-2 thermoplastic composites, it was found that for a good interply bonding, the processing temperature goes above 600°C, whereas for hot pressing and autoclave processing, the manufacturer's recommended processing temperature is 380°C to 400°C Shorter melt times (1 sec to 4 sec) and higher heating rates (more than 20,000°C/min) during thermoplastic tape winding limit the amount of diffusion, therefore a higher processing temperature is needed for sufficient molecular interdiffusion. Higher processing temperatures would result in lower viscosity and higher diffusivity, which will cause a greater degree of resin flow and interdiffusion. A higher degree of resin flow and interdiffusion would result in better interply bond properties. Saint-Royre and coworkers

[59] found that the minimum temperature required for good welding of polyethylene layers increases from 145°C to 214°C with the increase in heating rate from 20°C/min to 400°C/min.

To determine the minimum temperature required for good interply bonding, experiments were performed at various amounts of heat supply and at various speeds The temperature history for each case was recorded To check the bonding between layers, the specimen was peeled manually using the end of the tape after the ring was manufactured.

It was found for 146 SCFH nitrogen flow rate at 905°C, 67.2 kN/m consolidation force, and a tape speed of 28 mm/sec, the maximum temperature reached during the second spike was above 580°C and the maximum temperature during third spike was above 490°C Here the lower limit in the maximum temperature is presented Because of the insufficient sampling rate of the instrument, it is possible that the exact peak temperature is not recorded by the instrument In this case, it was found that the outer four plies (four circumferential length) peeled off easily because of insufficient bonding between the plies.

By lowering the tape speed from 28 mm/sec to 13 3 mm/sec for same condition, the maximum temperature recorded during the second spike was above 680°C and during the third spike was above 580°C (Fig.5.3). For this case, only the top ply (one circumferential length) peeled off easily. After one circumferential length, manual peeling of the tape became difficult, and the tape end was broken due to the good consolidation It is obvious from this test that when the temperature between plies goes above 680°C, better consolidation is achieved.

With further decrease of the tape speed to 6 28 mm/sec for the same heat intensity (146 SCFH), the maximum temperature during second spike was above 840°C, and during the third spike it was above 780°C (Fig.5.2). The top ply (one circumferential length) for this case came apart easily. Peeling of the tape became difficult after one circumferential length due to good bonding between the plies.

For tape speeds higher than 28 mm/sec for 146 SCFH gas flow rate, poor consolidation between plies was achieved By increasing the heat intensity from 146 SCFH to 264 SCFH, the maximum temperature at the consolidation point increases for the same tape speed. For 264 SCFH flow rate and 67.2 kN/m consolidation force, immediate bond formation was achieved for 13 mm/sec to 28 mm/sec tape speeds. The maximum temperature was above 600°C during 264 SCFH gas flow rate and at tape speed of 28 mm/sec (Fig. 5.4). From this study it was observed that for the case when maximum temperature during second spike was lower than 600°C, ply consolidation was found to be poor

5.6 Crystallinity Study

Measurement of crystallinity was done by using differential scanning calorimetry (DSC) Approximately 5 mg samples were taken from different layers. The DSC scans were done from 100°C to 400°C with scanning rates of 20°C/min as shown in Figs. 5.5-5.7. Cold crystallization peaks were not observed for hot-gas processed samples as shown in Figs.5.5 - 5.7. The results of the crystallinity for various processing parameters are tabulated in Table 5.1. For a ring processed at 146 SCFH and 3 58 mm/sec tape speed (sample number 1), crystallinity at the third-ply from inside was found to be 36.64% whereas for the outer-most layer (the tenth-ply), crystallinity was found to be 28.99%. For comparison purposes, the crystallinity of unprocessed APC-2 tape was also determined and found to be 29.4%. Third layer has more crystallinity compared to the outer layer probably because of the annealing of the sample and lower cooling rate. To the author's knowledge, the effect of high heating rates and short melt times on crystallinity kinetics is unknown. At this point it is not sure whether all the crystallinity in a ply dissolves when the ply undergoes temperatures above 400°C at heating rates higher than 20,000°C/min and melt times in the range of 1 sec to 4 sec. The melting of a semicrystalline polymer is a complicated phenomenon. Lee [64] showed that the crystal structure requires considerable time to be completely destroyed For short dwell times during laser and hot-gas aided process, residual crystallinity may exist in the melt More research needs to be done to develop crystallinity models for the thermoplastic tape winding process.

5.7 Process-induced Deformation

Residual stress is measured indirectly from process-induced deformation because there is no direct technique available for measuring of internal stresses To measure the process-induced deformation, rings were cut using a very fine (0 3mm thick) diamond cutter at low speeds. After cutting, it was found that the rings in most cases opened up For some of the rings made by hot-gas processing, it was found that some portion at the ends of the ring overlapped because of the internal stresses Process-induced deformations were determined by measuring the distance between two ends of the ring Table 5.1 shows process-induced deformations in the samples in the plane of the ring (r-0 plane) for various processing parameters. Deformation when there is an opening is considered to be positive and in the case when there is overlapping is considered as negative (Table 5.1).

For the present case, minimum process-induced deformation was obtained for 264 SCFH nitrogen flow rate at 905°C, 13.3 mm/sec tape speed and 100.8 kN/m consolidation force. At this specific processing condition, highest bond strength (ILSS) was achieved for the process range studied and is discussed in section 5.9.

5.8 Optical Microscopic Study

A microscopic study was performed to investigate the quality of consolidation during hot-gas processing. Figures 5.8, 5 9, and 5.10 show the micrographs of well consolidated rings processed at different processing parameters. Voids at interply locations were not observed. From the micrograph, some resin-rich areas and non-uniformity in the

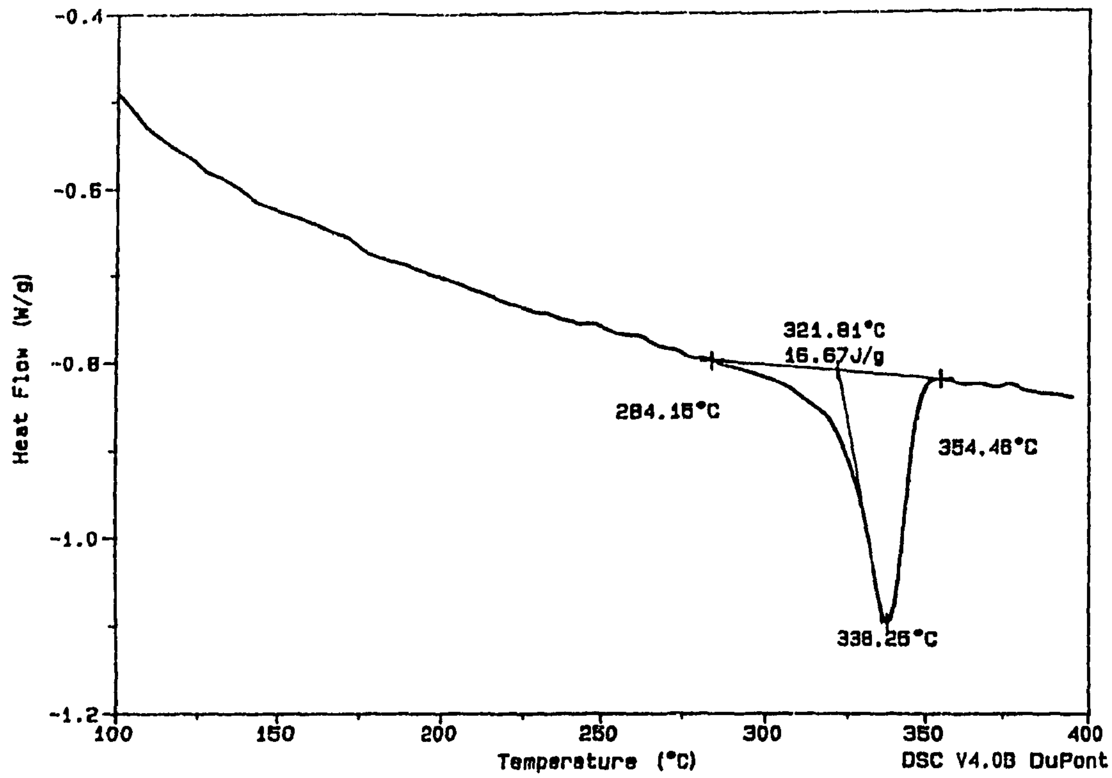

Fig. 5.5 DSC thermogram for a hot gas processed sample for nitrogen flow rate of 146 SCFH, 3.58 mm/sec tape speed, and 100.8 kN/m consolidation pressure. The sample was obtained from third ply.

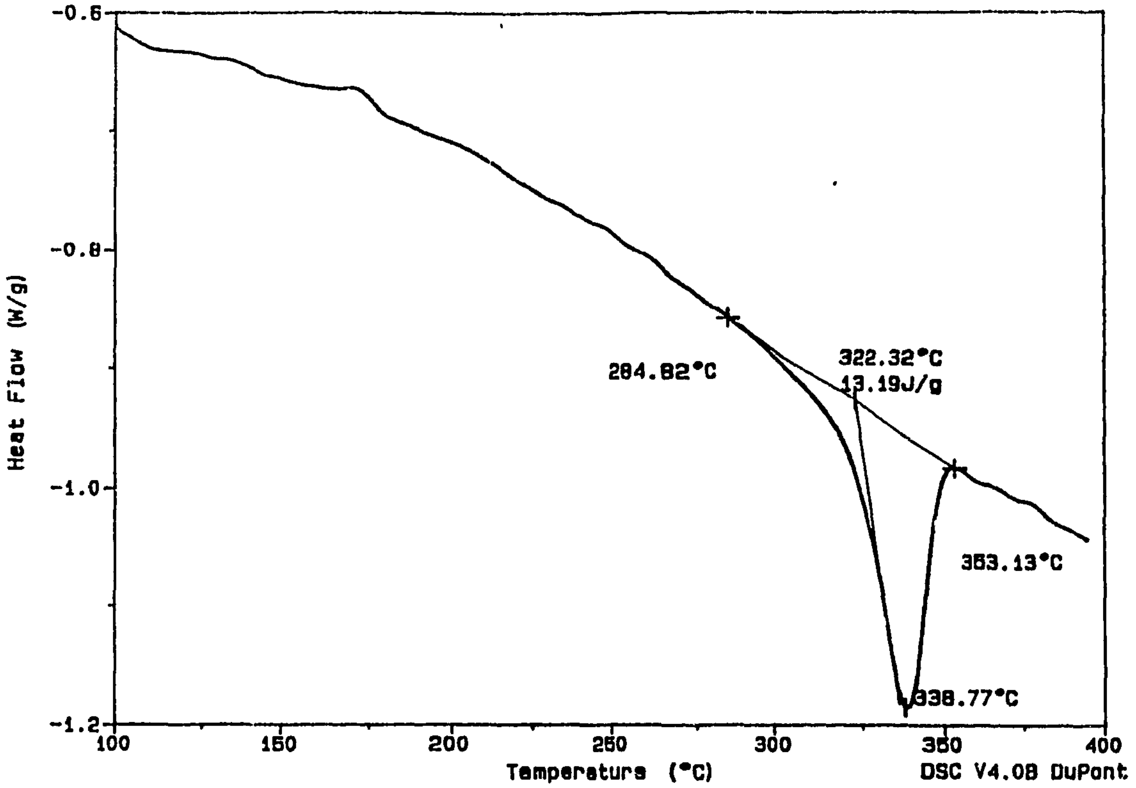

Fig. 5.6 DSC thermogram for a hot gas processed sample for nitrogen flow rate of 146 SCFH, 3.58 mm/sec tape speed, and 100.8 kN/m consolidation pressure. The sample was obtained from top layer (10th ply).

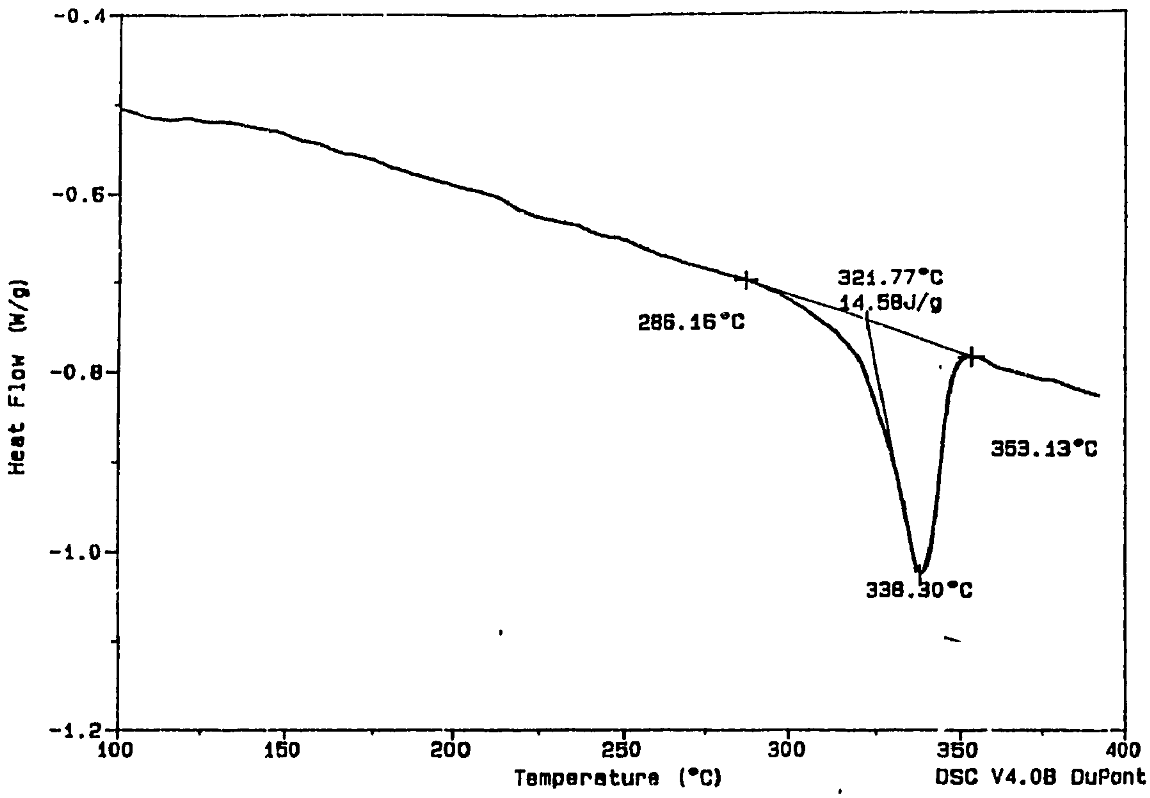

Fig. 5.7 DSC thermogram for a hot gas processed sample for nitrogen flow rate of 264 SCFH, 28 mm/sec tape speed, and 100.8 kN/m consolidation pressure. The sample was obtained from 5th layer.

Table 5.1 Crystallinity and process induced deformation of the hot gas aided processed samples.

Sample number	Processing parameters					Experimental Results			
	Nitrogen Temperature (°C)	Nitrogen flow rate		Tape speed (mm/sec)	Consolidation pressure (kN/m)	Quality of consolidation (microstructure study)	Process induced deformation (mm)	DSC Results	
		SCFH	m^3/hr.					Layer number	Crystallinity
1	905	146	2.55	3.58	100.8	Good	+ 8.53	3 10	36.64 % 28.99 %
2	905	146	2.55	6.28	100.8	Good	− 8.8	2 6	34.85 % 35.51 %
3	905	146	2.55	13.3	100.8	Voids	+ 3.23	5	32.81 %
4	905	264	3.45	13.3	100.8	Good	+ 1.46	5 10	36.11 % 33.25 %
5	905	264	3.45	28.0	100.8	Good	− 5.19	5 10	32.04 % 33.73 %

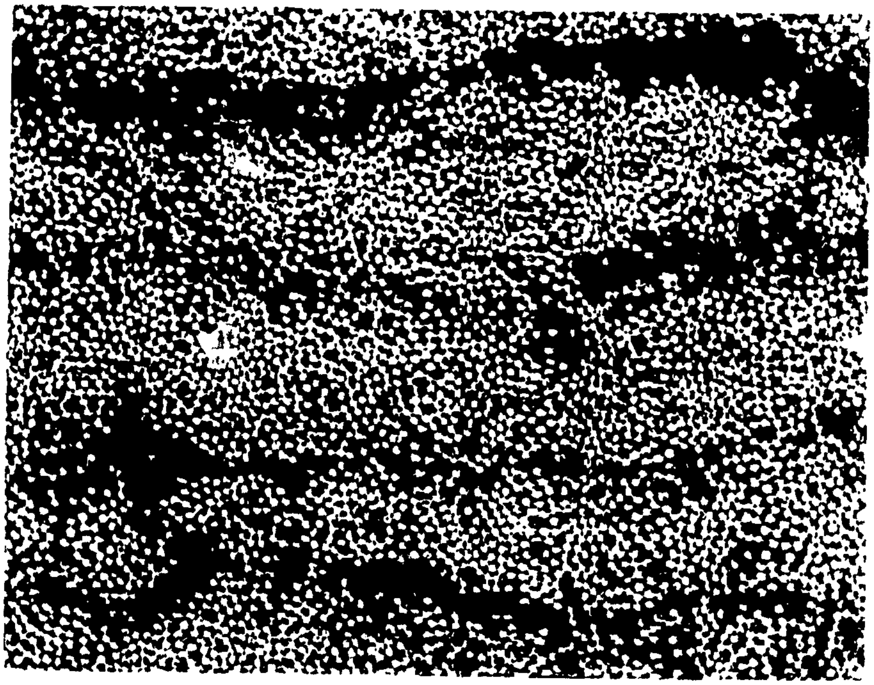

Fig. 5.8 Micrograph of a cross-section for a ring processed at nitrogen flow rate of 146 SCFH, 100.8 kN/m consolidation pressure and at a tape speed of 6.28 mm/sec (200X).

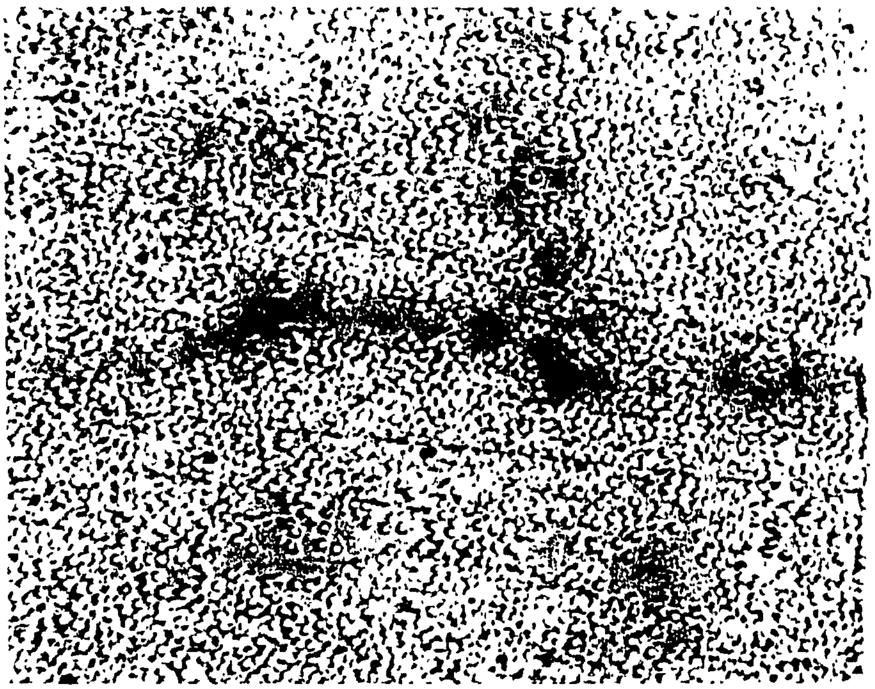

Fig. 5.9 Cross-sectional view of the consolidated ring at 264 SCFH nitrogen flow rate, 100.8 kN/m consolidation pressure and at a tape speed of 28.0 mm/sec (200X).

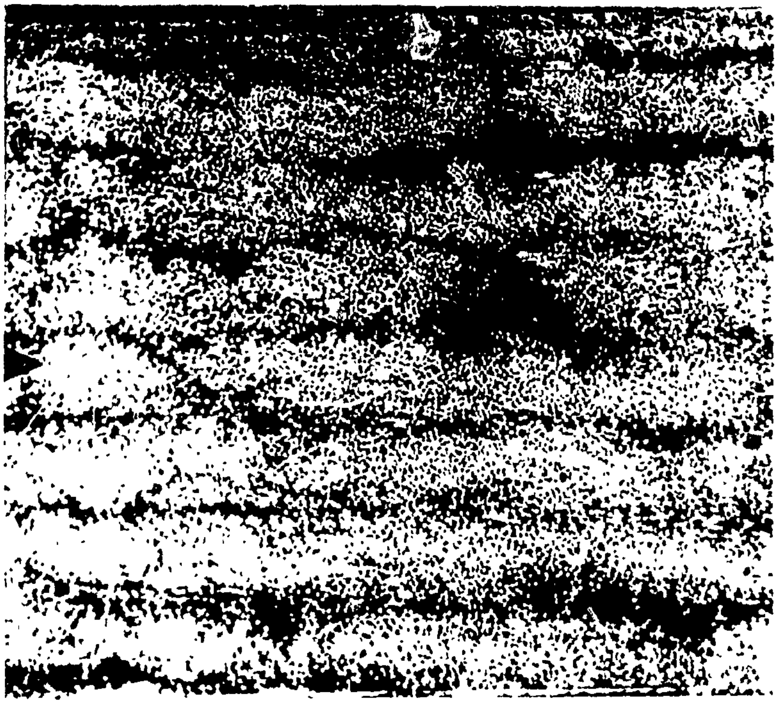

Fig. 5.10 Cross-sectional micrograph of a ring processed at 264 SCFH, 100.8 kN/m consolidation pressure and 28.0 mm/sec tape speed (100X).

fiber distribution could be observed. Different plies could be easily distinguished from the micrographs. From the microstructure study, it was found that at 3.58 mm/sec tape speed (sample number 1), the resin-rich area was minimal compared to the 6 28 mm/sec (sample number 2) and 13 3 mm/sec (sample number 3) tape speeds. At some locations, it was difficult to distinguish interply interfaces at lower speeds. It may be because some of the matrix materials were being vaporized (weight loss) or because a better squeezing - out process was taking place at lower speeds During laser processing [65], smoke was observed at lower speeds Smoke during hot-gas processing was not visible because of the high velocity of the hot-nitrogen-gas.

5.9 Characterization of Intelply Bonding

Quality of interply bonding is determined similar to the method described in chapter 3 for laser processed samples. Short beam shear tests, double cantilever curved beam tests and scanning electron microscopic tests are performed to characterize the joining between plies. Same experimental procedure for above tests was followed as discussed in chapter 3. Results of the tests ar mentioned below

5.9.1 Short Beam Shear Tests

Short beam shear test is performed similarly to the procedure described in chapter 3. Results of the SBS test are tabulated in table 5.2. For the present case, hot-gas processed samples gave better interlaminar properties as compared to the laser processed samples. Uniformity of heat distribution across the width of the specimen and longer melt times causes improved results for hot-gas processed samples.

After the test, samples were examined microscopically to determine the type of failure mode. In all the cases failure was found to be dominant by horizontal shear. A micrograph of the center region of a hot-gas processed sample at 264 SCFH and at 28 0 mm/sec tape speed (sample number 5, table 5.2) is shown in Fig. 5.11. The apparent ILSS

Table 5 2 Effect of processing parameters on the quality of the interply bond for hot gas processed APC-2 samples.

Sample number	Processing parameters					Experimental results		
	Nitrogen Temperature (^oC)	Nitrogen flow rate		Tape speed (mm/sec)	Consolidation pressure (kN/m)	Interlaminar Shear strength (Mpa)	DCCB results	
		SCFH	m^3/hr				Crack length (mm)	Crack propagation load/unit width (N/mm)
1	905	146	2.55	3.58	100.8	38.74	29.21	2.22
2	905	146	2.55	6.28	100.8	42.20	28.12	2.52
3	905	146	2.55	13.3	100.8	27.11	32.05	1.18
4	905	264	3 45	13.3	100.8	54.17	29.38	1.64
5	905	264	3.45	28.0	100.8	35.47	28.18	1.49

Fig. 5.11 Center region of a damaged specimen. Specimen was processed by hot gas at 264 SCFH, 28.0mm/sec tape speed, and 100.8kN/m consolidation pressure.

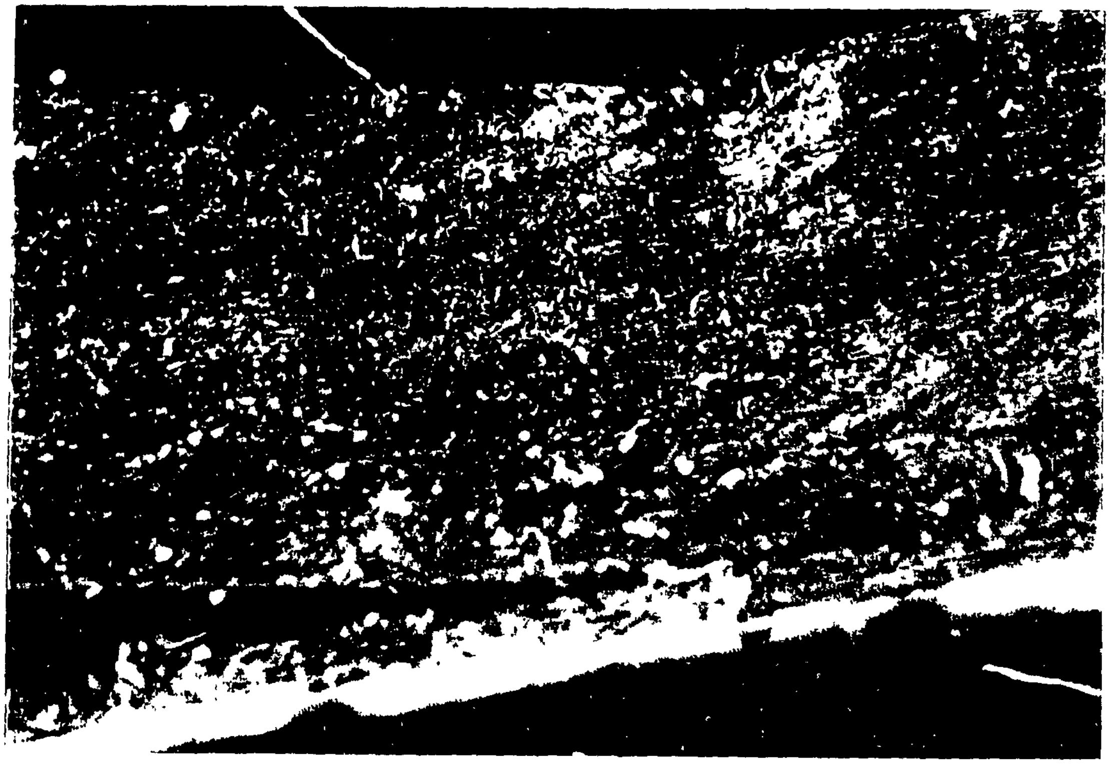

Fig. 5.12 Failure mode during SBS test for a sample processed at 264 SCFH, 13.3 mm/sec tape speed, and 100.8kN/m consolidation pressure.

Fig. 5.13 Damaged sample processed at 146 SCFH, 13.3mm/sec tape speed, and 100.8kN/m consolidation pressure

for this case is found to be 35.47 MPa. Plastic deformation at the center region of the sample is not visible. Some matrix crushing below the loading point was observed. Majority of the delamination failure took place on one side of the sample In most cases of hot-gas processed samples, interply failures were predominant near the bottom surface, which shows insufficient bonding in first few plies.

By decreasing the tape speed from 28.0 mm/sec to 13.3 mm/sec for 264 SCFH, apparent ILSS increases from 35.47 MPa to 54.17 MPa. Interlaminar failure for this case is shown in Fig. 5.12. Left hand side of the bottom layer got delaminated from rest of the plies. A small amount of matrix crushing below the loading nose was observed.

With the reduction in heat intensity from 264 SCFH to 146 SCFH for the same tape speed of 13.3 mm/sec, apparent ILSS reduced by approximately 50 % to 27.11 MPa. Several interply failures on left hand side of the sample were observed (Fig.5.13). Majority of the delaminations were near top and bottom plies. This locates the weaker zone in the sample. For same heat intensity (146 SCFH), maximum bond strength (42.2 MPa) was achieved at 6.28 mm/sec tape speed. With further reduction in tape speed from 6.28 mm/sec to 3.58 mm/sec, apparent ILSS decreased to 38.74 MPa because of the degradation of the matrix material.

5.9.2 Double Cantilever Beam Tests

Double cantilever beam tests were performed similarly to the method discussed in chapter 3 for characterizing the quality of bond. One quarter length of the ring was taken as a test specimen. Aluminum foil was kept during processing between the fifth and sixth layer as a crack initiator. The sample was loaded on a MTS machine at a cross head speed of 1 mm/min. During the tests, delaminations above the initial crack was observed similarly to the laser processed samples. Interlaminar stress through the thickness is the cause of delamination for curved samples. Because of the initiation of multiple cracks during the DCCB test, fracture toughness is not measured. Instead crack propagation load

/ unit width is measured and is chosen as a parameter for characterizing the bond quality The results of DCCB tests are tabulated in Table 5 2 For 146 SCFH flow rate, crack propagation load / unit width is found to be higher at 6 28 mm/sec tape speed. With the increase in tape speed to 13.3 mm/sec or decrease in tape speed to 3 58 mm/sec gave decreased value of crack propagation load

For hot-gas processed samples, delaminations above the initial crack was observed for 146 SCFH and 13.3 mm/sec tape speed. For a sample processed at 264 SCFH and 28.0 mm/sec tape speed, delamination was observed in the beginning, which stopped moving later on. In other cases of hot-gas processed samples, delamination above the desired crack was not observed For hot-gas processed samples, bonding is reasonably uniform through out the width

5.9.3 Fractography

Scanning electron microscopic study was performed to gain a qualitative indication of degree of bonding between ply interface and fiber/matrix interface. To study fracture surface details, smaller specimens were cut from the crack propagation zone of DCCB samples processed at various processing conditions and were examined in the SEM Prior to this operation, specimen was coated with a thin [10 nm] gold layer .

The major contribution to energy absorption during the interlaminar fracture can be attributed to the deformation and fracture of the polymer matrix, whereas minor effect can be due to fiber fracture events. For studying the fiber fracture events, photographs were taken at a magnification of 70 and for the purpose of studying matrix failure between plies and fiber/matrix interface, photographs were taken at a magnification of 500.

The fracture surface obtained in hot-gas processed samples is found to be different from the mode I and II fracture surface of APC-2 samples processed in an autoclave or

Fig. 5.14 Micrograph of a fracture surface for a sample processed by hot gas at 264 SCFH, 13.3mm/sec tape speed, and 100.8kN/m consolidation pressure (500X).

Fig. 5.15 Fracture surface of a hot gas processed sample at 264 SCFH, 28.0 mm/sec tape speed, and 100.8kN/m consolidation pressure (500X).

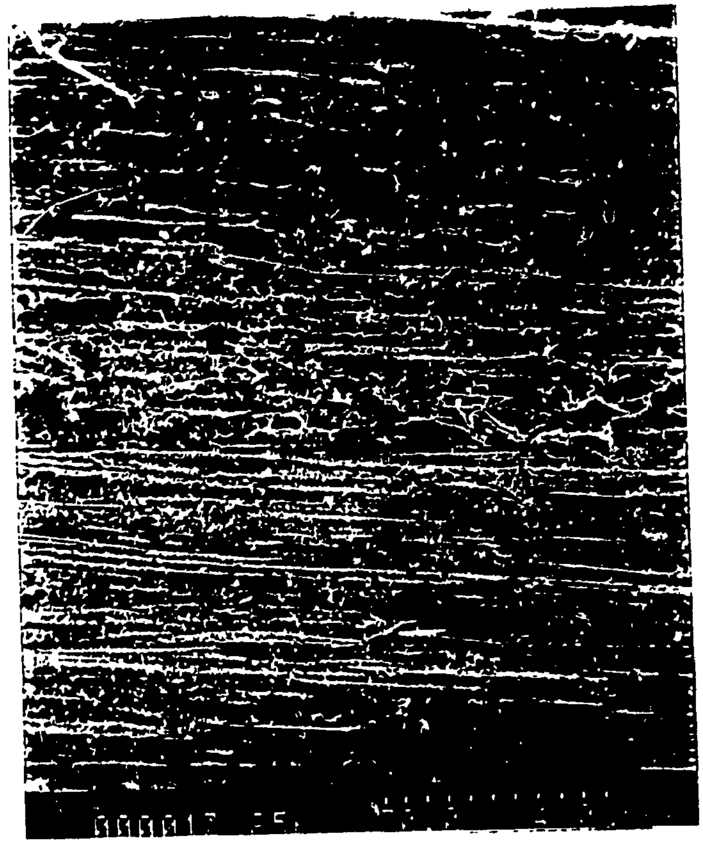

Fig. 5.16 Micrograph of a fracture surface for a sample processed by hot gas at 264 SCFH, 13.3mm/sec tape speed, and 100.8kN/m consolidation pressure (70X).

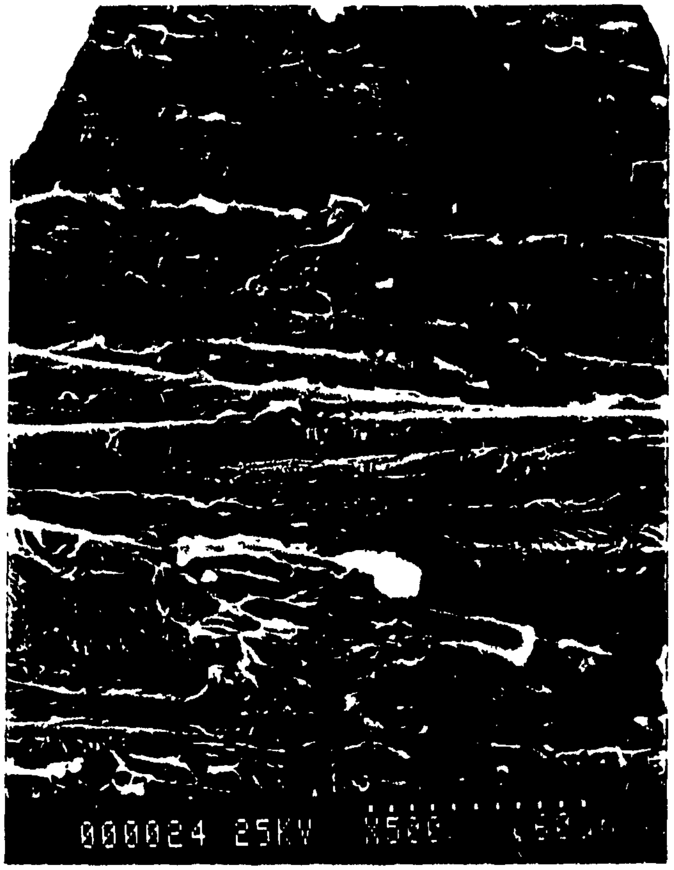

Fig. 5.17 Fracture surface of a sample processed by hot gas at 146 SCFH, 13.3mm/sec tape speed, and 100.8kN/m consolidation pressure (500X).

hot press as reported in the literature [1,71] and as discussed in chapter 3 It can be noted here that the temperature history during the tape winding is quite complex as compared to the hot press or autoclave operation Small matrix fractures are found to be spread at the interface as shown in Figs 5 14, 5.15, and 5.16. Small matrix fractures are also observed in laser processed samples It can be noted here that at these processing parameters, interlaminar shear strengths and the value of crack propagation loads are larger In a sample processed by hot-gas at a nitrogen flow rate of 146 SCFH and at a tape speed of 13 3 mm/sec, matrix plastic deformation and river patterns are observed as shown in Fig. 5.17. Failure in this sample was found to be dominant by matrix deformation and cracking and not by fiber/matrix interface failure. At this processing condition (146 SCFH and 13.3 mm/sec tape speed), quality of the bond is found to be poor as mentioned in Table 5 2. From fractography, it can be inferred that the matrix property is influenced by the selection of processing parameters

5.10 Conclusions

Experimental results on the hot-gas processing of APC-2 composites by the thermoplastic tape winding are presented. The use of hot-nitrogen-gas demonstrated good interply bonding between plies.

The temperature history during the winding process was measured and was found to be complex. The heating rates higher than 20,000°C/min., cooling rates more than 4,000°C/min. and shorter melt times in the range of 1 sec to 4 sec, required the processing temperature more than 600°C for better interply bonding during hot-gas processing. Several parameters were found to influence the properties of the bond. Effects of heat intensity, tape speed, and consolidation force on crystallinity, process-induced deformation and quality of consolidation were examined Crystallinities larger than that of the as received APC-2 tape were observed. Void free consolidation was achieved during hot-gas processing.

SBS tests, DCCB tests and SEM study were performed for characterizing the interply bond quality With the increase in heat intensity, bond strength (ILSS) was found to increase. Based on SBS test results for hot-gas processed samples, best processing condition was found to be 264 SCFH nitrogen flow rate at 905°C, 13.3mm/sec tape speed and 100.8 kN/m consolidation force per unit width of the tape

CHAPTER 6

MANUFACTURE OF COMPLEX PARTS BY TAPE WINDING AND TAPE LAYING

6.1 Summary

The aim of the study presented in this chapter is to describe methods for the fabrication of complex composite parts by thermoplastic tape winding and tape laying process. The tape winding process can be used for the production of closed parts such as cylinders, non-axisymmetric rings etc., and the tape laying process can be used for the fabrication of open parts such as curved beams, leaf springs etc. Advantages of the thermoplastic tape winding and tape laying are not yet exploited because of lack of understanding about the kinematics of these processes. A new approach is presented to study the kinematics of winding and tape laying for the manufacture of complicated shapes. This approach is applied for the production of elliptical composite rings

During the thermoplastic tape winding process, proper heat and pressure are applied at the contact point of the roller and mandrel to consolidate the laminate. Heat can be supplied by laser or hot nitrogen gas or any other heat source For the fabrication of non-axisymmetric thermoplastic composite rings, the contact point changes with change in the mandrel position. Moreover, tape speed is found to vary for a constant rotational speed of a non-axisymmetric mandrel. With the changes in tape speed, the amount of heat at the contact point has to change for uniform heating of the laminate, otherwise the component quality may suffer. This chapter discusses the problems associated with the manufacture of non-axisymmetric shapes such as elliptical rings and presents a solution by performing a kinematic study.

During the tape laying process, a moveable head consisted of heaters, coolers and rollers move at a certain speed to get uniform bonding between plies. A method is presented for determining this head speed such that the tape feed rate remains constant for uniform bonding of the laminate

6.2 Introduction

In the thermoplastic tape winding and tape laying process for non-axisymmetric parts, fiber reinforced thermoplastic tape is laid down on the tool while heat and pressure are applied at the contact point as shown in Figs. 6.1 and 6.2 respectively. The necessary amount of heat supplied for good interply bonding depends upon the material properties and tape speed Several models have been developed for the tape laying and tape winding process which address the problems of heating, crystallinity, consolidation and residual stresses [5,6,7,9] All these models deal with the manufacture of a flat plate by tape laying process or manufacture of a circular cylinder by tape winding process.

During the manufacture of circular rings by tape winding technique, the tape speed remains constant for constant mandrel speeds during one cycle, whereas for non-axisymmetric rings the tape speed varies with time for a constant mandrel speed. In the manufacture of thin circular rings, the amount of heat supplied remains almost constant for constant mandrel speed, whereas for the fabrication of non-axisymmetric rings, heat intensity can not be kept constant with the change in tape speed. In other words tape speed has to be maintained constant for the same heat intensity. Another complication in the fabrication of a non-circular ring is due to the fact that the contact point changes with the change in mandrel angular position. Sometimes the roller and mandrel get in the way of the laser beam. Because of these problems, a method is developed to determine the mandrel speed while maintaining a constant tape speed for non-axisymmetric convex mandrel shapes. The roller and mandrel are moved in such a way that the heating at the contact point is obtained without any interference from the roller and mandrel. To the author's knowledge, a study on the kinematics of thermoplastic tape winding and tape laying process for manufacturing complex thermoplastic composite parts is not yet available in the literature.

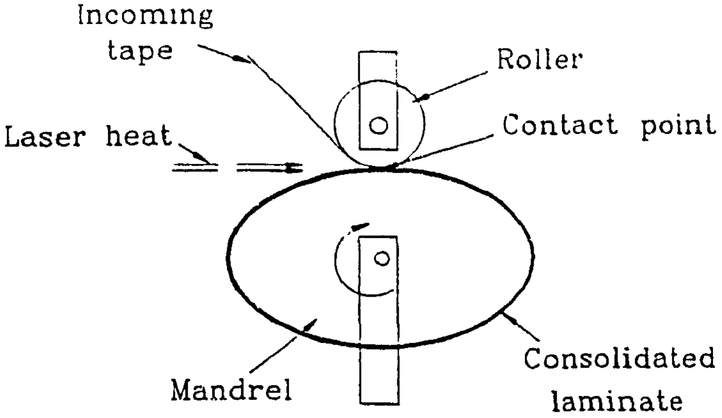

Fig. 6.1 Schematic diagram of the thermoplastic tape winding process for the manufacture of elliptical rings.

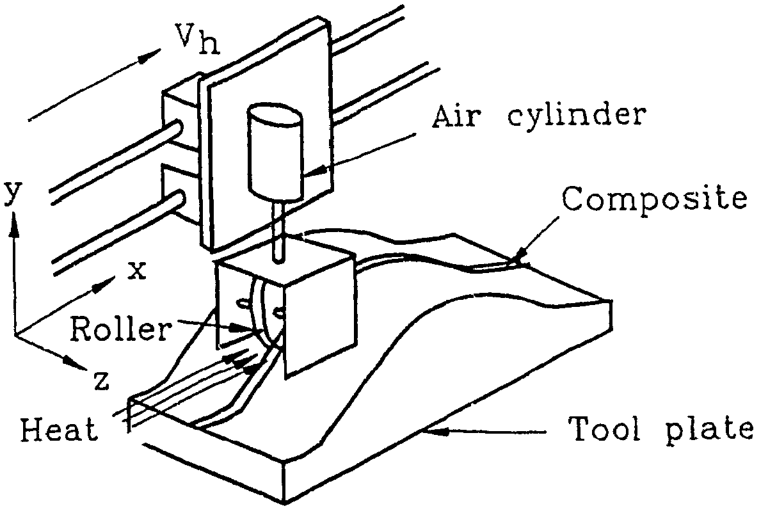

Fig. 6.2 Illustration of a tape laying process.

In conventional automobiles, steel coil springs in conjunction with shock absorbers are used as both front and rear suspensions A Vertical load on a coil spring creates torsional as well as direct shear stresses in the coil Although fiber reinforced plastic composites have higher energy storage capacities than steel, they have in general poor resistance to shear stresses Unidirectional fiber reinforced plastic composites have tensile and flexural strengths comparable to or higher than most common spring steels. Because of high strength to weight ratio, and higher tensile and flexural properties, springs comprising of elliptical rings can be used as a suspension system for automobiles [81]. Mallick [81,82] designed and developed elliptical springs for automobile suspension systems. Elliptical rings were manufactured by dry winding of 76.2 mm wide fiber reinforced epoxy tapes to various thicknesses over a collapsible elliptic mandrel Spring elements were removed from the mandrel after curing at 149°C for at least 14 hrs From the study it was found that the elliptic spring has potential of saving as much as 50% by weight in a typical automotive suspension system as compared to the steel coil spring [81,82] In this work a method for the manufacture of elliptical rings by the thermoplastic tape winding is presented.

The objective of this investigation is to address the problem concerning the fabrication of complex thermoplastic composite parts and presents a solution by performing kinematic study. A generalized formula is developed to determine the tape speed, and roller movement during the thermoplastic tape winding.

6.3 Kinematic Model for Thermoplastic Tape Winding

Understanding the kinematics of tape winding is important to determine the tape speed for various mandrel shapes. During the tape winding process, heat is supplied at the contact point to melt the incoming tape. For laser heating, the laser beam is kept stationary and, the roller and mandrel are moved in such a way that the contact point remains at the same horizontal plane. This is done because of the problem in moving the laser beam with the change in contact point as shown in Fig 6.3. It is clear from the figure that at certain positions of the elliptical mandrel, the mandrel and roller get in the way of the laser beam In order to be incident at the moving contact point, one way is to move the laser beam up and down Change in the direction of the laser beam for the present instance can not be achieved only by using a tilting mirror The mirror has to move up, down and tilt in order to direct the laser beam at the desired location To avoid the problems associated with the alignment and movement of the laser beam, it was decided that the laser remain fixed and the roller and mandrel will move in such a way that the contact point remains at the same horizontal plane as shown in Fig 6 4 Different positions of the roller and the mandrel are determined by performing a kinematic study For this study, the roller is replaced by a flat plate without any loss of generality As outlined in Fig 6.5 the contact point between the mandrel and a flat plate determines the position of the roller for different mandrel positions Determination of the tape speed and contact point positions for any convex mandrel shape is done as follows

Let the mandrel profile be represented in polar co-ordinates by the radius r given as function of the polar angle Φ in the form,

$$r = F(\phi) \tag{6.1}$$

Angle Φ is measured counterclockwise from the x axis which is engraved in the mandrel. The driving angle θ is measured between the fixed x' axis and x axis. Now consider loop OPQRO, where the horizontal component is given by

$$d+e = r\cos(\theta+\phi) \tag{6.2}$$

and the vertical component is:

$$h = r\sin(\theta+\phi) \tag{6.3}$$

The angle υ between the radius vector and the outward normal vector at any point of the mandrel profile is given by [83],

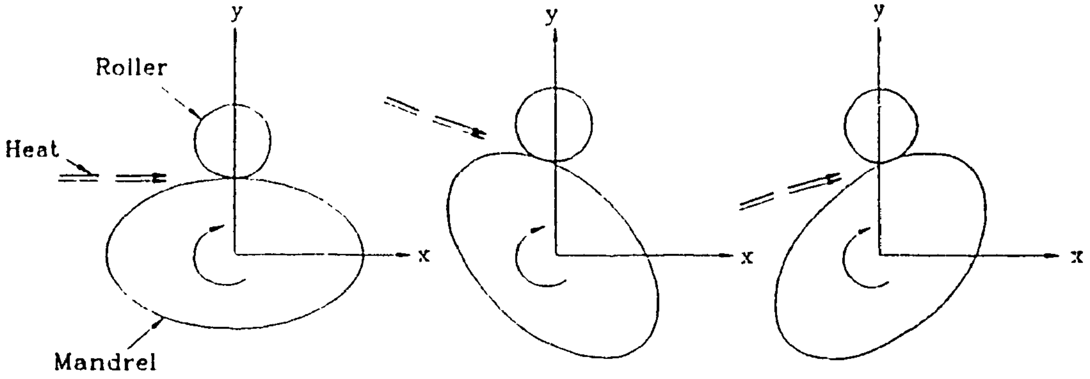

Fig 6 3 Mandrel and roller positions at different time of winding for the case when roller is free to move only along y axis

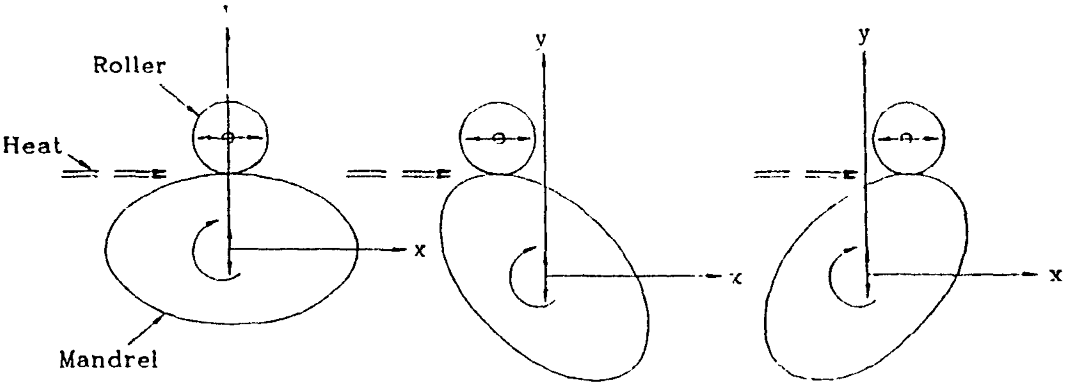

Fig. 6.4 Mandrel and roller positions at different time of winding for the case when laser heat source remains stationary.

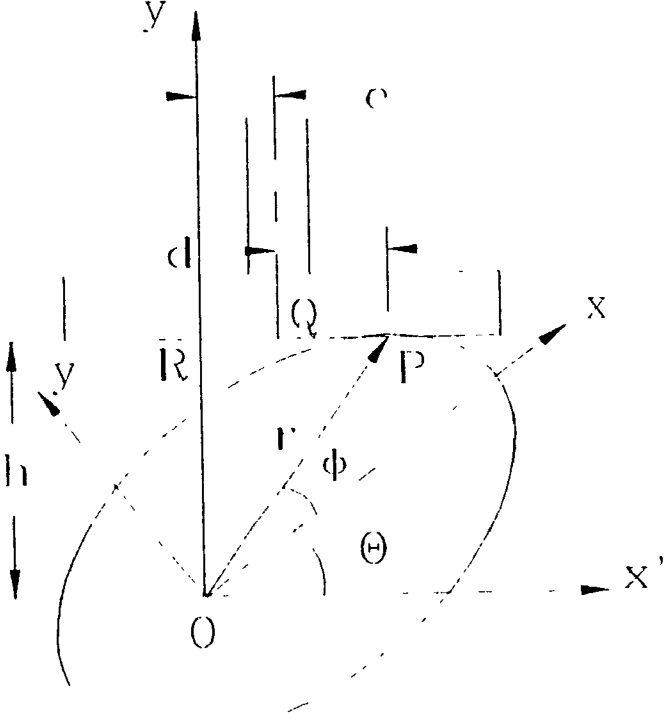

Fig. 6.5 Determination of roller position for a typical mandrel profile.

$$v = \tan^{-1}\left(-\sigma \frac{dF}{d\Phi}, \sigma F\right) \qquad (6.4)$$

where σ, the sign indicator, is defined by

$$\sigma = \begin{pmatrix} 1 \\ -1 \end{pmatrix} \quad if \ \frac{d\Phi}{ds} \begin{pmatrix} \geq 0 \\ < 0 \end{pmatrix} \qquad (6.5)$$

and s represents the oriented arc length on the mandrel profile.

From triangle OPR,

$$\theta + \phi + v = \pi/2 \qquad (6.6)$$

For any value of Φ, υ is determined by equation 6.4 and then θ is determined by equation 6.6. The value of h is determined by equation 6.3 and value of d is determined by equation 6.2. For the case when e=0, roller position (d) from y axis is determined by,

$$d = r\cos(\theta + \phi) \qquad (6.7)$$

6.4 Calculation of Mandrel Speed for a Constant Tape Speed

For a consistent bonding between the two layers, the heat intensity should be uniform. This is assured by keeping the tape speed constant. For non-circular rings, the tape speed varies for a constant mandrel speed. Tape speed V_t can be given by:

$$V_t = \frac{ds}{dt} \tag{6.8}$$

where ds is the arc length between two points of the mandrel. For two close points on the mandrel profile, arc length can be given by [83]:

$$ds=\sqrt{dx^2 + dy^2} \tag{6.9}$$

$$ds=\sqrt{(x_2-x_1)^2+(y_2-y_1)^2} \tag{6.10}$$

where,

$x_1 = r_1 \cos \Phi_1$, $x_2 = r_2 \cos\Phi_2$, $y_1 = r_1 \sin\Phi_1$, $y_2 = r_2 \sin \Phi_2$

r_1 and r_2 are the radii for positions Φ_1 and Φ_2 respectively. For tape speed of V_t, $dt = ds/V_t$. dt is the time taken by the mandrel to reach to position Φ_2 from position Φ_1 .

For calculation purposes, small increments in Φ are given and corresponding values of the mandrel position θ are determined using Eq.6.6 as explained earlier. Mandrel speed, N, in revolutions per minute (rpm) for a tape speed of V_t in length/sec is calculated by:

$$N = \frac{\theta_2-\theta_1}{2\pi} \cdot \frac{60\,V_t}{ds} \tag{6.11}$$

Figure 6.6 shows the mandrel speed for a constant tape speed of 6 cm/sec for an elliptical mandrel with a semi-major axis of 7.8 cm and semi-minor axis of 3.9 cm. The effect of a constant mandrel speed (10 rpm) on the tape speed for the same elliptical mandrel is shown in the Fig.6.7. In both the cases the roller and mandrel move as shown in Fig.6.4. It is clear from Fig. 6.7 that the tape speed varies a lot during one cycle. Change in the tape speed may severely effect the quality of the bond between layers if proper control on heating is not maintained.

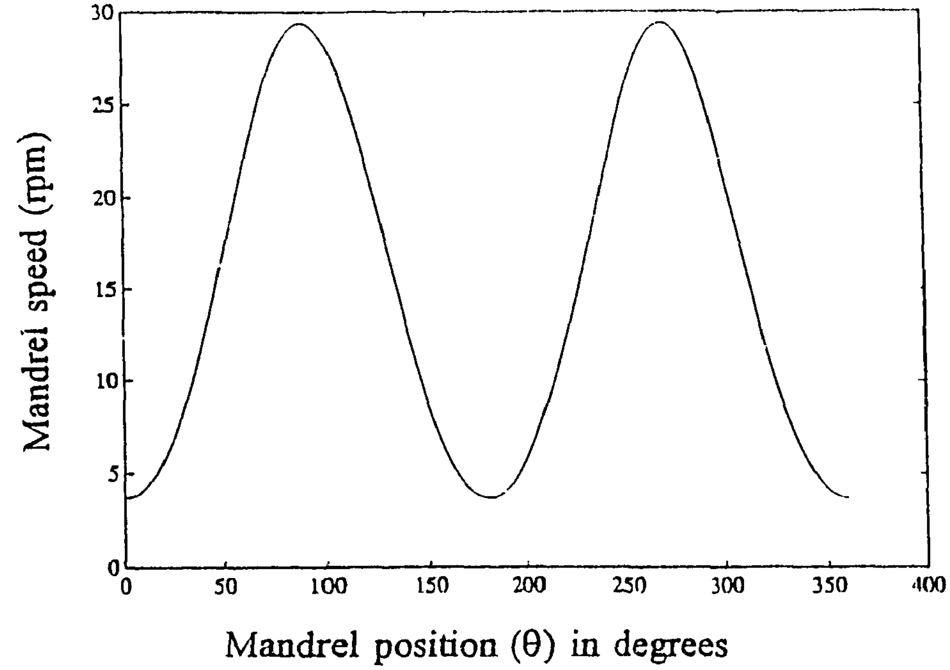

Fig. 6.6 Mandrel speed for a constant tape speed of 6 cm/sec for an elliptical mandrel having a semi-major axis of 7.8 cm and semi-minor axis of 3.9cm.

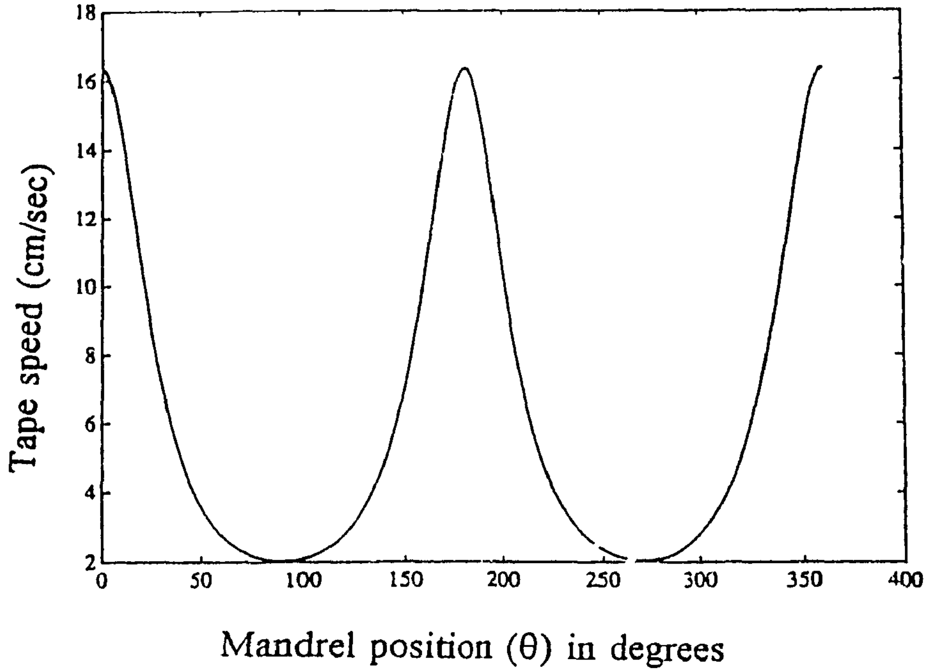

Fig. 6.7 Effect of constant mandrel speed (10 rpm) on tape speed for an elliptical mandrel having a semi-major axis of 7.8 cm and semi-minor axis of 3.9cm.

6.5 Kinematic Model for Thermoplastic Tape Laying

In the thermoplastic tape laying process or fiber placement process [84], tapes containing a matrix-fiber mixture are laid on the predetermined surface of the tool and required processing temperatures and pressures are applied continuously as the tape is being laid down. The amount of heat supplied for better consolidation depends upon the tape speed as well as tape and tool material properties. A moveable head, consisting of heaters, coolers, and rollers is mounted above the tool plate as shown in Fig. 6.2. The heaters and coolers heat or cool the composite from above, while the rollers apply a known amount of force P to the plate.

Assume that the head moves at a constant speed V_h along the x direction and the roller moves along the x direction as well as along y direction depending upon the shape of the tool (Figs. 6.2 and 6.8). The z direction is along the width of the tape as shown in Fig. 6.2. The roller moves up and down (along y direction) because of the consolidation force applied by an air cylinder.

Let the desired shape of the composite be defined by:

$$y = f(x) \qquad (6.14)$$

At any time t_1 , roller is in contact with the composite surface at the point (x_{1c}, y_{1c}) as shown in Fig.6.8. At that point, position (x_{1r} , y_{1r}) of the roller can be obtained by

$$x_{1r} = x_{1c} - r \, . \sin[\ \tan^{-1}(\frac{dy}{dx})_1] \qquad (6.15)$$

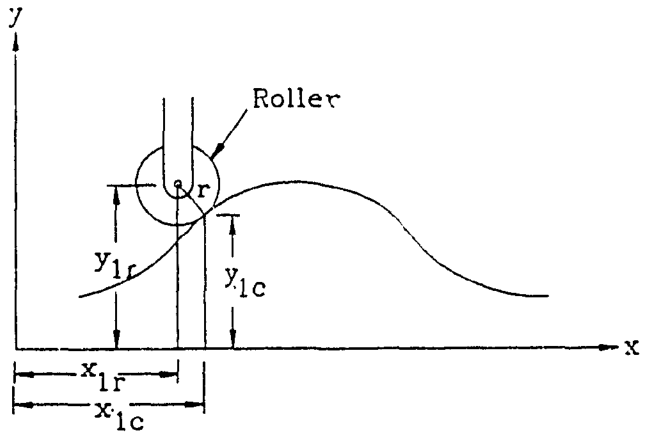

Fig. 6.8 Movement of a roller during tape laying operation.

$$y_{1r} = y_{1c} + r \cdot \cos\left[\tan^{-1}\left(\frac{dy}{dx}\right)_1\right] \tag{6.16}$$

where r is radius of the roller and $(dy/dx)_1$ is the slope of the composite surface at time t_1 To develop a relationship between the tape speed and head speed, a small increment dx_{1c} is given to x_{1c}. For the new position (x_{2c},y_{2c}), the roller position (x_{2r},y_{2r}) is determined in the similar manner as,

$$x_{2r} = x_{2c} - r \cdot \sin\left[\tan^{-1}\left(\frac{dy}{dx}\right)_2\right] \tag{6.17}$$

$$y_{2r} = y_{2c} + r \cdot \cos\left[\tan^{-1}\left(\frac{dy}{dx}\right)_2\right] \tag{6.18}$$

Value of y_{2c} is calculated by Eq. 6.14. The tape speed V_t for a small increment dx_{1c} can be given by:

$$V_t = \frac{\sqrt{(x_{2c}-x_{1c})^2 + (y_{2c}-y_{1c})^2}}{dt} \tag{6.19}$$

where dt is the time required to reach to point (x_{2c},y_{2c}) from (x_{1c},y_{1c}). Speed of the head which moves along the x direction is given by:

$$V_h = \frac{x_{2r} - x_{1r}}{dt} \tag{6.20}$$

Replacing the value of dt from Equation 6.19,

$$V_h = \frac{x_{2r} - x_{1r}}{\sqrt{(x_{2c}-x_{1c})^2 + (y_{2c}-y_{1c})^2}} \cdot V_t \tag{6.21}$$

Above equation is used for determining the head speed for achieving a constant tape speed during the tape laying operation.

6.7 Experimental Set-up

A set up as shown in figure 6.9 was designed and developed for the manufacture of elliptical rings The movement of steel roller and steel mandrel is shown in Fig 6 4. The mandrel is rotated by a motor and is moved up and down using air pressure. The roller moves back and forth using a cam attached to the system. The cam profile is generated by performing a kinematic study. A controller was developed to vary the speed of the mandrel as required The controller was interfaced with the computer and a user friendly program was developed to generate the winding motion based on the current algorithm A 65 Watt CO_2 laser (MPB Technologies Inc) having a wave length of 10.6 μm was used for the experiment. The six millimeter diameter laser beam is directed by two mirrors to the contact point The circular laser beam size is converted to elliptical beam (having a semi-major axis of 3 6 mm and semi-minor axis of 1 mm at the contact point) by two coplanar lenses to get a more concentrated heat source at the contact point.

Validation of the kinematic model is done by performing experiments on an liptic mandrel with semi-major axis of 6 cm and semi-minor axis of 4.5 cm. Mandrel speeds (similar to Fig 6.6) are determined using the kinematic model for constant tape speeds of 1 cm/sec, 2 cm/sec, and 3 cm/sec. A thermoplastic tape was marked and scaled for the measurement of tape speeds. The mandrel was run at a speed determined by the kinematic model and the scaled tape was wound on the mandrel. The tape speed was measured during winding process and was found to give desired constant speed. Several elliptical rings having 10, 15 and 25 plies were successfully manufactured using the laser as a heat source (Fig.6.10). Rings were fabricated using Carbon/PEEK (APC-2) thermoplastic composites tape

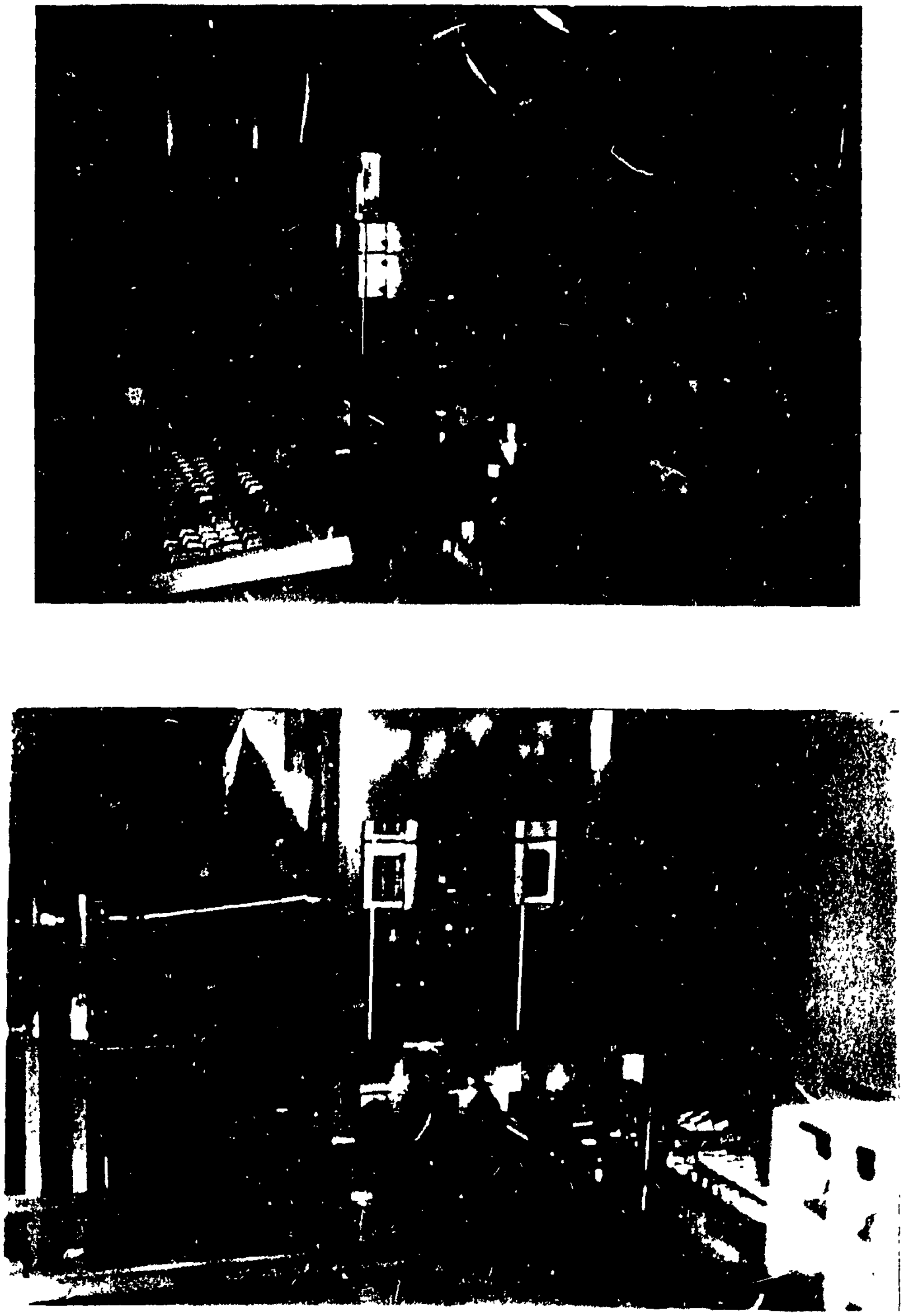

Fig. 6.9 Photographs from back and front of the experimental set up for the production of elliptical rings

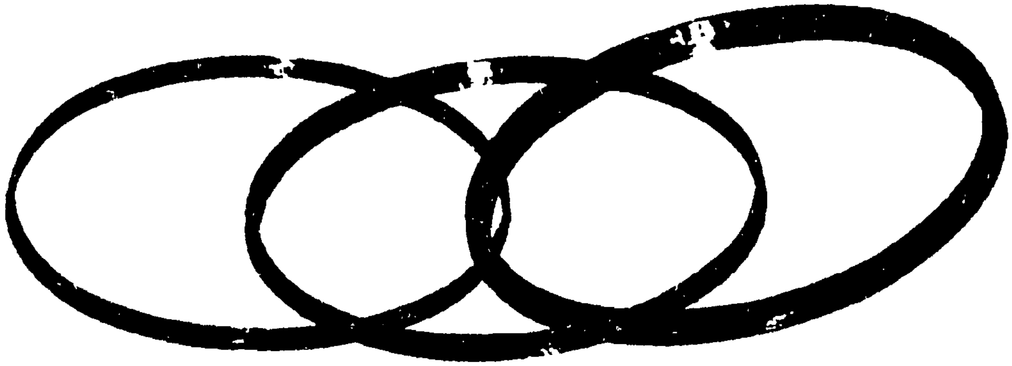

Fig. 6.10 Sample elliptical rings having 10, 15 and 25 plies.

6.8 Conclusions

Problems during the fabrication of non-circular shapes by thermoplastic tape winding and tape laying techniques are discussed and solutions are presented by developing kinematic models. Verification of the models was done by performing experiments on a mandrel with elliptic cross-section. A set-up was designed and developed for the production of elliptical rings using laser as a heat source

During the thermoplastic tape winding technique, heat and pressure are applied at the contact point to consolidate the laminate. Selection of heat intensity depends upon material properties as well as tape speeds. It is found from the kinematic study that the tape speed changes during winding process for non-axisymmetric shapes for a constant mandrel speed. The present study suggests that the maintenance of a constant tape speed during the fabrication of non-circular shapes is desired for an uniform bond quality Generalized formulae are presented for determining the machine motions for obtaining a constant tape speed during the tape winding and tape laying process.

PART II FILAMENT WINDING

CHAPTER 7

A KINEMATIC MODEL FOR FILAMENT WINDING OF NON-AXISYMMETRIC CYLINDRICAL MANDRELS

7.1 Summary

Filament winding technique has not been used to its overall capacity because of insufficient understanding of the kinematics of filament winding In order to effectively utilize the capability of the filament winding technique, a Geometric Approach, based on the algebraic and trigonometric relations is presented to determine the machine motions for generating desired fiber distribution on axisymmetric, non-axisymmetric, cylindrical, and non-cylindrical mandrel shapes

The analytical model thus developed is found to be extremely useful tools for laying down the fiber on a predetermined path in lieu of costly techniques such as teach in programming, simulation, CAD/CAM, etc. It is suggested that a sophisticated filament winding machine is not always necessary to fabricate complex structures A filament winding machine with two degrees of freedom can perform the same task on various types of mandrel surface with fewer driven parts, higher accuracy, and lower manufacturing cost. The method presents exact solution for determining the winding motions for mandrels, which have polygonal cross-sections

This chapter discusses the kinematic aspects of the filament winding for cylindrical mandrels having a smooth convex cross-section Determination of winding motions for cylindrical mandrels with polygonal cross-sections and non-cylindrical mandrels with axisymmetric and non-axisymmetric cross-sections are covered in chapters 8 and 9 respectively A method is proposed in this chapter to determine the motion of delivery point relative to the mandrel to ensure that the fiber laydown is of the predetermined path over the mandrel Experimental verification of the process is done on a cylindrical mandrel with an elliptic cross-section with a semi-major axis (a) of 77 98 mm (3 07") and semi-minor axis (b) of 39 98 mm (1 574") All the experiments are performed on a computer controlled filament winding machine having two degrees of freedom. Effects of location of the delivery point, mandrel geometry, and fiber winding angle on the delivery point motion are discussed

7.2 Introduction

Exact fiber placement generated by the filament winding makes the process suitable for the production of technically high quality composite components. The components which are currently in developmental stage often have a complicated geometry, and when such components are produced, the manufacturing process must guarantee the production of the desired winding path on the mandrel surface.

Exploitation of the filament winding technique has not been made properly because of insufficient knowledge about the kinematics of filament winding. Filament winding technique can be used for the fabrication of a variety of composite components but at present, use of filament winding is mostly limited to the manufacture of circular cylinder and axisymmetric shapes.

Figure 7.1 shows a schematic diagram of a two axis filament winding machine, in which the mandrel rotates at a constant speed and the delivery point moves back and forth for generating a desired fiber distribution on the mandrel surface The desired fiber trajectory is obtained by knowing the relative speeds of the mandrel and delivery point. Several techniques such as teach-in-programming [29], simulation [33], CAD/CAM [38,39], etc. are available for the determination of machine motions. These methods are described in detail in chapter 1. In all these methods, either velocities of the mandrel and delivery point are determined, or relative positions of the mandrel and delivery point are calculated. These values are then fed into the computer of a filament winding machine

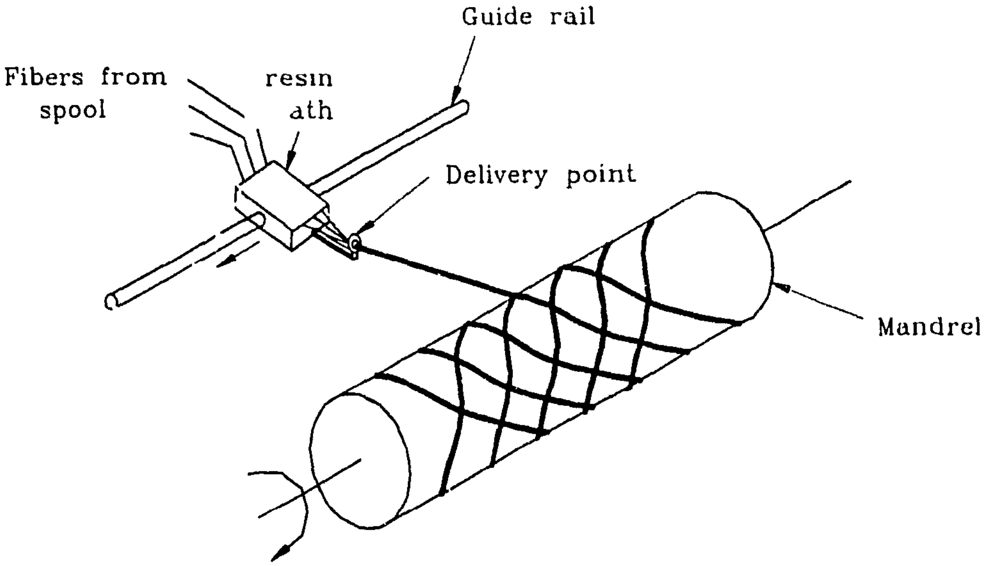

Fig. 7.1 Schematic diagram of a thermoset filament winding process.

to generate the desired motion Allard et al. [43] reported that the kinematics of filament winding on an elliptic cross-section is complex Kirberg et al [85] reported the use of CAD/CAM technique since the computation of control data would require much mathematical effort This thesis presents a Geometric Approach for the determination of machine motions In this approach, geometrical and trigonometrical relations are used to calculate the delivery point positions corresponding to the mandrel's angular positions for a given mandrel's geometry, fiber winding angle, and experimental set-up conditions. This method is very suitable for performing the kinematic analysis of winding motion for specific combinations of fiber winding angle, delivery point distance, etc The important aspect of Geometric Approach is that it determines the winding motion for a filament winding machine with only two-degrees-of-freedom Thus it is evident that the present technique can be applied to any filament winding machine since every filament winding machine has at least two-degrees-of-freedom Moreover, many filament winding industries have only two-axis machines. Therefore, the present approach can be useful for such industries for the manufacture of non-circular components

This chapter provides a solution for helical winding on non-axisymmetric cylindrical mandrels having any smooth convex cross section represented by $r = F(\phi)$, where first derivatives $dF/d\phi$ are continuous. The present method can not be used for the mandrels having rectangular, hexagonal or any polygonal cross-sections, where first derivative $dF/d\phi$ is not continuous. To solve such problems, a method has been proposed in chapter 8

7.3 Comparisons Between Thermoset and Thermoplastic Filament Winding

In the thermoset filament winding, thermoset resin (in liquid form) reinforced with the fiber is wound on the surface of the mandrel at the desired orientation (Fig.7.1), whereas in the thermoplastic filament winding, thermoplastic is supplied with the fiber in powder form such as in powder coated towpreg or in fiber form such as in commingled yarn. In the thermoplastic filament winding heat and pressure are applied at the contact point of the roller and madrel for melting and consolidation of thermoplastics (Fig 7 2) In the process, laydown, melting, and consolidation are obtained in a single step which thereby avoids curing stage which is necessary with thermosets Both techniques have their advantages and disadvantages. The thermoset filament winding requires less sophistication and the quality of consolidation achieved in a thermoset wound component is very high as compared to a thermoplastic wound component. In theromplastic filament winding, four advantages are apparent as compared to thermosets. First is the potential of non-geodesic winding and manufacture of concave surfaces by thermoplastic filament winding. The second advantage is the ability to post form the structure Filament wound sections can be remoulded in other ways. For example, a box section can be cut in half and reconsolidated to form an ' I ' beam [3]. The thermoplastic filament winding is a clean process The final advantage of thermoplastics is that there is no need for an autoclave. This feature, which compensates for the relatively slow winding speed, is particularly exploitable in the manufacture of very large structures that would otherwise require impossibly large autoclaves. An additional feature of large thick structures is that it may not be convenient to wind them all at one time. with thermoplastic materials an interruption in the process has no effect - there is no consideration of shelf life

7.4 Process Formulation

Figure 7.3 shows the cross-sectional view of the mandrel and fiber position at any driving angle θ for an arbitrary mandrel cross-section. Fiber CD is perpendicular to the longitudinal axis of the mandrel passing through point C The driving angle θ is measured between fixed X axis and an axis x engraved in the mandrel The fiber delivery point is located at point D at a distance d from mandrel's axis of rotation Let the profile of a mandrel's cross-section be represented in polar co-ordinate as,

$$r = F(\phi) \tag{7.1}$$

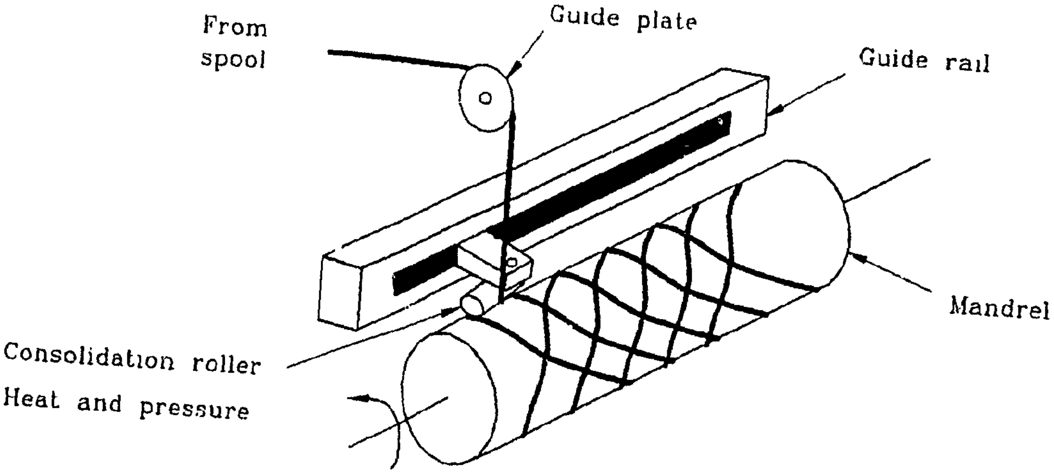

Fig. 7.2 Illustration of a thermoplastic filament winding.

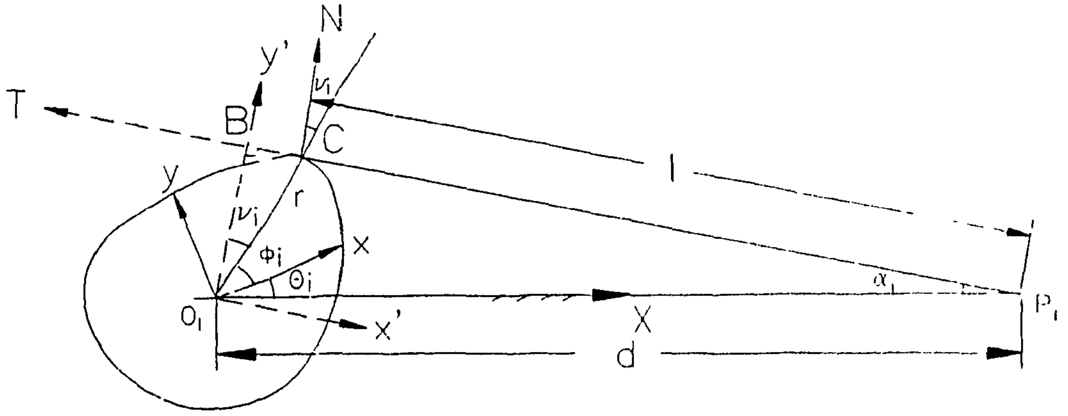

Fig. 7.3 Fiber and mandrel position at any arbitrary angle θ.

where r is the radius at any polar angle ϕ measured from the axis x as shown in the Fig 7 3

For determining the winding motion, first various geometric parameters, ν, α, l, θ corresponding to polar angle ϕ are calculated similar to the kinematic analysis of CAM with oscillating flat faced follower [86]. These terms are shown in Fig. 7.3 and defined later.

The angle ν between the radius vector and the outward normal vector at any point on the surface can be found by finding an expression for a unit tangent vector and unit normal vector.

Let T represent a unit tangent vector at point C, which moves in the direction of increasing arc length and traces out mandrel profile as shown in the Fig.7.3. The complex radius vector AC with respect to x axis can be represented by,

$$z = re^{i\phi} = F(\phi)\, e^{i\phi} \tag{7.2}$$

The unit tangent vector along the direction of T can be given by,

$$T = \frac{dz}{ds} = \frac{dz}{d\phi}\,\frac{d\phi}{ds}$$

or,

$$T = \left(\frac{dF}{d\phi} + iF\right) e^{i\phi}\,\frac{d\phi}{ds} \tag{7.3}$$

where s represents the oriented arc length on the mandrel profile. It is clear from Fig. 7.3 that fiber CD is always tangential to the mandrel profile at the point of contact (C) for properly tensioned fiber delivery system.

The outward unit normal (N) can be given by [86],

$$N = -iT$$

which using Eq.(7 3) yields,

$$N = (-i\frac{dF}{d\phi} + F)\, e^{i\phi} \frac{d\phi}{ds}$$

or,

$$N = e^{i\phi}(F\frac{d\phi}{ds} - i\frac{dF}{d\phi}\frac{d\phi}{ds}) \tag{7.4}$$

So magnitude of the angle which N makes with the x axis is given by

$$argN = \phi + \arctan_2 (-\frac{d\phi}{ds}\frac{dF}{d\phi}, \frac{d\phi}{ds} F) \tag{7.5}$$

or

$$argN = \phi + \arctan_2 (-\sigma \frac{dF}{d\phi}, \sigma F) \tag{7 6}$$

where σ is the sign indicator defined as,

$$\sigma = \begin{pmatrix} 1 \\ -1 \end{pmatrix} \quad if \quad \frac{d\phi}{ds}\begin{pmatrix} \geq 0 \\ < 0 \end{pmatrix} \tag{7.7}$$

From Fig.7.3 we can also see that

$$arg\ N = \phi + \nu \tag{7 8}$$

Thus on comparing Eq. (7.6) and Eq. (7.8),

$$\nu = \arctan_2 \left(-\sigma \frac{dF}{d\phi} , \sigma F \right) \qquad (7\ 9)$$

The instantaneous fiber length (l), and angle α which fiber makes with X axis can be found from following two loop equations for a loop ABCD. By taking components along moving axes (x',y'), where y' axis is normal to the fiber CD, we have,

$$r \sin\nu + l - d\cos\alpha = 0 \qquad (7.10)$$

$$r\cos\nu - d\sin\alpha = 0 \qquad (7.11)$$

so,

$$\sin\alpha = r\cos\nu \ / \ d \qquad (7.12)$$

and

$$l = d\cos\alpha - r\sin\nu \qquad (7.13)$$

Equations 7.12 and 7.13 can also be obtained by equating components along the fixed axes (X, Y).

Driving angle θ can be obtained from triangle ABD.

$$\theta + \phi + \nu = \pi/2 - \alpha$$

so,

$$\theta = \pi/2 - \alpha - \phi - \nu \qquad (7.14)$$

Above equations can be easily solved if we take ϕ as independent variable. For a fixed value of ϕ Eq.(7.1) gives r, Eq. (7.9) gives ν, Eq.(7.12) defines α, Eq.(7.13) defines l and Eq.(7.14) defines θ. Corresponding to this angular position (θ) of the mandrel, delivery point positions are determined for desired fiber winding angle and the procedure is explained in next section

7.5 Calculations of Delivery Point Positions for Helical Winding on Mandrel Surface

For calculation of relative positions of the mandrel and delivery point, the perimeter of the given cross-section is assumed to be made of n linear segments. Linear segments are made between polar angles (ϕ_1 ,ϕ_2), (ϕ_2 ,ϕ_3), (ϕ_3 ,ϕ_4), .. (ϕ_{n-1} ,ϕ_n) A linear segment i is defined by the segment on the perimeter between polar angles ϕ_i and ϕ_{i+1} . Then all the variables r_i , θ_i , l_i , v_i , α_i are calculated as stated above for each polar angle ϕ_i .

After determining the values of θ_i , l_i , v_i , α_i for various magnitudes of ϕ_i with stationary delivery point, the delivery point positions are calculated as follows for the desired fiber orientation (θ_f). Here the winding angle (θ_f) is measured from the transverse axis of the mandrel to the fiber direction as shown in Fig.7 4 for the sake of convenience. Thus the angle, the fiber makes with the longitudinal axis will be (90 - θ_f).

Calculations of delivery point positions are based on the principle that any smooth curve can be assumed as made of infinite number of linear segments. The smaller is the linear segment, the more accurate the result will be. Linear segment is selected because fiber just overlaps the segment i when mandrel reaches to θ_{i+1} from θ_i In between, fiber remains at the vertex of the side. With this assumption the perimeter of the cross section can be approximated with small error. For example perimeter of a circle of radius 3.07" (77.98 mm) can be found by dividing the perimeter into 720 equally distributed linear segments. The error on the length of the perimeter was found to be 0.0003% which can be considered as negligible.

Suppose initially the mandrel's reference axis x makes an angle θ_i from the fixed axis X as shown in Fig.7.4. In this position the fiber touches at point C_i , which is at

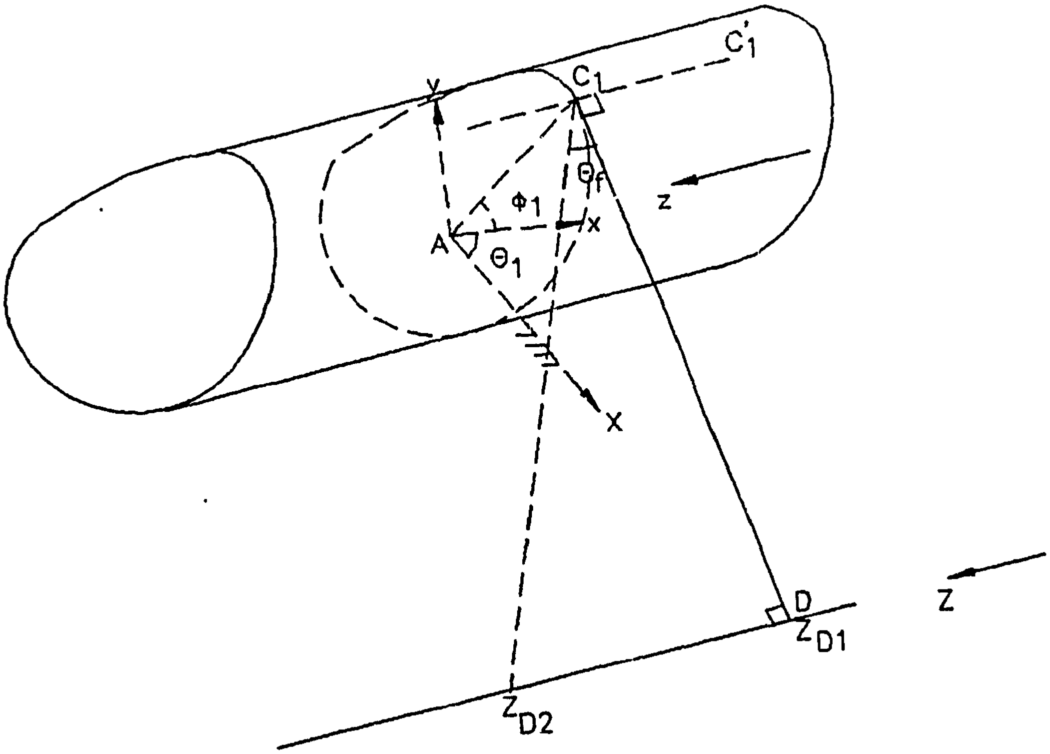

Fig. 7.4 Mandrel and delivery point position for a fiber winding angle of θ_f.

polar angle ϕ_i measured from the reference axis x. Fiber delivery point is at a generic point D which is at a distance of d from the mandrel axis of rotation At the beginning of winding, let the co-ordinate of the fiber delivery point be Z_{D1} Line C_1 D is perpendicular to the C_1 C_1' as shown in Fig.7 4 C_1 C_1' is a line parallel to the longitudinal axis of the mandrel. Let the co-ordinate of the point C_1 be (x_1 ,y_1 ,z_1) with respect to the mandrel's rotating axis (x,y,z), where,

$$x_1 = r_1\cos\phi_1 \ , \ \ y_1 = r_1\sin\phi_1 \ , \ \ z_1 = Z_{D1}$$

To make a fiber winding angle θ_f between points C_1 and C_2 , the fiber should be laid down making an angle of θ_f on the linear segment between polar angles ϕ_1 and ϕ_2 and that it should touch the mandrel at a point C_2 C_2 is the contact point between fiber and mandrel when the mandrel reaches to θ_2 corresponding to ϕ_2 . Co-ordinate of point C_2 is given by

$$x_2 = r_2\cos\phi_2 \ , \ y_2 = r_2\sin\phi_2 \ , \ z_2 = z_1 + ds_{12}\tan\theta_f \tag{7 15}$$

Where θ_f is the fiber winding angle and ds_{12} is the length of the linear segment between polar angle ϕ_1 and ϕ_2 given by,

$$ds_{12} = \sqrt{(x_2-x_1)^2 + (y_2-y_1)^2} \tag{7 16}$$

Correspondingly, delivery point should move to Z_{D2} during the time when mandrel reaches to next position θ_2 , such that,

$$Z_{D2} = (l_2+ds_{12})\tan\theta_f + Z_{D1}$$

or,

$$Z_{D2} = (l_2+ds_{12})\tan\theta_f + z_1 \tag{7.17}$$

where, l_2 is the fiber length C_2 D at position θ_2. D is a generic point on the delivery point axis such that C_1D is always perpendicular to the delivery axis as shown in Fig.

7.5. Through this reference line C_iD, fiber winding angle is measured. Various values of l_i corresponding to ϕ_i have already been calculated. l_i is the distance between the fiber delivery point (D) and the contact point C_i

Similarly, for another small increment in ϕ when the mandrel reaches θ_3 , the co-ordinate of fiber contact point C_3 should be such that.

$$x_3 = r_3\cos\phi_3 \ , \ y_3 = r_3\sin\phi_3 \ , \ z_3 = z_2 + ds_{23}\tan\theta_f \tag{7.18}$$

where,

$$ds_{23} = \sqrt{(x_3-x_2)^2 + (y_3-y_2)^2} \tag{7.19}$$

Correspondingly delivery point should reach to Z_{D3} such that

$$Z_{D3} = (l_3+ds_{23})\tan\theta_f + z_2 \tag{7.20}$$

In general, we can say that the fiber lies on the mandrel surface at a point C_i making an angle θ_f from transverse axis of the mandrel such that:

$$x_i = r_i\cos\phi_i \ , \ y_i = r_i\sin\phi_i \ , \ z_i = z_{i-1} + ds_{i-1,i}\tan\theta_f \tag{7.21}$$

where,

$$ds_{i-1,i} = \sqrt{(x_i-x_{i-1})^2 + (y_i-y_{i-1})^2} \tag{7.22}$$

Corresponding delivery point position should be such that,

$$Z_{Di} = (l_i+ds_{i-1,i})\tan\theta_f + z_{i-1} \tag{7.23}$$

Thus we can locate all the delivery point positions for complete revolution of the mandrel.

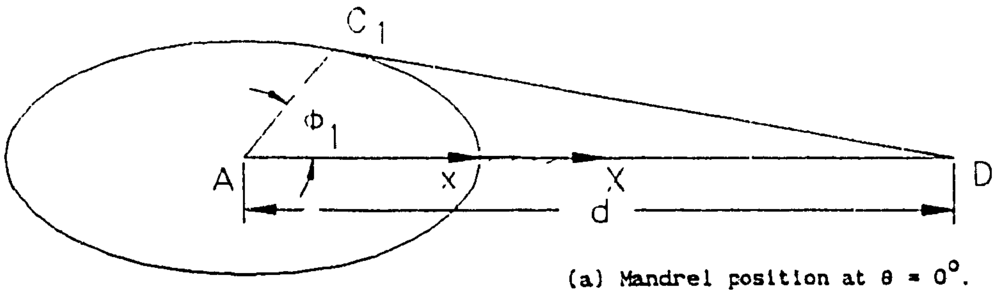

(a) Mandrel position at θ = 0°.

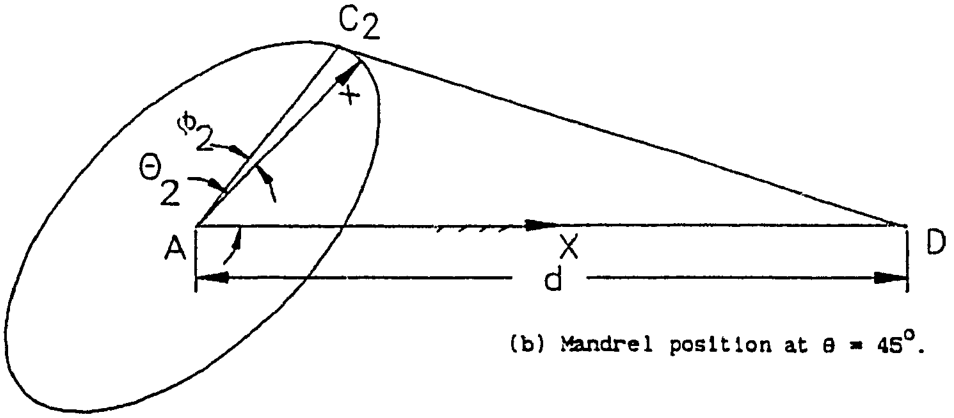

(b) Mandrel position at θ = 45°.

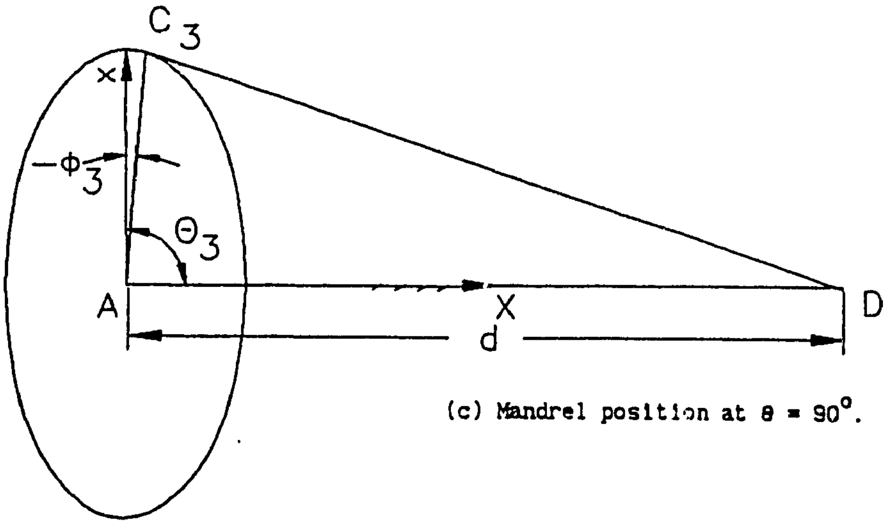

(c) Mandrel position at θ = 90°.

Fig. 7.5 Fiber positions at various mandrel positions: (a) θ=0°, (b) θ=45°; (c) θ=90°.

7.6 Delivery Point Velocity

Filament winding machines which have velocity feed back control, may require velocity of the delivery point and mandrel's rotational speed as input data for generating the desired fiber distribution. Once the co-ordinates of delivery point relative to mandrel's positions are known, delivery point velocity is calculated as follows.

Average velocity of the delivery point between any two points i and i+1 can be represented as follows,

$$V_{i,i+1} = \frac{Z_{Di+1} - Z_{Di}}{t_{i+1} - t_i} \tag{7.24}$$

where t represents the time.

Suppose the mandrel is rotating at a constant speed of N rpm. then,

$$V_{i,i+1} = 360.N.\frac{Z_{Di+1} - Z_{Di}}{\theta_{i+1} - \theta_i}$$

Substituting values of Z_{Di} and Z_{Di+1} from Eq.(7.23), gives

$$V_{i,i+1} = 360.N.(\frac{(l_{i+1} + ds_{i,i+1})\tan\theta_f + z_i - (l_i + ds_{i-1,i})\tan\theta_f - z_{i-1}}{\theta_{i+1} - \theta_i})$$

Upon substituting the value of z_i from Eq.(7.21), finally we get

$$V_{i,i+1} = 360.N.(\frac{(ds_{i,i+1} + l_{i+1} - l_i}{\theta_{i+1} - \theta_i})\tan\theta_f \tag{7.25}$$

So the average velocity between any segment is dependent on change in the fiber length (l_i), arc length of the segment ($ds_{i,i+1}$), fiber winding angle (θ_f) and the mandrel rotational speed (N).

For the case of a circular cylinder, the fiber length and arc length remain constant for equally spaced polar angle therefore the average velocity remains constant for the same fiber winding angle.

Thus for a circular cylinder,

$$V_{i,i+1} = 360.N.(\frac{ds_{i,i+1}}{\theta_{i+1} - \theta_i})\tan\theta_f \tag{7.26}$$

$$V_{i,i+1} = c.\tan\theta_f \tag{7.27}$$

where c is a constant. For the constant fiber winding angle,

$$V_{i,i+1} = c_1 \tag{7.28}$$

where c_1 is another constant.

7.7 Kinematics on an Elliptical Mandrel

The Geometric approach is applied to perform the kinematic analysis on various types of elliptical cross-sections with ellipticity e = 0.25, 0.51, 1.0 and a semi-major axis (a) of 3.07" (77.98 mm). Ellipticity e is defined as the ratio of a semi-major axis (a) and semi-minor axis (b) i.e. e=b/a. Figure 7.5 shows positions of the fiber contact point for various mandrel positions of an elliptic mandrel. It is clear from the figure that the point C_i varies with the mandrel rotation whereas for a circular cylinder, position of point C_i remains constant with respect to the fixed axis X.

Mandrel profile in terms of cartesian co-ordinate can be represented by,

$$\frac{x^2}{a^2} + \frac{y^2}{b^2} = 1 \qquad (7.29)$$

Replacing x = r cos ϕ , y = r sin ϕ the elliptical profile can be written in polar co-ordinate (r = F (ϕ)) as,

$$r = \frac{a \, . \, b}{\sqrt{b^2\cos^2\phi + a^2\sin^2\phi}} = F \qquad (7.30)$$

Angle ν between a radius vector and an outward normal vector at any point on the mandrel surface can be obtained from Eq.(7.9) as,

$$\nu = \arctan_2 \left(-\sigma \frac{dF}{d\phi} , \sigma F \right)$$

dF/dϕ for the present case will be,

$$\frac{dF}{d\phi} = -0.5a.b(a^2-b^2)\sin 2\phi \, [b^2\cos^2\phi + a^2\sin^2\phi]^{-3/2} \qquad (7.31)$$

For a particular value of ϕ, ν can be calculated using equations (7.30) and (7.31). Other variables such as α, l, and θ corresponding to ϕ is obtained using equations 7.12, 7.13, and 7.14 respectively. Delivery point positions corresponding to the mandrel rotation are calculated using equation 7.23. For performing the kinematic analysis on an elliptical mandrel, perimeter of the ellipse is divided into 1440 linear segments. Calculations of above parameters such as r_i , θ_i , l_i , ν_i , α_i , Z_{Di} are performed for ϕ = 0.0° , 0.25° , 0.5° , 0.75° , 1.0° ... and so on with an increment of 0.25°.

Variation of the polar angle (ϕ) relative to the mandrel rotation θ for e = 0.25, 0.51, 1.0 are given in Figs.7 6 and 7 7 for delivery point distances (d) of 29 72" (754 89 mm) and 11.81" (299 97 mm) respectively In the case of a circular mandrel i e e = 1 0, variation in polar angle is proportional to the variation in driving angle θ. For all mandrel shapes, semi-major axis is kept at 3.07" (77.98 mm).

Figure 7.8 shows variation of the fiber length (l) relative to the mandrel rotation for e = 0.25, 0.51, 1.0 and d = 29.72" (754.89 mm) and 11.81" (299 97 mm). For the case of circular mandrel (e=1), the fiber length (l) remains constant with the change in mandrel rotation.

Movement of the delivery point relative to the mandrel rotation for $\theta_i = 30°$ is plotted in Fig.7.9 for e=0.25, 0.51, 1.0 and d = 29.72" (754.89 mm) and 11.81" (299.97 mm). Corresponding velocity diagram is shown in Fig. 7 10. Fig.7 11 shows the velocity of delivery point for e=.51, d = 29.72" (754.89 mm) and for various fiber winding angles.

7.8 Experimental Verification

Experimental verification of the process is done on a cylindrical mandrel having an elliptical cross-section with a semi-major axis of 3.07" (77.98 mm) and semi-minor axis of 1.57" (39.98 mm). In the beginning of the experiment, the mandrel was kept at $\theta = 0.0°$ and the delivery point was kept such a way that the fiber direction was perpendicular to the longitudinal axis of the mandrel. The distance of delivery point from mandrel's axis of rotation was kept at 29.72" (754 89 mm). Calculations were made to find out the delivery point positions (Z_{Di}) for nearly one revolution of the mandrel with the increment of 0 25° in ϕ for various fiber winding angles θ_f as discussed earlier. Co-ordinates (θ_i ,Z_{Di}) are then transferred to the computer of the filament winding machine for generating required winding motions.

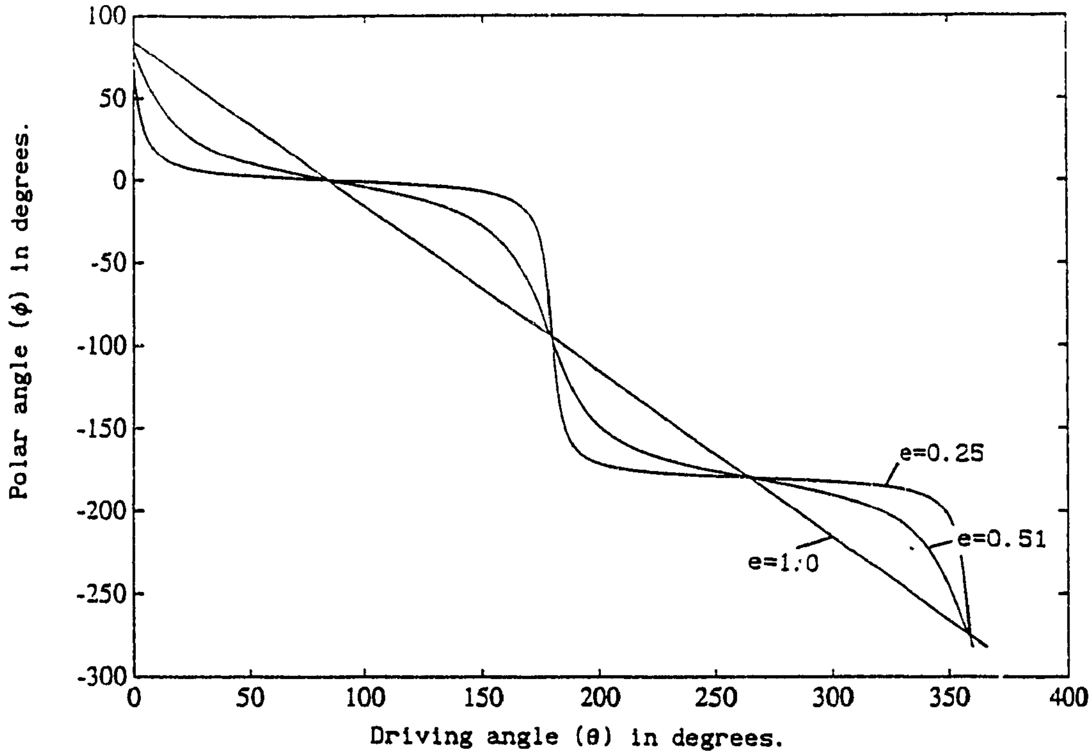

Fig. 7.6 Variation of polar angle (ϕ) relative to θ for e = 0.25, 0.51, 1.0, and d = 29.72".

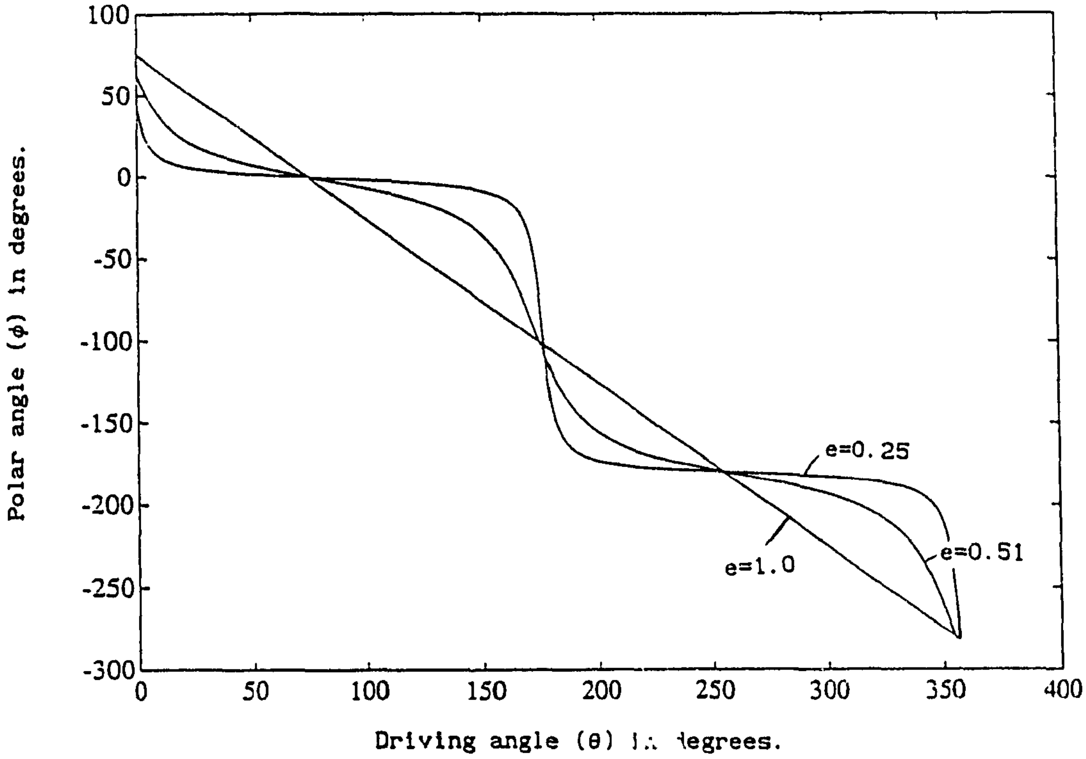

Fig. 7.7 Variation of polar angle (ϕ) relative to θ for e = 0.25, 0.51, 1.0, and d = 11.81".

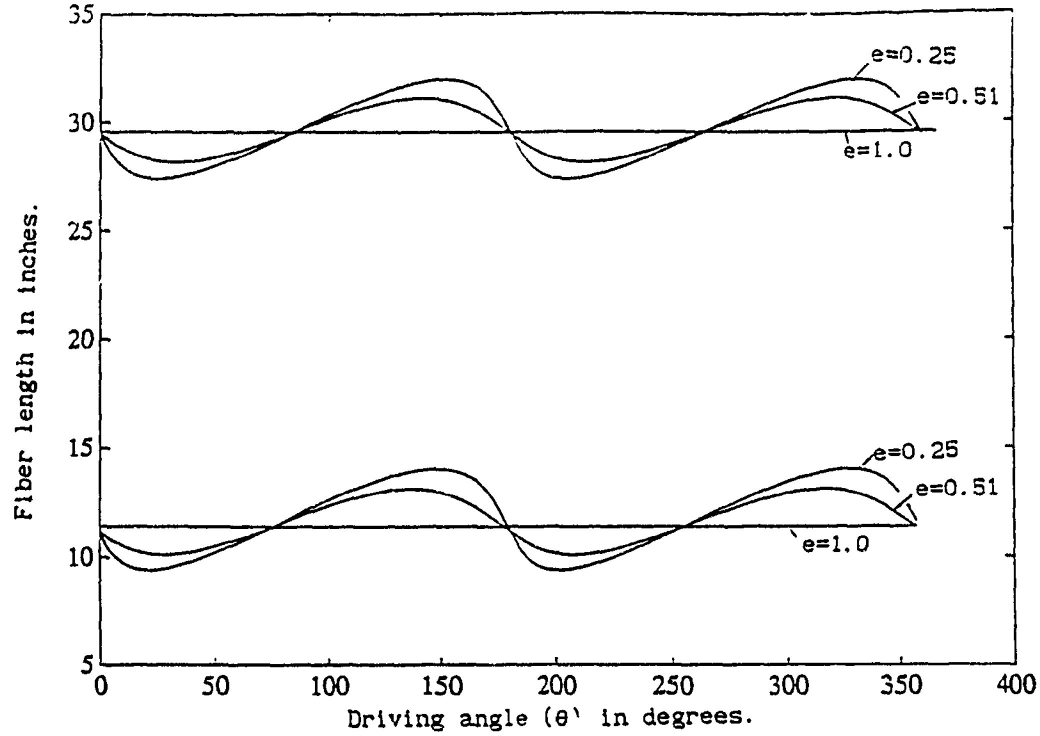

Fig. 7.8 Effect of delivery point distance on fiber length (l) for e = 0.25, 0.51 and 1.0.

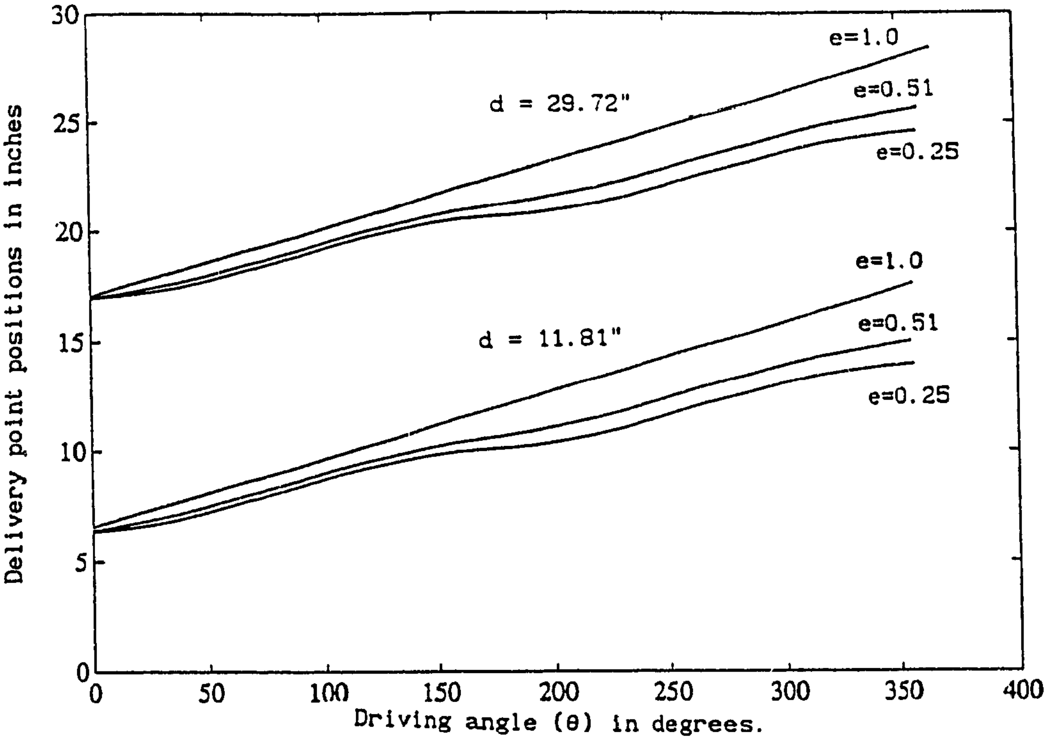

Fig. 7.9 Effect of delivery point distance on the movement of delivery point for e = 0.25, 0.51 and 1.0.

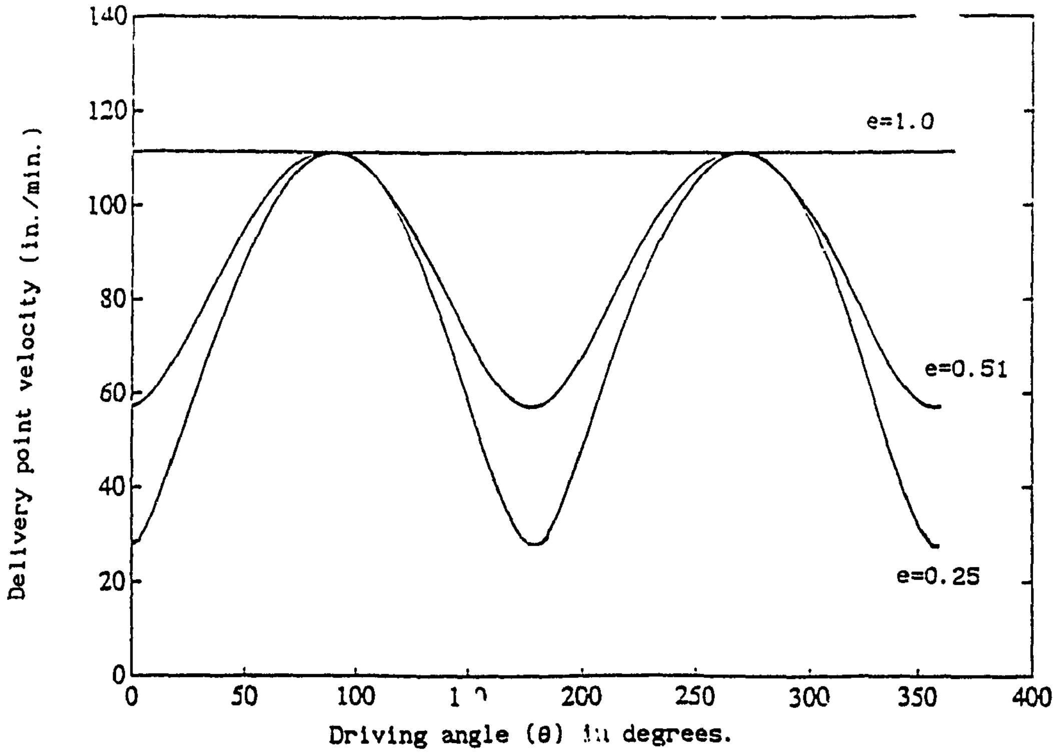

Fig. 7.10 Delivery point velocity relative to θ for e = 0.25, 0.51, 1.0, d = 29.72", θ_f= 30° and N = 10 rpm.

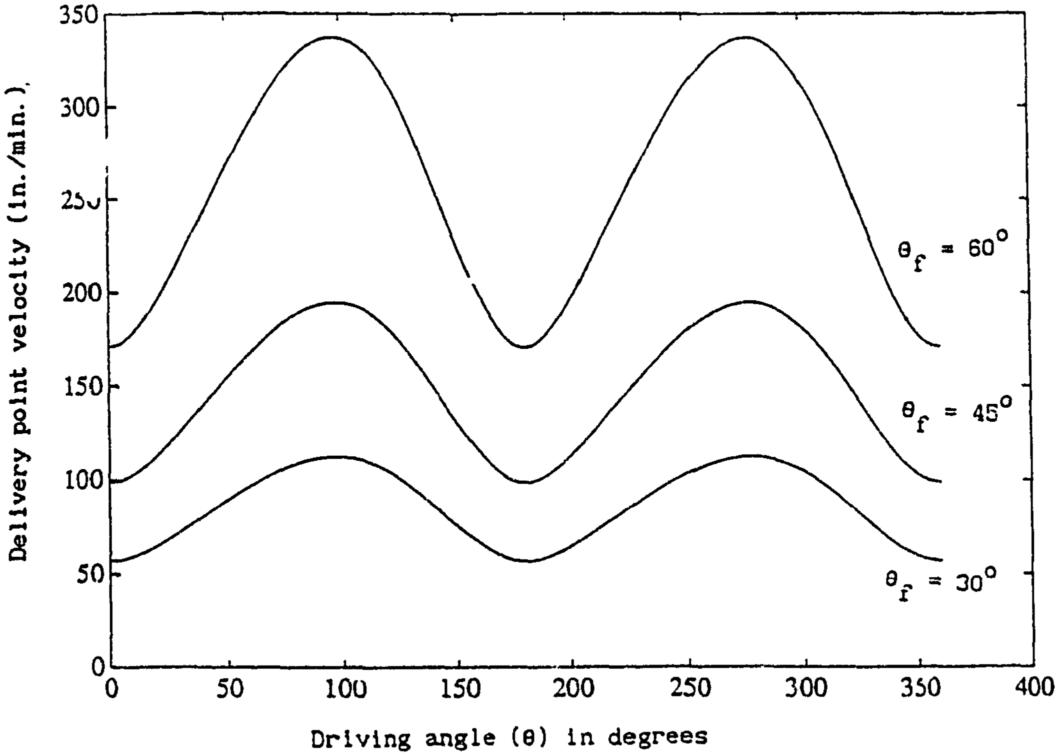

Fig. 7.11 Delivery point velocity relative to θ for e = 0.51, d = 29.72", N = 10 rpm, and θ_f= 30°, 45°, and 60°.

To measure the fiber winding angle on a mandrel surface, a sheet of paper was wrapped over the mandrel surface and then tests were performed to get the desired fiber winding angle (θ_f) of 30°. After the completion of winding, the fiber path was traced with a pen Paper was then unwrapped to measure the fiber winding angle The experimental value was found in the range of 29 7° - 30 3° in comparison to the desired fiber winding angle of 30°. The error (maximum of 1%) in getting desired θ_f may be due to errors in measuring the exact delivery point distance from the mandrel axis of rotation, truncation error during computations, etc.

It is obvious from Fig. 7.9 that the delivery point moves a significant distance to the get desired winding angle (θ_f) of 30° at the point of start and then it follows a smooth motion. During the experiment, delivery point was made to reach to Z_{D2} first and then mandrel and delivery point moved simultaneously.

7.9 Effect of Various Parameters on Delivery Point Motion

7.9.1 Effect of mandrel geometry

Mandrel geometry affects the delivery point motion significantly. Fig.7.9 shows the trend of delivery point motions relative to the mandrel rotation for θ_f = 30° and for e = 0 25, 0.51, 1.0 keeping semi-major axis equal to 3.07" (77.98 mm) for all the cases. The figure shows the carriage motion for delivery point distances (d) of 29.72" (754.89 mm) and 11.81" (299 97 mm). Figure 7.9 is plotted assuming Z_{D1} = 0.0 mm. Fig.7.10 shows the average velocity of the delivery point relative to the mandrel position for a constant mandrel speed (N) of 10 rpm. Velocity during first segment is obviously very high and is not shown in the figure. It is clear from the Fig.7.10 that for a circular mandrel, velocity remains constant for a constant fiber winding angle.

7.9.2 Effect of fiber winding angle

With the increase in θ_f , the required velocity also increases. It is clear from Eq.

7.25 that for a given mandrel shape and given delivery point distance (d), $(ds_{i,i+1} + l_{i+1} - l_i) / (\theta_{i+1} - \theta_i)$ remains constant for a particular segment for various θ_f . So,

$$(V_{i,i+1})_{\theta_{f2}} - (V_{i,i+1})_{\theta_{f1}} = 360.N.(\frac{(ds_{i,i+1} + l_{i+1} - l_i)}{\theta_{i+1} - \theta_i}) \ (\tan\theta_{f2} - \tan\theta_{f1})$$

or,

$$(V_{i,i+1})_{\theta_{f2}} - (V_{i,i+1})_{\theta_{f1}} = k_{i,i+1}(\tan\theta_{f2} - \tan\theta_{f1}) \qquad (7.32)$$

where $k_{i,i+1}$ is equal to $[360.N.(ds_{i,i+1} + l_{i+1} - l_i)] / (\theta_{i+1} - \theta_i)$.

Velocity curves for θ_f = 30°, 45°, 60° and for e = 0.51 and d = 29.72" (754.89 mm) are shown in Fig. 7.11 for constant mandrel speed (N) of 10 rpm.

7.9.3 Effect of Location of the Delivery Point

Location of the delivery point axis with respect to mandrel's rotational axis can be changed either by orienting the delivery point axis as shown in Fig. 7.12 keeping the distance (d) constant, or by changing the distance (d) between both the axes. In practice, for the same 'd' , change in orientation is done for two reasons; in the first mandrel's axis of rotation is changed due to change in diameter of the cylinder e.g. mandrel's axis of rotation is moved upwards with the increase in radius of the cylinder. In another case, for safety or for increasing the floor space, carriage axis can be shifted from floor to the wall. In such cases, knowledge regarding the effect of orientation or delivery point distance can be helpful.

It is clear from Fig.7.12 and Eq.7.25 that by orienting the delivery point D by λ degrees as shown in Fig.7.12 b, same velocity trend is obtained as that for the case in Fig.7.12 a but after the mandrel has rotated by λ degrees. Equation 7.25 does not

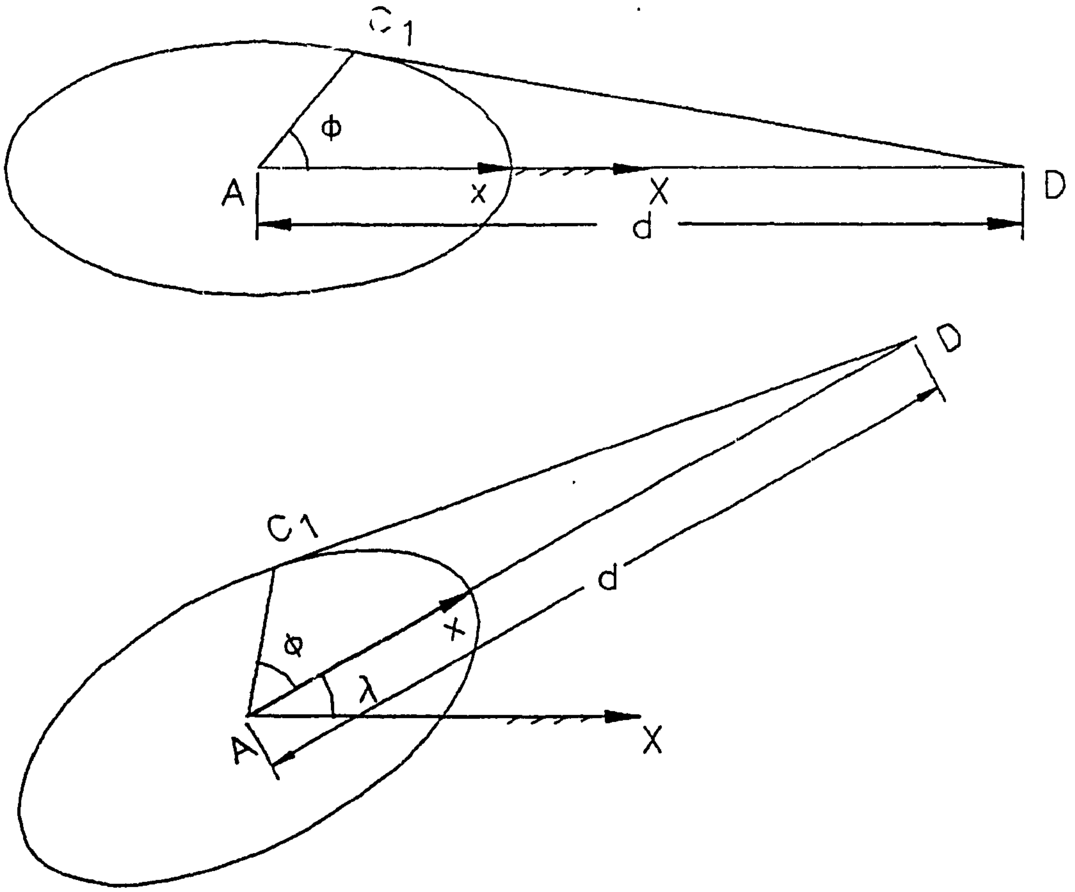

Fig. 7.12 Mandrel and fiber position at different delivery point locations.

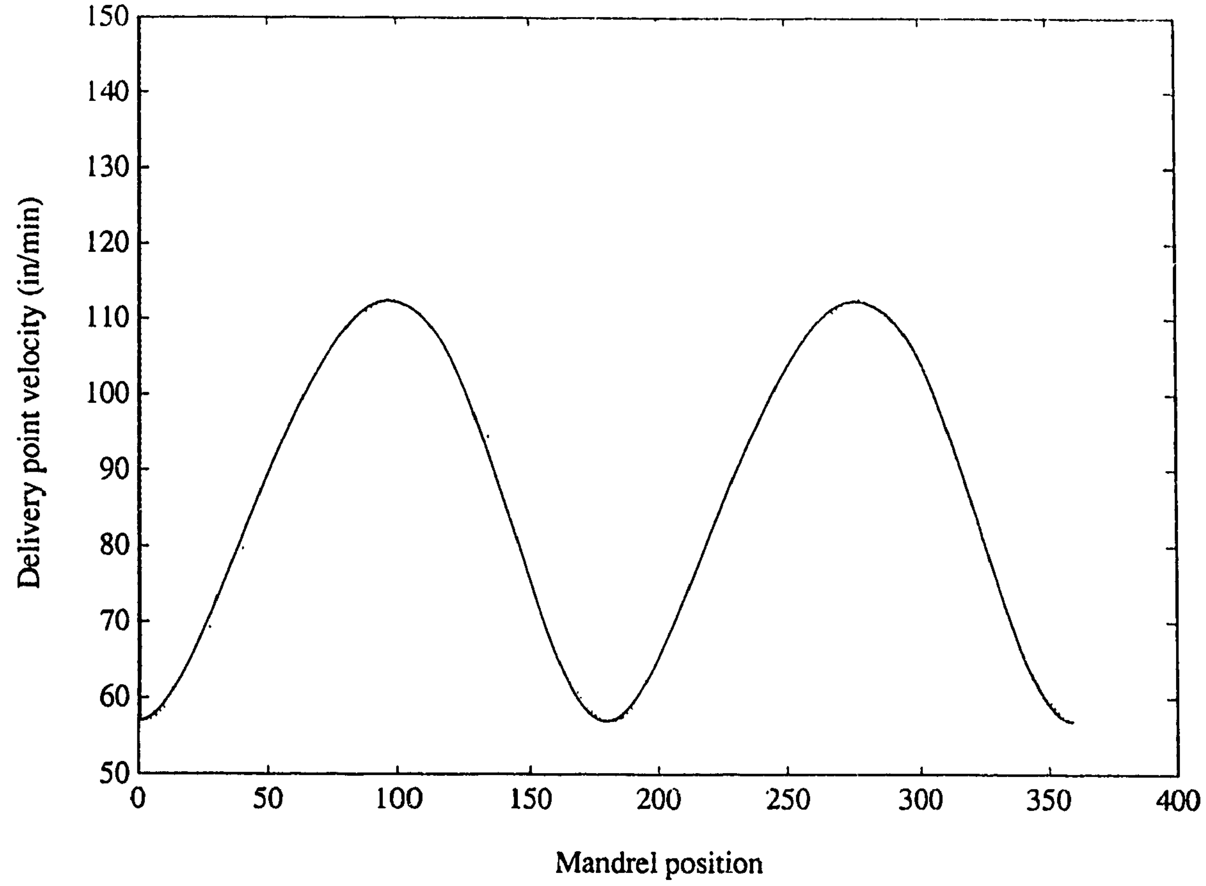

Fig. 7.13 Delivery point velocity relative to mandrel position for e = 0.51, d = 29.72" and 11.81", N = 10 rpm, and θ_f= 30°.

contain any term related to the carriage orientation angle λ. In above case delivery point was kept at the same distance d

With the change in delivery point distance d, the contact point of the fiber and mandrel changes for the same mandrel position. Fig. 7.9 shows the delivery point movements for d = 29 72" (754 89 mm) and 11.81" (299.97 mm). Fig. 7.13 shows the effect of the delivery point distance on the delivery point velocity.

7.10 Advantages of Geometric Approach

Geometric Approach presented in this chapter has the following advantages over other techniques.

(a) Teach-in-programming technique consumes lot of time and effort due to its trial and error method.

(b) Simulation technique and CAD/CAM technique are expensive. Sometimes these techniques require a sophisticated filament winding machine for generating the desired fiber winding angle distribution For filament winding machines with five or six degrees-of -freedom, the most difficult and time consuming part is to convert delivery point co-ordinates into five or six simultaneous axes of motion such that the net effect of motion of each degree of freedom should match with the desired movement of the delivery point location.

(c) Present technique is suitable for even simplest form of a filament winding machine, which has only 2 or 3 degrees of freedom. This reduces the cost of filament winding machine.

(d) Geometric Approach is very suitable in performing the kinematic analysis of filament winding i e effect of delivery point distance, mandrel speed, and other winding parameters on winding motion can be easily determined.

(e) Present approach determines the winding motion in a few seconds and thus reduces the overall manufacturing time.

(f) Cost of determining the winding motion is quite less in the present technique.

(g) Present technique avoids the complex movement of feed eye, and the winding motion obtained by the present technique is found to be smooth and collision free.

7.11 Conclusions

A Geometric Approach is presented for the determination of winding motions for generating desired fiber angle distributions on the surface of non-axisymmetric cylindrical mandrels. Based on the present algorithm, a computer code is developed for performing the kinematic analysis of filament winding. The study shows that a two-axis filament winding machine can laydown the fiber on a desired path on non-axisymmetric cylindrical mandrels.

CHAPTER 8

A KINEMATIC MODEL FOR FILAMENT WINDING OF CYLINDRICAL MANDRELS WITH POLYGONAL CROSS-SECTION

8.1 Summary

A Geometric Appraoach is presented to determine the winding motion for filament winding of non-axisymmetric cylindrical mandrels with convex polygonal cross-sections. Experimental verification of the process is done on mandrels having rectangular and hexagonal cross-sections. All the experiments are performed on a computer controlled filament winding machine having two-degrees-of-freedom. Effects of location of the delivery point, mandrel geometry, and eccentricity in the rotational axis of the mandrel on machine motions are discussed.

8.2 Introduction

Fiber reinforced composite parts are gaining importance in highly stressed automobile and machine components such as drive shafts, cross-members, and robot arms. Most of these parts have complicated geometry without any rotational symmetry. As Kirberg et.al. [85] reported that the computation of control data for non-axially symmetrical component geometries would require much mathematical effort. The use of CAD/CAM systems to determine the control data for non-axisymmetric components was suggested [38,39].

A procedure to determine the control data for non-axisymmetric cylindrical mandrels with smooth convex cross-sections (represented by $r = F(\phi)$, where first derivatives $dF/d\phi$ are continuous) was discussed in Chapter 7. The method was successfully used to study the kinematics of filament winding on cylindrical mandrels with elliptical and circular cross-sections. It can not be used for mandrels with rectangular, hexagonal, or other polygonal cross-sections The functions describing the cross-section of these mandrels do not have continuous first derivatives.

The procedure discussed here is useful in determining the trajectory of delivery point for exact fiber placement on the non-axisymmetric cylindrical mandrels with convex polygonal cross-sections such as rectangular beams, pipes, etc. The procedure was experimentally verified for mandrels with rectangular and hexagonal cross-sections.

8.3 General Procedure

Based on the Geometric Approach, a model is proposed for kinematic analysis of a cylindrical mandrel with a convex polygonal cross section. The whole procedure is divided into following main parts.

* determination of the mandrel shape geometry,
* determination of the experimental set-up conditions such as finding the distance (d) of the delivery point axis from mandrel's rotational axis,
* calculation of delivery point positions for various mandrel positions for desired fiber orientations. These relative positions of the mandrel and delivery point are then transferred into the computer of a filament winding machine for generating required motion.

The complete procedure is performed in the following steps (an illustration of the process takes the example of a hexagonal cross-section as shown in Fig.8.1):

(1) Divide the cross-section into triangles as shown in Fig.8.1 by joining vertices of the triangles to the axis of rotation (O) of the mandrel. Vertices and sides are named as shown in Fig.8.1.

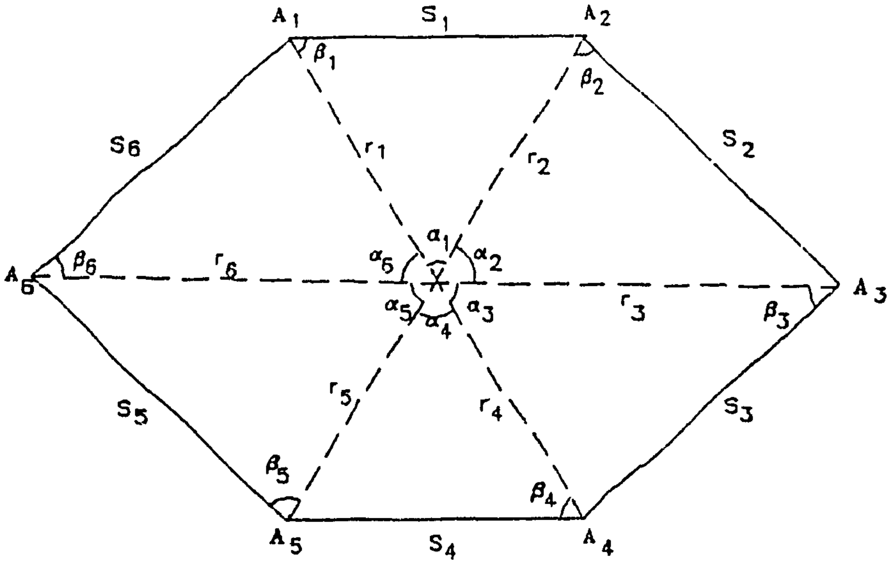

Fig. 8.1 Different geometric parameters on hexagonal cross-section.

(2) Determine the values of various parameters such as r_i , s_i , α_i , β_i from the mandrel geometry for each triangle as shown in Fig 8 1 where r_i is the distance of the vertex A_i from center O, s_i . is the length of side $A_i A_{i+1}$; α_i . is the angle made by line A_iO and A_{i+1} O at point O; and β_i is the angle made by side $A_i A_{i+1}$ with OA_i at point A_i . Once all the values of r_i and α_i are known then s_i and β_i are computed using cosine formula for a triangle.

(3) Measure d, the distance of delivery point (D) from the axis of rotation (O) of the mandrel, from the experimental set-up as shown in Fig.8.2. It is assumed that the delivery point axis and mandrel's axis of rotation are parallel, and the delivery point distance d is a constant. In general, for a two-axis filament winding machine, these two axes are parallel. At the beginning of the winding process, delivery point D is kept perpendicular to the longitudinal axis of the mandrel as shown in Fig 8.3

(4) Suppose at the beginning of the winding, the fiber is at vertex A_i Let a moving axis x is engraved in the mandrel which passes through point O and A_i as shown in Fig.8.2. Let at the beginning of the winding the mandrel's moving axis x is at $\theta = 0.0°$ as shown in Fig.8.2. From the experimental set up determine the angle ϕ which the moving axis x makes with line OD i e $\angle A_i$ OD.

(5) Find length A_iD for a triangle OA_iD as shown in Fig 8 4 using the law of cosine. Here A_iD is the distance between the vertex A_i and delivery point (D) at the time when fiber just overwraps the side $A_i A_{i+1}$. The above situation is determined when $\angle OA_iD$ is equal to β_i as shown in Fig.8.4. All A_i D values are obtained for the same delivery point position:

$$d^2 = A_iD^2 + r_i^2 - 2A_iDr_i\cos\beta_i$$

$$d^2 = r_i^2 + (A_iD - r_i\cos\beta_i)^2 + - (r_i\cos\beta_i)^2$$

$$A_iD = r_i\cos\beta_i + \sqrt{(r_i\cos\beta_i)^2 + (d^2 - r_i^2)} \qquad (8.1)$$

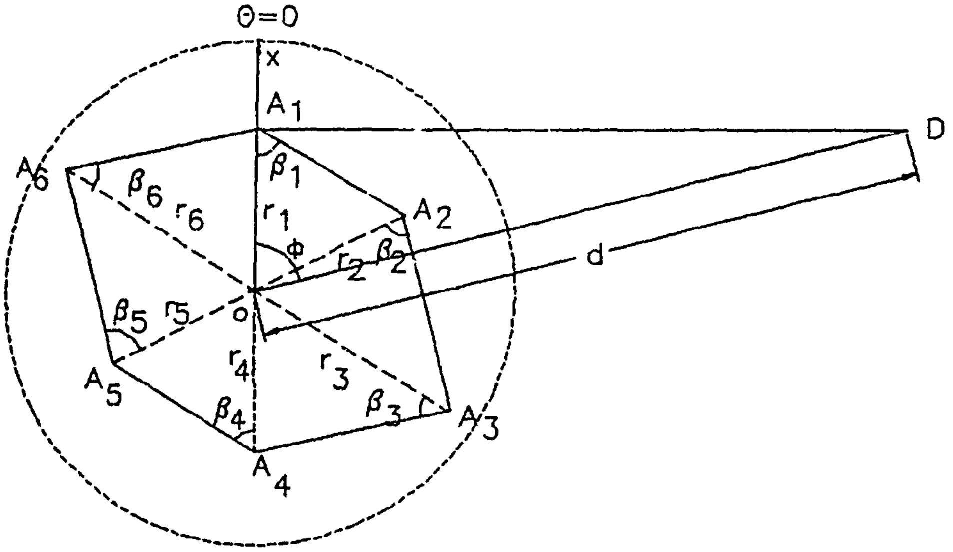

Fig. 8.2 Mandrel and fiber position at the beginning of winding.

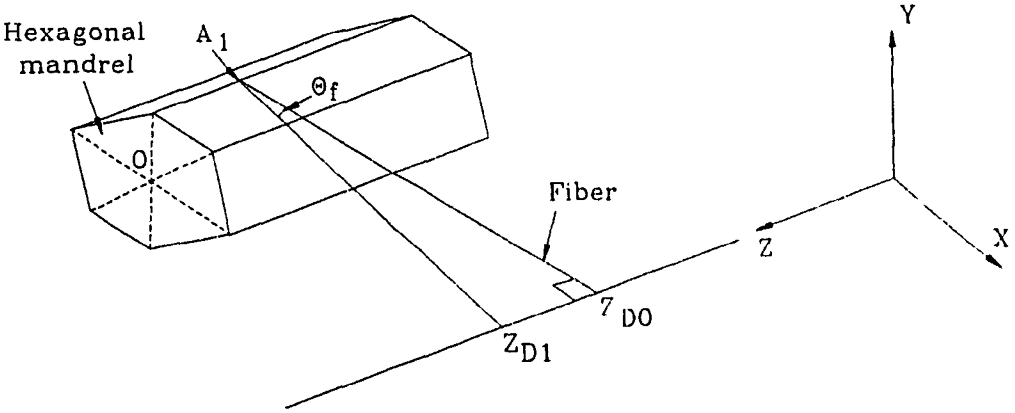

Fig. 8.3 Mandrel and delivery point positions.

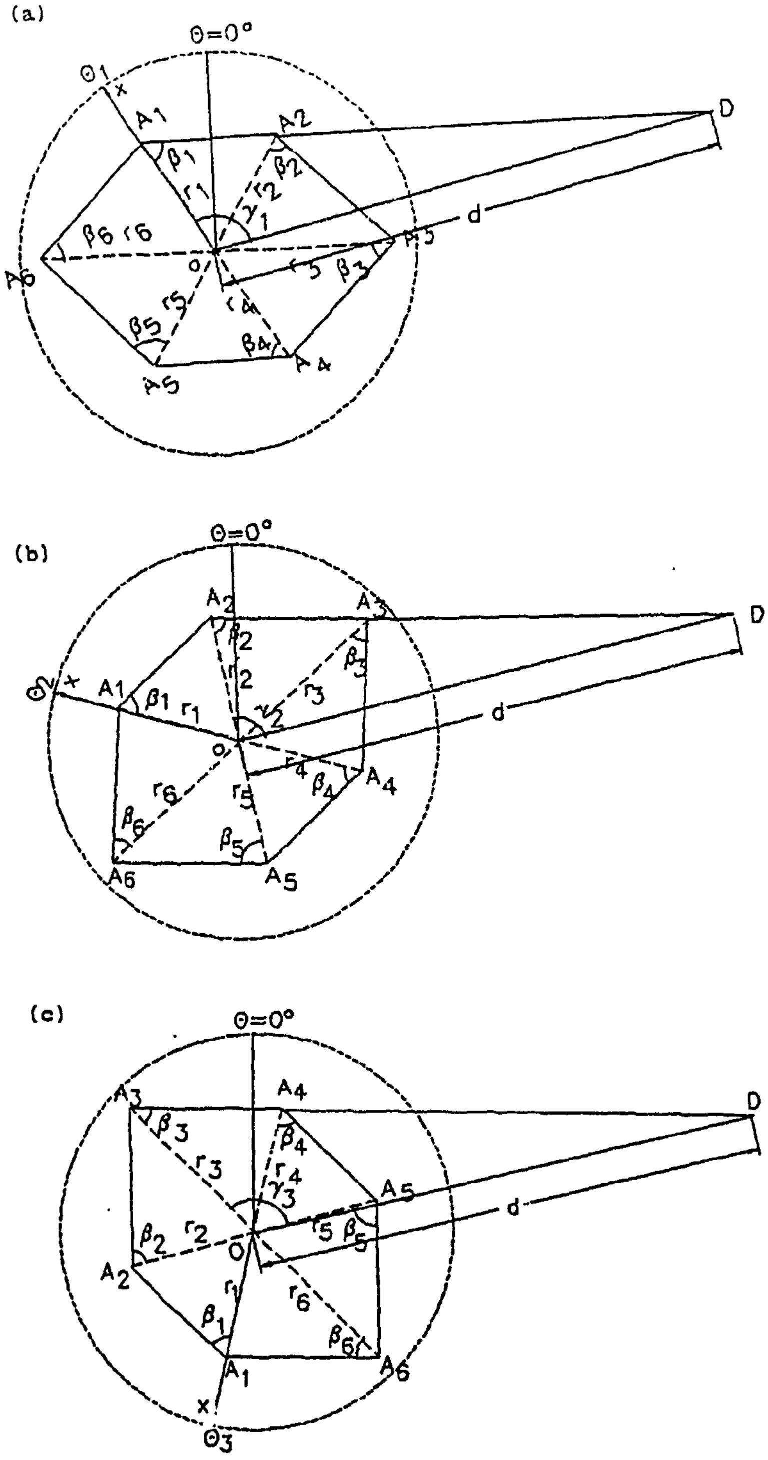

Fig. 8.4 Different mandrel positions at which the fiber just overwraps the side.

(6) Find angle γ_i i.e., $\angle A_i OD$ from the triangle OA_iD using the law of cosine γ_i is the angle when the fiber just overwraps the side $A_i A_{i+1}$ as shown in Fig.8.4.

$$A_iD^2 = r_i^2 + d^2 - 2.r_i.d.\cos\gamma_i$$

$$\cos\gamma_i = \frac{r_i^2 + d^2 - A_iD^2}{2.r_i.d} \tag{8.2}$$

(7) Determine various mandrel positions θ_i, for which fiber just overwraps side the A_iA_{i+1} as follows. Suppose at the beginning of the winding, mandrel position is as shown in Fig.8.2. The fiber overwraps the side $A_1 A_2$ when this side just coincides with the fiber A_1 D as shown in Fig.8.4a. This situation is obtained when the mandrel goes to position θ_1 (Fig. 8.4a). The value of θ_1 is calculated as follows,

$$\theta_1 = \gamma_1 - \phi \tag{8.3}$$

Similarly the side $A_2 A_3$ coincides with the fiber when mandrel reaches to θ_2 as shown in Fig.8.4b. The value of θ_2 is calculated as follows.

$$\theta_2 = \gamma_2 + \alpha_1 - \phi \tag{8 4}$$

Similarly the mandrel position θ_3 for side $A_3 A_4$ (Fig.8.4 c) is calculated as follows:

$$\theta_3 = \gamma_3 + \alpha_1 + \alpha_2 - \phi \tag{8.5}$$

In general, the mandrel position θ_i for side $A_i A_{i+1}$ is calculated as follows:

$$\theta_i = \gamma_i + \sum_{j=1}^{j=i-1} \alpha_j - \phi \quad (for\ i\geq 2) \tag{8.6}$$

Value of θ_1 is calculated from Eq.8.3.

(8) After determining various mandrel positions θ_i , for which fiber just overwraps the side $A_i A_{i+1}$, corresponding delivery point positions Z_{Di} for desired winding angle are determined as follows. For the sake of convenience, angle θ_f is measured from the transverse axis of the mandrel as shown in Fig.8.3. So the fiber winding angle from longitudinal axis of the mandrel will be $(90 - \theta_f)$. Suppose at the beginning of the winding, mandrel position is at $\theta_o = 0.0°$ and the delivery point position is at Z_{D0} (Fig.8.3). Z_{D0} is the position when fiber $A_1 D$ is perpendicular to the mandrel's longitudinal axis passing through point A_1 (Fig.8.3). For the side A_1A_2 to be overwrapped by the fiber with a winding angle of θ_f , the delivery point should reach to Z_{D1} , by the time mandrel reaches to θ_1 . The value of Z_{D1} is calculated as follows:

$$Z_{D1} = z_1 + A_1 D \tan\theta_f \tag{8.7}$$

where

$$z_1 = Z_{D0}$$

Similarly for side 2,

$$Z_{D2} = z_2 + A_2 D \tan\theta_f \tag{8.8}$$

where

$$z_2 = z_1 + s_1 \tan\theta_f \tag{8.9}$$

In general for side i,

$$Z_{Di} = z_i + A_i D \tan\theta_f \quad (for\ i \geq 1) \tag{8.10}$$

where

$$z_i = z_{i-1} + s_{i-1} \tan\theta_f \quad (for\ i \geq 2) \tag{8.11}$$

(9) These values of the mandrel and delivery point positions (θ_i ,Z_{Di}) are then fed into the computer controlled filament winding machine, in order to get desired fiber winding angle on the mandrel surface. Calculation of the delivery point positions for various mandrel shapes and delivery point locations are illustrated in the following example. Calculations are made for nearly one revolution of the mandrel. It is to be noted here that even the simple hand calculations without using a computer is sufficient to determine the winding motion. Thus present technique is cost-effective as compared to the teach-in-programming, CAD/CAM, simulation, etc.

8.3.1 Rectangular cross-section

The rectangular cross-section (Fig.8.5) used for the illustration has the following values for various parameters;

s_1 = 84.99 mm, s_2 = 140.00 mm, s_3 = 84.99 mm, s_4 = 140.00 mm,
r_1 = 81.89 mm = r_2 = r_3 = r_4
α_1 = 62.52° , α_2 = 117.48° , α_3 = α_1 = 62.52°, α_4 = α_2 = 117.48°
β_1 = 58.74° , β_2 = 31.26°, β_3 =58.74 , β_4 = 31.26°
and let θ_f = 30° .

The distance of the delivery point d from the mandrel's axis of rotation was kept at 754.89 mm. Values of A_1D, A_2D, A_3D, A_4D are found using Eq.8.1.

$$A_1D = r_1\cos\beta_1 + \sqrt{(r_1\cos\beta_1)^2 + (d^2 - r_1^2)}$$

A_1 D = 794.26 mm.

Similarly,

$$A_2D = r_2\cos\beta_2 + \sqrt{(r_2\cos\beta_2)^2 + (d^2 - r_2^2)}$$

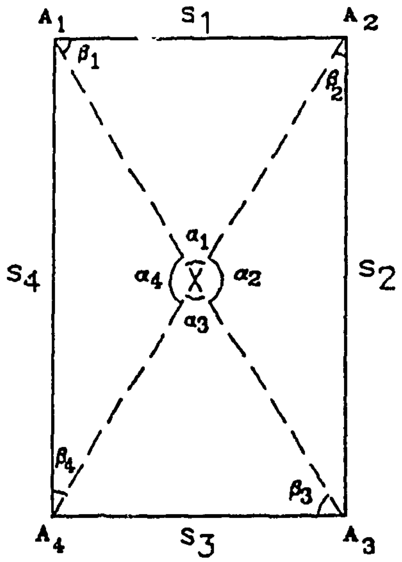

Fig. 8.5 Rectangular cross-section used for the experiment.

$A_2D = 823.80$ mm, $A_3D = 794.26$ mm, $A_4D = 823.80$ mm

Values of angle γ_i i.e., $\angle A_i OD$ are found using Eq.8 2.

$$\cos\gamma_i = \frac{r_i^2 + d^2 - A_iD^2}{2.r_i.d}$$

$\gamma_1 = 115.946°$. Similarly, $\gamma_2 = 145.508°$ $\gamma_3 = 115\,946°$ $\gamma_4 = 145\,508°$.

Suppose at the beginning of the experiment for the mandrel position of $\theta_o = 0.0°$, the moving axis x makes an angle of 60° from the line OD as shown in Fig.8 6. So $\phi = 60°$.

Values of θ_i for which a side $A_i A_{i+1}$ just gets overwrapped by fiber the was found using Eq.8.3 and Eq.8.6.

$$\theta_1 = \gamma_1 - \phi$$

$\theta_1 = 115.946° - 60° = 55.946°$

Similarly,

$$\theta_2 = \gamma_2 + \alpha_1 - \phi$$

Thus by calculation, $\theta_2 = 147.508°$, $\theta_3 = 235.946°$, $\theta_4 = 327.508°$

Delivery point positions Z_{D1} , Z_{D2} , Z_{D3} , Z_{D4} corresponding to θ_1 , θ_2 , θ_3 , θ_4 for desired fiber winding angle (θ_f) of 30° are calculated using Eq. 8.10 and Eq.8.11. Let at the beginning of the winding, fiber A_1D was kept perpendicular to the longitudinal axis of the mandrel passing through the point A_1 . At that time the delivery point position was at $Z_{D0} = 0.0$ mm. So $z_1 = 0.0$ mm.

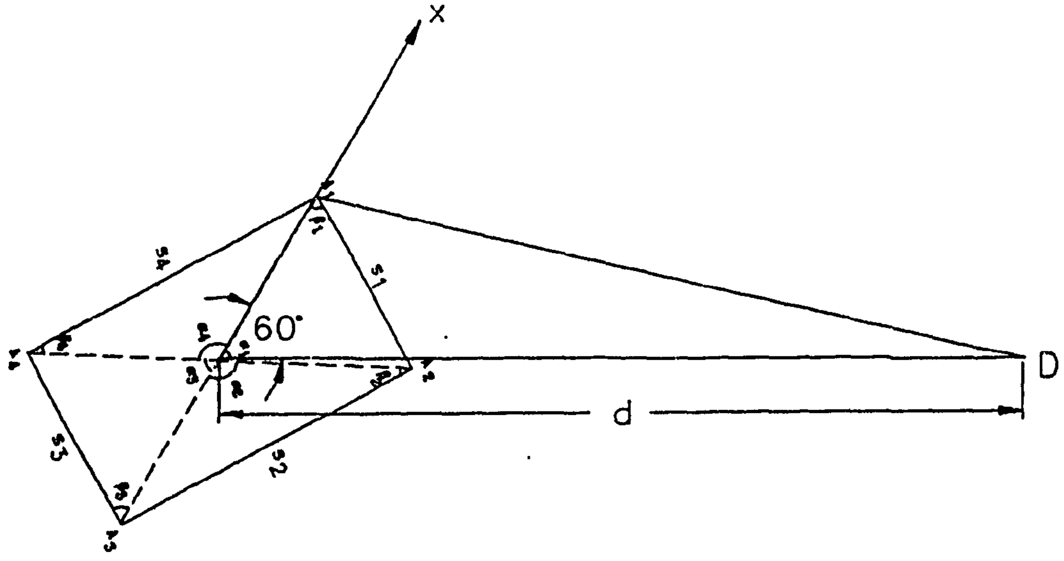

Fig. 8.6 Mandrel position at the beginning of winding.

$$Z_{D1} = z_1 + A_1 D \tan\theta_f$$

Z_{D1} = 0.0 + 794.23 tan 30

Z_{D1} = 458.55 mm

Similarly for side 2, $Z_{D2} = z_2 + A_2 D \tan\theta_f$,

where

$z_2 = z_1 + s_1 \tan\theta_f$,

So,

z_2 = 49.07, and Z_{D2} = 524 69mm.

Similarly, Z_{D3} = 588.44 mm, Z_{D4} = 654.56 mm

It is shown above that at time t = 0, the mandrel position was at θ_0 = 0.0° and delivery point position was at Z_{D0} = 0.0 mm. For the fiber winding angle of 30° on the side $A_1 A_2$, when the mandrel reaches to θ_1 = 55.946° , the delivery point should reach to Z_{D1} = 458.55 mm. Subsequently for the same fiber winding angle (θ_f) of 30° on the side 2, when the mandrel goes to θ_2 = 147.508° , delivery point should go to 524.69mm. Similarly for the side 3, points θ_3 and Z_{D3} , and for side 4 points θ_4 and Z_{D4} , should coincide. For further rotations of the mandrel, delivery point would follow the same trend as followed in the first one revolution of the mandrel. Values of Z_{Di} corresponding to θ_i are shown in Fig.8.7 for d = 754.89 mm and d = 119.99 mm. It is obvious that the path of the delivery point between two points Z_{Di} and Z_{Di+1} does not affect the fiber orientation.

8.3.2 Hexagonal cross-section

The hexagonal cross-section used for the experiment is shown in Fig. 8.1.

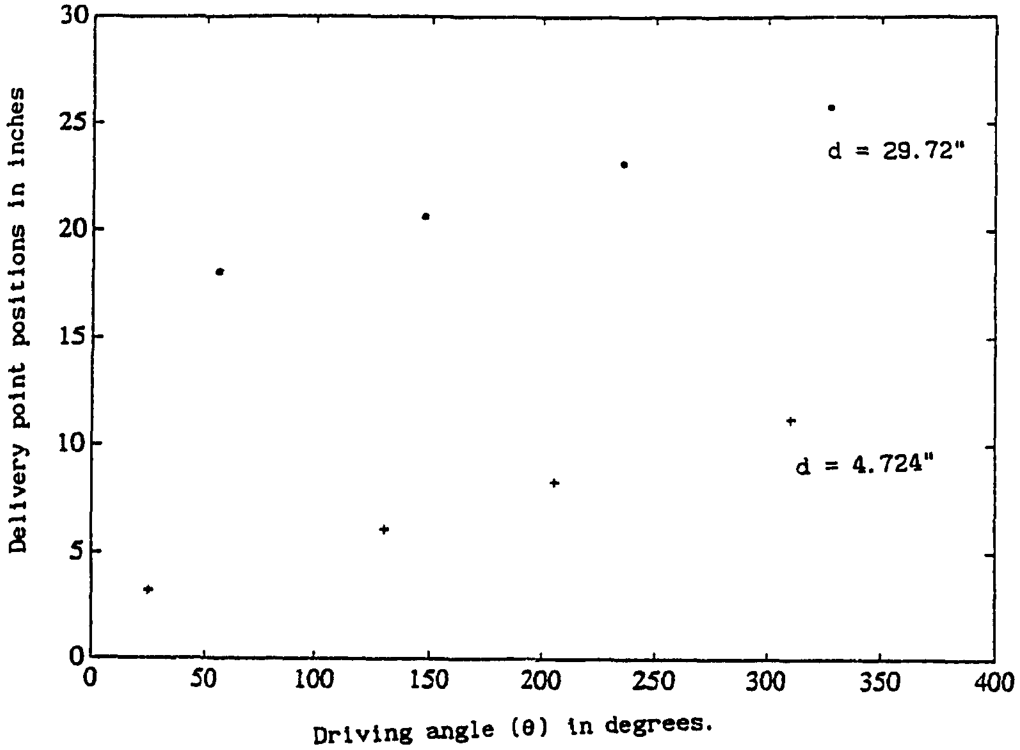

Fig. 8.7 Delivery point movements for rectangular cross-section at different values of d and $\theta_f = 30^\circ$.

Values of r_i and α_i for the cross-section are as follows.

$r_1 = 81.89$ mm, $r_2 = 81.89$ mm, $r_3 = 112.50$ mm
$r_4 = 81.89$ mm, $r_5 = 81.89$ mm, $r_6 = 109.47$ mm
$\alpha_1 = 62.52^\circ$ $\alpha_2 = 58.74^\circ$ $\alpha_3 = 58.74^\circ$
$\alpha_4 = 62.52^\circ$ $\alpha_5 = 58.74^\circ$ $\alpha_6 = 58.74^\circ$

Calculations of the mandrel and delivery point positions are done as discussed earlier. Various values of the delivery point positions Z_{Di} corresponding to θ_i are plotted in Fig.8.8 for d = 754.89 mm, $\theta_f = 15^\circ$.

8.3.3 Hexagonal Mandrel with Eccentricity

In this example, the same hexagonal mandrel shown in Fig.8.1 is used but with axis of rotation shifted to O_e as shown in Fig.8.9. In this case triangles are formed by joining vertices of the sides to the axis of rotation O_e . Values of r_i and α_i are as follows:

$r_1 = 27.69$ mm, $r_2 = 74.90$ mm, $r_3 = 148.28$ mm
$r_4 = 135.99$ mm, $r_5 = 116.79$ mm, $r_6 = 92.96$ mm
$\alpha_1 = 101.4^\circ$, $\alpha_2 = 38^\circ$, $\alpha_3 = 41.6^\circ$
$\alpha_4 = 38^\circ$, $\alpha_5 = 53^\circ$, $\alpha_6 = 88^\circ$

Calculation of the delivery points relative to the mandrel positions are done as discussed earlier. Various values of θ_i , Z_{Di} are plotted in Fig.8.8 for d = 754.89 mm, $\phi = 90^\circ$, and $\theta_f = 15^\circ$. It is clear from the Fig. 8.8 that the values of θ_i , Z_{Di} change with the change in axis of rotation.

8.3.4 Effect of Location of the Delivery Point

Experiments were performed on a rectangular mandrel with various of delivery point distances and orientations. It was found similar to the case discussed in

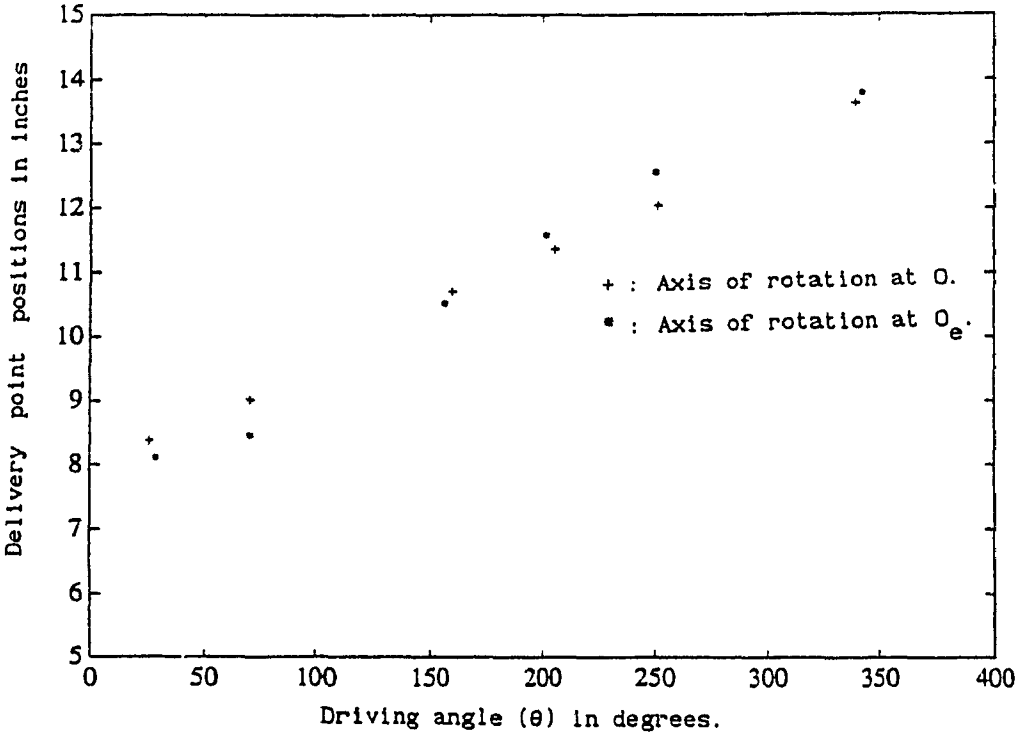

Fig. 8.8 Delivery point movements for hexagonal cross-section with different axis of rotation and $\theta_r = 15°$.

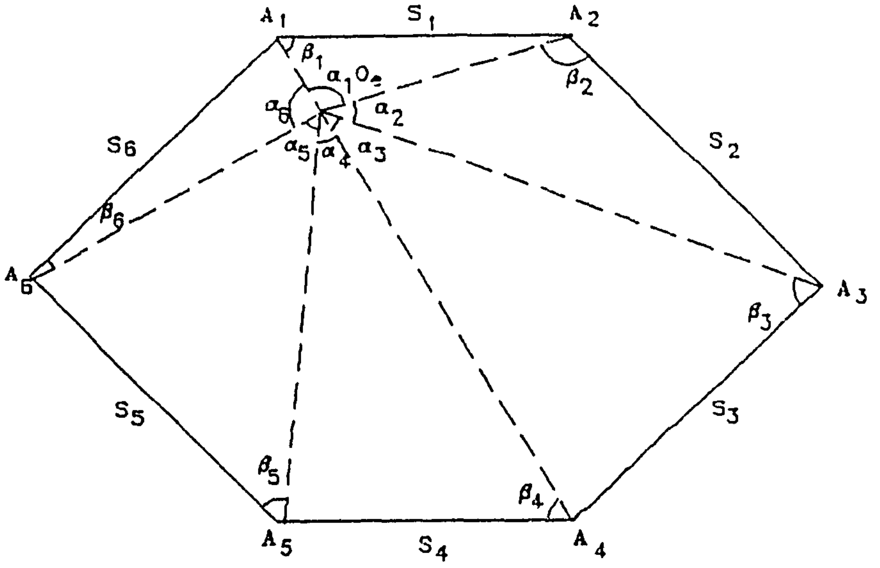

Fig. 8.9 Hexagonal cross-section with axis of rotation passing through point O_e.

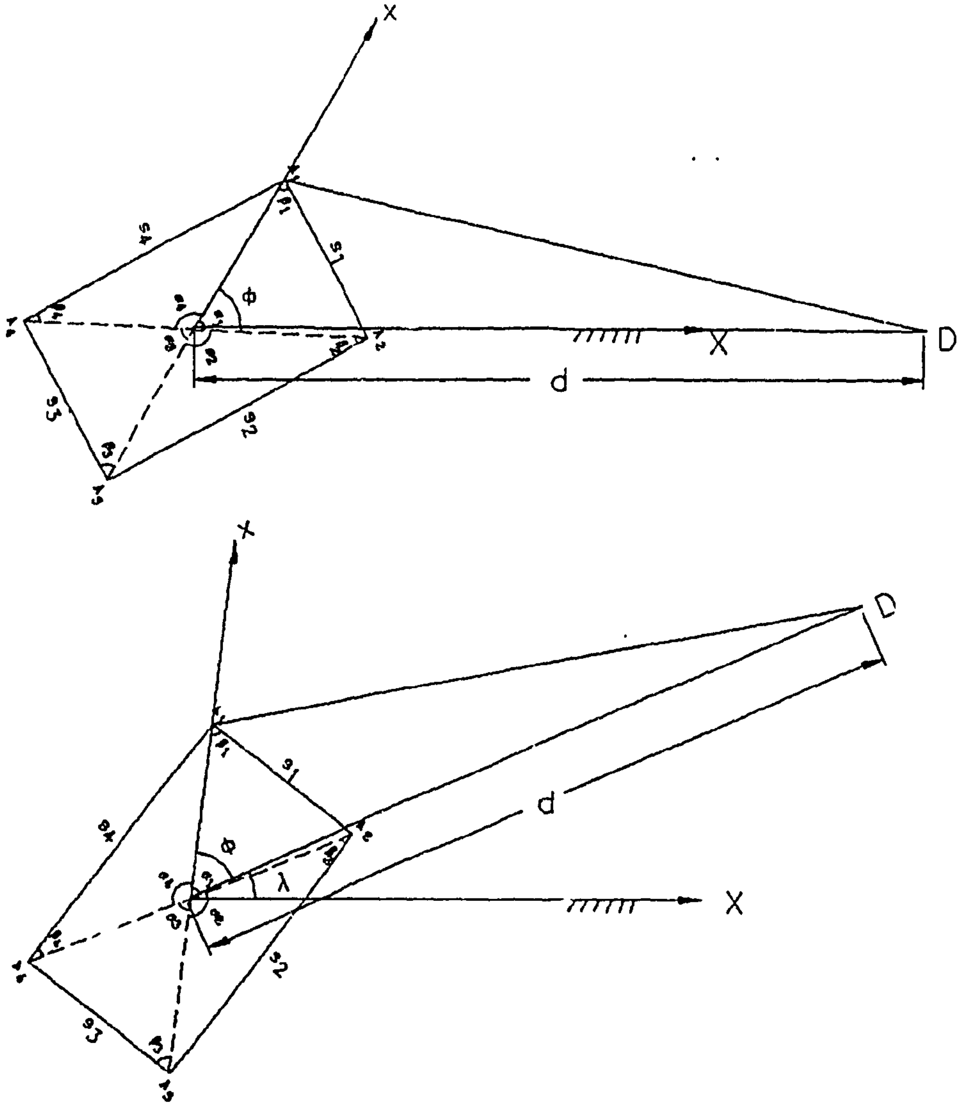

Fig. 8.10 Mandrel and fiber position at different delivery point locations.

chapter 7 that orienting the delivery point by any angle λ keeping the d same (Fig.8.10), does not affect the trend of the delivery point movement, i e $Z_{Di+1} - Z_{Di}$ / $\theta_{i+1} - \theta_i$ remains the same For the same value of d , A_i D, γ_i , Z_{Di} do not change. Values of θ_i get shifted to new values due to change in ϕ but $\theta_{i+1} - \theta_i$ remains the same.

With the reduction in delivery point distance d, total distance travelled by the delivery point gets reduced for the same mandrel rotation. Fig. 8.7 shows delivery point positions for d = 119.99 mm and for d = 754.89 mm for the same rectangular mandrel.

8.4 Experimental Verification

The present technique was experimentally verified for cylindrical mandrels with rectangular and hexagonal cross-sections. All the experiments were performed on a computer controlled filament winding machine with two-degrees-of-freedom. Mandrel rotation and carriage motion are the two degrees of freedom of the machine. Tests were performed for mandrels with rectangular and hexagonal cross-section with various values of the delivery point locations and fiber winding angles In the start of the winding, mandrel was at $\theta = 0.0°$ and the delivery point was kept perpendicular to the longitudinal axis of the mandrel. From the experimental set-up, angle ϕ, delivery point distance d, and co-ordinate of the delivery point were measured. Calculations were made to find the trajectory of the delivery point for rectangular and hexagonal cross-sections as discussed earlier for the desired fiber winding angle. Co-ordinates (θ_i , Z_{Di}) were then entered into the computer controlled filament winding machine.

To measure the fiber winding angle on a mandrel surface, a sheet of paper was wrapped on the mandrel surface and the mandrel was rotated for nearly one revolution of the mandrel. Experiments were carried out for delivery point distances (d) of 119.9mm, 754.8mm, and for fiber winding angles of 15° and 30°. After completion of the winding, the fiber path was marked on the paper which then was unwrapped from the mandrel for the measurement. A maximum of 1% difference was found in the experimental value and the desired fiber winding angle. This small error is due to errors in measuring the exact delivery point distance d, angle ϕ, and truncation errors during computation.

8.5 Conclusion

A method based on the Geometric Approach is presented for the exact calculation of the winding motion for filament winding of non-axisymmetric cylindrical mandrels with convex polygonal cross-sections. A filament winding machine with only two-degrees -of-freedom can be sufficient to get the desired fiber winding angle. The method provides means to compute trajectory of the delivery point relative to the mandrel rotation with very little effort even without any need of a computer program. Using the procedures discussed in this chapter and in chapter 7, it is possible to determine the kinematics of filament winding on cylindrical mandrels having cross-sections with combinations of a curve profile and a linear segment.

CHAPTER 9

DIRECT KINEMATICS OF FILAMENT WINDING

9.1 Summary

Previous chapters 7 and 8 deal with the kinematics of filament winding for cylindrical mandrels, whereas in this chapter a method based on Geometric Approach is presented for the determination of winding motion for non-cylindrical mandrels.

Based on the algorithm presented in this chapter, a user friendly computer program "DIRECTKIN" was developed to study the direct kinematics of filament winding. Using the program "DIRECTKIN", effects of location of the delivery point, fiber winding angle distribution, and mandrel shape geometry on winding motions are determined. Experimental verification of the model is performed on a McClean Anderson filament winding machine for conical and pyramid structures.

Nomenclatures:

$A_{j,i}$= a point on an edge j at the co-ordinate z_i . First subscript denotes the point on the edge number j and second subscript denotes zth co-ordinate of the point.

$A'_{j,i}$ = a point at the intersection of a line parallel to the z axis and passing through point $A_{j,i+1}$, and a line passing through points O_i and $A_{j,i}$.

$A_{1,1}$ = fiber position on the mandrel at the beginning of winding. Fiber is at edge 1 and at co-ordinate z_1 .

d = delivery point distance from z axis i.e. perpendicular distance between z and M_D axis.

du_j = angle inscribed by a face j at z axis i.e.$\angle A_{j,i} O_i A_{j+1,i}$ or $u_{j+1} - u_j$.

Edge j = a line u_j equal to a constant.

Face j = a trapezoidal face including edges j and j+1. Edges are in increasing order opposite to the mandrel rotation.

M_D = axis of movement of the delivery point.

M_{Di} = delivery point position corresponding to mandrel position θ_i to get fiber winding angle of θ_{fi} at co-ordinate z_i on the mandrel surface.

O_i = a point on the z axis at co-ordinate z_i .

P_i = a point at the intersection of M_D axis and a line perpendicular to the z axis at point O_i.

$r_{j,i}$ = perpendicular distance of any point $A_{j,i}$ from the z axis. First subscript denotes the edge number and second subscript denotes the zth co-ordinate.

$s_{j,i}$ = length of the line $A_{j,i}$ $A_{j+1,i}$.

u_j = polar angle at the cross-section.

v = normalized axis along z axis v varies from 0.0 to 1.0.

z = rotational axis of the mandrel.

z_i = co-ordinate of a point at z axis.

α_j = angle inscribed by a face j at z axis i.e. $\angle A_{j,i}\ O_i\ A_{j+1,i}$.

$\beta_{j,i}$ = $\angle O_i\ A_{j,i}\ A'_{j+1,i}$

$\gamma_{j,i}$ = $\angle A_{j,i}\ O_i P_i$. It is the angle when fiber just over-wraps the face j.

$\phi_{j,i}$ = wedge angle made by edge j on the trapezoidal face j-1 at co-ordinate z_i. When j=1, face number is equal to the total number of faces.

μ = angle which line O_i $A_{1,i}$ makes with the line O_i P_i at the beginning of winding.

ν_j = angle made by an edge j with the z axis.

θ_i = mandrel orientation when the fiber, which was at co-ordinate z_i , just over-wraps the trapezoidal face at a desired winding angle.

θ_0 = initial mandrel position.

θ_{fi} = fiber-winding angle made from the transverse axis of the mandrel when the fiber is at co-ordinate z_i on the mandrel surface.

θ'_{fi} = fiber-winding angle on a cylindrical plane corresponding to θ_{fi} .

9.2 Introduction

In previous chapters 7 and 8, kinematic models based on the Geometric Approach were presented for the determination of machine motions for filament winding of non-axisymmetric cylindrical mandrels with curved and polygonal cross-sections In this Geometric Approach, geometrical and trigonometrical relations are used to determine the delivery point positions for obtaining desired fiber winding angle on the mandrel surface. Curved cross-sections are assumed as made of many linear segments and thus mandrel is considered as made of many rectangular surfaces For a mandrel with a polygonal cross-section such as rectangular or hexagonal, Geometric Approach presents exact winding motion for generating the desired fiber winding angle. For a curved cross-section, the accuracy of the approach increases as the number of linear segments increases. In previous chapters, winding on non-cylindrical mandrels was not addressed. In this chapter, a generalized model is presented, which can determine the winding motion for a variety of structures including non-cylindrical mandrels with axisymmetric or non-axisymmtric cross-sections The algorithm developed in this chapter can also be used to determine the winding motion for the cylindrical mandrels but the algorithm presented in chapters 7 and 8 are simple because of mandrel's cylindrical nature.

This chapter as well as previous chapters 7 and 8 deal with the direct kinematics of filament winding, which is defined as the process of determining winding motion for a desired fiber winding angle on the mandrel surface. In this method, the composite components are represented by a ruled surface or by an axis of revolution A ruled surface covers broad range of mandrel surface e.g. a mandrel surface which has rectangular or hexagonal cross-section at one end and circular or elliptical cross-section at another end.

9.3 Kinematic Model

An analytical model is developed to study the kinematics of filament winding for the manufacture of various types of composite components which are represented by axis of revolutions or by ruled surfaces. Axis of revolutions and ruled surfaces cover large number of mandrel shapes as discussed in section 9.3 1 The model is mainly divided into three steps In the first step, the mandrel shape is defined by mathematical equations and then various geometric parameters of the mandrel such as tapering angle, and wedge angle are determined In the second step, experimental set-up conditions such as axis of movement of the delivery point, mandrel's rotational axis, and fiber winding angle are defined. Distance of delivery point from mandrel's axis of rotation is calculated. Initial fiber position and mandrel orientation are described. To avoid the complexity of the delivery point movement, it is assumed that the delivery point moves along a straight line. In the third step, delivery point motion is determined using geometrical and trigonometrical relations. Finally validity of the present model is done by performing experiments on a filament winding machine.

9.3.1 Computation of geometric parameters of the mandrel :

In the present analysis, a mandrel surface is assumed as made of trapezoidal faces as described later. For each of the trapezoidal face, taper angle and wedge angle are determined as follows. For convenience this section is divided into following parts.

9.3.1.1 Defining mandrel shape:

Mandrel surfaces for various shapes are defined as follows.

9.3.1.1.1 Axisymmetric mandrels:

The surface of axisymmetric mandrel is generated by revolving a curve called generator about an axis called z axis and is represented by,

$$r = f(z) \tag{9.1}$$

where, r is the radial distance of a point on the mandrel surface and z is the axis of revolution Cone, ellipsoid, paraboloid, spheroid and other axisymmetric mandrels (Figs.9.1a and 9.1b) is represented in the form of Eq.9.1

9.3.1.1.2 Ruled surfaces:

A ruled surface covers wide range of mandrel surfaces. Axisymmetric, non-axisymmetric, cylindrical, and non-cylindrical mandrel surface can be defined using the concept of a ruled surface [87,88]. Ruled surfaces solve the following problem: given two space curves c_1 and c_2 , both defined over the same parameter interval $u \in [0,1]$, find a surface r such that it contains both curves as opposite boundary curves. More precisely: find a function r such that,

$$r(u,0) = c_1(u), \quad r(u,1) = c_2(u) \tag{9.2}$$

where u is an angle as shown in Fig. 9.1c.

Clearly, the stated problem has infinitely many solutions. T e simplest solution is

$$r(u,v) = (1-v)\, c_1(u) + v c_2(u)$$

or,

$$r(u,v) = (1-v)\, r(u,0) + v r(u,1) \tag{9.3}$$

where v is an axis along z axis (Fig. 9.1c) such that, $0 \leq u,v \leq 1$.

Ruled surfaces have the familiar flavor of linear interpolation: every isoparametric line u = constant is a straight line segment, as illustrated in Figs.9.1a, 9.1c and 9.1d. The input curves r(u,0) and r(u,1) can be of any form defined over the same parameter interval. For instance, one end can be circular or elliptical or any shape and other end can be a polygon or any other shape. Thus, there is a large number of mandrel shapes which can be defined by ruled surfaces. For the case when both

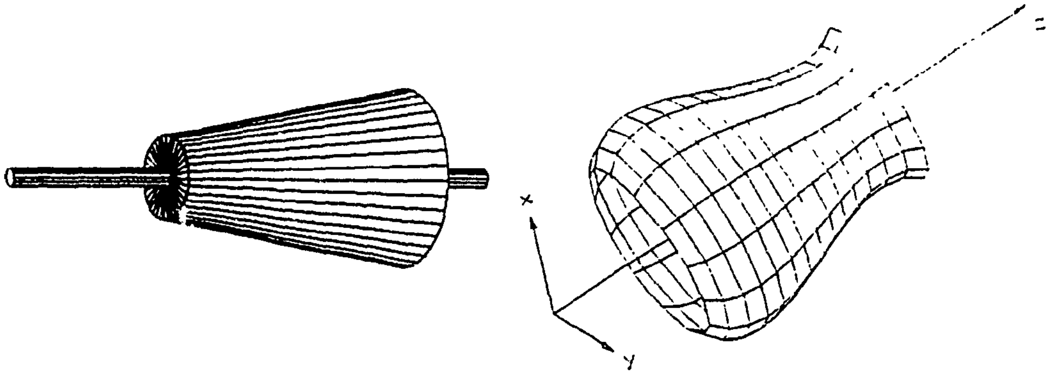

(a) Cone (b) nozzle

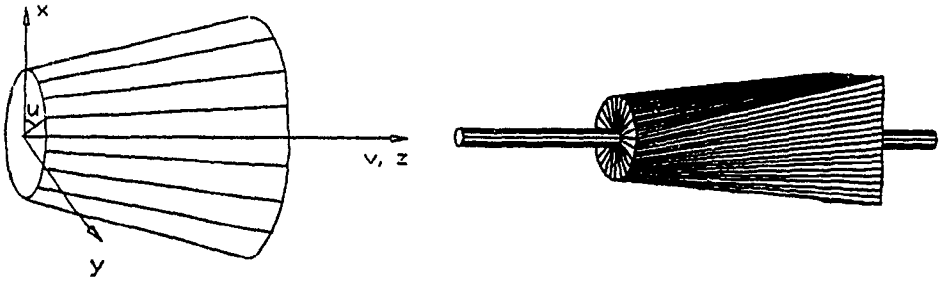

(c) Both ends elliptical (d) One end circle and other end square

Fig. 9.1 Trapezoidal faces on axisymmetric and non-axisymmetric surfaces.

the ends of the mandrel have elliptical cross-sections with different semi-major (a) and semi-minor (b) axes then,

$$r(u,0) = \frac{a_1 . b_1}{\sqrt{b_1^2 \cos^2 2\pi u + a_1^2 \sin^2 2\pi u}} \tag{9.4}$$

$$r(u,1) = \frac{a_2 . b_2}{\sqrt{b_2^2 \cos^2 2\pi u + a_2^2 \sin^2 2\pi u}} \tag{9.5}$$

Equation of the ruled surface will be

$$r(u,v) = (1-v)\ r(u,0) + v r(u,1) \tag{9.6}$$

where, $0 \leq u,v \leq 1$.

The cross-section of the mandrel at any value of v can be determined from above relation.

9.3.1.2. Approximation of the mandrel surface:

To determine the relative positions of the mandrel and delivery point for desired fiber lay down path. a mandrel surface is approximated as made of trapezoidal faces as shown in Fig.9.1. Accuracy in laying down the fiber on desired path increases with the increase in total number of trapezoidal faces. Assuming that the mandrel rotates about the z axis as shown in Fig.9.1, trapezoidal faces are constructed as follows.

9.3.1.2.1 Ruled surfaces:

A cone comes in the category of axisymmetric mandrels as well as ruled surfaces where two boundary curves are circles. For ruled surfaces, u = constant, represents a straight line Draw straight lines for $u = u_1$, $u = u_2$, $u = u_3$ ....$u = u_n$ with a small increment in polar angle u as shown in Fig 9.1c. Now consider the perimeter of the two boundary curves as made of linear segments by joining the points on perimeter at $u = u_1$, $u = u_2$, $u = u_3$ . ... $u = u_n$ by straight lines. With this assumption, the perimeter of the cross-section can be approximated with little error. For example, the perimeter of a circle of radius 77.98 mm (3.07 in.) can be found by dividing the perimeter into 720 equally distributed linear segments. The error on the length of the perimeter was calculated to be 0.0003 % which can be considered as negligible.

Now assume that the edge 1 is represented by a straight line $u = u_1$, edge 2 is represented by a straight line $u = u_2$, and similarly edge j is represented by $u = u_j$. Edge numbers are in an increasing order opposite to the mandrel rotation. Now assume that the face 1 is a flat plane whose boundaries are edges 1, 2 and two linear segments between u_1 and u_2 at boundary curves. Similarly any j^th^ face is a trapezoidal face consisted of j , j+1 edges and two linear segments between u_j and u_{j+1} polar angles at boundary curves. Thus there are n number of tapered faces and n number of edges for n polar angles. The more the number of tapered faces, the better the approximation of the mandrel surface.

9.3.1.2.2 Axisymmetric mandrels

Structures like nozzles, ellipsoid, paraboloid etc. come under this category. Such surfaces can be approximated as made of series of truncated cones as shown in Fig.9.1b. For each cone tapered faces are formed as discussed in previous section for the cone.

9.3.1.3. Determination of taper angle for each edge:

9.3.1.3.1 For ruled surfaces:

The taper angle of an edge is defined as the angle which it makes with the rotational axis (z axis) of the mandrel It is clear that all the edges of an axis of revolution and ruled surface (whose boundary curves are closed curves) intersect the z axis at some points. Taper angles for different edges of a non-axisymmetric tapered mandrel are different whereas the taper angle for all the edges of a cone are the same

Taper angle (v_j) for an edge j is given by,

$$v_j = \tan^{-1} \left(\frac{r(u_j,1) - r(u_j,0)}{l}\right) \tag{9.7}$$

where l is the length of the mandrel.

9.3.1.3.2 Axisymmetric mandrels

We have assumed the surface of an ellipsoid and nozzle as consisted of series of truncated cones. Now consider an ith truncated cone between z_i and z_{i+1} co-ordinates. Assuming that the truncated cones are made of n number of trapezoidal faces as discussed earlier. Tapering angle for all the edges of a truncated cone is the same. Tapering angle of any edge on an ith truncated cone can be found from following relation.

$$v_i = \tan^{-1} \left(\frac{f(z_{i+1}) - f(z_i)}{z_{i+1} - z_i} \right) \tag{9.8}$$

9.3.1.4. Calculation of wedge angle for trapezoidal face:

9.3.1.4.1 Ruled surfaces

Consider a tapered face j as shown in Fig.9.2, which is made with edges j and j+1. Let the boundary curves are at z = z_a and at z = z_b The angle $\phi_{j+1,i}$ which is made by an edge j+1 with the line $A_{j+1,i}$ - q is called wedge angle made by edge j+1 on the trapezoidal face j at co-ordinate z_i . To determine the wedge angle, extend the edges till it intersects the z axis at point I as shown in the Fig.9.2. Now consider the triangle $IA_{j,a}A_{j+1,a}$. The wedge angle $\phi_{j+1,a}$ for the triangle is determined by knowing the angle between line I $A_{j+1,a}$ and Ip. The length of each side of the triangle and wedge angle are calculated as follows Length of the line I $A_{j,a}$ is found from following relation.

$$IA_{j,\,a} = \frac{r(u_j,0)}{\sin \nu_j} \tag{9.9}$$

where ν_j is the taper angle for the edge j and $r(u_j ,0)$ is the radial distance of the point $A_{j,a}$ from the z axis.

Similarly length of the line I $A_{j+1,a}$ is given by,

$$IA_{j+1,\,a} = \frac{r(u_{j+1},0)}{\sin \nu_{j+1}} \tag{9.10}$$

Let length of the line $A_{j,a}A_{j+1,a}$ is $s_{j,a}$, which is determined from following relation.

$$s_{j,\,a} = \sqrt{r^2(u_j,0) + r^2(u_{j+1},0) - 2.r(u_j,0).r(u_{j+1},0).\cos du_j} \tag{9.11}$$

where $du_j = u_{j+1} - u_j$.

Area (A) of the triangle $IA_{j,a}A_{j+1,a}$ is determined from following relation.

$$A = \sqrt{s.(s-a).(s-b).(s-c)} \tag{9.12}$$

where s = (a + b + c)/2, and a, b, c are the length of edges of the triangle i.e. values of $IA_{j,a}$, $IA_{j+1,a}$ and $s_{j,a}$ for the triangle $IA_{j,a}A_{j+1,a}$.

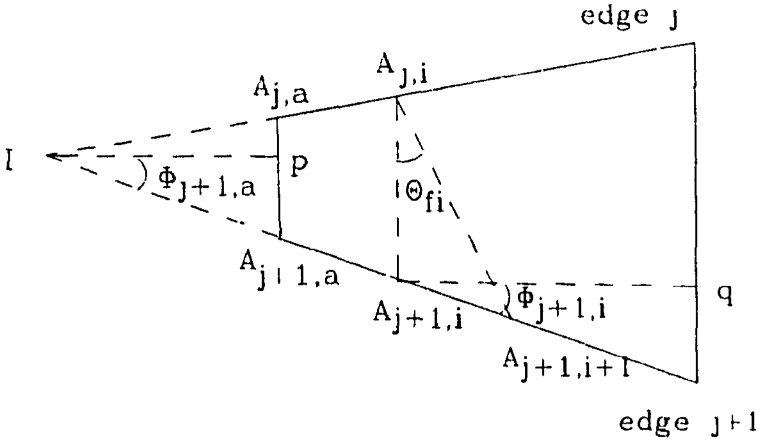

Fig. 9.2 Wedge angle in a typical trapezoidal face.

The perpendicular distance ($h_{j,a}$) between the point I and the base $A_{j,a}A_{j+1,i}$ is determined using following relation

$$h_{j,0} = \frac{2.A}{s_{j,0}} \tag{9.13}$$

The wedge angle ($\phi_{j+1,a}$) of a trapezoidal face j, which edge j+1 makes with line Ip is determined from following relation.

$$\phi_{j+1,a} = \cos^{-1}\left(\frac{h_{j,a}}{IA_{j+1,a}}\right) \tag{9.14}$$

It is obvious from Fig. 9.2 that $\phi_{j+1,i} = \phi_{j+1,a}$. Similarly for every trapezoidal face wedge angle is determined using above relation.

9.3.1.4.2 Axisymmetric mandrels:

Wedge angle for an axisymmetric mandrel is determined from following relation.

$$\phi_{j+1,i} = \sin^{-1}\left(\frac{(s_{j,i+1} - s_{j,i})\cos v_{j+1}}{2(z_{i+1} - z_i)}\right) \tag{9.15}$$

where $s_{j,i}$ represents the length of the line $A_{j,i}\ A_{j+1,i}$ and $s_{j,i+1}$ represents the length of the line $A_{j,i+1}\ A_{j+1,i+1}$ and are found from following relations.

$$s_{j,i} = f(z_i)\ .\ \sqrt{2 - 2\cos(u_{j+1} - u_j)} \tag{9.16}$$

$$s_{j,i+1} = f(z_{i+1})\ .\ \sqrt{2 - 2\cos(u_{j+1} - u_j)} \tag{9.17}$$

9.3.2 Defining experimental set-up conditions:

After the mandrel shape is defined and various parameters of the mandrel's geometry are calculated, experimental set-up conditions such as mandrel position, delivery point position and fiber position in the beginning of winding are defined Let's consider a non-axisymmetric tapered mandrel with elliptical cross-sections at both ends of the mandrel as shown in Fig.9.3. Let rotational axis of the mandrel coincides with the z axis of the mandrel as shown in Fig.9.3. Let the location of one end of the mandrel be at $z = z_a$ and other end is at $z = z_b$. Let end curves lie on planes perpendicular to the z axis. At $z = z_a$, the elliptic curve is represented by,

$$r(u,0) = \frac{a_1 . b_1}{\sqrt{b_1^2 \cos^2 2\pi u + a_1^2 \sin^2 2\pi u}} \tag{9.18}$$

At $z = z_b$ the elliptic curve is represented by

$$r(u,1) = \frac{a_2 . b_2}{\sqrt{b_2^2 \cos^2 2\pi u + a_2^2 \sin^2 2\pi u}} \tag{9.19}$$

Let the delivery point moves along M_D axis as shown in Fig.9.3. Assuming that the z and M_D axes are parallel and a line perpendicular to them has the same reading, i.e. 0.0 on both the axes starts from the same perpendicular line and the scale on both the axes are same. Perpendicular distance between z and M_D axes is d as shown in Fig.9.3. Let any point on the z axis at co-ordinate z_i be O_i and a corresponding point on the M_D axis be P_i such that $O_i P_i$ is perpendicular to the z axis at point O_i . For determining the winding motions, mandrel surface is assumed as made of many trapezoidal faces as explained earlier. Let any point on an edge j of the mandrel at co-ordinate z_i be represented by $A_{j,i}$.

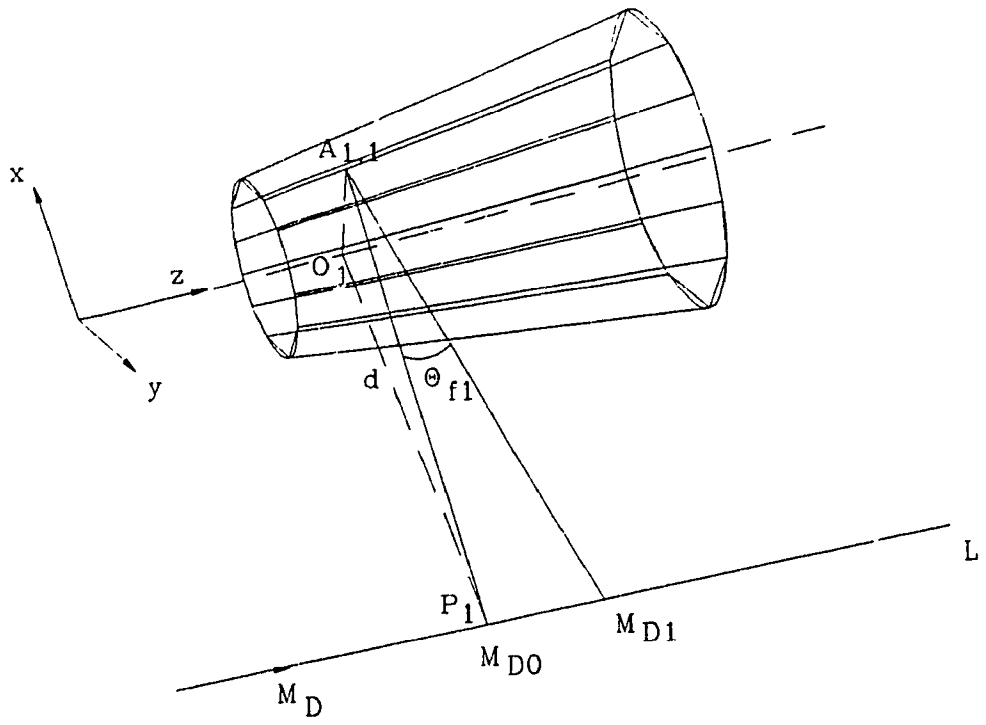

Fig. 9.3 Mandrel and delivery point positions.

Initially fiber is kept at a point $A_{1,1}$ on edge 1 and at co-ordinate z_1 as shown in Fig.9.3. In the beginning, let fiber $A_{1,1}$ P_1 be perpendicular to the M_D axis i e $\angle A_{1,1} P_1 L = 90°$ as shown in Fig.9.3.

To measure the initial mandrel orientation, consider two reference lines O_1 $A_{1,1}$ and O_1 P_1. In the beginning for mandrel position of $\theta = \theta_0$, the angle between reference lines O_1 $A_{1,1}$ and O_1 P_1 i.e. $\angle A_{1,1}O_1P_1$ is measured. Let $\angle A_{1,1}O_1P_1 = \mu$. Value of μ is calculated experimentally. For a circular cross-sectioned mandrel, it is calculated using the relation $\mu = \cos\ (r_{1,1} / d)$, where $r_{1,1}$ is the radius of the circular cross-section and d is the distance between z and M_D axis. For mandrels with elliptical and other non-axisymmetric cross-sections, analytical calculation of μ is done as discussed in chapter 7. Mandrel positions for consecutive winding are determined by knowing the angle between lines O_i $A_{j,i}$ and O_i P_i.

9.3.2.1 Calculation of fiber winding angle

9.3.2.1.1 For Geodesic winding:

A geodesic path is the shortest distance between two points on a surface thus fiber wound under tension along a geodesic path is stable. For rotationally symmetric surfaces, geodesic positioning of the fiber can be described by Clairaut's condition [73] According to this condition, the product of the radius r and the sine of the fiber winding angle θ_f remains constant i.e. $r_i\ .\sin\theta_{fi} = c$. Thus by knowing initial winding angle θ_{f1} and initial radius of the core r_1, fiber winding angle θ_{fi} at various points of the mandrel surface can be determined using above relation for a geodesic winding.

9.3.2.1.2 For Non-geodesic winding:

It is well known that for a surface, greatest winding stability is obtained if the winding is performed on geodesic lines. This restricts the choice of fiber angles on a structure and is an obstacle to the production of optimized composite components.

Non-geodesic winding is necessary for winding complicated shapes for stability of the fiber [38,39,89]. Non-geodesic winding is the process in which the friction between the resin impregnated fiber and the base is utilized to prevent any slippage between them. For stable winding, fibers are wound on constant slippage line [39]. Xian-li Li et.al. presented the non-geodesic stable winding condition for the axisymmetric mandrels such as conical, ellipsoidal, paraboloidal, spherical surfaces [90].

Non-geodesic winding equation for a conical surface is given by [90],

$$\frac{d\theta_{fi}}{dz_i} = \frac{\tan\theta_{fi}}{r_{j,i}} (k\sin\theta_{fi} + \tan v_j) \tag{9.20}$$

where θ_{fi} is the fiber winding angle, $r_{j,i}$ is the radius, k is the co-efficient of friction and v_j is the tapering angle of the cone. By solving above differential equation using Runge Kutta method, fiber-winding angle at various point of a conical mandrel can be determined for known k value for non-geodesic winding.

9.3.3 Calculation of delivery point motion:

Once the mandrel shape geometry and experimental set-up conditions are defined, co-ordinates of mandrel and delivery point positions are determined in following steps. Fiber path on a face is defined and free length of the fiber is calculated. Relative positions of the mandrel and delivery point are determined incrementally for each face using algebraic and trigonometrical relations.

9.3.3.1 Determination of distance of a point $A_{j,i}$ from mandrel's axis of rotation:

Let the perpendicular distance of any point $A_{j,i}$ from the z axis be $r_{j,i}$, which can be determined as follows.

$$r_{j,i} = \tan v_j\,(z_i - z_a) + r_{j,a} \tag{9.21}$$

where $r_{j,a} = r(u_j, 0)$.

The value of $r_{j,i}$ can also be determined using the relation $r_{j,i} = r(u_j, v_i)$, where $v_i = (z_i - z_a)/(z_b - z_a)$

Determination of winding motion is divided into two parts. In the first part winding motion is determined for the case when fiber moves in the upward direction (from smaller cross-section to the larger cross-section) in the mandrel as shown in Fig.9.3. In the second part, the fiber returns towards the downward direction (from larger cross-section to the smaller cross-section) after completion of the upward winding

Winding motion during upward direction:

Determination of winding motion means the calculation of relative positions of the mandrel and delivery point at different times of the winding. For this mandrel positions and fiber positions are calculated incrementally using geometric and trigonometric relations. Various parameters such as fiber position, fiber length, etc. are determined in each stage as follows.

9.3.3.2 Determination of Fiber Position (z_i) on the Mandrel Surface

For determining the winding motion, mandrel surface is divided into n trapezoidal faces. Fiber is laid down at a specific angle at these faces. To describe the path of the fiber on a face, zth co-ordinate of the fiber on each face is determined. Position of the fiber on an edge of a mandrel is calculated as follows. It is pointed out that for the case of axis of revolution and ruled surfaces, all the edges of tapered faces pass through the rotational axis (z axis) of the mandrel.

Consider a trapezoidal face 1, which is consisted of edge 1, edge 2, and two linear segments at boundary curves between polar angles u_1 and u_2 as shown in Fig.9.4 Line $A_{1,1}$ $A_{2,1}$ is the fiber position on face 1 for fiber winding angle of 0°.

Suppose it is desired that the fiber lies down on the face 1 along line $A_{1,1}$ $A_{2,2}$ making an angle of θ_{f1} from line $A_{1,1}$ $A_{2,1}$ as shown in Fig.9.4. Here for the sake of convenience fiber winding angle is measured from the transverse axis of the mandrel. The fiber winding angle from longitudinal axis of the mandrel will be $90° - \theta_{f1}$.

The z^{th} co-ordinate of point $A_{2,2}$ is determined by finding the length $A_{2,1}$ $A_{2,2}$ as shown in Fig.9.4 and Fig.9.5. Length $A_{2,1}$ $A_{2,2}$ is determined from triangle $A_{1,1}$ $A_{2,2}$ $A_{2,1}$ as follows. In triangle $A_{1,1}A_{2,2}A_{2,1}$

$\angle A_{2,1}\ A_{1,1}\ A_{2,2} = \theta_{f1}$, $\angle A_{2,2}\ A_{2,1}\ A_{1,1} = 90° + \phi_{2,1}$,

$\angle A_{1,1}\ A_{2,2}\ A_{2,1} = 90 - \theta_{f1} - \phi_{2,1}$,

and length $A_{1,1}\ A_{2,1} = \sqrt{r_{1,1}^2 + r_{2,1}^2 - 2.\ r_{1,1} \cdot r_{2,1}\ .\cos du_1}$

Angle du_1 is the angle between line O_1 $A_{1,1}$ and O_1 $A_{2,1}$ at z_1 i.e. $du_1 = u_2 - u_1$. Applying the law of sines for the triangle $A_{1,1}$ $A_{2,1}$ $A_{2,2}$ [91],

$$A_{2,1}A_{2,2} = \frac{A_{1,1}A_{2,1}\sin\theta_{f1}}{\sin(90^o - \theta_{f1} - \phi_{2,1})} \tag{9.22}$$

In general the distance between points $A_{j+1,i}$ and $A_{j+1,i+1}$ is calculated as follows [91].

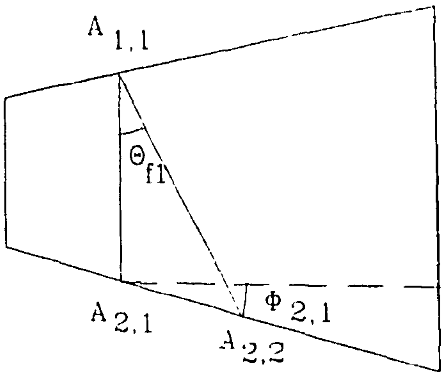

Fig. 9.4 Fiber position on tapered face 1.

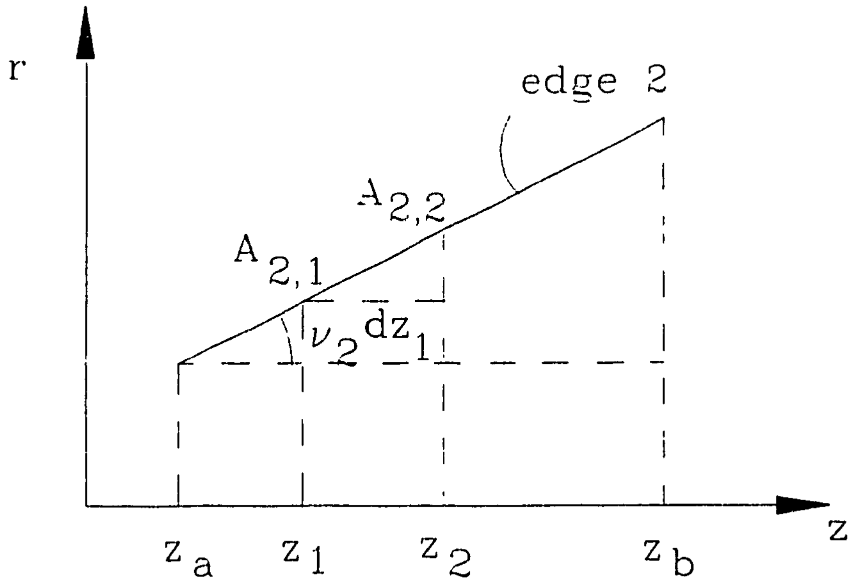

Fig. 9.5 Calculation of z^{th} co-ordinate of point $A_{2,2}$

$$A_{j+1,i}A_{j+1,i+1} = \frac{A_{j,i}A_{j+1,i}\sin\theta_{fi}}{\sin(90^o - \theta_{fi} - \phi_{j+1,i})} \quad (9.23)$$

The z^{th} co-ordinate of point a $A_{2,2}$ i.e. z_2 can be determined from Fig.9.5 as follows.

$$z_2 = z_1 + dz_1$$

Where z_1 is the z^{th} co-ordinate of point $A_{1,1}$ or $A_{2,1}$.

$$dz_1 = A_{2,1}\ A_{2,2}\ \cos\ v_2$$

Therefore,

$$z_2 = z_1 + A_{2,1}A_{2,2}\cos v_2 \quad (9.24)$$

In general z^{th} co-ordinate of point $A_{j+1,i+1}$ i.e. z_{i+1} is calculated by

$$z_{i+1} = z_i + A_{j+1,i}A_{j+1,i+1}\cos v_{j+1} \quad (9.25)$$

where

$$dz_i = A_{j+1,i}A_{j+1,i+1}\cos v_{j+1} \quad (9.26)$$

9.3.3.3 Construction of a cylindrical plane

A cylindrical plane about z axis and passing through points $A_{j,i}$ and $A_{j+1,i+1}$ is constructed to make calculation simpler for determining the winding motion [91]. With the assumption of a cylindrical plane, the approach is similar to the method discussed in chapters 7 and 8 for cylindrical mandrels. It can be observed by extending the cylindrical plane, that the delivery point axis M_D lies in the cylindrical plane at some particular mandrel position θ_i and thus the delivery point position M_{Di} corresponding to the mandrel position θ_i for desired winding angle can be easily calculated by considering it as a plane geometry problem. Construction of a cylindrical plane is done as follows.

To make an angle θ_{f1} on the face 1, fiber should lie down along the line $A_{1,1}$ $A_{2,2}$. Now consider a plane $A_{1,1}$ $A'_{2,1}$ $A_{2,2}$, where point $A'_{2,1}$ is obtained by drawing a line $A_{2,2}$ $A'_{2,1}$ parallel to the z axis and a line passing through points O_1 and $A_{2,1}$ as shown in Fig.9.6. In this case plane $A_{1,1}$ $A'_{2,1}$ $A_{2,2}$ becomes cylindrical plane with respect to the z axis and the calculation of winding motion is done similarly to the cylindrical mandrel case.

9.3.3.4 Calculation of parameters of cylindrical plane:

Determination of various parameters such as $A_{j,i}$ $A'_{j+1,i}$, $\beta_{j,i}$ ($\angle O_i A_{j,i} A'_{j+1,i}$) of cylindrical plane are done as follows [91].

$$A_{j,i}A'_{j+1,i} = \sqrt{r^2_{j,i} + r^2_{j+1,i+1} - 2.r_{j,i}.r_{j+1,i+1}.\cos du_j} \qquad (9.27)$$

where $du_j = u_{j+1} - u_j$.

$$\cos\beta_{j,i} = \frac{r_{j,i}^2 + A_{j,i}A'^{2}_{j+1,i} - r_{j+1,i+1}^2}{2.r_{j,i}.A_{j,i}A'_{j+1,i}} \qquad (9.28)$$

9.3.3.5 Calculation of fiber length

Fiber length $A_{j,1}$ P_i for the case when fiber just overwraps the tapered face j by θ_{fi} winding angle can be determined as follows [91].

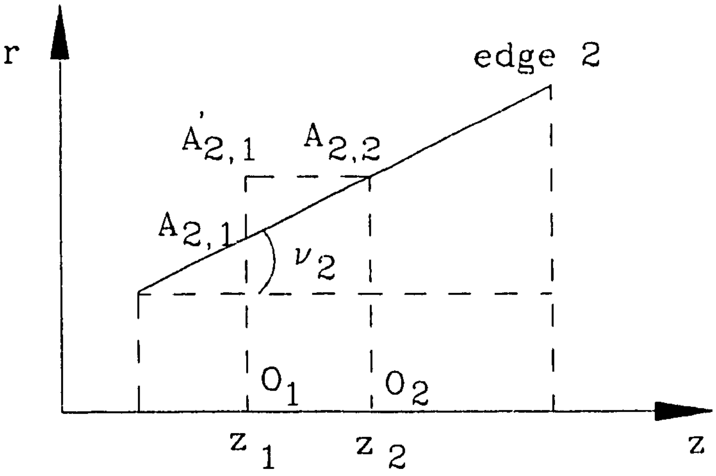

Fig. 9.6 Location of point $A'_{2,1}$.

$$A_{j,i}P_i = r_{j,i}\cos\beta_{j,i} + \sqrt{(r_{j,i}\cos\beta_{j,i})^2 + (d^2 - r_{j,i}^2)} \tag{9.29}$$

9.3.3.6 Calculation of winding angle (θ'_{fi}) for a cylindrical plane

The angle which the fiber makes with the transverse axis on the tapered face is not the same as the angle on a cylindrical plane. Since the calculation for delivery point positions are performed using cylindrical plane, it is necessary to determine the winding angle which the fiber will make on a cylindrical plane corresponding to the angle on the tapered face. The fiber angle θ'_{fi} on a cylindrical plane $A_{j,i}\ A'_{j+1,i}A_{j+1,i+1}$ corresponding to the fiber winding angle θ_{fi} on a tapered face is determined as follows [91].

$$\theta'_{fi} = \tan^{-1}\ (dz_i\ /\ A_{j,i}\ A'_{j+1,i}\ )$$

Upon substituting the value of dz_i from Eq.9.26,

$$\theta'_{fi} = \tan^{-1}\left(\frac{A_{j+1,i}A_{j+1,i+1}\cos\nu_{j+1}}{A_{j,i}A'_{j+1,i}}\right) \tag{9.30}$$

9.3.3.7 Calculation of delivery point and mandrel positions

The final step in the calculation of relative positions of the delivery point and the mandrel at various instants of the winding are done using following relations [91].

$$M_{Di} = z_i + A_{j,i}P_i\tan\theta'_{fi} \tag{9.31}$$

$$\theta_i = \gamma_{j,i} + \sum_{j=2}^{j=i} du_{j-1} - \mu + \theta_0 \quad (for\ i \geq 2) \tag{9.32}$$

where $du_j = u_{j+1} - u_j$. Other terms such as z_i, $A_{j,i}$ P_i, θ'_{fi}, μ, and θ_0 are already defined and calculated. Value of $\gamma_{j,i}$ is calculated as follows.

$$\gamma_{j,i} = \cos^{-1}\left(\frac{r_{j,i}^2 + d^2 - A_{j,i}P_i^2}{2.r_{j,i}.d}\right) \tag{9.33}$$

If the value of i is more than the total number of tapered faces n then the value of $du_j = du_{j-n}$. Similarly if the value of i is more than the k^th^ times the total number of tapered faces n, then the value of $du_j = du_{j-(k.n)}$.

For face 1, M_{D1} and θ_1 are calculated using following equations [91].

$$M_{D1} = z_1 + A_{1,1}P_1 \tan\theta'_{f1} \tag{9.34}$$

$$\theta_1 = \gamma_{1,1} - \mu + \theta_0 \tag{9.35}$$

For the rest of the faces we use above generalized equations 9.31 and 9.32 to determine the delivery point positions corresponding to the mandrel angular position. Above generalized formulas are written assuming that the winding starts from point $A_{1,1}$.

Winding motion during downward direction:

Winding motion analysis for downward winding is done similarly to the upward winding. Calculation of various parameters for downward winding are done using equations developed for upward winding and by substituting θ_{fi} by $-\theta_{fi}$.

Once the co-ordinates of mandrel positions (θ_i) and delivery point positions (M_{pi}) for one complete stroke are determined then repetition of above trajectory is generally done after indexing the mandrel If new sets of data for other strokes are required then it is determined in a similar manner Studies on the kinematics of filament winding during start-up and reversal period are covered in chapter 10

9.4 Implementation of the Method on a Computer

Based on the method described above, an interactive computer program DIRECTKIN was developed to determine the winding motions for upward and downward winding to get the desired fiber winding angle on various types of cylindrical and non-cylindrical mandrels. Thus by feeding mandrel's shape geometry such as $r = c_1$ (u) and $r = c_2(u)$ at boundaries, length of the mandrel (l), initial experimental set-up values such as d and μ. winding motions can be generated for desired fiber winding angle (θ_{fi}).

The program is written in Fortran language. The Flow Chart for this algorithm is shown in Fig.9.7. Experiments were performed on a conical mandrel with length 156.7 mm, end radii 57.00mm and 98.8 mm, and tapering angle $v = 14.59^\circ$ Delivery point distance d was kept at 450 mm. In the beginning of winding, fiber was at a radius $r = 57.00$mm on the mandrel and at $z_1 = 0.00$mm.

Based on the above algorithm, delivery point motion relative to the mandrel motion are determined for $\theta_f = 10^\circ$. The result is shown in Fig 9 8. The data thus obtained were transfered to the computer of a McClean Anderson filament winding machine and experiments were conducted After the winding, experimental values of fiber winding angle at various positions of the mandrel were measured The maximum error between the predicted and experimental values in θ_f were found to be 1° The error between the predicted and experimental values may be accounted due to various reasons Human error in the measurement of experimental set-up conditions and mandrel shape

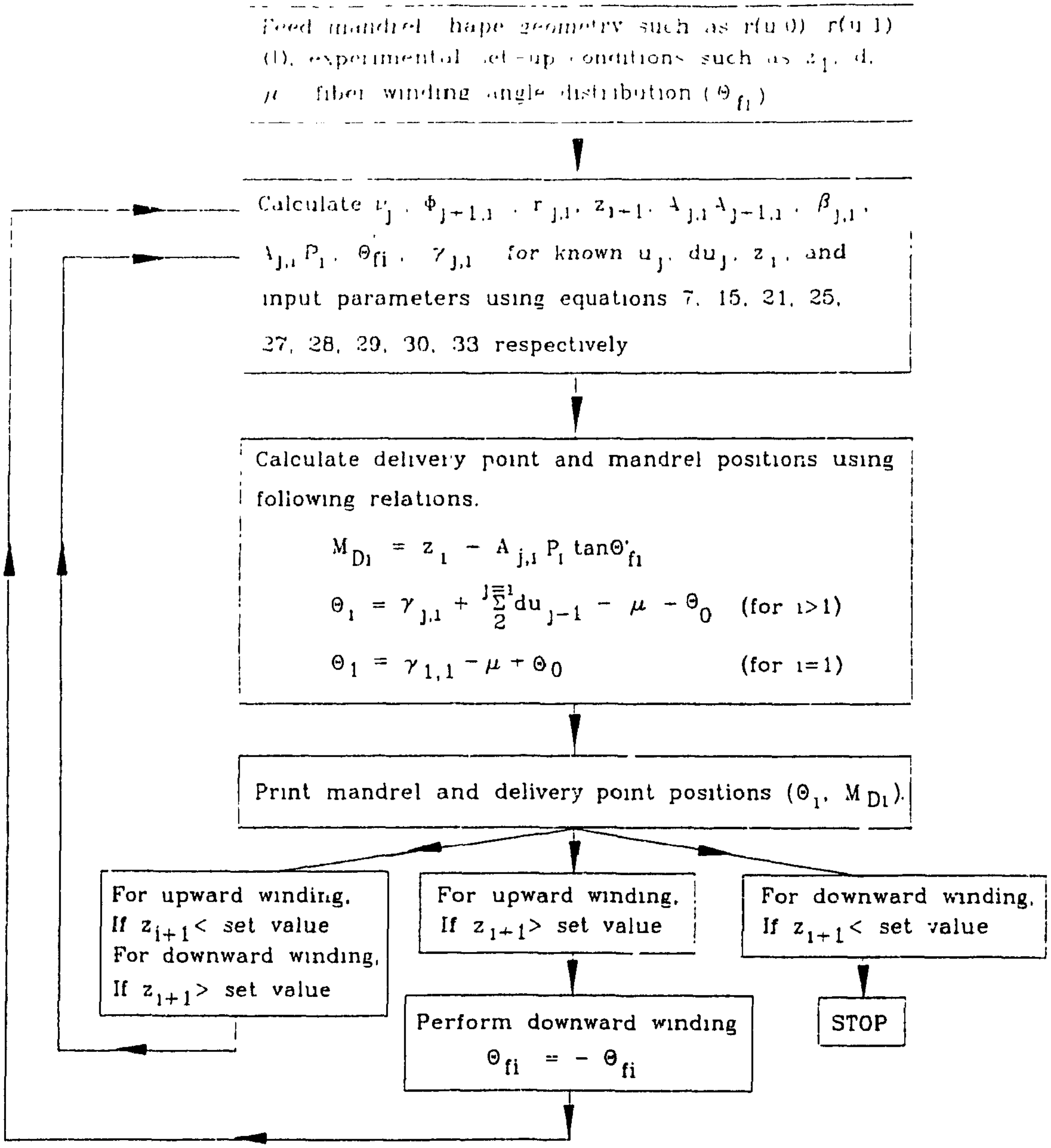

Fig. 9.7 Flow chart for the computer program DIRECTKIN.

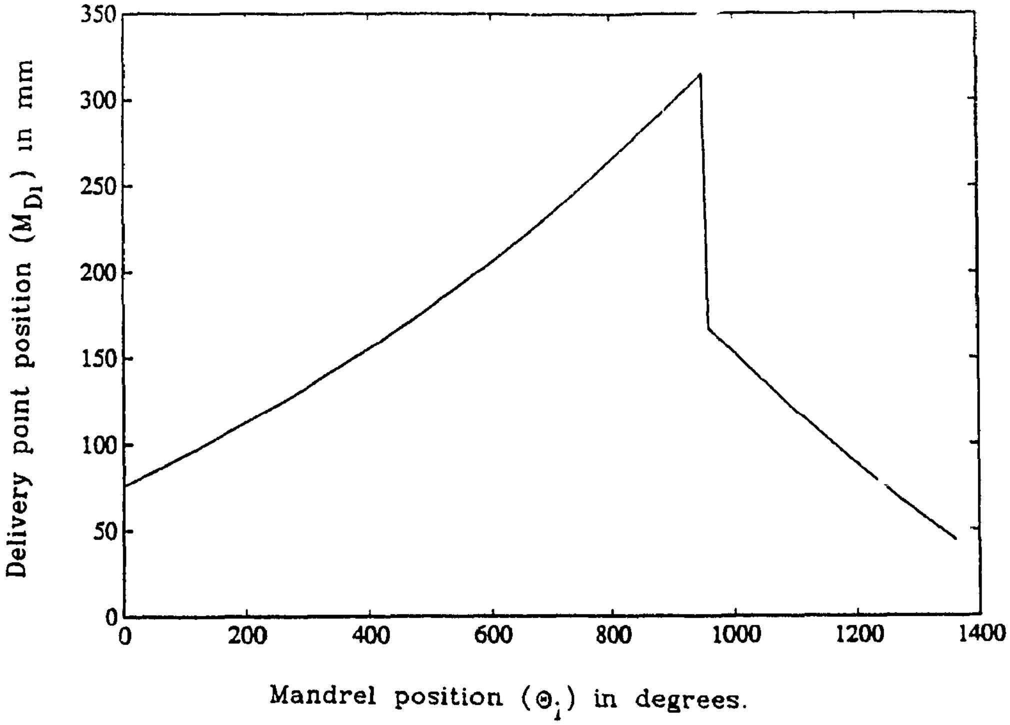

Fig. 9.8 Mandrel and delivery point positions for θ_f= 10° for a conical mandrel.

geometry, and truncation error during data transfer could be possible causes of the error.

9.5 Effect of Winding Parameters on Winding Motions

Effects of delivery point distance d and fiber winding angle θ_f on winding motions are shown in figures 9 9 and 9 10 respectively for a conical mandrel with $\nu = 14.59^\circ$. In all the cases it was assumed that the winding starts at $z_1 = 0.0$ and at a radius r = 57.00mm Figure 9 9 shows the winding motion for delivery point distance d = 300mm, 450mm, and 600mm for fiber winding angle of 15°. Winding motions for fiber winding angle of 5° , 15° , 25° and d = 450mm are shown in Fig. 9.10. It is evident from Figs 9.9 and 9 10 that with the increase in delivery point distance d and θ_f , total distance travelled by the delivery point also increases for the same amount of mandrel rotation.

Mandrel geometry affects the winding motion trajectory. For different mandrel shapes, the delivery point movement is different. Figure 9.11 shows the winding motions for different tapering angle $\nu = 5.0^\circ$, 14.59°, and 20° for a conical mandrel. In all the cases, winding was started at $z_1 = 0$ 0mm and at a radius r = 57.00mm Figure 9 12 shows the θ_f distribution over the mandrel surface for the geodesic and non-geodesic winding on a conical mandrel with tapering angle $\nu = 14.59^\circ$, starting radius r = 57.00mm at $z_1 = 0.0$mm, d = 450 mm., initial fiber winding angle $\theta_f = 10^\circ$ and for different values of frictional coefficients. Corresponding winding motions for the geodesic and non-geodesic winding are shown in Fig.9.13.

Winding motion for a cylindrical mandrel with an elliptic cross-section was also determined using computer program DIRECTKIN and was found to be the same as presented in chapter 7 It is to be noted here that the experimental verification of the algorithm presented in chapter 7 is already done for a cylindrical mandrel with an elliptical cross-section. Experimental verfication of the present method is also done on a tapered mandrel with rectangular cross-section.

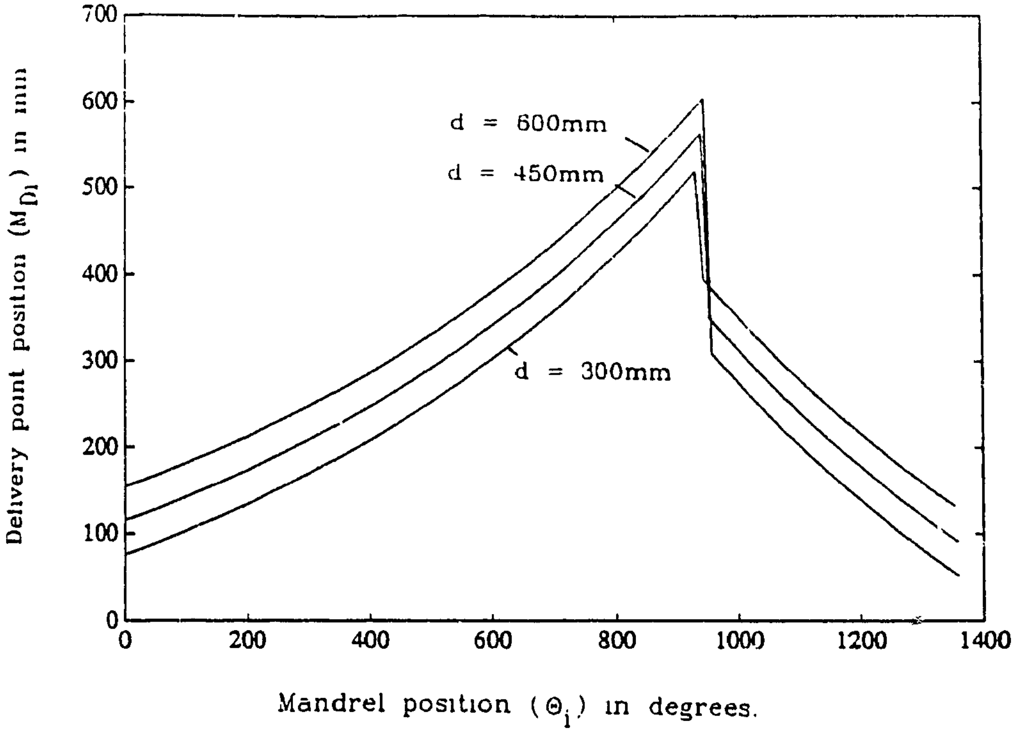

Fig. 9.9 Effect of delivery point positions on winding motion for a conical mandrel.

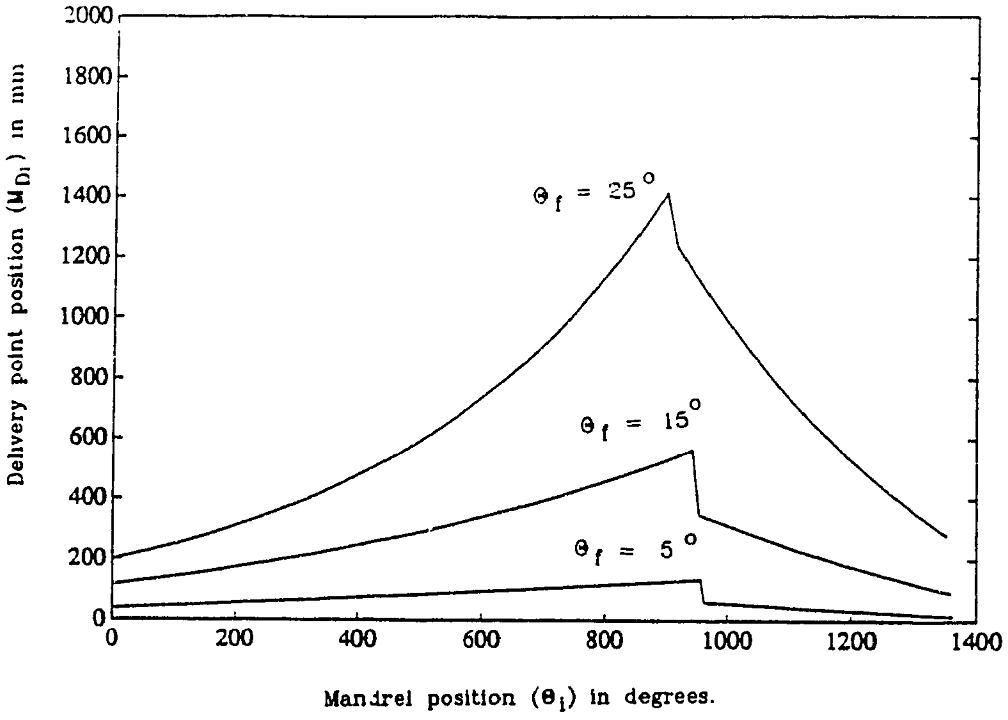

Fig. 9.10 Effect of fiber winding angle on winding motion for a conical mandrel.

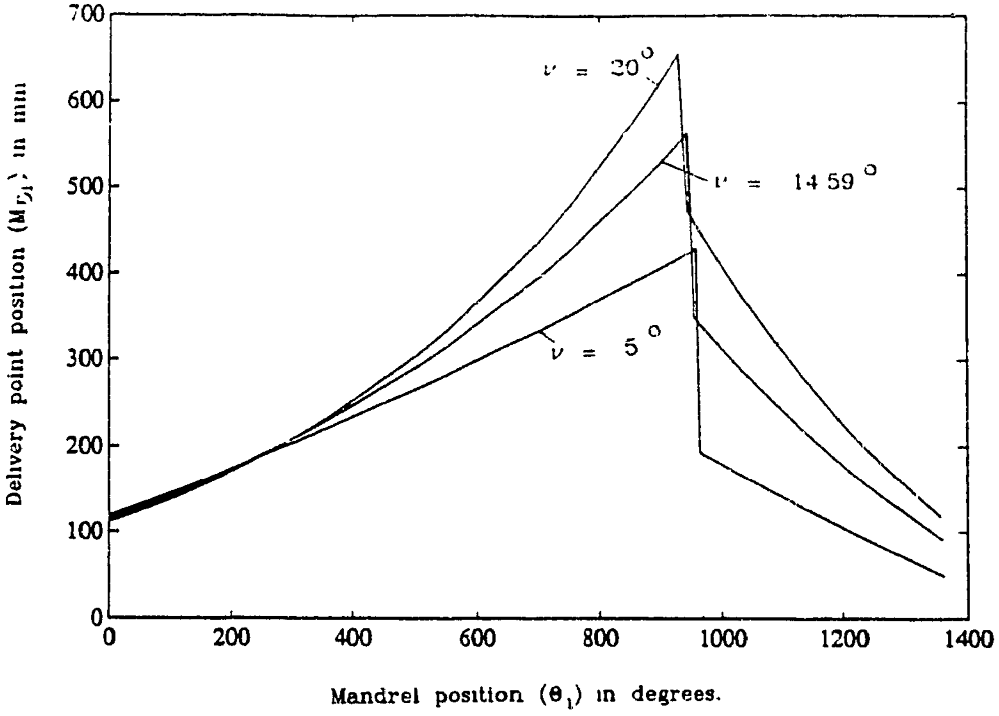

Fig. 9.11 Effect of tapering angle of a cone on winding motions.

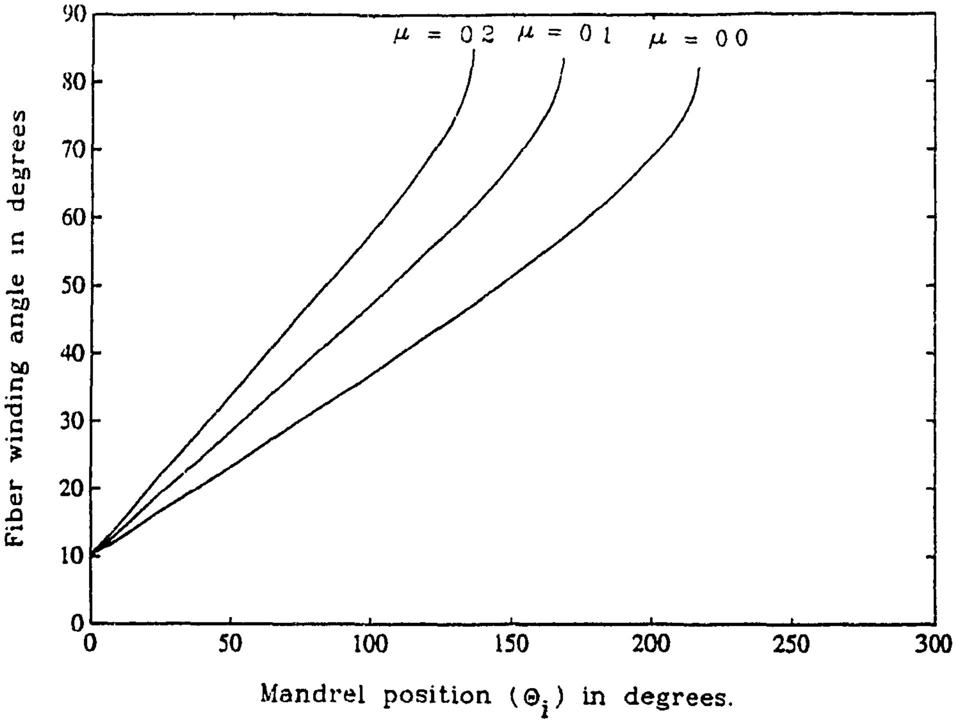

Fig. 9.12 Fiber winding angle distribution for friction coefficients (μ) of 0.0, 0.1 and 0.2 on a conical mandrel.

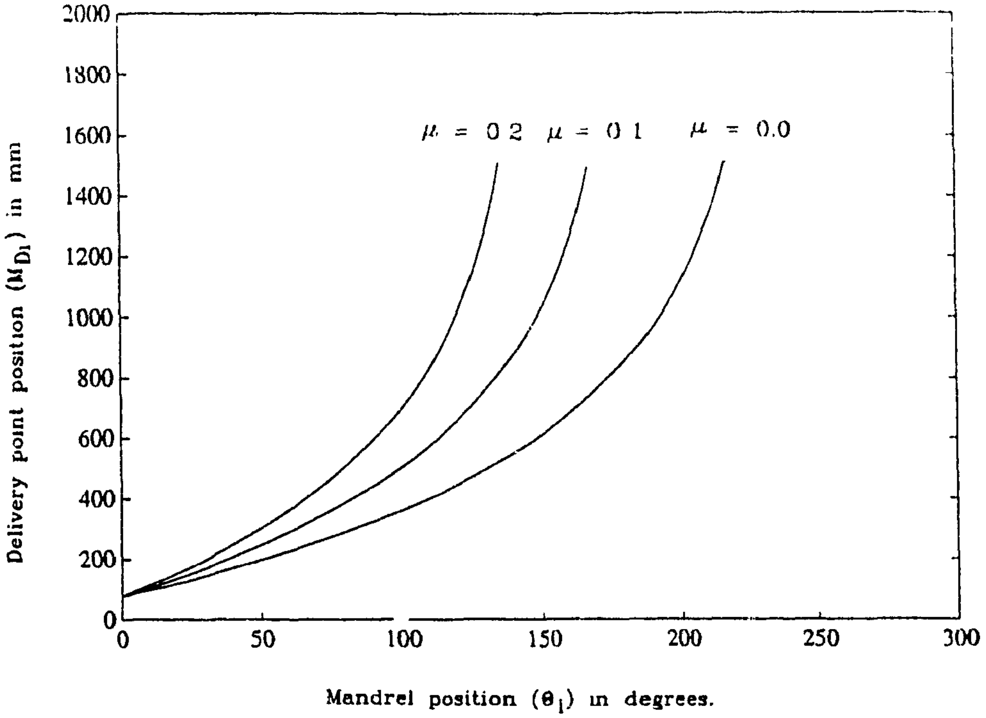

Fig. 9.13 Winding motion for friction coefficients (μ) of 0.0, 0.1 and 0.2 for a conical mandrel.

9.6 Filament Winding on non-cylindrical mandrels with polygonal cross-sections

The algorithm described in this chapter is also applied with few modifications for the manufacture of non-cylindrical mandrels where both the ends are polygonal cross-sections [91] The first step, computation of geometric parameters (9.3.1) for these types of structures is straight forward Mathematical equations are not needed to define the mandrel surface Cross-sections of both the ends are defined by the distance of each longitudinal edge from the axis of rotation and by the angle inscribed by each circumferencial edge at the axis of rotation [91] Mandrel surface is not approximated because all the faces are trapezoidal faces The delivery point motion relative to the mandrel motion are determined by following the second step (9 3 2) and third step (9.3.3) of this chapter The complete procedure for the determination of winding motion is described in detail in reference [91].

The concept presented in this chapter can be utilized for the manufacture of composite drive shafts for aerospace industries as designed by Gross and Goree [92]. The drive shaft had triangular cross-section at one end and circular cross-section at another. Non-circular end cross-section allows for mechanical interference between the end-fitting and the tube end during torque transmission Using present technique such complex components can be filament wound This approach is not only useful in filament winding operation with thermoset and thermoplastic resin but the concept can also be applied to various other fields such as thermoplastic tape winding, tape laying, laser cutting, etc

9.7 Conclusions

A technique based on Geometric Approach is presented to determine the machine motions for generating desired fiber angle distribution on axisymmetric, non-axisymmetric, cylindrical, and non-cylindrical mandrel shapes. The study shows that a filament winding machine with two-degrees-of-freedom can laydown the fiber on a desired path with good accuracy for a variety of composite components. Winding motion obtained for two-axis filament winding machine is found to be smooth and can be easily generated.

An interactive computer program DIRECTKIN was developed to perform the study on the direct kinematics. The aim of writing this program is to study the effect of mandrel shape geometry, experimental set-up conditions, fiber winding angle distribution on winding motions.

CHAPTER 10

INVERSE KINEMATICS OF FILAMENT WINDING

10.1 Summary

There are no available techniques for the prediction of fiber angle distribution for various mandrel shapes under different conditions of mandrel's rotations and delivery point motions. In this chapter a novel approach based on the geometric and trigonometric relations is developed for predicting the fiber laydown path for a given equation of motion for the delivery point. This is important during the start-up and reversal periods of the filament winding operation. During the start-up period, the delivery point accelerates from a velocity of zero to a final value in some interval of time, whereas during the reversal period the delivery point decelerates to zero velocity and then accelerates to a final velocity.

Equations of motion for the delivery point are presented to have smooth start-up and reversal periods. Closed form solutions are developed to compute the fiber winding angle distribution on various types of cylindrical mandrels with axisymmetric and non-axisymmetric cross-sections, whereas numerical solutions are presented for non-cylindrical mandrels. Fiber slackening phenomena during a reversal period is discussed.

Based on the current approach, an interactive computer program INVERSEKIN is developed to determine fiber winding angle distributions for a given equation of motion, mandrel shape geometry and experimental set-up conditions. Effects of winding parameters on fiber position and fiber winding angle distributions are discussed.

Nomenclatures:

$A_{j,i}$ = a point on an edge j at co-ordinate z_i

$A'_{j,i}$ = a point at the intersection of a line parallel to the z axis and passing through point $A_{j,i+1}$, and a line passing through points O_i and $A_{j,i}$

$A_{1,1}$ = fiber position on a mandrel at the beginning of winding. Fiber is at edge 1 and at co-ordinate z_1 .

d = delivery point distance from the z axis i.e. perpendicular distance between z and M_D axis.

dt = small increment in time

du_j = angle inscribed by a face j at the z axis i.e. $\angle A_{j,i}\, O_i\, A_{j+1,i}$ or $u_{j+1} - u_j$

Edge j = a line at u_j equal to a constant.

Face j = a trapezoidal face including edges j and j+1. Edges are in increasing order opposite to the mandrel rotation.

M_D = axis of movement of the delivery point.

M_{Di} = delivery point position corresponding to mandrel position Θ_i to get fiber winding angle of Θ_{1i} at co-ordinate z_i on the mandrel surface.

O_i = a point on the z axis at co-ordinate z_i .

P_i = a point at the intersection of M_D axis and a line perpendicular to the z axis at a point O_i .

$r_{j,i}$ = perpendicular distance of a point $A_{j,i}$ from the z axis

$s_{j,i}$ = length of the line $A_{j,i}\, A_{j+1,i}$.

u_j = normalized polar angle at the cross-section. u varies from 0 to 1.

v = normalized axis along z axis. v varies from 0 to 1.

z = rotational axis of the mandrel.

z_i = co-ordinate of a point at z axis.

α_j = angle inscribed by face j at z axis i.e. $\angle A_{j,i}\, O_i\, A_{j+1,i}$.

$\beta_{j,i}$ = $\angle O_i\, A_{j,i}\, A'_{j+1,i}$.

$\gamma_{j,i}$ = $\angle A_{j,i}\, O_i\, P_i$. It is the angle when fiber just over-wraps the face j.

$\phi_{j,i}$ = wedge angle made by edge j on the trapezoidal face j-1 at co-ordinate z_i .

μ = angle which line O_1 $A_{1,1}$ makes with the line O_1 P_1 at the beginning of winding

ν_j = angle made by an edge j with the z axis

θ_i = mandrel position at time t_i

θ_0 = initial mandrel position

θ_{fi} = a fiber winding angle made from transverse axis of the mandrel for the case when fiber is at co-ordinate z_i on the mandrel surface.

θ'_{fi} = a fiber winding angle on a cylindrical plane corresponding to θ_{fi} .

10.2 Introduction

In previous chapters 7, 8, and 9, the problem of computing the position of delivery point relative to the mandrel position is discussed for a given fiber laydown path on a mandrel In this chapter the following problem is investigated: given the trajectory of motion of the delivery point and mandrel, how to compute the fiber position and fiber winding angle on various mandrel shapes. In previous chapters, direct kinematics of filament winding is studied, whereas in this chapter inverse kinematics of filament winding is discussed.

During a filament winding process, the delivery point undergoes small sections of acceleration and deceleration in which the carriage unit is reversed without impact. Dynamic loads in these sections are usually large so the maximum operating speed of the mechanism depends in many respects on the equation of motion.

Kinematic analysis of winding process during the middle section i.e. away from the start-up and reversal process is discussed in previous chapters for various types of mandrel surfaces. However, there have not been reports in the literature to determine the fiber winding angle distribution from given equations of motion of the delivery point. This is important during start-up and reversal period of the delivery point. During a start-up period delivery point starts at zero velocity and reaches to a final velocity in some interval of time Similarly, during the reversal period. delivery point decelerates to zero velocity and accelerates to a final velocity in some interval of time During these start-up and reversal periods, delivery point should follow a smooth and continuous motion to avoid impact and vibration of the machine Discontinuous motions of delivery point may cause fiber breakage or fiber slackening during winding process Charrier et al [93] determined the fiber angle distribution during start-up and reversal periods for the circular cylinder case.

In this chapter, simple equations of motion for the delivery point, similar to the motion of robot arms are presented [94]. Once the trajectory of the delivery point is defined, a model based on the geometric approach is developed to determine the fiber winding angle distributions on various types of axisymmetric, non-axisymmetric, cylindrical and non-cylindrical mandrels. The present analysis is helpful in designing the composite components and in selecting suitable equations of motion for the delivery point. This could also avoid the accumulation of excessive materials at two ends of the mandrel.

10.3 Problem Statement

The problem of determining the fiber laydown path on a given mandrel for known equations of the delivery point motions is studied For this, a simplest form of filament winding machine which has two-degrees-of-freedom is considered Mandrel rotation and delivery point motion are the two degrees of freedom of the machine. For dynamic stability of the mandrel, it is considered to be rotating at a constant speed Delivery point follows a specific equation of motion for smooth start-up and reversal period. If the motion of the delivery point is not smooth and continuous, it might create excessive fiber tension or fiber slackening. Fiber tension might cause fiber breaking during start-up and reversal period.

In this chapter a method is developed to compute the fiber position and orientation (θ_f) on various types of axisymmetric, non-axisymmetric, cylindrical and non-cylindrical mandrels for known equations of motion of the delivery point. Fiber slackening phenomena during reversal period is discussed.

10.4 Trajectory Generation for a Delivery Point

Trajectory means a time history of position, velocity, and acceleration of any degree of freedom. Usually, it is desirable that the delivery point motion be smooth and continuous to avoid vibration and impact on the machine. In order to guarantee smooth paths, some sort of constraints on equation of the motion is required. There are many ways a path for delivery point can be defined depending on the number of constraints [95,96,97].

10.4.1 Cubic Polynomials:

Consider a delivery point moving along M_D axis from its initial position M_{D0} to a final position M_{Df} in a certain amount of time (t_f). During the start-up period, initial velocity of the delivery point is zero and the final velocity is of certain value.

Position constraints can be written as follows,

$$M_D(0) = M_{D0}, \quad M_D(t_f) = M_{Df} \tag{10.1}$$

Velocity constraints are,

$$M'_D(0) = 0.0 \quad M'_D(t_f) = M'_{Df} \tag{10.2}$$

These four constraints can be satisfied by a polynomial of at least third degree. A cubic polynomial has the form,

$$M_D(t) = k_0 + k_1.t + k_2.t^2 + k_3.t^3 \tag{10.3}$$

Velocity and acceleration along this trajectory are,

$$M'_D(t) = k_1 + 2.k_2.t + 3.k_3.t^2 \tag{10.4}$$

$$M''_D(t) = 2.k_2 + 6.k_3.t \tag{10.5}$$

Fulfilling the four desired constraints, we have,

$$\begin{aligned} k_o &= M_{DO},\quad k_1 = 0.0, \\ k_2 &= \frac{3}{t_f^2}(M_{Df} - M_{DO}) - \frac{M'_{Df}}{t_f} \\ k_3 &= -\frac{2}{t_f^3}(M_{Df} - M_{DO}) + \frac{M'_{Df}}{t_f^2} \end{aligned} \tag{10.6}$$

Figure 10.1 shows the position, velocity and acceleration diagram for following constraints of the delivery point; $M_{D0} = 0.0$, $M_{Df} = 350$mm, $t_f = 20$ sec , $M'_{D0} = 0.0$, $M'_{Df} = 0.0$ mm/sec.

10.4.2 Second Degree Polynomial:

Second degree polynomial is used when only three constraints are required to be

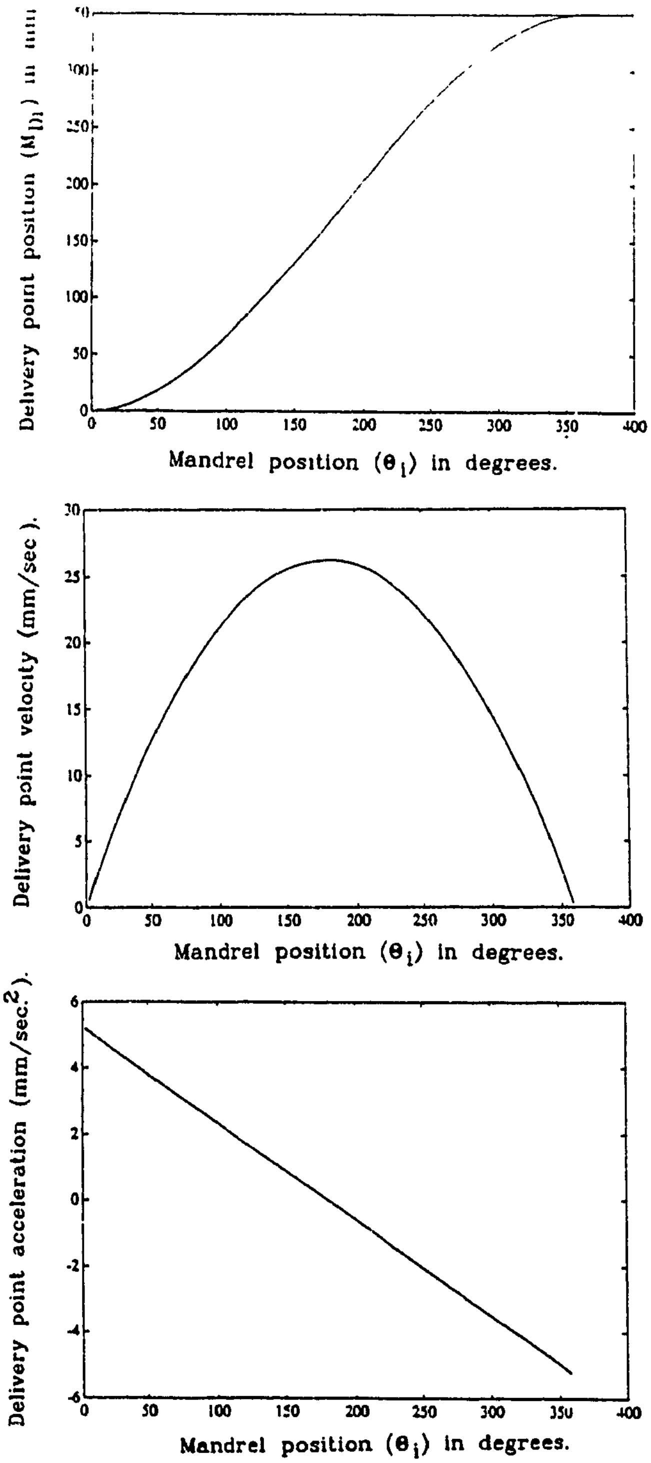

Fig. 10.1 Position, velocity and acceleration diagram for delivery point for M_{D0} = 0.0 mm, M_{Df} = 350.0 mm, M'_D (0) = 0.0 mm/sec, M'_D (t_f) = 0.0 mm/sec, t_f = 20 sec.

satisfied. In a second degree polynomial equation, a constant acceleration is used to move the delivery point.

10.5 Calculation of Fiber Winding Angle Distibution

Inverse kinematic solutions are divided into two categories. closed form solutions and numerical solutions. Closed form solutions are presented for axisymmetric and non-axisymmetric cylindrical mandrels whereas numerical solutions which are of iterative nature are presented for non-cylindrical mandrels. Numerical solution can also be applied for cylindrical mandrels.

In the previous section, equations of motion for the delivery point are presented. Once the motion is known, fiber winding angle distributions for various mandrel shapes are determined as follows. For simplicity of the analysis, mandrel is considered to be rotating at a constant speed of N rev./sec

10.5.1 Closed Form Solutions:

10.5.1.1 For a Circular Cylinder:

For a circular cylinder, when the velocity (M'_D) of the delivery point and the speed (N) of the mandrel is known then, fiber winding angle (θ_f) can be determined from following relation,

$$\theta_f = \tan^{-1} \left(\frac{M'_D}{2\pi r N} \right) \tag{10.7}$$

where, r is the radius of the cylinder.

10.5.1.2 Non-axisymmetric cylinders with curved cross-sections:

Figure 10 2 shows the cross-sectional view of a mandrel with an arbitrary mandrel cross-section Let profile of the mandrel's cross-section be represented in polar co-ordinate as $r = F(\phi)$ [83]. Velocity of the delivery point between any small interval of time t_i and t_{i+1} can be given by,

$$M'_{Di,i+1} = \frac{dM_D}{dt} = \frac{M_D(t_{i+1}) - M_D(t_i)}{t_{i+1} - t_i}$$

where, delivery point position M_D is in mm and the time t_i is in sec.
For a mandrel rotating at N rev./sec., $M'_{Di,i+1}$ is given by

$$M'_{Di,i+1} = \frac{2\pi N . M_D(t_{i+1}) - M_D(t_i)}{\theta_{i+1} - \theta_i} \qquad (10.8)$$

where, θ_i is the mandrel position in radian at a time t_i .

It has been found from the Geometric Approach [83] that

$$M_D(t_{i+1}) - M_D(t_i) = (ds_{i,i+1} + l_{i+1} - l_i)\tan\theta_f \qquad (10.9)$$

where, $ds_{i,i+1}$ is the arc length of the mandrel surface between polar angles ϕ_i and ϕ_{i+1} [83]. ϕ_i is the angle which the radius vector $O_i C_i$ makes with the engraved axis x for mandrel position of θ_i , l_i is the distance between fiber delivery point P_i and the fiber contact point (C_i) on the mandrel surface for fiber to be perpendicular to the longitudinal axis of the mandrel [83]. For detail, please see chapter 7. From Eq. 10.8 and 10.9,

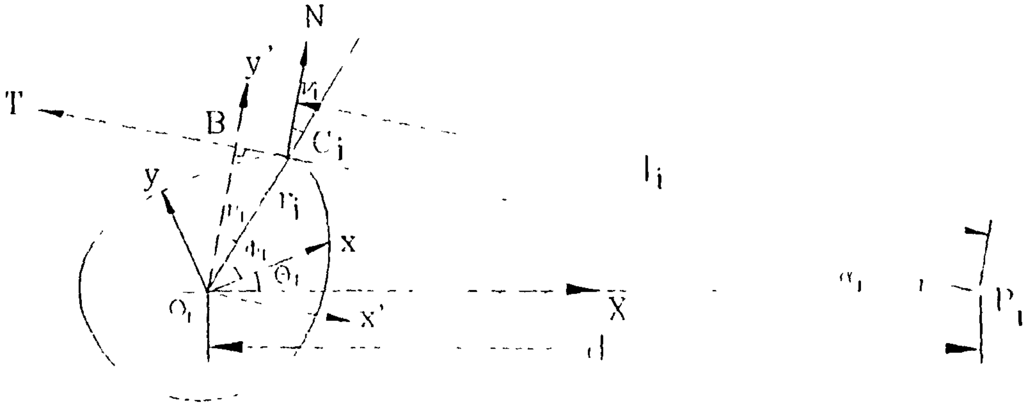

Fig. 10.2 Fiber and mandrel position at any arbitrary angle θ_i .

$$\theta_f = \tan^{-1}\frac{M'_{Dl,l+1}\ (\theta_{l+1}-\theta_l)}{2\pi N.(ds_{l,l+1}+l_{l+1}-l_l)} \qquad (10.10)$$

For a circular cylinder, $l_{i+1} - l_i = 0.0$ [83] and $ds = r\,d\theta$. Substituting these values in Eq.10.10, simplifies it to Eq. 10.7.

It is clear from Eq.10.10 that for a non-axisymmetric cylindrical mandrel, fiber angle distribution depends on the velocity trend of the delivery point and the initial position of the fiber on the mandrel surface.

Figure 10.3 shows the fiber angle distributions for a circular cylinder with radius 78mm and for an elliptical mandrel with semi-major axis of a=78mm and semi-minor axis of b=39mm for the velocity diagram shown in Fig.10.1. The delivery point distance d was kept at 755mm for both the cases

10.5.1.3 Cylindrical mandrels with polygonal cross-sections:

In the case of a polygonal cross-section, trajectory of velocity of the delivery point does not affect the fiber winding angle distribution [98]. Fiber winding angles on the faces of the mandrel depends on the delivery point positions at which fiber just overwraps the respective faces. Between these delivery point positions, trajectory of the delivery point does not affect the winding angle.

To determine the fiber winding angle on each face of the mandrel for a given equation of motion of the delivery point, consider a hexagonal mandrel as shown in Fig.10.4a. For better understanding of the present method, please see reference paper [98].

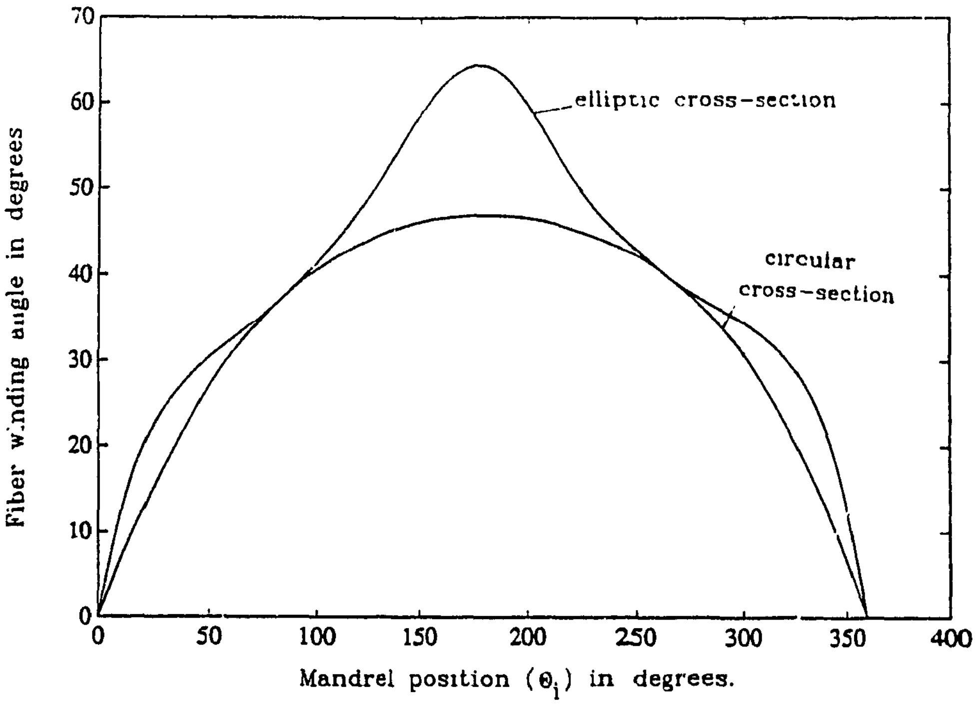

Fig. 10.3 Fiber winding angle distribution for cylindrical mandrels having circular and elliptical cross-section.

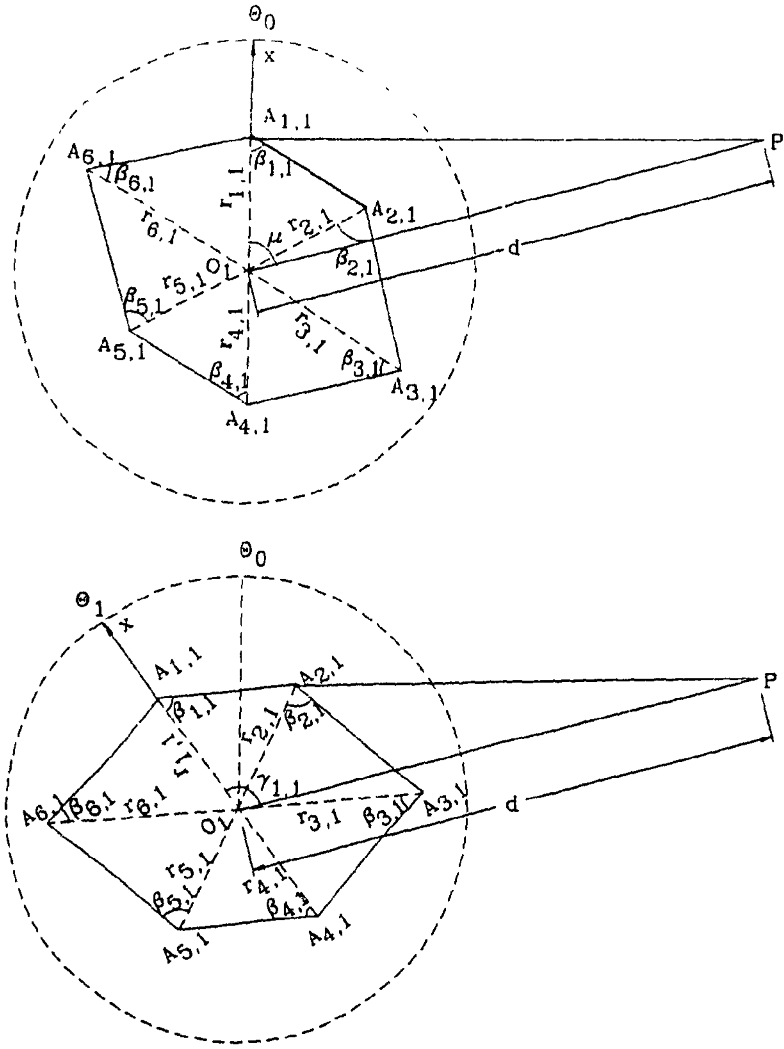

Fig. 10.4 Fiber path on hexagonal mandrel at different mandrel position.

In Fig.10.4a, P_1 is the delivery point at a distance d from the axis of rotation (O_1) of the mandrel, $A_{1,1}P_1$ is the fiber length. In the beginning of winding, let the mandrel be at $\theta = 0$ and $\angle A_{1,1} O_1 P_1$ is μ as shown in Fig 10 4a. Assuming that in the beginning the fiber was at an edge 1 and at co-ordinate z_1 Let the mandrel rotates at a constant speed and the delivery point remains stationary. At this stage, mandrel positions thus time for which the fiber overwraps corresponding mandrel faces are determined. Once the time (t_i) is known then the delivery point positions corresponding to time t_i are determined from the equation of motion of the delivery point. Finally, using algebraic and trigonometric relations, fiber winding angle is calculated.

The time t_1 at which the fiber overwraps the face 1 is determined as follows. Here face 1 is represented by line $A_{1,1} A_{2,1}$. It is clear from the Fig.10.4b that the fiber overwraps the face 1 when line $A_{1,1} A_{2,1}$ coincides with fiber $A_{1,1} P_1$. In that case,

$$\angle A_{1,1} O_1 P_1 = \gamma_{1,1} = 2\pi N t_1 + \mu \tag{10.11}$$

where, N is the mandrel speed in rev./sec.

In general,

$$\gamma_{j,i} = 2\pi N t_j + \mu - \sum_{j=2}^{j=i} \alpha_{j-1} \tag{10.12}$$

where α_j is the angle inscribed by face j at the center O. i.e. $\alpha_j = \angle A_{j,i}\, O_i\, A_{j+1,i}$.
From triangle $A_{1,1}\, O_1\, P_1$

$$A_{1,1} P_1^2 = r_{1,1}^2 + d^2 - 2 r_{1,1} d \cos(2\pi N t_1 + \mu) \tag{10.13}$$

where $r_{1,1}$ is the distance of the point $A_{1,1}$ from O_1 . $r_{j,i}$ is known from the geometry of the mandrel shape.

In general,

$$A_{j,i}P_i^2 = r_{j,i}^2 + d^2 - 2r_{j,i}d\cos(\gamma_{j,i}) \tag{10.14}$$

The condition for which the fiber overwraps the face 1 (line $A_{1,1}A_{2,1}$) is given by; $\angle O_1 A_{1,1} A_{2,1} = \beta_{1,1} = \angle O_1 A_{1,1} P_1$. So from triangle $O_1 A_{1,1} P_1$,

$$d^2 = r_{1,1}^2 + A_{1,1}P_1^2 - 2.r_{1,1}.A_{1,1}P_1.\cos(\beta_{1,1})$$

or,

$$A_{1,1}P_1 = r_{1,1}\cos\beta_{1,1} + \sqrt{(r_{1,1}\cos\beta_{1,1})^2 + (d^2 - r_{1,1}^2)} \tag{10.15}$$

All the terms on RHS of the equation 10.15 is known from the mandrel shape geometry and experimental set-up conditions. Replacing the value of $A_{1,1}P_1$ in Eq. 10.13, exact time t_1 for which the fiber overwraps the face 1 can be determined. In general above equation 10.15 can be written as

$$A_{j,i}P_i = r_{j,i}\cos\beta_{j,i} + \sqrt{(r_{j,i}\cos\beta_{j,i})^2 + (d^2 - r_{j,i}^2)} \tag{10.16}$$

where $\beta_{j,i} = \angle O_i A_{j,i} P_i$

Similarly, times t_2 , t_3 , ... for which fiber overwraps the faces 2, 3 ... and so on can be determined. For known value of time t_1 , the fiber winding angle (θ_{f1}) on face 1 is predicted using following steps.

During this t_1 sec., delivery point reaches to M_{D1} position which is determined by the equation of motion. From reference [98],

$$M_{D1} = z_1 + A_{1,1}P_1\tan\theta_{f1} \quad (10.17)$$

where, $z_1 = M_{D0}$ which is the initial delivery point position for fiber to be perpendicular to the longitudinal axis of the mandrel. Thus,

$$\theta_{f1} = \tan^{-1}\frac{(M_{D1} - z_1)}{A_{1,1}P_1} \quad (10.18)$$

All the terms on RHS of the above equation is known, so θ_{f1} is calculated from above equation 10.18. In general, delivery point positions are given by [98],

$$M_{Di} = z_i + A_{j,i}P_i\tan\theta_{fi} \quad (10.19)$$

where,

$$z_i = z_{i-1} + s_{j-1,i-1}\tan\theta_{fi-1} \quad (10.20)$$

$s_{j-1,i-1}$ is the width of j-1 face. For example $s_{1,1}$ is the width of the face 1, i e. distance between the points $A_{1,1}$ and $A_{2,1}$. It is assumed here that in the beginning fiber was at point $A_{1,1}$

So,

$$\theta_{fi} = \tan^{-1}\frac{(M_{Di} - z_i)}{A_{j,i}P_i} \quad (10.21)$$

Thus fiber winding angle distribution for a given equation of motion of the delivery point can be determined.

10.5.2 Numerical Solution For Non-cylindrical Mandrels

A Variety of non-cylindrical mandrels can be represented by axis of revolutions or by ruled surfaces [87] As discussed in the previous chapter 9, ruled surfaces represent many types of cylindrical and non-cylindrical mandrels. In the case of non-cylindrical mandrels, calculation of exact time t_i becomes difficult [95,96,97]. The equation involves sine, cosine and higher order functions of t_i.

A numerical solution is presented here to determine the fiber winding angle distribution for non-cylindrical mandrels. In this approach, a small increment in time (dt) is given and a corresponding check is performed for fiber to overwrap the respective face of the mandrel. In the case when fiber does not overwrap the face then a radial gap between the mandrel surface and fiber is calculated. In the present method, the time t_i for which fiber overwraps the respective face is determined by minimizing the radial gap.

Following steps are performed for calculating the fiber laydown path by the numerical technique. For better understanding of the method, study on the direct kinematics of filament winding (chapter 9) can be helpful.

10.5.2.1 Defining mandrel shape geometry:

10.5.2.1.1 Axisymmetric mandrels:

The surface of an axisymmetric mandrel is represented by,

$$r = f(z) \tag{10.22}$$

where, r is the radial distance of any point on mandrel's surface and z is the axis of revolution [87].

10.5.2.1.2 Ruled surfaces:

Variety of cylindrical and non-cylindrical mandrels can be represented by a ruled surface. A ruled surface is defined by [87],

$$r(u,v) = (1-v)\,r(u,0) + v r(u,1) \tag{10.23}$$

where, $0 \leq u,v \leq 1$. For present case, u is normalized by dividing polar angle by 2π and v is normalized by dividing z co-ordinate by length of the mandrel.

The input curves (boundary curves) r(u,0) and r(u,1) can be of any form defined over the same parameter interval. For instance, one end can be circular or elliptical or any shape and other end can be a polygon or any other shape. Thus, there is a large number of mandrel shapes which can be defined by the ruled surface. For the case when both the ends of the mandrel have elliptic cross-sections with different semi major and semi minor axis then,

$$r(u,0) = \frac{a_1 . b_1}{\sqrt{b_1^2 \cos^2 2\pi u + a_1^2 \sin^2 2\pi u}} \tag{10.24}$$

$$r(u,1) = \frac{a_2 . b_2}{\sqrt{b_2^2 \cos^2 2\pi u + a_2^2 \sin^2 2\pi u}} \tag{10.25}$$

In the case of a ruled surface, every isoparametric line u = constant is a straight line as shown in Fig.10.5a.

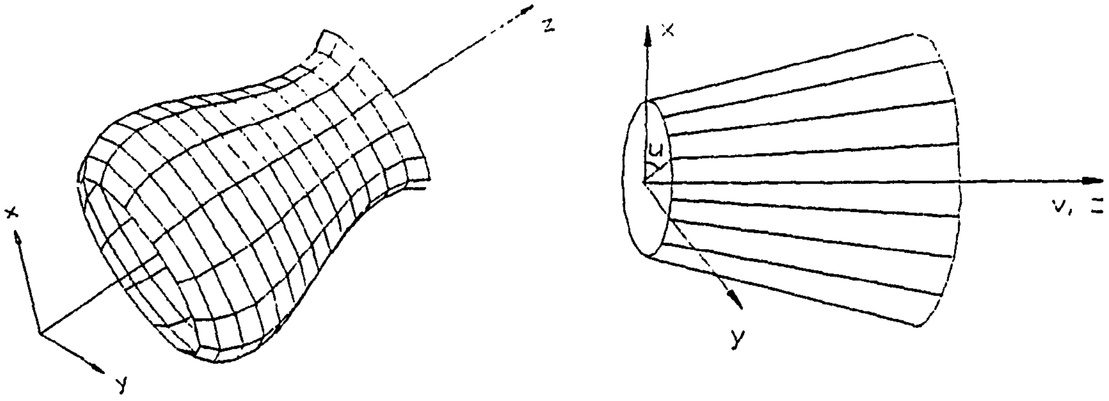

(a) nozzle

(b) both ends elliptical

Fig. 10.5 Trapezoidal faces on axisymmetric and non-axisymmetric surfaces.

10.5.2.2. Approximation of the mandrel surface:

For the present analysis, the mandrel surface has been approximated as made of many number of trapezoidal faces as shown in Fig.10.5 and as explained in previous chapter. For ruled surfaces, trapezoidal faces are constructed by drawing straight lines for $u = u_1$, $u = u_2$, ...$u = u_n$ with small increments in polar angle u and by joining the points of perimeter at $u = u_1$, $u = u_2$, $u = u_3$ ....$u = u_n$ by straight lines as shown in Fig.10.5a.

Now assume that any edge j is represented by a line $u = u_j$. Edge numbers are in increasing order opposite to the mandrel rotation. Let any jth face be a trapezoidal face consisted of j , j+1 edges and two linear segments between u_j and u_{j+1} polar angles at boundary curves. Thus n number of tapered faces are constructed for n divisions of the boundary curves. The more is the number of tapered faces, the better is the approximation of a mandrel surface.

Structures having axis of revolution e.g. nozzles, ellipsoid, paraboloid etc. can be approximated as made of series of truncated cones as shown in Fig.10.5b.

10.5.2.3 Calculation of time (t_1) for which fiber overwraps the respective face:

Consider a trapezoidal face 1 as shown in Fig.10.6. Let the mandrel be rotating at a speed of N rev./sec. In the beginning let the mandrel is at θ_0 , fiber is at z_1 , and $\angle A_{1,1}O_1P_1 = \mu$ as shown in Figs. 10.6 and 10.7. Figure 10.7 shows the side view of the mandrel position. After t_1 sec., the mandrel goes to θ_1 position and is calculated as follows:

$$\theta_1 = \theta_0 + 2\pi N t_1 \tag{10.26}$$

and the $\angle A_{1,1}O_1P_1$ will have following new value:

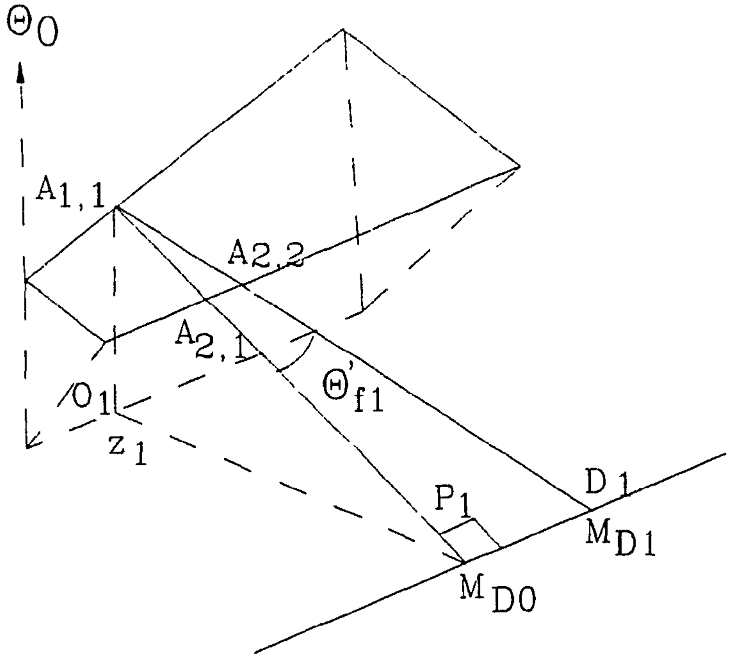

Fig. 10.6 Position of delivery point for a trapezoidal face.

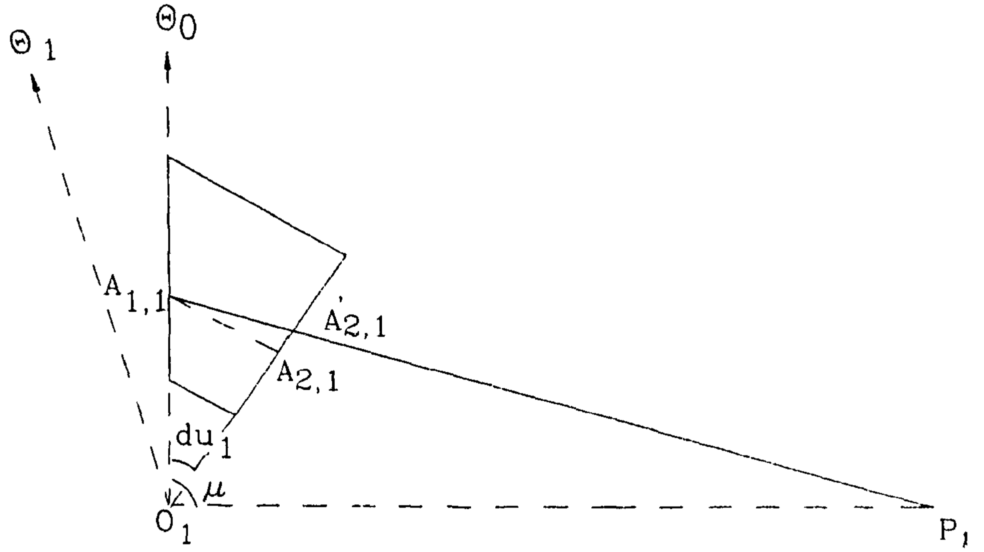

Fig. 10.7 Side view of the fiber and a trapezoidal face.

$$\angle A_{1,1} O_1 P_1 = \gamma_{1,1} = 2\pi N t_1 + \mu \qquad (10.27)$$

During this time t_1, the delivery point reaches to M_{D1} from $M_{D0} = z_1$. Figure 10.7 is the side view, when mandrel is seen along z axis. It is to be noted here that the delivery point positions and mandrel positions are changing with time according to the equation of motion

To determine the value of time t_1 for which fiber $A_{1,1} M_{D1}$ overwraps the face 1, following terms at time t_1 are calculated.

The magnitude of the fiber length $A_{1,1} P_1$ at time t_1 is calculated from the triangle $A_{1,1} O_1 P_1$ using the law of cosine,

$$A_{1,1} P_1 = \sqrt{r_{1,1}^2 + d^2 - 2 r_{1,1} d \cos(\gamma_{1,1})} \qquad (10.28)$$

where $r_{j,i} = r(u_j, v_i)$ as explained in previous chapter.

Let $\angle O_1 A_{1,1} P_1 = \eta_{1,1}$ then,

$$\eta_{1,1} = \cos^{-1}\left(\frac{{r_{1,1}}^2 + {A_{1,1}P_1}^2 - d^2}{2.r_{1,1}.A_{1.1}P_1}\right) \qquad (10.29)$$

Let $\angle P_1 A_{1,1} M_{D1} = \theta'_{f1}$, then from triangle $P_1 A_{1,1} M_{D1}$,

$$\theta'_{f1} = \tan^{-1} \frac{(M_{D1} - M_{D0})}{A_{1,1} P_1}$$

or,

$$\theta'_{f1} = \tan^{-1} \frac{(M_{D1} - z_1)}{A_{1,1}P_1} \qquad (10.30)$$

Now consider a triangle O_1 $A_{1,1}$ $A'_{2,1}$ where the point $A'_{2,1}$ is at the intersection of the line $A_{1,1}$ P_1 and O_1 $A_{2,1}$. Here the point $A'_{2,1}$ may be on the surface of the mandrel or may not be. To determine whether the point $A'_{2,1}$ lies on the surface of the mandrel, the distance between the points O_1 and $A'_{2,1}$ is calculated using the law of sine as follows.

$$A_{1,1}A'_{2,1} = \frac{r_{1,1}.\sin(2\pi.du_1)}{\sin(\pi - 2\pi.du_1 - \eta_{1,1})} \qquad (10.31)$$

$$O_1A'_{2,1} = \frac{A_{1,1}A'_{2,1}.\sin(\eta_{1,1})}{\sin(2\pi.du_1)} \qquad (10.32)$$

In above equations 10.31 and 10.32, the angle du_j is multiplied by 2π to get the value of angle in radians. This is done since u_j is normalized from 0 to 1 by dividing the polar angle by 2π as mentioned earlier. Now suppose at the time t_1 for the mandrel position of θ_1, fiber overwraps the face 1. In that case, the fiber would touch edge 2 at the point $A_{2,2}$ at the co-ordinate z_2. The magnitude of z_2 and $O_2A_{2,2}$ are calculated as follows.

$$z_2 = z_1 + dz_1 \qquad (10.33)$$

$$dz_1 = A_{1,1}A'_{2,1}\tan\theta'_{f1} \qquad (10.34)$$

$$O_2A_{2,2} = r_{2,2} = z_2.\tan\nu_2 + r(u_2,0) \qquad (10.35)$$

The taper angle (ν_j) for an edge j is given by,

$$v_j = \tan^{-1}\left(\frac{r(u_j,1) - r(u_j,0)}{l}\right) \tag{10.36}$$

where l is the length of the mandrel.

If the fiber overwraps the face 1 at time t_1 then,

$$O_1A'_{2,1} = r_{2,2} \tag{10.37}$$

If it does not overwrap the mandrel face then there will be a radial gap between the fiber and mandrel's face, which is given by,

$$error = O_1A'_{2,1} - r_{2,2} \tag{10.38}$$

In the present approach, above error is minimized to a reasonable value. In order to do this, a small increment (if error is positive) or small decrement (if error is negative) of dt in time t_1 is given and the magnitudes of O_1 $A'_{2,1}$ and $r_{2,2}$ are determined for the new value of time t_1 using above steps. For fast convergence of the solution, larger value of dt is selected for a large value of error and smaller dt is selected for the small value of error. Once the time t_1 for a least error is known then the fiber winding angle θ_{f1} on face 1 corresponding to θ'_{f1} on the cylindrical plane is calculated using following relation,

$$\theta_{f1} = \sin^{-1}\left(\frac{\sin\theta'_{f1}}{\cos v_2}.\cos\phi_{2,1}\right) \tag{10.39}$$

Above equation can be derived as follows. From triangle $A_{1,1}$ $A'_{2,1}$ $A_{2,2}$,

$$\sin\theta'_{f1} = \frac{A'_{2,1}A_{2,2}}{A_{1,1}A_{2,2}} \tag{10.40}$$

$$\cos\nu_2 = \frac{A'_{2,1}A_{2,2}}{A_{2,1}A_{2,2}} \tag{10.41}$$

Location of the point $A'_{2,1}$ for the case when fiber overwraps the face 1 is shown in Fig.10.8. Value of cos ν_2 is determined from triangle $A_{2,1}$ $A'_{2,1}$ $A_{2,2}$ as shown in Fig.10.8. Therefore,

$$\frac{\sin\theta'_{f1}}{\cos\nu_2} = \frac{A_{2,1}A_{2,2}}{A_{1,1}A_{2,2}} \tag{10.42}$$

From triangle $A_{1,1}$ $A_{2,1}$ $A_{2,2}$ for the trapezoidal face 1 as shown in Fig. 10.9,

$$\frac{\sin\theta_{f1}}{\sin(90^\circ+\phi_{2,1})} = \frac{\sin\theta_{f1}}{\cos(\phi_{2,1})} = \frac{A_{2,1}A_{2,2}}{A_{1,1}A_{2,2}} \tag{10.43}$$

Using equations 10.42 and 10.43 we can derive Eq.10.39. In the case when fiber does not overwrap the mandrel face, a small increment in time is given and it is examined whether the fiber overwraps the face 1 for the new time. Since the mandrel and delivery point positions are constantly changing, recalculation of all the parameters given in Eq.10.26 to Eq.10.38 for the new time $t_1 = t_1 + dt$ is performed. Finally comparison in the error with the set value of error is performed. Set value of error can be selected depending on the accuracy required. For ideal case error should be zero. If it is greater than the set value, reiteration of the above procedures for the new value of time is

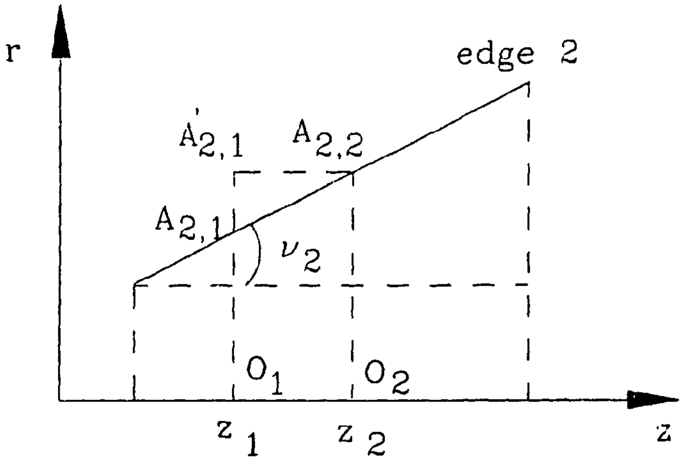

Fig. 10.8 Location of point $A'_{2.1}$.

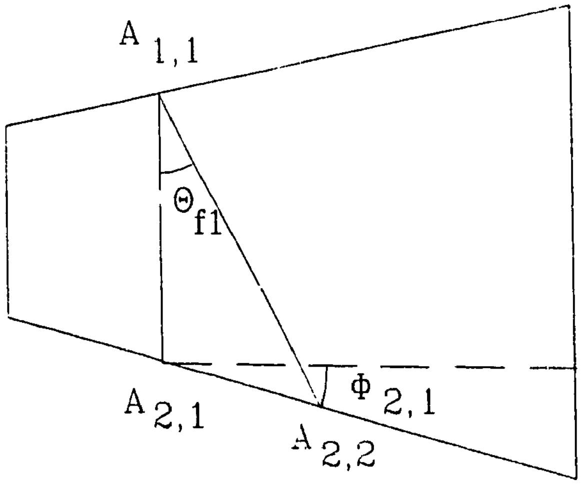

Fig. 10.9 Fiber position on tapered face 1.

performed If it is less than the set value, calculation of time t_i and fiber winding angle θ_i for other consecutive faces are performed in the similar manner.

Equations 10.26 through 10.39 can be generalized for consecutive winding as follows.

$$\theta_i = \theta_0 + 2\pi N t_i \qquad (10.44)$$

and

$$\gamma_{j,i} = 2\pi N t_i + \mu - 2.\pi.\sum_{j=2}^{j=i} du_{j-1} \quad (for j \geq 2) \qquad (10.45)$$

If the value of i is more than the total number of tapered faces n then the value of $du_j = du_{j-n}$. Similarly if the value of i is more than kth times the total number of tapered faces n, then the value of $du_j = du_{j-kn}$. The equations are writen with the assumption that the winding starts from the point $A_{1,1}$.

$$A_{j,i}P_i = \sqrt{r_{j,i}^2 + d^2 - 2.r_{j,i}.d.\cos(\gamma_{j,i})} \qquad (10.46)$$

$$\eta_{j,i} = \cos^{-1}\left(\frac{r_{j,i}^2 + A_{j,i}P_i^2 - d^2}{2.r_{j,i}.A_{j,i}P_i}\right) \qquad (10.47)$$

$$\theta'_{n} = \tan^{-1} \frac{(M_{Di} - z_i)}{A_{j,i}P_i} \qquad (10.48)$$

$$A_{j,l}A'_{j+1,l} = \frac{r_{j,l}.\sin(2\pi.du_j)}{\sin(\pi-2\pi.du_j-\eta_{j,l})} \tag{10.49}$$

$$O_lA'_{j+1,l} = \frac{A_{j,l}A'_{j+1,l}.\sin(\eta_{j,l})}{\sin(2\pi.du_j)} \tag{10.50}$$

$$z_{l+1} = z_l + dz_l \tag{10.51}$$

$$dz_l = A_{j,l}A'_{j+1,l}\tan\theta'_{fl} \tag{10.52}$$

$$r_{j+1,l+1} = z_{l+1}.\tan\nu_{j+1} + r(u_{j+1},0) \tag{10.53}$$

$$error = O_lA'_{j+1,l} - r_{j+1,l+1} \tag{10.54}$$

$$\theta_{fl} = \sin^{-1}\left(\frac{\sin\theta'_{fl}}{\cos\nu_{j+1}}.\cos\phi_{j+1,l}\right) \tag{10.55}$$

The formula given in Eq.10.44 to Eq.10.55 is used to determine the fiber laydown path for known equations of the motion.

A closed form equation can be developed to determine the exact time (t_i) for which, fiber just overwraps the respective face. This equation becomes complicated in t_i, which contains sine, cosine and higher order functions of t_i, which is difficult to solve. This is the reason, a numerical solution is presented for determining the fiber laydown path for non-cylindrical mandrels. This technique can also be applied for cylindrical mandrels.

10.6 Implementation of the Method on a Computer

An interactive computer program INVERSEKIN is developed to perform the inverse kinematic analysis for a variety of mandrel shapes. The program determines the fiber position and fiber winding angle distribution on the mandrel surface for a given equation of motion of the delivery point, mandrel shape geometry, and experimental set up conditions The user is asked to feed the constraints on the equation of motion, values on the mandrel shape geometry (e g. values on semi-major axis (a), semi-minor axis (b), length of the mandrel etc.), values on experimental set up conditions e.g. d, μ, etc. The program is written in Fortran language. The Flow Chart for the present algorithm is shown in Fig 10.10.

10.7 Experimental Verification

The present model is experimentally verified on a computer controlled McClean Anderson filament winding machine. The computer code INVERSEKIN was used for the prediction of fiber angle distribution for a given equation of the motion. Experimental verification of the method was done on a conical mandrel having length 156.7mm, end radii 57.0mm and 98.0mm Delivery point distance (d) from mandrel's axis of rotation was 450.0 mm. For axisymmetric mandrels, μ is calculated using following relation [83], $\mu = \cos^{-1}(r/d)$. The method was verified for starting as well as for reversal process.

10.7.1 Start-up period:

Figure 10.1 represents the position, velocity and acceleration diagram of the delivery point for $M_{D0} = 0.0$, $M_{Df} = 350$mm, $t_f = 20$ sec., $M'_{D0} = 0.0$, $M'_{Df} = 0.0$ mm/sec. A schematic diagram of the start-up process is shown in Fig. 10.11. In the beginning, the fiber was at radius $r =$ 57.00mm, and at $z_1 = 0.0$ mm. Values of θ_i, M_{Di} as shown in the position diagram of Fig 10.1 were fed into the computer and then machine was run to follow the equation of motion. A thread in the form of a fiber was wound on the

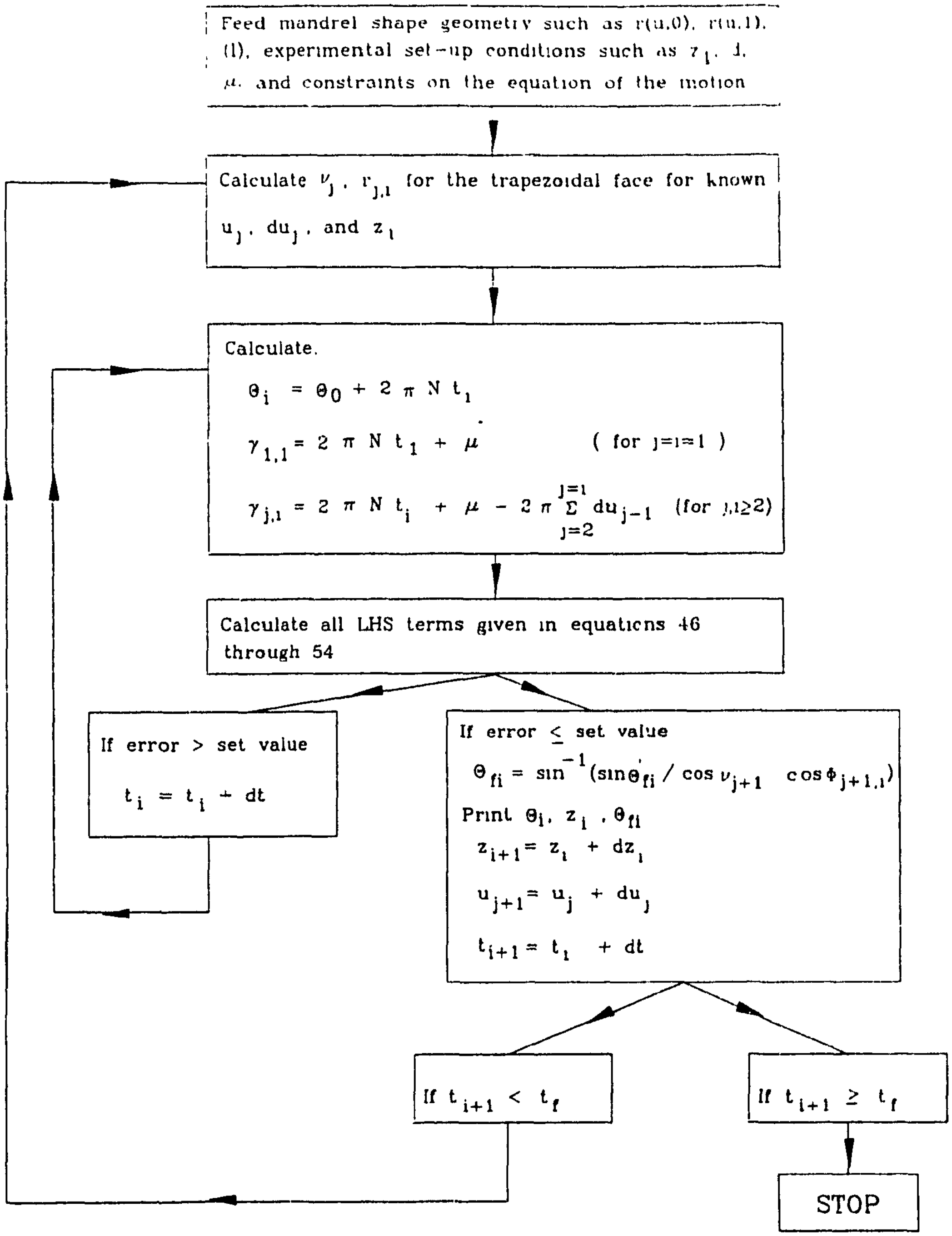

Fig. 10.10 Flow chart for the numerical solution for computer program INVERSEKIN.

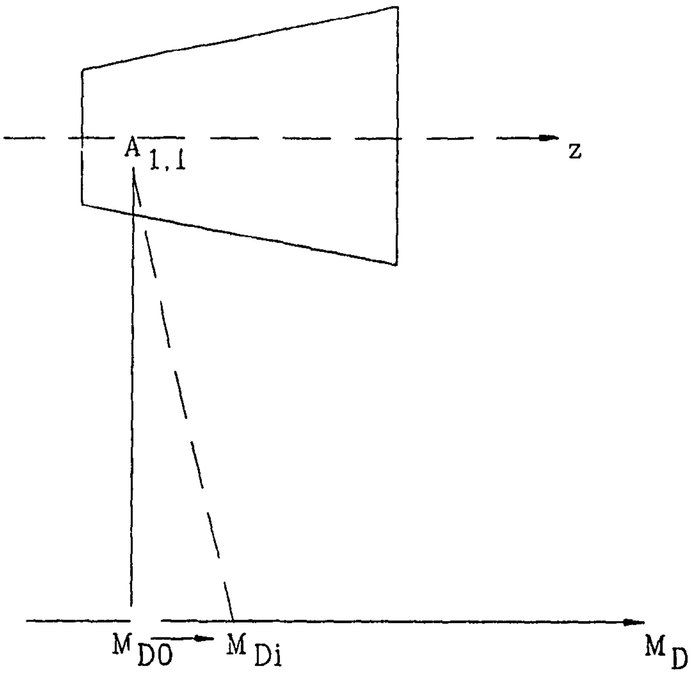

Fig. 10.11 Schematic diagram of start - up period.

mandrel surface and the laydown path was marked for the known equation of motion performed using a thread. Results on the experimental and predicted values of θ_i are shown in Fig.10.12. Maximum of 1° difference was found compared to the predicted value. Here error is not represented in terms of the percentage error to avoid the confusion.

10.7.2 Reversal period:

Figure 10.13 shows a schematic diagram of the mandrel and delivery point positions during a reversal period Fiber was kept at z_i = 100mm on the mandrel surface. Position, velocity, and acceleration diagram of the delivery point for M_{D0} = 160.0mm, M_{Df} = 0.0mm, t_f = 20 sec., M'_{D0} = 0.0, M'_{Df} = 0.0 mm/sec are shown in Fig.10.14. Results on the experimental value and the predicted value of the fiber winding angle for the delivery point trajectory of Fig.10 14 is shown in Fig 10 15 Experimental results agree well with the predicted value with the maximum difference in angle of 1° .

10.8 Fiber Slackening During Reversal Period

Fiber slackening phenomenon can be observed during a reversal process. To understand this phenomenon, let's assume that the mandrel is not rotating and delivery point is moving towards the left side as shown in the figure 10.13. It is obvious from the figure that the fiber length $A_{j,i}$ M_{Di} shortens as delivery point moves towards left and thus fiber loosening takes place. Due to the loosening of the fiber during the reversal process, there may be abrupt change in the fiber winding angle on the mandrel surface, which may cause fiber slippage. Fiber slackening should be avoided to get smooth fiber winding angle distribution on the mandrel surface.

To avoid the fiber slackening, the mandrel need to rotate at such a speed that at any two instants of time, the fiber length $A_{j,i}$ M_{Di} should increase. Value of $A_{j,i}$ M_{Di} is

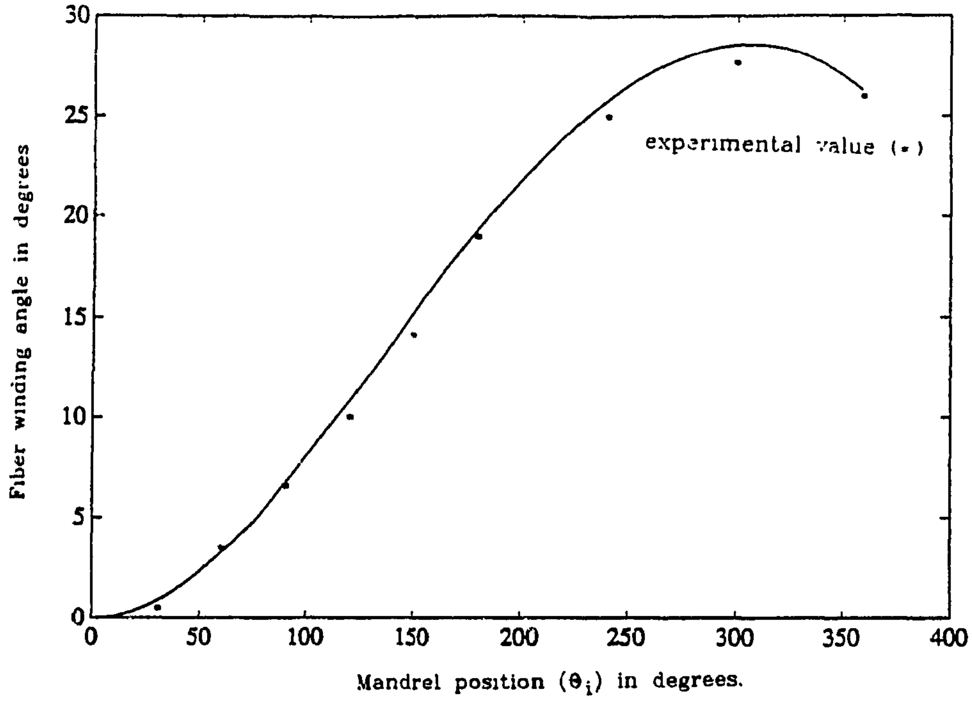

Fig. 10.12 Predicted and experimental value on fiber winding angle distribution during start - up period for a conical mandrel.

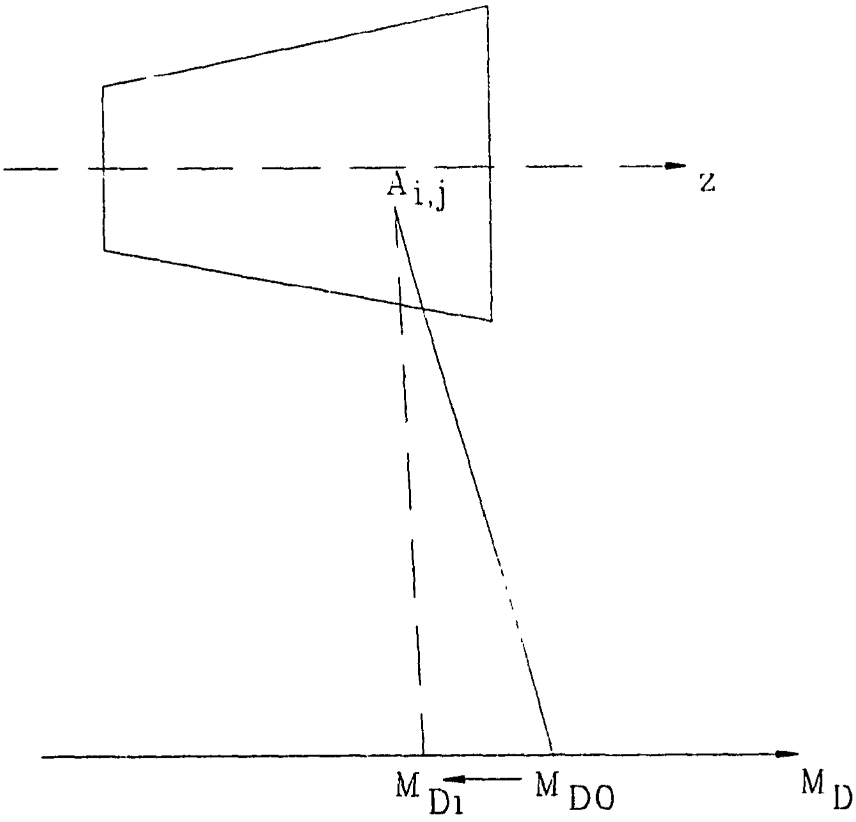

Fig. 10.13 Motion of delivery point during reversal period.

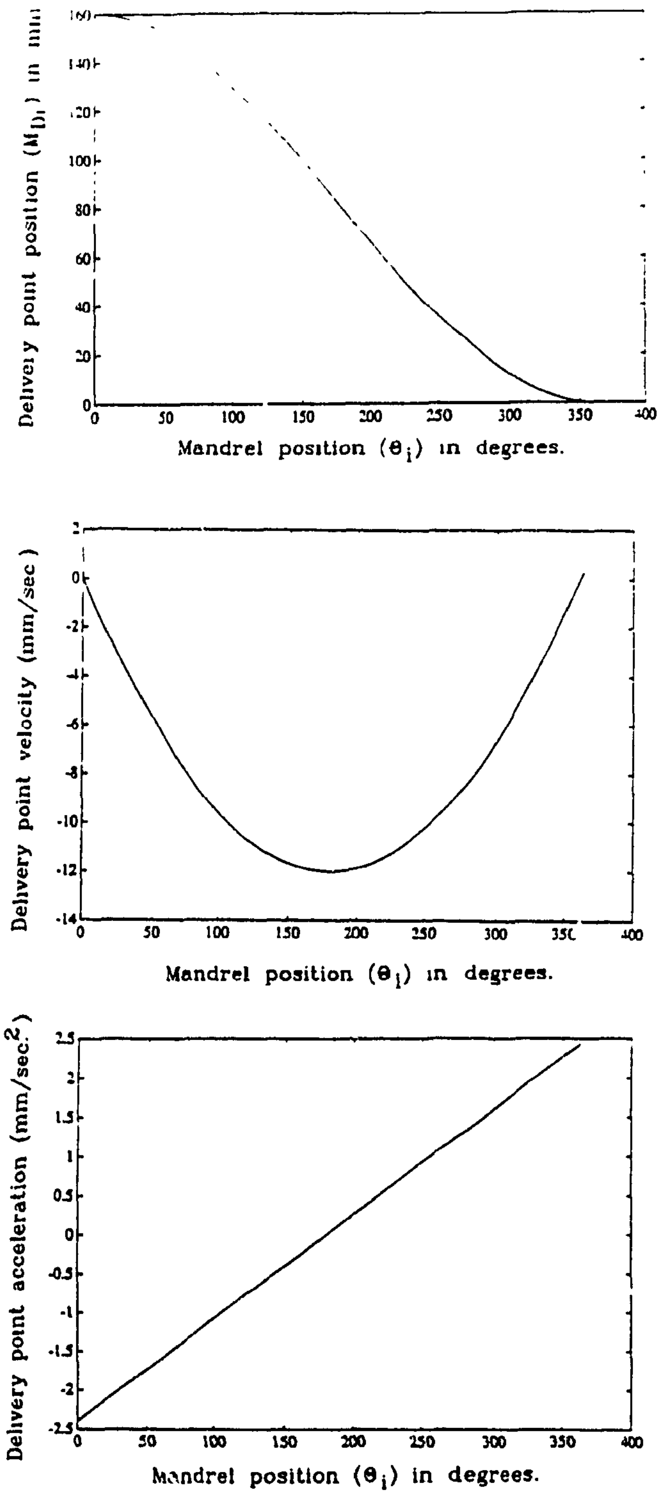

Fig. 10.14 Position, velocity and acceleration diagram for delivery point for M_{D0} = 160.0 mm, M_{Df} = 0.0 mm, M'_D (0) = 0.0 mm/sec, M'_D (t_f) = 0.0 mm/sec, t_f = 20 sec.

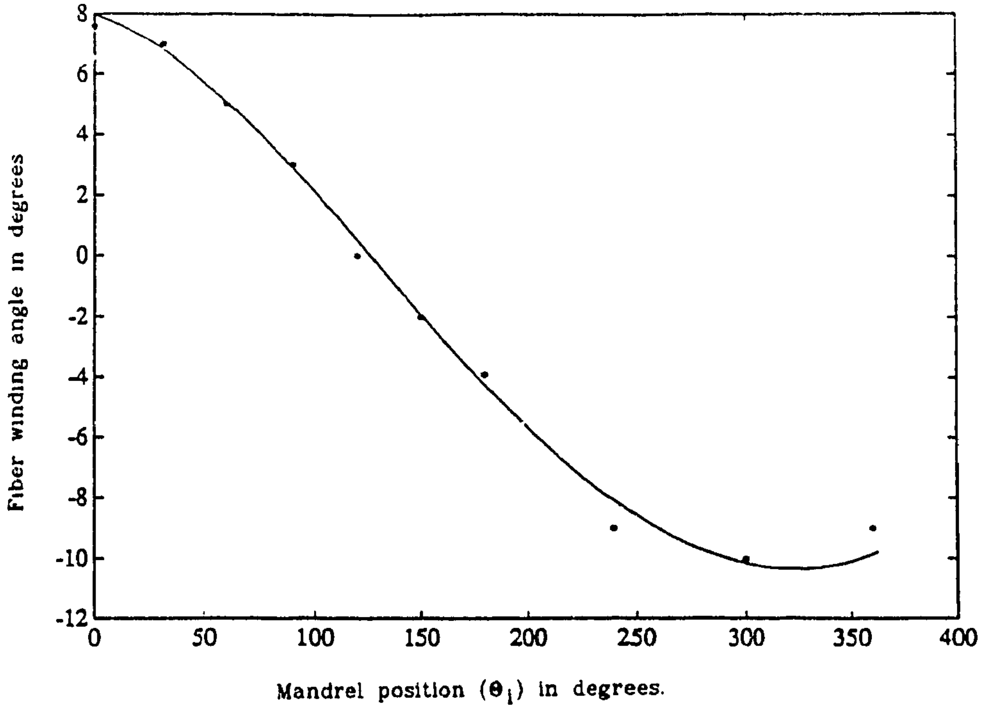

Fig. 10.15 Experimental (*) and prdicted value of fiber winding angle distribution during reversal period for a conical mandrel.

calculated by following relation.

$$A_{j,i}M_{Di} = \frac{A_{j,i}P_i}{\cos\theta'_{fi}} \tag{10.56}$$

Value of $A_{j,i}$ P_i is determined by Eq.10.46 and θ'_{fi} is determined by Eq.10.48.

10.9 Effect of Winding Speed on Fiber Distribution

With the change in winding speed (N), fiber distribution on the mandrel surface changes for the same trajectory of the delivery point. Figures 10.16 and 10.17 show the effect of winding speed N on the fiber orientation and fiber position respectively for the delivery point trajectory as shown in the Fig.10.14. The winding was started on the same conical mandrel (with $\nu = 14.59°$) at $z_1 = 0.0$ and at radius $r = 57.00$mm. It is evident from the figures that with the increase in winding speed, rate of change of θ_f with respect to the mandrel position decreases and fiber distribution takes place in larger length of the mandrel.

10.10 Effect of Delivery Point Distance on Fiber Distribution

Figures 10.18 and 10.19 show the effect of delivery point distance d on the fiber orientation and fiber position respectively. It is obvious from the figures that with the increase in delivery point distance d, the rate of change of the fiber winding angle and the fiber position with respect to the mandrel position decreases. For larger delivery point distance, fiber distribution on the mandrel surface takes place in smaller length of the mandrel with smaller difference in fiber winding angle.

10.11 Conclusion

A method is developed to determine the fiber angle distribution for given equation

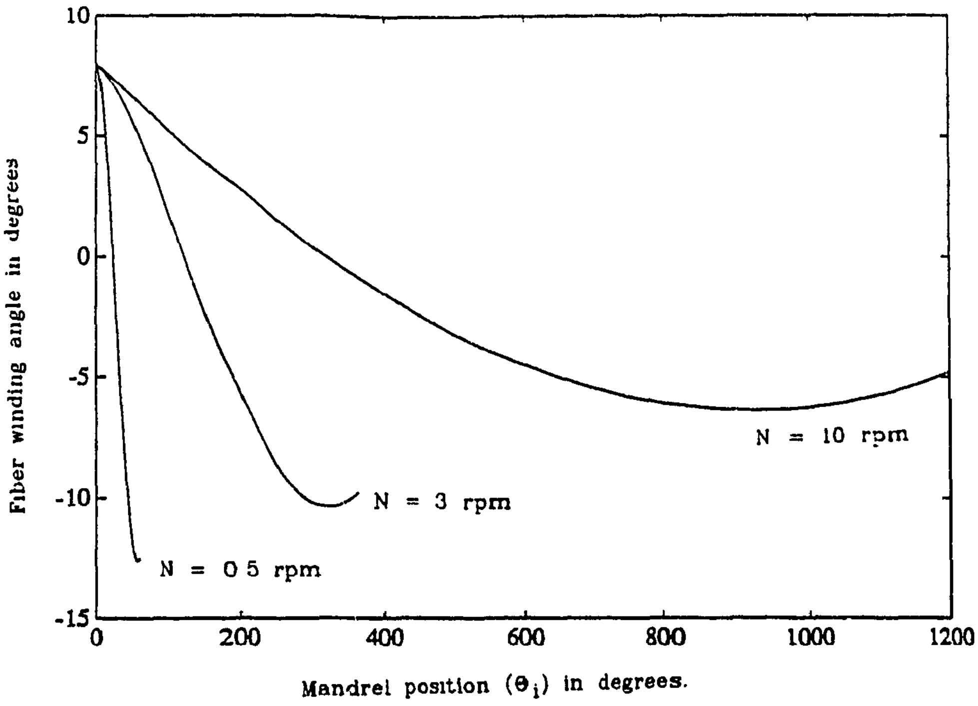

Fig. 10.16 Effect of mandrel speed (N rpm) on fiber winding angle distribution for a conical mandrel during reversal period.

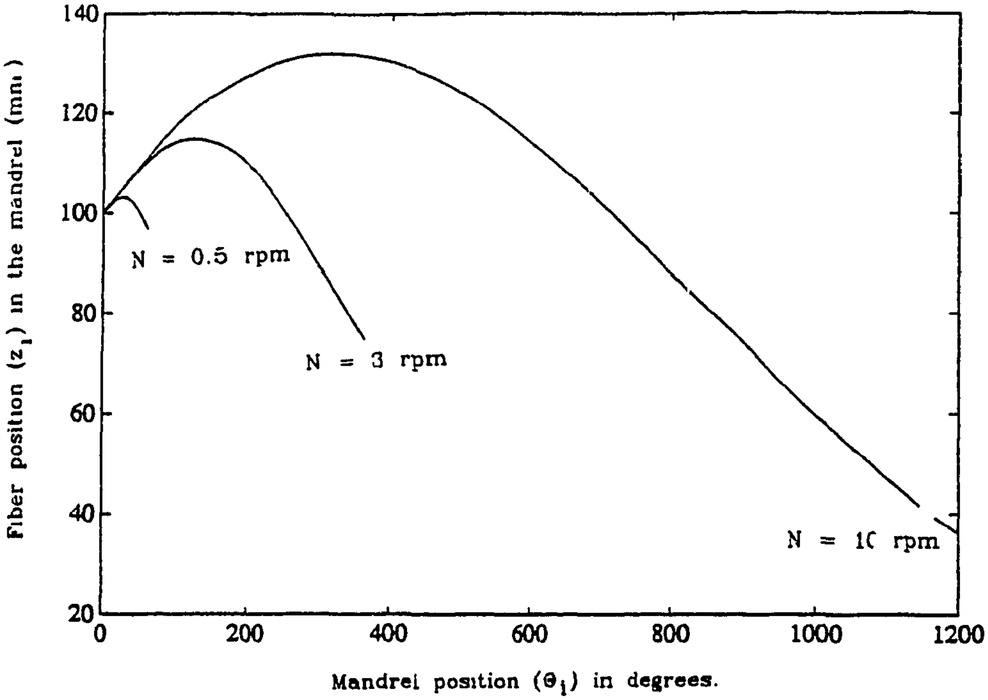

Fig. 10.17 Effect of mandrel speed (N rpm) on fiber position during reversal period.

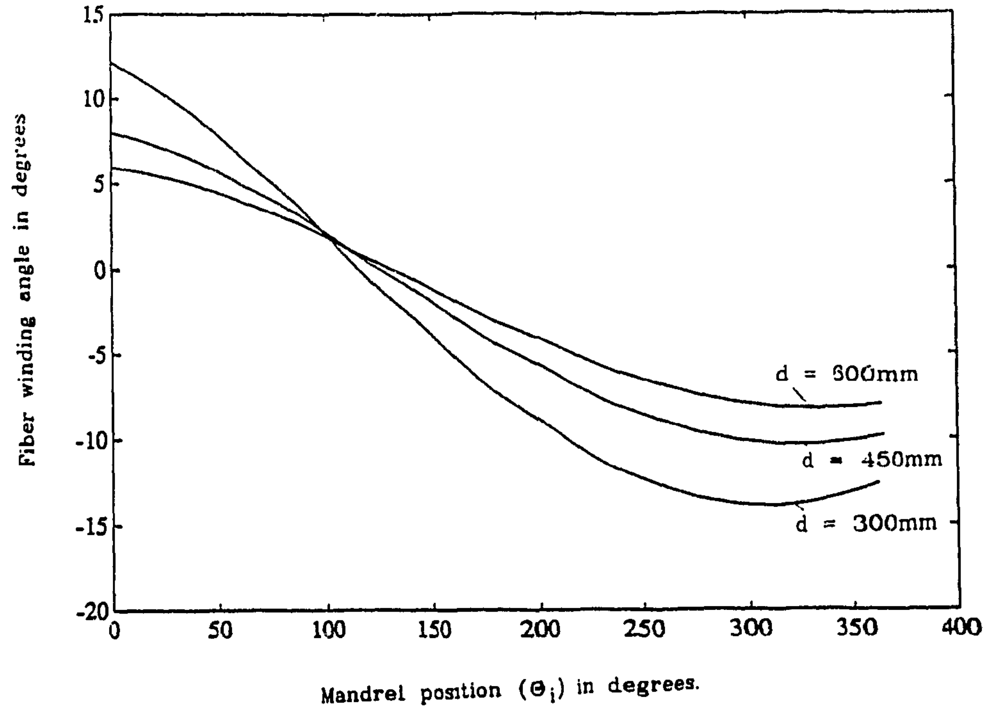

Fig. 10.18 Effect of delivery point distance on fiber winding angle distribution for a conical mandrel during reversal period.

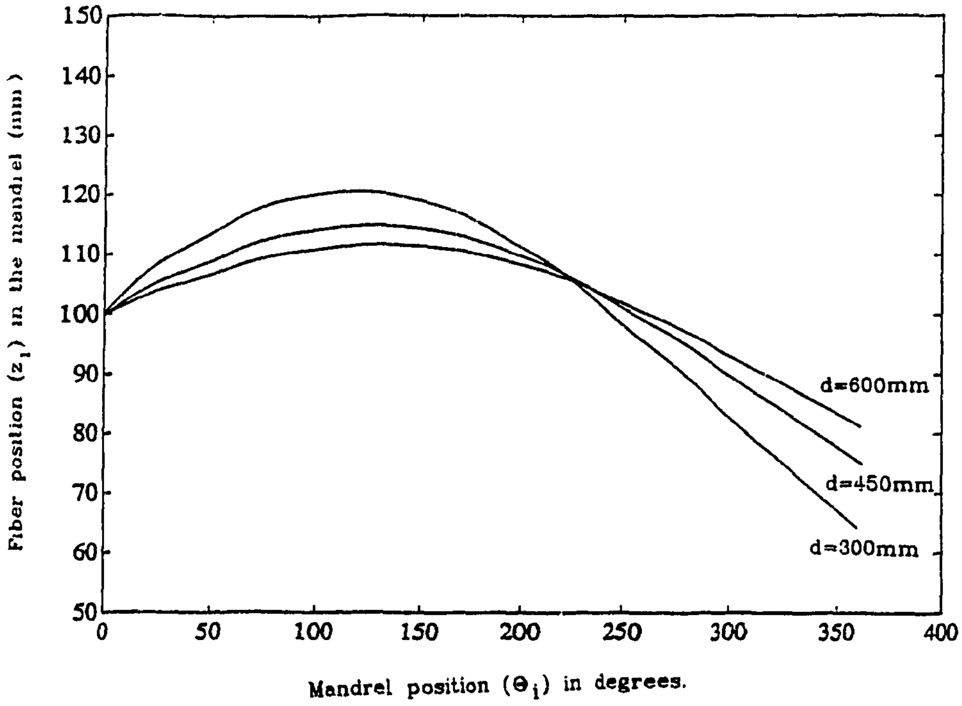

Fig. 10.19 Effect of delivery point distance on fiber position for a conical mandrel during reversal period.

of motion of the delivery point. A Closed form solution is presented to solve the inverse kinematics of filament winding for cylindrical mandrels with axisymmetric and non-axisymmetric cross-sections, whereas numerical solution is presented for non-cylindrical mandrels with axisymmetric and non-axisymmetric cross-sections.

An interactive computer program INVERSEKIN is developed to perform the study on inverse kinematics. The purpose of writing this program is to determine the effect of mandrel shape geometry, experimental set-up conditions, winding speed, etc. on fiber position and fiber winding angle distribution on the mandrel surface.

CHAPTER 11

CONCLUSIONS, CONTRIBUTIONS, AND SUGGESTIONS FOR FUTURE WORK

11.1 Conclusions and Contributions

During this study several contributions were made in the field of processing and characterization of advanced thermoplastic composites and in the area of low cost manufacturing of complex composite components by thermoplastic tape winding, tape laying, and filament winding Ultimate objectives of the present study are threefold: to be able to understand the influence of process parameters on the quality of a part; to investigate a testing method which can more easily detect the extent of bond strength; to develop cost effective techniques for the manufacture of complicated structures by thermoplastic tape winding, tape laying and filament winding The first part of the thesis (chapters 2 to 6) deals with the laser aided and gas aided processing of advanced thermoplastic composites (APC-2). Effects of dominant process parameters such as amount of heat supply, tape speed, and consolidation pressure on physical and mechanical behaviour of composite parts were investigated Process models which relate the dominant process parameters to the temperature profile and degree of consolidation were presented. Accuracy of the models were assessed by performing experiments. Microscopic study was performed to examine the quality of consolidation whereas DSC (differential scanning calorimetry) tests were carried out to determine the amount of crystallinity in the sample Influence of process parameters on internal stress generation was studied by measuring the process induced deformations. Characterization of interply bonding was performed by double cantilever curved beam (DCCB) tests, short beam shear (SBS) tests and fractographic studies. Quantitative analysis of effects of dominant process parameters on the quality of bond was performed using Taguchi method. A method for the manufacture of non-axisymmetric cylindrical shapes by thermoplastic tape winding and fabrication of complex open structures by thermoplastic tape laying was presented. Problems during the production of complex shapes by on-line consolidation process were addressed and solutions are presented by performing kinematic studies

Second part (chapters 7-10) of the thesis deals with the fabrication of axisymmetric, non-axisymmetric, cylindrical and non-cylindrical composite structures by filament winding technique. Several kinematic models based on Geometric Approach are presented for the manufacture of wide variety of composite components. Kinematic models thus developed were found to be extremely useful tools for laying down the fiber on predetermined path in lieu of costly techniques such as teach in programming, simulation, CAD/CAM, etc. The models presented are for the two-axis filament winding machine and thus any filament winding industry can use the present technique for the fabrication of a variety of composite structures. Techniques for the prediction of fiber angle distribution on a variety of mandrel shapes for known machine motions are not available. A novel approach based on Geometric Approach is developed for determining the fiber laydown path for known equation of motion of the delivery point This is important during start-up and reversal period of the filament winding operation.

The important contributions of this thesis can be summarized in following items.

1. Process models which relate the amount of heat supply, tape speed, and consolidation force to the temperature distribution, heating rate, cooling rate, melt time, and degree of intimate contact during tape consolidation process are presented.

2. Two automated processing devices for the fabrication of thermoplastic rings having circular and elliptical cross-sections were designed and built for the thermoplastic tape winding operation.

3. Suitable manufacturing conditions for laser-assisted and hot-gas-assisted processing were determined

4. Qualitative analyses of effects of amount of heat supply, tape speed and consolidation pressure on temperature distribution, crystallinity, process induced deformation, and quality of interply bonding were performed

5. Quantitative analyses of effects of amount of heat supply, tape speed and consolidation pressure on the quality of bond were evaluated using Taguchi method. Percentage contributions of individual parameter on the bond strength were calculated using ANOVA technique.

6. Optimum processing conditions for laser and hot-gas processing were investigated.

7. Kinematic models for the manufacture of non-axisymmetric shapes by thermoplastic tape winding and tape laying technique are presented

8. A new approach, Geometric Approach, is developed for the kinematic analysis of filament winding. Computer codes are developed for kinematic analysis of filament winding on axisymmetric, non-axisymmetric, cylindrical, and non-cylindrical composite structures

9. Kinematic models were developed for the manufacture of axisymmetric, non-axisymmetric, cylindrical and non-cylindrical composite components by filament winding. All the models were developed for two-axis filament winding machine and thus two-axis filament winding machines can be used for the fabrication of a variety of composite components.

10. Technique for the prediction of fiber angle distribution for known equations of motion of delivery point are not available. This is important during start-up and reversal process of filament winding operation. Based on the Geometric Approach, closed form and numerical solutions are presented for the prediction of fiber angle distribution

on axisymmetric, non-axisymmetric, cylindrical, and non-cylindrical mandrel surface for known equations of motion of the delivery point.

11.2 Suggestions for Future Work

Though significant contributions have been made in the area of on-line consolidation process and filament winding process, further work needs to be conducted in following areas for the improvement of these manufacturing technology.

1. In this study effect of amount of heat supply, tape feed rate, and consolidation pressure on temperature distribution, crystallinity, process induced deformations, and quality of bond are determined. It will be interesting to see the effect of tape and tool temperature, and cooling rate on above factors Cooling rate and dwell time can be controlled by using additional heaters after the consolidation roller.

2. Influence of laser power higher than 65 W are not examined because of limitation of the equipment. Since the quality of bond increases with the increase in laser power, a study on the effect of higher laser power could be useful.

3. Other thermoplastic composites such as polyphenylene sulfide (PPS) Ryton AC 40-60, Nylon/Graphite etc. can be used to see the feasibility of the process.

4. Effect of high heating rate and shorter melt time on crystallinity kinetics are not known. In the on-line consolidation process material undergoes heating rate more than 20,000°C / min, melt time in the range of 0.5 sec to 4 sec and cooling rate more than 4,000°C / min. Therefore development of crystallinity model for on-line consolidation process could be interesting.

5. Polymer degradation is another area that needs to be better understood, especially for PEEK and other high temperature thermoplastic resin. Effect of rapid

heating rate on degradation of thermoplastic composites could be helpful for estimating the processing window.

6. Fabrication of complex shaped structures using the models presented in this study could be very useful.

7. Testing of thermoplastic elliptical rings for the use of automobile suspension system can produce useful results.

8. Development of market-oriented computer software based on the current models can be very useful for low cost composites manufacturing by filament winding and thermoplastic tape winding.

REFERENCES

1. International Encyclopedia of Composites, Editor, Stuart M. Lee, VCH publishers, 1990

2. T.W. Chou, R.L. McCullough, and R.B Pipes, "Composites" Scientific American, Vol. 254, No. 10, pp. 192-203, 1986.

3. F. N. Cogswell, "Thermoplastic Aromatic Polymer Composites", Publisher, Butterworth - Heinemann Ltd., 1992.

4. Advanced Thermoplastic Composites: Characterization and Processing, Editor, H.H. Kausch, Publisher, Carl Hanser Verlag, 1993.

5. E.P. Beveler and S.I. Guceri, "Thermal analysis of laser assisted thermoplastic matrix composite tape consolidation ", Journal of Heat Transfer, v110, 424, 1988.

6. S.M. Grove, "Thermal modelling of tape laying with continuous carbon fibre reinforced thermoplastic", Composites, vol.19, p367, 1988

7. M.N. Ghasemi Nejhad, R.D. Cope, and S.I. Guceri, "Thermal analysis of in-situ thermoplastic composite tape laying" Journal of thermoplastic composite materials, vol. 4, p.20-45, 1991.

8. B.J. Anderson and J.S. Colton, "Automation of thermoplastic composite processing", Journal of Composite Materials, vol. 24, p.150, 1990

9. S.C. Mantell and G.S. Springer, "Manufacturing process models for thermoplastic composites", Journal of Composite Materials, vol.26, no.16, 1992.

10. M.N. Ghasemi Nejhad, J.W. Gillespie, R.D. Cope, "Prediction of Process-induced stresses for in-situ thermoplastic filament winding of cylinders, Composite Material Technology iIII, p.225.

11. S.C. Mantell and G.S. Springer, "Processing of thermoplastic composites in a press and by tape laying - Experimental results" Journal of Composite Materials, vol.26, no.16, 1992.

12. E. Beyeler, W. Phillips, and S.I. Guceri, "Experimental Investigation of laser-assisted thermoplastic tape consolidation", Journal of Thermoplastic Composite materials, vol.1, p.107, 1988.

13. D. Hauber, "Robotic filament winding with advanced thermoplastics", EM87-552, Society of Manufacturing Engineers, 1987.

14. D.E Hauber and L.A. Hill, "Automated fiber placement of thermoplastic composites on

complex shapes", EM90-658, Society of Manufacturing Engineers, 1990.

15 C Werdermann, K Friedrich, M Cirino, and R.B Pipes, "Design and fabrication of an on-line consolidation facility for thermoplastic composites", Journal of Thermoplastic Composite Materials, Vol 2, p293, 1989

16 C E Carpenter, and J S. Colton, "On- line consolidation mechanisms in thermoplastic filament winding (tape laying)", 38th International SAMPE Symposium, Anaheim, p 205, 1993.

17 V. Agarwal, "The role of molecular mobility in the consolidation and bonding of thermoplastic composite materials", Ph D. Dissertation, Materials Science Program, University of Delaware, Newark, DE, USA, 1991

18. D A. Belforte, "Laser / robot in the 1990s", Proceeding of the SPIE vol. 1276, CO_2 lasers and applications II, p 2, 1990.

19 D.A Belforte, "Laser Robotics : A moving technology" , Laser Optics, p. 2-6, Sept. 1985.

20 B.D. Thatcher and B J. Urban, "World's largest laser / robot system is a cost effective tool", Industrial Laser Review, p. 4-5, Dec. 1989.

21. P. Hoffmann, S. Biermann, M. Geiger, R. Nuss, "Three dimensional CO_2 laser material processing with gantry machine systems", Proceeding of the SPIE, vol. 1276, CO_2 lasers and applications II, p. 130, 1990

22. A. David, "Robotic manipulation for laser processing", High power lasers and their industrial applications, Proceeding of the SPIE, vol. 650, p. 262-270, 1986.

23. S. Yatsiv, A. Gabay, "A CO_2 laser mounted on a robot for dynamic cutting manipulations", Proceeding of the SPIE vol. 1276, CO_2 lasers and applications II, p. 142, 1990.

24. J. J. Luxon, "Industrial laser and their application," Prentice Hall Inc., Englewood Cliffs, 1984.

25. D. Belforte, M. Levitt, "The Industrial Laser Annual Handbook", PennWell Books, Tulsa, 1989 editions.

26. J.P. Denost, "Design of filament-wound rocket cases", AGARD lecture series no. 150, 1988.

27. K.L. Agarwal, "Effect of design/processing variables on the performance of high pressure filament wound composite pressure vessels", Advanced materials and structures from Research to Application, edited by J.Brandt, H.Honfeld, M.Nitzel, SAMPE European Chapter 1992, p403.

28. A. Amaldi, M.Marchetti, "Mechanical behaviour of filament wound carbon fibre reinforced epoxy resin tubes", Composite Material Technology III, p 79

29 M.Munro, Review of manufacturing of fiber composite components by filament winding", Polymer Composites, vol 9, no 5, p 352, October 1988

30. E.P. Calius, "Filament winding of composite cylinders" Ph.D. Thesis, Stanford University.

31. S.Y.Lee and G.S Springer, "Filament winding Cylinders", J. of Composite Materials, vol.24, p.1270, Dec 1990.

32. Z.Cai, T Gutowski and S.Allen, "Winding and consolidation analysis for cylindrical composite structures", J of Composite Materials, vol 26, no 9, p 1374, 1992

33. D O.Evans, "Simulation of Filament Winding", 30th Int SAMPE Symposium, p 1255, March 1985.

34. R.R.Roser, "Computer graphics streamline the programming of the filament winding machine", 30th Int. SAMPE Symposium, p 1231, March 1985.

35. R R. Roser, et al, "New generation computer controlled filament winding", 31st Int. SAMPE Symposium, p.810, April 1986.

36. D.L. Larson, et al, "Advancements in control systems for filament winding", 31st Int SAMPE Symposium, p222, April 1986

37. B.A.Wilson, "Filament Winding - past, present and future" 34th Int. SAMPE Symposium, p2429, May 1989.

38. G. Menges, M. Effing, "CADFIBER-A program system for design and production of composite parts" 43rd annual conference, Composites Institute, The Society of the Plastics Industry, Inc., Paper 20-D, February 1-5, 1988.

39. G.M. Wells, K.F. McAnulty, "Computer Aided filament winding using non-geodesic trajectories" in ICCM-VI and ECCM-2, Proceedings of the 6th International Conference on Composite Materials, London, UK, vol.1, pp.1.161, 1987.

40. K.V. Steiner, "Development of a robotic filament winding workststion for complex geometries", 35th Int. SAMPE Symposium, p.765, April 1990.

41. E. Bernard, A.Fahim, and M.Munro, "A CAD/CAM approach to robotic filament winding", CANCOM'91, Montreal, Quebec, Canada, 1991

42. S. A. Haq, "B-Spline Interpolationimproves filament winding controller's performance", 38th

Int SAMPE Symposium, p 163, May 1993

43 R.E Allard, J.M Charrier, S Goudreau, and L.P Hebert, "Helical filament winding on non-axisymmetric mandrels (Elliptic cross-section) - Kinematics and fiber angle distribution", 41st annual conference , Reinforced Plastics/Composites Institute, The society of the plastic industry, Inc. Paper 3-A, January 27-31, 1986

44. H. Hamouda, T J Kang and A. El-Shiekh, "On the mechanics of filament winding Part 1: A generalized model", 34th Int SAMPE Symposium, p 1130, May 1989.

45. E.D. Emerov, "Differential equation of motion of the winding point", Technology of textile Industry, USSR, p 91, No 2, 1960

46 E D. Emerov, "The equation of yarn winding on a surface of rotation", Technology of textile Industry, USSR, p.91, p 76, 1965.

47 M. Cirino, "Axisymmetric and cylindrically orthotropic analysis of filament winding", Ph.D. thesis, University of Delaware, Newark, DE, USA, 1989.

48. P.H Dara and A.C Loos, "Thermoplastic matrix composite processing model", Center for Composite Materials and Structures, Report CCMS-85-10, VPI-E-85-21, Virginia Polytechnic Institute and State University, Blacksburg, Virginia, USA, 1985.

49. A.C Loos and M.C. Li, "Modeling thermoplastic composite consolidation", p.491, ICCM-9, Spain, 1993.

50. W.I. Lee and G.S. Springer, "A model of the manufacturing process of thermoplastic matrix composites", Journal of Composite Materials, Vol 21, p. 1017, Nov. 1987.

51. R.C Don, R. Pitchumani and J.W. Gillespie, "Simulation of the transients in thermoplastic fiber placement", 39th Int SAMPE Symposium, p.1521, April 1994.

52. J.N Reddy, "An Introduction to the Finite Element Method", McGraw-Hill Inc., 1984.

53. S. Grove and D. Short, "Heat transfer in APC fabrication", Final report for I.C.I. PLC Petrochemicals and Plastic Division, Wilton, DE, 1984.

54. J.B Cattanch and F.N. Cogswell, "Processing with Aromatic Polymer Composites", Development in Reinforced Plastics, G. Pritchard, ed., Applied Science Publishers, New York, 1985.

55. D.J. Blundell, and F.M. Willmouth, "Crystalline morphology of the matrix of PEEK-Carbon Fiber Aromatic Polymer Composites", SAMPE Quarterly, Vol. 17, No. 2, pp. 50.1986.

56. Standard test method for apparent - ILSS of parallel fiber composites by short beam method, ASTM 2344 - 84, vol.15.03, Annual Book of ASTM Standards, 1992

57. C.M Tung, D.S. Gnanamuthu, R.J Moores and C.J. Leung, "Effect of Laser radiation on the rapid processing of graphite reinforced composites", 32nd Int SAMPE Symposium and exhibition, vol. 32, p. 476, 1987.

58. M. Day, J D. Cooney, and D.M. Wiles, "The thermal stability of Poly (aryl-Ether-Ether-Ketone) as assessed by thermogravimetry", Journal of Applied Polymer Science, 38, p.323-337, 1989.

59. D. Saint-Royre, D. Gueugnant, and D. Reveret, "Test methodology for the determination of optimum fusion welding conditions of polyethelene", Journal of Applied Polymer Science, 38, p.147, 1989.

60 S.K. Mazumdar and S V. Hoa, "Determination of manufacturing conditions for processing PEEK/Carbon thermoplastic composites using hot nitrogen gas by tape winding technique", Journal of Thermoplastic Composite Materials, In print.

61. D.J. Blundell, et al., "Crystalline morphology of the matrix of PEEK-Carbon fiber aromatic polymer composites, I Assessment of crystallinity" SAMPE Quarterly, Volume 16, No.4, pp 22-30, July 1985.

62. C.N. Velisaris, and J.C. Seferis, "Crystallization of polyetheretherketone (PEEK) matrices", Polymer Engineering and Science, 26:1574, 1986.

63. M.F. Talbott, G.S. Springer, and L.A. Berglund, "The effects of crystallinity on the mechanical properties of PEEK polymer and Graphite fiber reinforced PEEK" Journal of Composite Materials, Vol. 21, p.1056, November 1987.

64. Y. Lee and R.S. Porter "Effect of thermal history on crystallization of Poly (ether-ether-ketone)", Macromolecules, 21, p.2770-2776, 1988.

65. S.K. Mazumdar, and S.V. Hoa, "Experimental determination of process parameters for laser assisted processing of PEEK/Carbon thermoplastic composites", 38th International SAMPE Symposium, Anaheim, 1993.

66. J. M. Kennedy et al., "Characterization of interfacial bond strength by dynamic analysis", Journal of Composite Materials, vol.26, No.6, p.869, 1992.

67. P.J. Herrera-Franco and L.T. Drzal, "Comparison of methods for the measurement of

fiber/matrix adhesion in composites", Composites, Vol. 23, no.1, p.2, Jan. 1992.

68 R.A Bucher and J.A Hinkley, "Fiber/matrix adhesion in Graphite/PEKK composites", Journal of Thermoplastic Composite materials, Vol. 5, p.2, Jan. 1992.

69. K. Jud et al., "Fracture mechanics studies of crack healing and welding of polymers", Journal of Materials Science, 16, p 204, 1981.

70. R.A. Crick, D.C. Leach, P.J. Meakin and D.R. Moore, "International fracture morphology of carbon fibre / PEEK composites", Journal of materials science, vol. 22, p. 2094, 1987.

71. X.R. Xiao, J. Denault and T. Vu-Khanh, "The effect of low melt temperature on morphology and mode-I fracture toughness of PEEK/Carbon Composite" Journal of Thermoplastic Composite Materials, Vol.5, p.64, Jan. 1992.

72. S.K. Mazumdar and S.V. Hoa, "Processing of PEEK/Carbon thermoplastic composites using hot nitrogen gas by tape winding technique", Process Control and Instrumentation in Composite Materials Manufacturing, ASME Winter Annual Meeting, 1993.

73. S.K. Mazumdar and S.V. Hoa "Comparative effect of processing by hot gas and laser heating on properties of APC-2 (PEEK/Carbon) composite rings", ICCM-9, Madrid, Spain, July 1993.

74. R. K. Roy, A primer on the Taguchi Method, VNR Publishers, New York, 1990.

75. Taguchi, G., Introduction to Quality Engineering, UNIPUB, Kraus International Publications, New York, 1986.

76. T. B. Barker, Engineering Quality by design: Interpreting the Taguchi Approach, Marcel Dekker, Inc., New York, 1990.

77. D.J. Wilkins, V.M. Karbhari and D. A. Steenkamer, "The application of Taguchi Methodology for property and process enhancement in RTM", Proceeding of the American Society for Composites, p.843, 1991.

78. S.K. Mazumdar and S.V. Hoa, "Manufacturing of non-axisymmetric thermoplastic composite rings by tape winding technique", Second Canadian International Conference on Composites, CANCOM'93, Sept. 1993.

79. S.K. Mazumdar and S.V. Hoa, "Manufacturing of non-axisymmetric composite shapes by thermoplastic tape winding", Materials and Manufacturing Processes, Vol. 10, No. 1, p.47, 1995.

80. S.K. Mazumdar and S.V. Hoa, "Manufacturing of thermoplastic Composite parts by tape winding and tape laying techniques", 26th International Symposium on Automative Technology

and Automation, Germany, Sept. 1993.

81. P.K. Mallick "Design and development of composite elliptic springs for automotive suspensions" 40th Annual conference, Reinforced Plastic / Composite Institute, The Society of the Plastic Industry, Inc , Jan.28 - Feb.1, 1985, p.14c.

82. P.K. Mallick, "Static mechanical performance of composite elliptic springs", Journal of Engineering Materials and Technology, Transactions of the ASME, vol 109, p 22, January 1987.

83. S.K. Mazumdar and S.V. Hoa, "On the kinematics of filament winding on non-axisymmetric cylindrical mandrels, Part I; A generalized model", Composites Manufacturing, vol.2, no 1, p.23, 1991.

84. R. Pitchumani, S. Ranganathan, R.C. Don, and J.W. Gillespie, "Effects of processing conditions on void growth during thermoplastic fiber placement", p 71, AMD-Vol. 194, International Mechanical Engineering Congress and Exposition, ASME, Chicago, Illinois, 1994.

85. K. W. Kirberg, G. Menges, J. Mitscherling, "How to determine control data for filament winding" 42nd annual conference, Composites Institute, The Society of the Plastics Industry, Inc. Paper 6-F, February 2-6, 1987.

86. B. Paul, "Kinematics and dynamics of planar machinery", Prentice Hall, Inc. Englewood Cliffs, New Jersy, 1979.

87. S.K. Mazumdar and S.V. Hoa, "Filament winding on tapered axisymmetric and non-axisymmetric composite components", 13th International SAMPE conference, Hamburg, May, 1992.

88. G. Farin, "Curves and surfaces for computer aided geometric design· A practical guide", Academic Press Inc., Harcourt Brace Jovanovich Publishers, 1990.

89. G. Menges, R. Wodicka and H.L. Barking, "Non-geodesic winding on a surface of revolution", 33rd annual conference, Composites Institute, The Society of the Plastics Industry, Inc. , 1978, Paper 10-D.

90. Xian-li Li, Dao-hai Lin, "Non-geodesic winding equations on a general surface of revolution", p.1.153, Vol. 1, ICCM-VI and ECCM-2, London, UK, 1987

91. S.K. Mazumdar and S.V. Hoa "Algorithm for filament winding of non-axisymmetric tapered composite components having polygonal cross-section on two axes filament winding machine", Composites Engineering, Vol. 4, no.3, pp. 343-359, 1994.

92. R. S. Gross and J.G. Goree, "An experimental and analytical investigation of composite drive shafts with non-circular end cross--sections", Journal of composite materials, vol. 27, no.7, p.702, 1993.

93. J.M.Charrier, L.P. Hebert, and S.G. Maki, "Kinematics of filament winding on slender mandrels", 42nd annual conference, SPI, 20-A, Feb.1987.

94. J.J.Craig, Introduction to Robotics, Addison-Wesley Publishing company, 1989.

95. S.K. Mazumdar and S.V. Hoa, "Kinematics of filament winding during starting and reversal process for complex composite components", CSME Forum 1992, Transport 1992+,, Montreal, Canada, June 1992.

96. S.K. Mazumdar and S.V. Hoa, "Determination of fiber winding angle distribution during filament winding process for known winding motions", 2nd International Symposium on Composite Materials and Structures, August 1992, Beijing, China.

97. S.K. Mazumdar and S.V. Hoa, "Kinematics of filament winding during starting and reversal process for complex composite components", Transactions of the Canadian Society for Mechanical Engineering, vol. 17, no. 4A, p. 671, 1993.

98. S.K. Mazumdar and S.V. Hoa, "On the kinematics of filament winding on non-axisymmetric cylindrical mandrels, Part II: For convex polygonal cross-section", Composites Manufacturing, 2(1), p.31, 1991.